UNIVERSIDADE D
COIMBRA

Hazem Radwan Hadla

Predictive Load Angle and Stator Flux Control of SynRM Drives for the Full Speed Range

Thesis in the scope of the PhD in Electrical and Computer Engineering, specialization in Energy, supervised by Professor Sérgio Manuel Ângelo da Cruz and presented to the Department of Electrical and Computer Engineering of the Faculty of Sciences and Technology of the University of Coimbra.

August of 2018

UNIVERSIDADE D
COIMBRA

Faculty of Sciences and Technology

Predictive Load Angle and Stator Flux Control of SynRM Drives for the Full Speed Range

Hazem Radwan Hadla

Thesis in the scope of the PhD in Electrical and Computer Engineering, specialization in Energy, supervised by Professor Sérgio Manuel Ângelo da Cruz and presented to the Department of Electrical and Computer Engineering of the Faculty of Sciences and Technology of the University of Coimbra.

August of 2018

Acknowledgement

I wish to express my sincerest gratitude foremost to my supervisor Prof. Sérgio Cruz for his continuous support during my Ph.D study and research, for his patience, motivation, enthusiasm and immense knowledge. His guidance helped me during my research and writing of this thesis.

I gratefully acknowledge the global platform and scholarships provided to Syrian students. This has enabled me to pursue my study in Portugal. My sincere thanks and gratitude goes to Prof. Jorge Sampaio who took the initiative to support us when it seemed all doors were closed to us, in addition, I would like to express my deepest sense of appreciation to Dr. Helena Barroco who was present whenever I needed help.

I would like to thank the Instituto de Telecomunicações for being the host institution where the research work documented in this thesis was developed. In particular, I would like to thank the laboratory facilities which made it possible for me to carry out all the experimental work required. In addition, I would like to extend my thanks to the Department of Electrical and Computer Engineering at the University of Coimbra for offering me the use of their research facilities and making it possible for me to complete this research work.

My sincere thanks also goes to my fellow colleagues: Pedro Gonçalves, Sérgio Júnior and Diego García, for the time we worked and discussed together matters concerning our research topics. Their assistance aided me in my research work.

I want also to thank my friend Fran Correia and her family who supported and helped me immensely to pass through difficult times. Her advice was and is still so important to me.

Last but certainly not least, I would like to thank my family for their support, not just during this work but also during my entire life. I know both my family and myself have experienced great difficulty from living so far from each other and the inability to see each other for eight years. I hope one day we will meet again and forget all the hardships we have had in our lives. My dear parents and family, you are always in my thoughts and prayers, God bless and protect you.

Hazem Radwan Hadla

Abstract

Nowadays, several types of electric motors are utilized in industrial applications, namely induction motors (IMs), permanent magnet synchronous motors (PMSMs) and synchronous reluctance motors (SynRMs). Owing to the high cost of PMSMs and due to the rotor losses of IMs, SynRMs can be considered an ideal choice for some applications. These motors have a simple structure, are robust, and have a low cost due to the absence of permanent magnets or windings in the rotor.

To exploit the advantages of SynRM drives, an adequate control strategy is essential. In recent times, due to the development of fast and cheap microprocessors and FPGAs, the category of control strategies known as finite control set model predictive control (FCS-MPC) has attracted significant attention in both academia and industry. FCS-MPC has as main advantages, an intuitive and simple implementation, very fast dynamic response and the ability to tackle several constraints in a straightforward manner. Due to these advantages, it can be considered an ideal alternative to field-oriented control (FOC) and direct torque control (DTC) in high performance motor drives. In spite of its advantages, FCS-MPC has been barely proposed for the control of SynRM drives, especially if we consider that some applications require the drive system to operate in the full speed range.

This thesis proposes three different FCS-MPC control strategies for high-performance SynRM drives. The first two control strategies combine the concepts of active flux and torque control in order to operate the SynRM in the constant torque region. The first control strategy, baptized as predictive active flux and torque control (PAFTC), regulates the active flux and the electromagnetic torque of the SynRM in an independent manner. It follows the standard implementation steps of FCS-MPC, namely by predicting the values of the state variables for all possible switching states of the inverter, and by using a cost function with a weighting factor which needs to be tuned. A second control approach, known as simplified PAFTC (S-PAFTC), is a simplified version of the PAFTC in the sense that the predictions of the state variables are replaced by the calculation of an equivalent reference voltage, performed only once in a sampling period. This procedure leads to a smaller computational time, when the control strategy is implemented in a digital control

platform, and to the use of a cost function without any weighting factor, overcoming one of the challenging tasks in classical FCS-MPC strategies which is the choice of the optimal value(s) for the weighting factor(s). The simulation and experimental results obtained with these control strategies demonstrate the very good steady-state and dynamic response of the SynRM drive in the constant torque region.

With the aim to safely operate the SynRM drive in the full speed range, while ensuring at the same time the exploitation of all its potentialities and limits, including its operation with optimal efficiency, a third control strategy, known as predictive load angle and stator flux control (PLASFC), is proposed for SynRM drives.

The PLASFC, implemented in a stator flux reference frame, regulates the stator flux and the load angle of the SynRM in an independent manner. While the stator flux regulation is straightforward, the torque is regulated indirectly by controlling the load angle, bringing benefits in terms of a smooth transition between the different motor operating regions. Similarly to the S-PAFTC strategy, an equivalent reference voltage is calculated instead of predicting the values of the motor state variables for all possible switching states of the inverter, and the cost function does not include any weighting factor.

In the PLASFC strategy, the SynRM is easily operated in the full speed range: constant torque region (including zero speed), constant power region and constant load angle region, the last two being part of what is usually known as field-weakening (FW) region. With this control strategy, the voltage, current and load angle limits are easily exploited by simple mathematical relations and saturation blocks. In addition, a loss minimization algorithm is developed and incorporated in this control strategy thus allowing to operate the SynRM with minimum copper losses for a given load torque. Furthermore, to improve the performance of the control system, some parameters namely the motor apparent inductances, are estimated online. Several simulation and experimental results presented demonstrate the excellent steady-state and dynamic performance of the SynRM drive when operating with the PLASFC strategy, thus clearly demonstrating the benefits of using FCS-MPC strategies in the field of electric drives in general and SynRM drives in particular.

Keywords: Field-weakening, Finite control set, Full speed range, Model Predictive Control, Synchronous reluctance motor.

Resumo

Atualmente, diversos tipos de motores elétricos são utilizados em aplicações industriais, nomeadamente os motores de indução (IMs), os motores síncronos de ímanes permanentes (PMSMs) e os motores síncronos de relutância (SynRMs). Devido ao elevado custo dos PMSMs e às perdas no rotor dos motores de indução, os SynRMs podem ser considerados a escolha ideal para algumas aplicações. Estes motores possuem uma estrutura simples, são robustos e têm um baixo custo de fabrico devido à ausência de ímanes permanentes ou enrolamentos no rotor.

De modo a explorar toda as vantagens dos acionamentos baseados em SynRMs, é essencial uma estratégia de controlo adequada. Recentemente, em virtude do desenvolvimento de microprocessadores e FPGAs mais rápidos e económicos, a categoria de controlo conhecida como controlo preditivo baseado em modelos de estados finitos (FCS-MPC) tem despertado um especial interesse no mundo académico e na indústria. O FCS-MPC tem várias vantagens, tais como uma implementação simples e intuitiva, uma rápida resposta dinâmica e a possibilidade de considerar várias restrições de uma forma direta. Devido a estas vantagens, o FCS-MPC pode ser considerado uma alternativa ideal ao controlo por orientação de campo (FOC) e ao controlo direto de binário (DTC) em acionamentos de alto desempenho. Apesar das suas vantagens, o FCS-MPC ainda tem sido pouco utilizado no controlo de acionamentos baseados em SynRMs, especialmente se considerar que algumas aplicações necessitam que o acionamento opere em toda a gama de velocidades.

Esta dissertação propõe três estratégias de controlo FCS-MPC para acionamentos de alto desempenho baseados num SynRM. As duas primeiras estratégias de controlo combinam os conceitos do fluxo ativo e do controlo de binário, de modo a operar o SynRM na região de binário constante. A primeira estratégia, denominada controlo preditivo do fluxo ativo e de binário (PAFTC), regula o fluxo ativo e o binário eletromagnético do SynRM de forma independente. A estratégia PAFTC segue a estrutura padrão do FCS-MPC, uma vez que prevê os valores futuros das variáveis de estado para todos os estados de comutação possíveis do inversor, e utiliza uma função de custo com um peso que necessita de ser sintonizado. Uma segunda abordagem de controlo, denominada PAFTC simplificado (S-PAFTC), é uma

versão simplificada do PAFTC uma vez que o cálculo das predições das variáveis de estado é substituído pelo cálculo das tensões de referência equivalentes, realizado apenas uma vez num período de amostragem. Esta estratégia de controlo possui um tempo de execução menor, quando implementada numa plataforma de controlo digital e, faz uso de uma função custo sem qualquer peso, ultrapassando um grande desafio das estratégias FCS-MPC clássicas, que é a escolha do(s) valor(es) ótimo(s) para o(s) peso(s). Os resultados de simulação e experimentais obtidos com estas estratégias de controlo mostram excelente desempenho do acionamento baseado no SynRM na região de binário constante, tanto em regime permanente como em regime dinâmico.

Com o objetivo de operar o acionamento baseado no SynRM de forma segura em toda a gama de velocidades, e ao mesmo tempo assegurar que todas as suas potencialidades e limites são explorados, incluindo uma operação com eficiência ótima, uma terceira estratégia de controlo, conhecida como controlo preditivo do ângulo de carga e fluxo estatórico (PLASFC), é proposta para acionamentos baseados em SynRMs.

A estratégia de controlo PLASFC, implementada no referencial do fluxo estatórico, controla o fluxo estatórico e o ângulo de carga do SynRM de forma independente. Enquanto que a regulação do fluxo estatórico é direta, a regulação do binário é realizado de forma indireta através do controlo do ângulo de carga, o que conduz a uma transição suave entre as diferentes regiões de operação do motor. Tal como na estratégia S-PAFTC, as tensões de referência equivalentes são calculadas ao invés de prever os valores futuros das variáveis de estado do motor para todas os estados de comutação do inversor possíveis, e a função custo não inclui qualquer peso.

Na estratégia PLASFC, o SynRM é facilmente operado em toda a gama de velocidades: região de binário constante (incluindo a velocidade zero), região de potência constante e região de ângulo de carga constante, sendo que as últimas duas regiões pertencem à região normalmente designada por região de campo enfraquecido (FW). Com esta estratégia de controlo, os limites de tensão, corrente e ângulo de carga são facilmente explorados através de relações matemáticas simples e blocos de saturação. Adicionalmente, um algoritmo de minimização de perdas é desenvolvido e incorporado nesta estratégia de controlo, permitindo que o SynRM opere com perdas no cobre mínimas para um dado binário de carga. Além disso, para melhorar o desempenho do sistema de controlo, alguns parâmetros tais como as

indutâncias aparentes do motor são estimadas em tempo real. Por fim, são apresentados múltiplos resultados de simulação e experimentais que demonstram um excelente desempenho do acionamento baseado no SynRM quando operado através da estratégia PLASFC tanto em regime permanente quanto em regime dinâmico, demonstrando claramente os benefícios da utilização das estratégias FCS-MPC no campo dos acionamentos elétricos em geral e, particularmente, nos acionamentos baseados em SynRMs.

Palavras-chave: Campo enfraquecido, Controlo de estados finitos, Gama de velocidades completa, Controlo preditivo baseado em modelos, Motor síncrono de relutância.

Table of Contents

List of Figures

List of Tables

List of Symbols

B_m	Viscous friction coefficient	N.m.s/rad
J_m	Rotor inertia of SynRM	kg.m^2
K_p	Proportional gain of the PI speed controller	
K_p^{ui}	Proportional gain of the PI of the stator flux and load angle observer	
L_d, L_q	Apparent inductances of the stator windings, in dq-axes	H
$\hat{L}_d, \hat{L}_q$	Estimated apparent inductances of the stator windings, in dq-axes	H
L_d^{inc}, L_q^{inc}	Self-incremental inductances of the stator windings, in dq-axes	H
L_{dq}^{inc}, L_{qd}^{inc}	Cross-incremental inductances of the stator windings, in dq-axes	H
R_c	Iron loss resistance	Ω
R_s	Stator resistance	Ω
S	Inverter switching state	
S_i	Sectors of the stator flux space vector	
T_D	Inverter dead-time	μs
T_e	Electromagnetic torque	N.m
T_e^*	Reference torque	N.m
$\hat{T}_e$	Estimated electromagnetic torque	N.m
T_i, T_i^{ui}	Integral time of PIs used in the speed controller and stator flux observer	s
T_L	Load torque	N.m

T_n	Rated torque	N.m
T_s	Sampling time	μs
U_{dc}	DC-link voltage	V
$U_{n(motor)}$	Motor rated voltage	V
i_a, i_b, i_c	Stator phase currents	A
i_d, i_q	Stator phase currents in the dq rotor reference frame	A
i_{ds}, i_{qs}	Stator phase currents in the $d_s q_s$ stator flux reference frame	A
i_α, i_β	Stator phase currents in the $\alpha\beta$ reference frame	A
i_s	Stator current magnitude	A
i_{dc}	DC-link current	A
i_{max}	Maximum inverter output current	A
p	Number of pole-pairs	
p_1, p_2, p_3	Coefficients of the interpolation polynomial	
u_{comp}	Compensation term of the stator flux and load angle observer	V
u_{max}	Maximum inverter voltage	V
u_d, u_q	Stator phase voltages in the dq rotor reference frame	V
u_d^*, u_q^*	Reference voltages in the dq rotor reference frame	V
u_{ds}, u_{qs}	Stator phase voltages in the $d_s q_s$ stator flux reference frame	V
u_{ds}^*, u_{qs}^*	Reference voltages in the $d_s q_s$ stator flux reference frame	V
u_α, u_β	Stator phase voltages in the $\alpha\beta$ reference frame	V

δ	Load angle	rad
δ_{max}	Maximum load angle	rad
ξ	SynRM saliency ratio	
θ_i	Stator current angle	rad
θ_i^{opt}	Optimal stator current angle	rad
θ_m	Mechanical rotor position	rad
θ_r	Electrical rotor position	rad
θ_{ψ_a}	Active flux angle	rad
$\hat{\theta}_{\psi_s}$	Estimated stator flux angle	rad
λ_{ψ_a}, λ_{ψ_s}	Weighting factors	
ψ_a	Active flux	Wb
ψ_a^*	Reference active flux	Wb
ψ_{an}	Rated active flux	Wb
$\hat{\underline{\psi}}_s$	Estimated stator flux	Wb
ψ_s^*	Reference stator flux	Wb
$\hat{\underline{\psi}}_s^i$	Space vector of the estimated stator flux using the current model	Wb
ψ_s^{opt}	Optimal stator flux value	Wb
$\hat{\underline{\psi}}_s^u$	Space vector of the estimated stator flux using the voltage model	Wb
$\hat{\psi}_{s\alpha}, \hat{\psi}_{s\beta}$	Estimated stator flux components in the $\alpha\beta$ stationary reference frame	Wb
ψ_d, ψ_q	Stator flux components in the dq rotor reference frame	Wb

Ω_m	Mechanical angular rotor speed	rad/s
Ω_m^*	Reference mechanical angular rotor speed	rad/s
ω_c	Cut-off angular frequency of the stator flux and load angle observer	rad/s
ω_r	Electrical angular rotor speed	rad/s

Subscript and Superscript

a, b, c	Components in phase coordinates (a,b,c)
d, q	Direct and quadrature components, in the dq rotor reference frame
α, β	Components in the $\alpha\beta$ reference frame
d_s, q_s	Direct and quadrature components, in the $d_s q_s$ stator flux reference frame
x^*	Reference value of quantity x
$\underline{x}$	Complex value of quantity x
$\hat{x}$	Estimated value of quantity x
x^p	Predicted value of quantity x

Acronyms

AC	Alternating Current
ASF	Average switching frequency
CAC	Current Angle Control
DC	Direct Current
DFVC	Direct Flux Vector Control
DMTC	Direct Mean Torque Control
DSP	Digital Signal Processor
DTC	Direct Torque Control
FCS-MPC	Finite Control Set Model Predictive Control
FDM	Fuzzy Decision-Making
FEM	Finite Element Method
FOC	Field-Oriented Control
FPGA	Field-Programmable Gate Array
FW	Field-Weakening
HDPC	Hierarchical Direct Predictive Control
IM	Induction Motor
IPMSM	Interior Permanent Magnet Synchronous Motor
3L-NPC	Three-Level Neutral-Point-Clamped Converter
LUT	Lookup Table
2L-VSI	Two-Level Voltage Source Inverter

MPC	Model Predictive Control
MPFC	Maximum Power Factor Control
MTPA	Maximum Torque Per Ampere
MTPF	Maximum Torque per Flux
MTPV	Maximum Torque per Voltage
PAFTC	Predictive Active Flux and Torque Control
PCC	Predictive Current Control
PI	Proportional-Integral
PLASFC	Predictive Load Angle and Stator Flux Control
PMSM	Permanent Magnet Synchronous Motor
PTC	Predictive Torque Control
PWM	Pulse Width Modulation
RLS	Recursive Least Squares
RTI	Real-Time Interface
S-PAFTC	Simplified Predictive Active Flux and Torque Control
SVM	Space Vector Modulation
SynRM	Synchronous Reluctance Motor
THD	Total Harmonic Distortion
VSD	Variable Speed Drive

1

Introduction

1.1 Research Background

In order to achieve a relatively lower cost, high accuracy and high operational efficiency, without using permanent magnets or rotor windings, synchronous reluctance motors (SynRMs) have recently received more attention as a competitive solution in the market of industrial motor drives. The SynRM is one of the oldest types of electric motors and it has, from time to time, attracted the attention of a considerable number of researchers [1]. The first theoretical introduction of the SynRM with reluctance torque production and sinusoidal magnetomotive force was initiated by Kostko in 1923 [2]. In that motor, a rotor cage was used because a pure reluctance machine does not have the self-starting capability. Up to the 1980's, SynRMs were almost neglected by researchers owing to their complex rotor design, poor power factor and low efficiency compared to induction motors (IMs) [3]. With the significant improvements in the rotor design of SynRMs, in conjunction with the advances in the field of power electronics and control of electric drives, the performance of SynRMs have been dramatically improved. Furthermore, by controlling the inverter which feeds the SynRM, there is no longer the need of using a cage in the SynRM rotor [4].

The SynRM geometry consists of two main parts: the stator and the rotor. The stator structure is analogous to the stator of an IM, which normally has several slots with distributed windings. The rotor geometry of the SynRM has different shapes [3, 5]. The first rotor geometry was introduced by Kostko in 1923 with segmental iron pieces and flux-barriers as shown in Fig. 1.1(a). In the 1930's, the anisotropic rotor structure was obtained by a typical rotor punching identical to IMs but by cutting out a few teeth as shown in Fig. 1.1(b) [6].

These motors generally have a low power factor and efficiency due to the small value of the saliency ratio, which represents the ratio between the inductances along the d- and q-axis, being defined as

$$\zeta = L_d/L_q. \tag{1.1}$$

(a) Kostko rotor [2]

(b) IM with a few removed teeth [6]

Fig. 1.1. First generation of SynRM rotors.

A second generation of SynRM rotors was introduced in the 1960's. It utilizes a segmental rotor construction as depicted in Fig. 1.2 [7]. The startup of the SynRM using this rotor type was achieved via a soft starter without adopting a cage in the rotor. In addition, the saliency ratio of this machine was much higher than the use of the first rotor generation. However, the poor efficiency and the low power factor have hindered the widespread use of such machine.

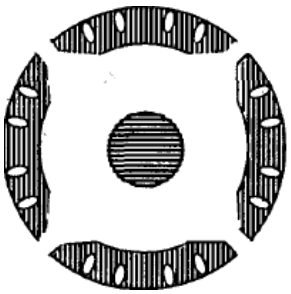

Fig. 1.2. Isolated segmented rotor [3].

In the 1970's, a modern rotor geometry was constructed, as shown in Fig. 1.3(a) [8]. The rotor was made of several axially-laminated steel sheets of "u" or "v" shape. These sheets are then stacked in the radial direction as shown in Fig. 1.3(a). With this rotor design, a saliency ratio as high as 16 is achievable [9]. Thus, the overall performance of the SynRM has been improved significantly in terms of efficiency and power factor. Despite the advantages

of the axially-laminated rotor, its structure is complicated and the cost of manufacturing is high. In addition, it is not mechanically strong and cannot operate at very high speeds [10].

Around the year 1990, the transverse-laminated rotor for SynRMs has been introduced [11]. This type of rotor has several flux barriers as seen in Fig. 1.3(b). The lamination of this rotor is similar to that of IMs by traditional punching, meaning that it is cheap and easy to manufacture [12]. Furthermore, it generates relatively low iron losses [13], being the most promising type of rotor for large-scale production in industrial applications.

(a) Axially-laminated rotor [3] **(b)** Transverse-laminated rotor [14]

Fig. 1.3. Modern SynRM rotor construction.

Due to the aforementioned advances in the rotor design of SynRMs, they have become recently an attractive alternative for permanent magnet synchronous motors (PMSMs) and IMs, due to subsequent main features [15–20]:

- There are no windings, magnets or cages in the rotor. Accordingly, the rotor of SynRMs is cheaper and lighter than the rotor of IMs or PMSMs with the same size.
- The rotor temperature is very low. Consequently, the torque per ampere is acceptable and independent of the rotor temperature unlike PMSMs and IMs.
- The stator of SynRMs is identical to that of IMs and PMSMs.
- The control methods for SynRMs are similar to those of IMs and PMSMs. The speed control without encoder (sensorless control) is much easier due to the magnetic anisotropy of the rotor [21, 22].
- The efficiency of SynRMs can be higher than that of IMs but is less than that of PMSMs of the same power rating. However, the use of rare-earth elements such as neodymium and dysprosium has certain drawbacks. The magnet materials are costly and can be subjected to price variations. Therefore, the use of rare-earth permanent

magnet motors in drive systems may not be economic in the future [23]. In addition, SynRMs have a wider speed range in comparison with PMSMs (the limitation for the maximum speed is purely mechanical), being particularly suitable to be used, for instance, in traction applications where the operation of the traction motors in the field-weakening (FW) region is a major requirements [24,25]. Moreover, problems such as the permanent magnets demagnetization and the performance variation with rising temperature do not exist [26].

The main disadvantage of SynRMs is its relatively low power factor. However, the power factor can be improved by adding a small quantity of low-cost permanent magnet material (ferrite) to the rotor core, being that motor called a permanent magnet assisted synchronous reluctance motor (PMa-SynRM) [27].

With the recent improvements in the rotor design of SynRMs, the SynRM fed by an inverter became a suitable drive system for industrial use. The first mass produced IE4 SynRM, which was marketed for common industrial loads such as fans, pumps and compressors, was presented by ABB in 2011 [28]. Two different types of ABB drive packages exist, firstly the IE4 super premium efficiency motor and an IE3 high output motor, both coupled with advanced ABB electric drive systems utilizing a direct torque control (DTC) scheme [29]. DTC drives combined with any of the SynRMs offer great energy savings potential for a large number of variable-speed pump and fan applications, in comparison with IMs [30]. It is worth mentioning that the German companies KSB and Siemens have also manufactured an efficient SynRM for pump, fan and compressor applications [31].

High performance, fast transient response and an appropriate control flexibility of electric drives is an essential requirement for various industrial applications [32]. The two most widespread control techniques that have been widely investigated and reported for SynRM drives are field-oriented control (FOC) and DTC [33–36]. In spite of FOC providing a great dynamic torque and flux response, its structure is complex due to the use of PI controllers and a space-vector pulse width modulation (SVPWM) block. Moreover, it requires some tuning effort to achieve a good performance. In contrast to FOC, DTC has a simpler structure as it does not have any axis transformation or modulation blocks. This control strategy directly selects an optimal voltage vector from a predefined switching table according to

the position of the stator flux vector and error signals provided by torque and stator flux hysteresis controllers. In spite of the fast dynamic response achieved by DTC, its performance degrades especially at low speeds and suffers from high torque and flux ripple, and variable switching frequency in a traditional implementation. Furthermore, a high sampling frequency is required for digital implementation of torque and flux hysteresis bands [37]. Moreover, DTC is also not flexible in the incorporation of some control constraints.

A different control approach, called model predictive control (MPC), has recently attracted widespread attention in both industry and academic communities [38–42]. MPC uses the system model to predict the future system states in discrete time. The outcomes of prediction are evaluated by a cost function, which is responsible for the optimal state prediction, according to the specified operating criteria and constraints. MPC offers several advantages, for instance, it has an intuitive design methodology, and it is capable of incorporating constraints and non-linearities in a straightforward way, as well as the ability of multivariable control. Therefore, MPC is considered a powerful alternative to both FOC and DTC in high performance electric motor drives [43]. Compared to FOC, MPC avoids the use of PI current and flux controllers and modulation blocks, hence leading to a very fast dynamic response. Compared to DTC, MPC uses a cost function rather than a switching table to select the best voltage vector to be applied, meaning that a better steady-state performance can be obtained. Despite the above mentioned advantages, MPC also presents two drawbacks such as a high computational burden, and the need to adjust weighting factors very often used in the cost function, being these topics for future research [44, 45]. Of course, if these drawbacks are solved, this can lead to a wider acceptance of MPC in industrial applications.

Using any of the aforementioned control strategies for SynRMs, the speed of the motor is increased up to the base speed. To fully utilize the wide speed range capabilities of the SynRM, a FW algorithm is required to comply with the voltage limit needed by the inverter. In electric drives for traction applications, such as in electric vehicles, the electric motors need to have a very high starting torque and a wide speed range of operation [46, 47]. The power requirement of these electric motors varies over time according to the driving schedules and road conditions, thus demonstrating the importance of expanding their speed range. During the vehicle acceleration, the electric motor drive in traction applications requires a high

torque to achieve fast acceleration. At cruising, the electric motor needs to run in a wide speed range, guaranteeing the production of an acceptable torque in a wide speed range.

SynRM electric drives can operate in a wide speed range. This speed range is typically divided into three regions as shown in Fig. 1.4 [48–50]:

- Constant torque region (Region I), which starts at zero speed and ends at motor base speed.
- Constant power region (Region II), comprised between the base speed and the speed where the load angle of the SynRM reaches its stability limit (typically 45°).
- Maximum torque per voltage (MTPV) region (Region III), also known as constant load angle region. In this region, the SynRM operates at very high speeds with a constant load angle in order to extend the torque control capability.

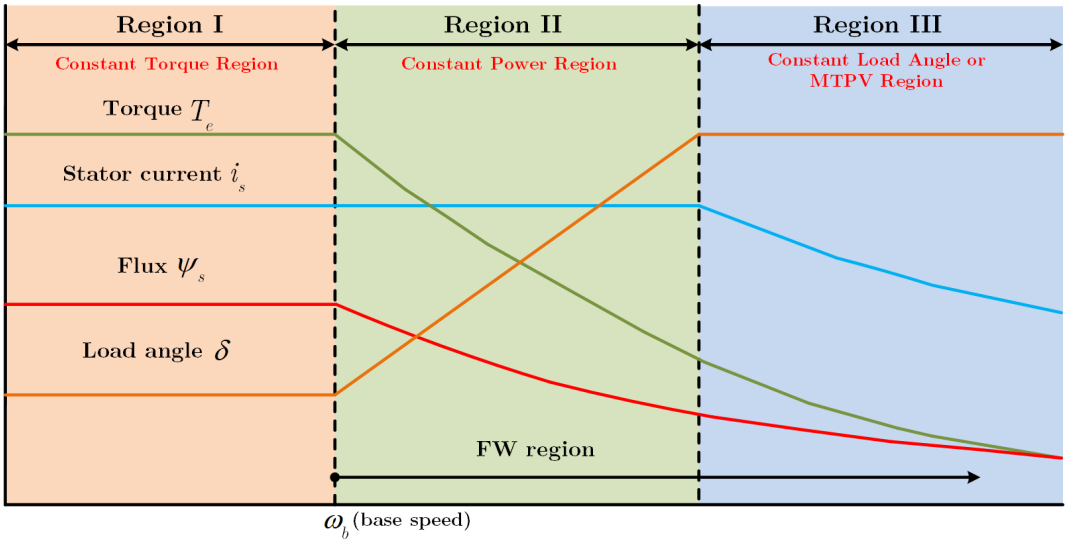

Fig. 1.4. Regions and limits of operation of a SynRM drive.

To fully exploit the torque and power potential of the SynRM drive and ensure a smooth transition between the regions mentioned above, the adopted control strategy must comply effectively with the inverter limits (current and voltage) as well as the load angle limitation [48]. In literature, the majority of the research work that propose control algorithms able to operate the SynRM in the FW region are based on FOC and DTC [50–53]. In the case of FOC, the FW operation is obtained by generating the optimal reference currents for Regions II and III with the aid of a motor model [52–54]. However, the effectiveness of this approach is highly reliant on the accurate identification of the motor model [54]. Furthermore, an

additional voltage control loop, which is cascaded with the current vector control loops, is required to correct the calculated current reference values in the MTPV region [53], thus increasing the complexity of the control scheme. In contrast to FOC, DTC regulates directly the stator flux and torque, thus the FW algorithm is implemented in a different way. In this control strategy, the voltage-limited operation is easy to be realized due to the direct regulation of the stator flux. On the contrary, the implementation of the MTPV limitation is not straightforward and it always requires some analytical work [50, 51]. In [51], the FW algorithm continuously monitors the duty ratio of the DTC in order to perform the transition between the different motor operating regions. In [50], the expressions of the FW and MTPV trajectories were written in a reference frame synchronized with the stator flux and used to calculate the references of flux and torque in order to respect the current and voltage limits. One can conclude that both in FOC and DTC, the FW algorithm cannot be directly implemented without further modifications to the respective standard control schemes. In view of this, a simple and robust FW algorithm for SynRM drives is highly desirable and preferable in a real-time implementation of a comprehensive control scheme.

1.2 Main Objectives and Contributions

MPC is an emerging alternative in the control of electric drives. In particular, finite control set MPC (FCS-MPC) seems to be a very promising category of control strategies in this field. FCS-MPC allows a flexible control scheme with very fast dynamics. However, it still suffers from two major drawbacks such as a relatively high calculation effort and difficulties in the proper selection of the weighting factors present in the cost function. These two issues demonstrate that FCS-MPC has to be improved until it can compete successfully with other control strategies.

On the other hand, the inclusion of a simple and robust FW algorithm with the traditional FCS-MPC algorithm, in order to exploit the full speed range of the SynRM drive, is an interesting research subject and will present a practical application. Unfortunately, the performance of FCS-MPC proposed for SynRM drives has not yet been explored in the full speed range. The main reason for this is the difficulty in controlling the SynRM along the

MTPV trajectory.

Taking into account all the limitations mentioned above, the main objective of this work is the development of a new FCS-MPC strategy which avoids the use of weighting factors and runs safely and efficiently the SynRM drive in the full speed range, in a relatively small calculation time.

This thesis presents three new FCS-MPC strategies for SynRM drives. The first two control strategies are developed in the rotor reference frame and use the active flux concept. They are called predictive active flux and torque control (PAFTC), and simplified predictive active flux and torque control (S-PAFTC), respectively. PAFTC follows the traditional implementation steps of FCS-MPC, thus it requires some effort to adjust the weighting factor used in the cost function. On the contrary, the S-PAFTC approach corresponds to a simplification of the PAFTC. By allowing a reduction of the calculation time required for the prediction process, and at the same time avoiding the use of weighting factors in the cost function. These two control strategies are evaluated through several simulation and experimental tests, both in steady-state and transient conditions, demonstrating the good performance of the SynRM drive thus obtained for speeds up to the rated one.

The third control strategy proposed in this work is developed in the stator flux reference frame, being named as predictive load angle and stator flux control (PLASFC). According to this control strategy, a simple cost function is evaluated and the prediction process is simplified in the same manner as in the S-PAFTC strategy. Moreover, due to the selection of the load angle and the stator flux as controlled variables, PLASFC is suitable and capable of exploiting effectively the torque and power potential of the SynRM drive in the full speed range. The literature shows that the incorporation of a loss optimization algorithm in FCS-MPC algorithms has been little investigated. Therefore, a loss minimization algorithm is developed and implemented in the PLASFC, in order to reduce the copper losses of the motor in Region I.

Finally, it is worth mentioning that in the three proposed control strategies, the magnetic saturation and cross-magnetic saturation characteristics of the SynRM have been taken into account. This means that the motor model includes self- and cross-incremental inductances,

as well as apparent inductances, where all of them depend on the currents components along the dq-axes.

1.3 Thesis Structure

The present thesis is organized into five chapters, including this one which introduces the research background, motivation and contributions.

Chapter 2 provides the literature survey for all control strategies in the domain of SynRM drives, with special focus on FCS-MPC strategies. The advantages and limitations of FCS-MPC strategies in comparison with the existing classical control schemes are pointed out.

Chapter 3 presents the mathematical model of the SynRM considering its non-linear magnetic characteristics. In addition, a brief description of the adopted method to identify the SynRM parameters is included. Furthermore, two new FCS-MPC strategies for SynRM drives using the active flux concept are presented and validated by simulation and experimental results obtained in both steady-state and transient conditions.

Chapter 4 starts with a general overview of the control strategies for SynRM drives in the FW region in order to supply the reader with the necessary theoretical background. Then, a predictive load angle and stator flux control strategy is presented. It gives a detailed description of each control block, such as the prediction model, FW algorithm, and stator flux and load angle observer. The robustness of the proposed control strategy against parameter uncertainties has also been described and supported with simulation results. In addition, the loss minimization algorithm, which is intended to increase the SynRM efficiency in the constant torque region, is also explained. Finally, simulation and experimental results are presented and discussed to verify the effectiveness of the proposed control strategy in the full speed range.

At the end, chapter 5 presents the main conclusions of this work and provides proposals for future work in this field of research.

2

State-of-the-Art of Control Strategies for SynRMs

In this chapter, the main control strategies applied to SynRM drives are briefly reviewed and analysed. The presentation of these strategies is grouped into three main categories: Field-Oriented Control; Direct Torque Control; Model Predictive Control.

2.1 Clarke and Park Transformations

Clarke and Park transformations are used in vector control systems, thus a brief explanation of these transformations is presented first.

Clarke transformation: This transformation is used to transform three phase quantities into a stationary two-axis orthogonal reference frame as shown in Fig. 2.1 [55,56]. The Clarke transformation is also known as the $\alpha\beta$ transformation and when applied to the current signals is given by

$$\begin{bmatrix} i_\alpha \\ \\ i_\beta \end{bmatrix} = \frac{2}{3} \begin{bmatrix} 1 & -\frac{1}{2} & -\frac{1}{2} \\ \\ 0 & \frac{\sqrt{3}}{2} & -\frac{\sqrt{3}}{2} \end{bmatrix} \cdot \begin{bmatrix} i_a \\ \\ i_b \\ \\ i_c \end{bmatrix}, \tag{2.1}$$

where i_a, i_b and i_c are the three-phase currents, and i_α and i_β are the current components in an orthogonal reference frame.

Park transformation: This transformation is used to transform the stationary reference

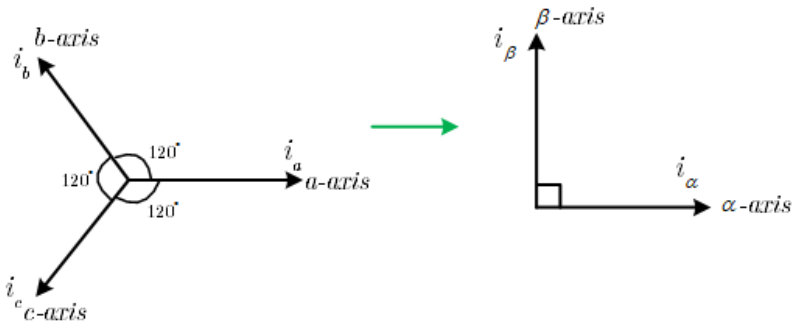

Fig. 2.1. The Clarke transformation applied to a system of three currents.

frame quantities into a rotating reference frame quantities as shown in Fig. 2.2. The Park transformation, which is also known as the dq transformation [57, 58], when applied to the currents is given by the following equations:

$$\begin{bmatrix} i_d \\ i_q \end{bmatrix} = \begin{bmatrix} \cos(\theta) & \sin(\theta) \\ -\sin(\theta) & \cos(\theta) \end{bmatrix} . \begin{bmatrix} i_\alpha \\ i_\beta \end{bmatrix}, \tag{2.2}$$

where i_d and i_q are the two current components in the rotating reference frame and θ is the angle between the α-axis and the d-axis.

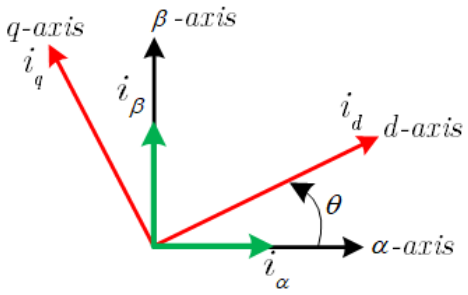

Fig. 2.2. The Park transformation.

In this section, a rotor reference frame is used as it is more suitable for the control of synchronous machines than the abc reference frame [55, 57–61]. The transformation to the rotor reference frame eliminates the time-varying inductances in the machine equations [55, 57–61]. The signals of the control loops are DC quantities in steady-state, making it easier to design the control system. The transformations above are not only used with the stator current, but also apply in general to other variables like voltages and flux linkages.

It is also handy to be able to transform currents, voltages or flux linkages from the $\alpha\beta$ (stationary) to the dq (rotor) reference frame and vice-versa. The transformation from the dq reference frame to the $\alpha\beta$ reference frame is usually called as the inverse Park transformation and is given by

$$\begin{bmatrix} i_\alpha \\ i_\beta \end{bmatrix} = \begin{bmatrix} \cos(\theta) & -\sin(\theta) \\ \sin(\theta) & \cos(\theta) \end{bmatrix} . \begin{bmatrix} i_d \\ i_q \end{bmatrix} . \tag{2.3}$$

2.2 Model of the SynRM

The voltage and flux equations of a SynRM in the rotor reference reference can be described as [61–64]:

$$\begin{cases} u_d = R_s i_d + \frac{d\psi_d}{dt} - \omega_r \psi_q \\ u_q = R_s i_q + \frac{d\psi_q}{dt} + \omega_r \psi_d \end{cases} \tag{2.4}$$

$$\begin{cases} \psi_d = L_d i_d \\ \psi_q = L_q i_q \end{cases} , \tag{2.5}$$

where u_d, u_q are the stator currents along the d- and q-axis, ψ_d, ψ_q are the stator flux linkage along d- and q-axis, L_d, L_q are the inductances along the d- and q-axis, R_s is the stator resistance, and ω_r is the angular electrical rotor speed.

The torque produced by the SynRM can be described in the rotor reference frame as follows:

$$T_e = \frac{3}{2} p \left(\psi_d i_q - \psi_q i_d \right) \tag{2.6}$$

$$T_e = \frac{3}{2} p \left(L_d - L_q \right) i_d i_q, \tag{2.7}$$

where p is the number of pole-pairs.

It is worth noting here that the electrical model of the SynRM is described here without taking into account the magnetic and cross-magnetic saturation effects. This phenomenon will be presented in more detailed in the following chapter.

2.3 Field-Oriented Control

The main principle of FOC is to decouple the stator currents into their flux and torque producing components, i_d and i_q, respectively. Thus, this method ensures an independent control of the flux and torque of the machine. In a SynRM, the electromagnetic torque is proportional to the product of the current components i_d and i_q in a rotor reference frame, and thus there is a degree of freedom in the choice of these currents since only the product is imposed for a given electromagnetic torque value [65]. Therefore, the fundamental question is how to generate the reference values of i_d and i_q, in the rotor reference frame, for a given reference torque.

Fig. 2.3 shows the general block diagram of a possible vector control system for a SynRM drive. As can be seen, the FOC method has three control loops. The outer control loop is aimed at controlling the rotor speed and generates the reference torque T_e^*. The two inner control loops regulate i_d and i_q in order to control the torque and flux of the machine. The reference and the measured d- and q-axis stator current components feed the two current loops which, with the aid of PI controllers, generate the reference voltages u_d^* and u_q^*. These voltages are then transformed from the rotor reference frame into a stationary reference frame, and feed the modulator which will generate the gate signals of the inverter power switches.

From Fig. 2.3, the decoupling terms are used in both current control loops in order to control the i_d and i_q independently. The decoupling terms, $\omega_r L_d i_d$ and $\omega_r L_q i_q$, are depicted from the two voltage equations of the SynRM (2.8)-(2.9).

$$u_d = R_s i_d + L_d \frac{di_d}{dt} - \omega_r L_q i_q \tag{2.8}$$

$$u_q = R_s i_q + L_q \frac{di_q}{dt} + \omega_r L_d i_d \tag{2.9}$$

The two voltage equations are coupled by the decoupling terms, $\omega_r L_d i_d$ and $\omega_r L_q i_q$. By subtracting/adding these terms in the current control loops, the two currents i_d and i_q can be controlled independently. This also simplifies the transfer function of the SynRM in the

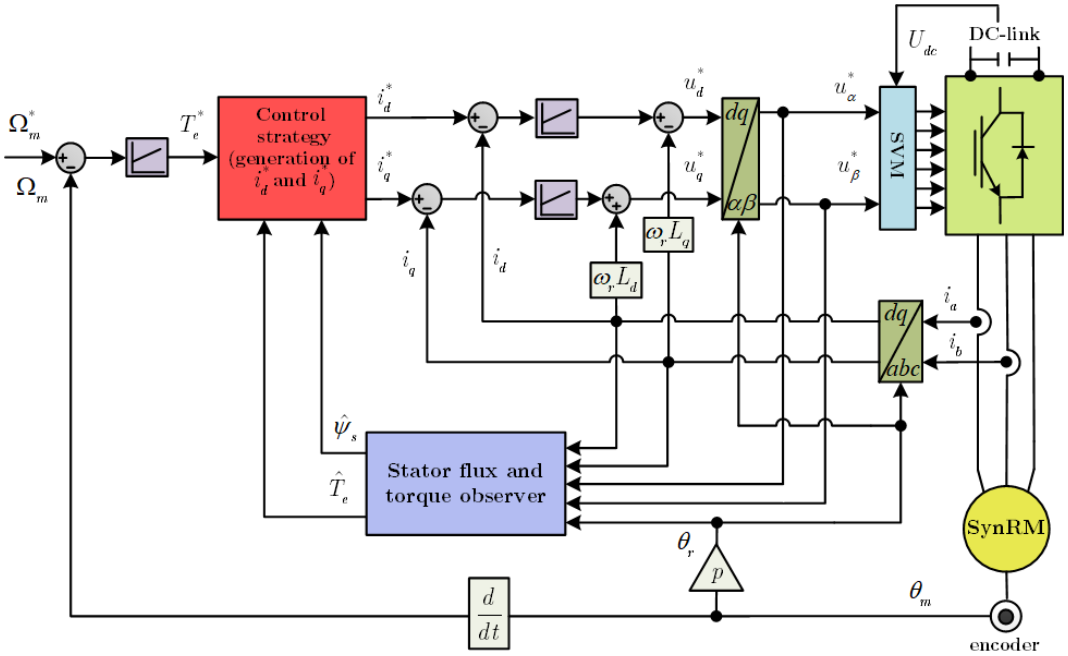

Fig. 2.3. Block diagram of a FOC system for a SynRM drive [65].

two current control loops.

After some mathematical manipulations, the following transfer function of the SynRM for the d- and q-current loops are obtained:

$$G_d(s) = \frac{1}{sL_d + R_s} = \frac{1}{R_s(sT_{sd} + 1)} \tag{2.10}$$

$$G_q(s) = \frac{1}{sL_q + R_s} = \frac{1}{R_s(sT_{sq} + 1)} \tag{2.11}$$

where $T_{sd} = \frac{L_d}{R_s}$ and $T_{sq} = \frac{L_q}{R_s}$ are the electrical time constants along the d- and q-axis, respectively, and s is the Laplace variable.

The closed-loop systems of the current control along the d- and q-axis are shown in Fig. 2.4 and Fig. 2.5, respectively. The inverter is usually included in the design procedure of these closed-loop systems as a delay equal to [66]

$$T_d = \frac{T_s}{2} \tag{2.12}$$

where T_s is the sampling time.

In the s plane, the delay introduced by the inverter can be approximated by a first order lag system as [66]

$$u_{dq}(s) = e^{-sT_s} u^*_{dq}(s) \approx \frac{1}{1+sT_d} u^*_{dq}(s) \tag{2.13}$$

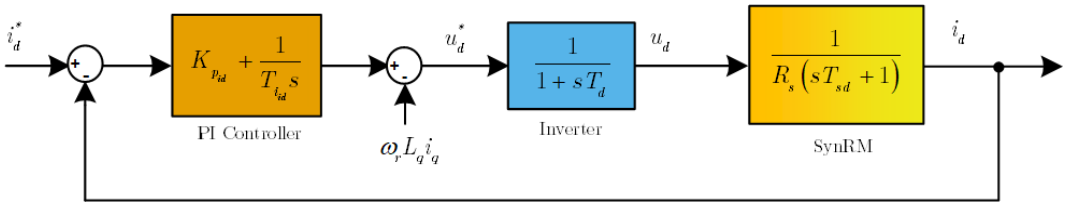

Fig. 2.4. Closed-loop system of the d-axis current control [66].

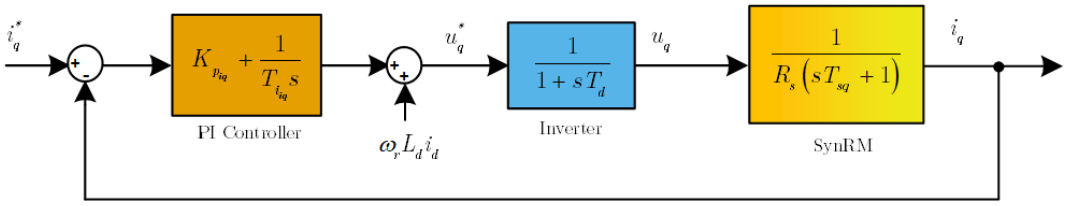

Fig. 2.5. Closed-loop system of the q-axis current control [66].

The design of the PI parameters of the current controllers can be usually carried out using the Amplitude optimum method or the pole placement method [67, 68].

The control strategies for the SynRM drive based on FOC can be divided into three main categories: constant i_d current control, current angle control (CAC) and active flux control [65, 69–74]. In the following sections, these categories of control strategies will be presented and analysed.

2.3.1 Constant i_d Current Control

According to this simple control method, the goal is to assign a constant value to i_d so that the electromagnetic torque is controlled directly by i_q. This control strategy is analogous to the operation principle of a DC motor with separate excitation, where the d-axis current corresponds to the excitation current and the q-axis current to the armature current [69, 70]. Thus, an independent control of torque and flux is achieved.

Using this control strategy, and at speeds below the base speed (ω_b), the value of i_d should

be maintained at

$$i_d^* = \frac{\psi_{smax}^*}{\sqrt{2}L_d}, \tag{2.14}$$

where ψ_{smax}^* represents the maximum value of the stator flux reference and L_d represents the inductance along the d-axis.

The maximum value of the stator flux reference is set to

$$\psi_{smax}^* = \sqrt{\frac{4\left|T_e^*\right| L_d L_q}{3p\left(L_d - L_q\right)}} \tag{2.15}$$

In the FW region, i_d^* decreases with the increase of the speed according to

$$i_d^* = \frac{\psi_{smax}^*}{\sqrt{2}L_d}\frac{\omega_b}{|\omega_r|}, \tag{2.16}$$

where ω_r is the electric rotor angular speed of the machine.

The reference value i_q^* for the q-axis current component is given by

$$i_q^* = \frac{2T_e^*}{3p\left(L_d - L_q\right)i_d^*}. \tag{2.17}$$

Due to the variation of L_d with i_d (which varies in the FW region due to magnetic saturation), the torque will not be directly proportional to the q-axis current component i_q. Therefore, other alternative methods such as self-tuning and model reference adaptive controllers should be adopted to generate the current reference i_q^*. Consequently, this type of vector control is only suitable for applications requiring speed control below the machine base speed ω_b [65].

2.3.2 Current Angle Control

By definition, the current angle θ_i represents the angle between the d-axis and the stator current vector $\underline{i}_s$, as shown in Fig. 2.6. There are three different strategies of the current angle control:

- Fast torque response control [74].
- Maximum power factor control (MPFC) [72].
- Maximum torque per ampere control (MTPA).

All the above control strategies depend on the tangent of the current angle θ_i. The d-axis and q-axis reference currents are generated from the reference value of the torque utilizing the values of tangent of the current angle, $\tan(\theta_i)$.

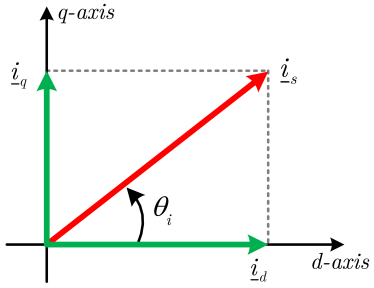

Fig. 2.6. Stator current components in the dq rotor reference frame.

Fast torque response control: To achieve a quick torque response in this control strategy, the current angle between the stator current vector and the d-axis should be equal to

$$\theta_i = \arctan\left(\frac{L_d}{L_q}\right). \tag{2.18}$$

Taking (2.18) into consideration, the reference currents along the d- and q-axis can be determined as follows:

$$i_d^* = \sqrt{\frac{2\,|T_e^*|}{3p\,(L_d - L_q)\tan\,(\theta_i)}} \tag{2.19}$$

$$i_q^* = \frac{i_d^*\ \mathrm{sgn}\,(T_e^*)}{\tan\,(\theta_i)}. \tag{2.20}$$

Maximum power factor control: The objective of MPFC is to maximize the power factor (PF), which is one of the fundamental quantities on any electric machine. To maintain the PF at its maximum value, the current angle θ_i must be set as

$$\theta_i = \arctan\sqrt{\frac{L_d}{L_q}} \tag{2.21}$$

The maximum power factor is therefore given by

$$PF_{\max} = \frac{\frac{L_d}{L_q} - 1}{\frac{L_d}{L_q} + 1}. \tag{2.22}$$

The reference stator current components can be obtained here using (2.19) and (2.20) with the current angle value determined by (2.21).

Maximum torque per ampere control: The role of the MTPA control strategy, as its name implies, is to maximize the electromagnetic torque for a given value of the motor supply current. This is equivalent to the minimization of the motor copper losses for each torque value, thus obtaining a high efficiency in the drive system [34, 52, 72].

To use this control strategy, it is necessary to develop a torque expression as a function of the supply current $\underline{i}_s$. From the vector diagram shown in Fig. 2.6, the two current components along d- and q-axis can be written as

$$\begin{cases} i_d = i_s \cos(\theta_i) \\ i_q = i_s \sin(\theta_i) \end{cases}. \tag{2.23}$$

The electromagnetic torque of the SynRM in the dq rotor reference frame is given by

$$T_e = \frac{3p}{2} (L_d - L_q) i_d i_q. \tag{2.24}$$

Replacing (2.23) into (2.24) gives the torque expression as a function of the supply current:

$$T_e = \frac{3p}{4} (L_d - L_q) {i_s}^2 \sin(2\theta_i). \tag{2.25}$$

From (2.25), it is obvious that for a given electromagnetic torque value, there is a certain current angle, θ_i^{opt}, that minimises the amplitude of the supply current i_s.

Many authors, for simplicity in the implementation of the MTPA strategy, neglected the effects of saturation and cross-magnetic saturation [34, 52, 72, 75, 76]. Under these conditions, the current angle which ensures a maximum torque as a function of i_s is obtained when the

term $\sin(2\theta_i)$ in (2.25) is maximum, which is equivalent to establish the following equation

$$\sin\left(2\theta_i^{opt}\right) = 1. \tag{2.26}$$

According to (2.26), under ideal conditions, the maximum torque per ampere is obtained when the current angle $\theta_i^{opt} = 45°$, that is when $i_d = i_q$. On the other hand, the effects of magnetic saturation and cross-magnetic saturation should be taken into account as SynRMs generally operate at a high level of saturation. This phenomenon causes a deviation of the optimal current angle from the value that it would have under ideal conditions. Accordingly, it has been proposed several ways to maximize the torque/ampere ratio considering this phenomenon [33, 77, 78]. In [33], both magnetic saturation and cross-magnetic saturation effects were considered to reach the MTPA operation. The optimal current angle required in each control iteration was modelled as a function of the torque T_e by

$$\theta_i^{opt} = p_1 T_e^2 + p_2 T_e^2 + p_3, \tag{2.27}$$

where p_1, p_2 and p_3 are coefficients of the interpolation polynomial.

With the optimal current angle given by (2.27) and the reference current i_q^* generated at the output of the speed controller, the reference current along the d-axis is determined by

$$i_d^* = \frac{i_q^*}{\tan\left(\theta_i^{opt}\right)}. \tag{2.28}$$

In [77], only the magnetic saturation effect was considered to operate the machine along the MTPA trajectory. In other words, the variation of L_d with i_d was experimentally evaluated, whereas L_q was set with a constant value. Thus, under this situation, the calculated optimal current angle will not be the one leading to the true MTPA trajectory as L_q is always affected by the motor operating conditions.

In [78], the authors clarified the importance of including the effect of magnetic saturation and cross-magnetic saturation to yield a satisfactory performance under MTPA operation. It was found that the current angle θ_i^{opt} is higher than 45° in most operating points. Further-

more, the reference current along the d-axis, is also not constant and depends on the required load torque. Thus, its values were obtained using finite element method (FEM) and stored in a lookup table (LUT) to satisfy the MTPA condition.

Finally, it is noteworthy that the SynRM drive can also be driven by a current controlled PWM inverter, without being combined with the voltage control loop, as in [52]. However, the control scheme, that combines the current and voltage control loops is more desirable especially due to voltage saturation constraints required at high speeds when the motor operates in the FW region [74].

2.3.3 Active Flux Control

By definition, the active flux ψ_a of an AC machine is the flux that multiplied by i_q gives the torque developed by the motor [71]:

$$T_e = \frac{3p}{2}\psi_a i_q. \tag{2.29}$$

The active flux ψ_a in a SynRM is given by

$$\psi_a = (L_d - L_q)\, i_d. \tag{2.30}$$

The active flux control is a combined current-voltage vector control strategy and its configuration is identical to the one presented in Fig. 2.3. The only difference is that the d- and q-axis reference currents are determined based on the active flux concept [71].

The reference current i_q^* is determined using the reference torque T_e^*, which is generated by the speed controller, and (2.29), being given by

$$i_q^* = \frac{2\, T_e^*}{3p\, \psi_{an}}, \tag{2.31}$$

where ψ_{an} is the rated active flux value of the machine.

The reference current i_d^* is provided by the active flux control loop, which employs a PI

controller that has as input the error between the rated and estimated active flux values. It is worth mentioning here that the active flux can be estimated with the aid of the stator flux observer.

In view of the aforementioned features, the active flux control allows an independent control of the active flux and electromagnetic torque of the SynRM. Furthermore, due to the fact that the active flux vector is always aligned with the d-axis, it can be used to estimate the rotor position at medium and high speeds with accuracy [79].

2.4 Direct Torque Control

DTC is a control method that regulates directly the developed torque and stator flux. The DTC scheme was initially proposed for IMs by Takahashi [80, 81] and leads to an excellent torque response using a less parameter sensitive model than FOC. Since its inception, it has been widely investigated and employed commercially by ABB due to its simplicity and very fast torque response and flux tracking capability even under load disturbances. Additionally, the computational effort of the DTC scheme is smaller than that of the FOC as reference frame transformations are not needed.

Fig. 2.7 shows the block diagram of a standard DTC scheme for SynRMs. It includes stator flux and torque observer, stator flux and torque hysteresis controllers and a switching table. Usually to implemented this control strategy, a measured DC-link voltage and the two currents are needed for the stator flux and torque estimation. In this control strategy, torque and stator flux are controlled directly and there is no need for the use of current control loops as in the case of FOC. This means the whole controller can be implemented in stator coordinates and no further coordinate transformations are required. The stator flux observer and torque estimator provides both the estimated stator flux $\hat{\psi}_s$ and torque $\hat{T}_e$. The torque reference T_e^* is generated with a speed controller, while the reference value of the stator flux magnitude, ψ_s^*, can be either a constant or a changeable value if FW operation is aimed at. The basic principle of DTC is to bound the torque error and the flux error to small hysteresis bands by choosing appropriate switching states of the inverter. This is achieved by using a switching table having as inputs the outputs of the torque hysteresis

controllers (H_T), the stator flux hysteresis controller (H_ψ) and the sector S_i in which the stator flux vector is located.

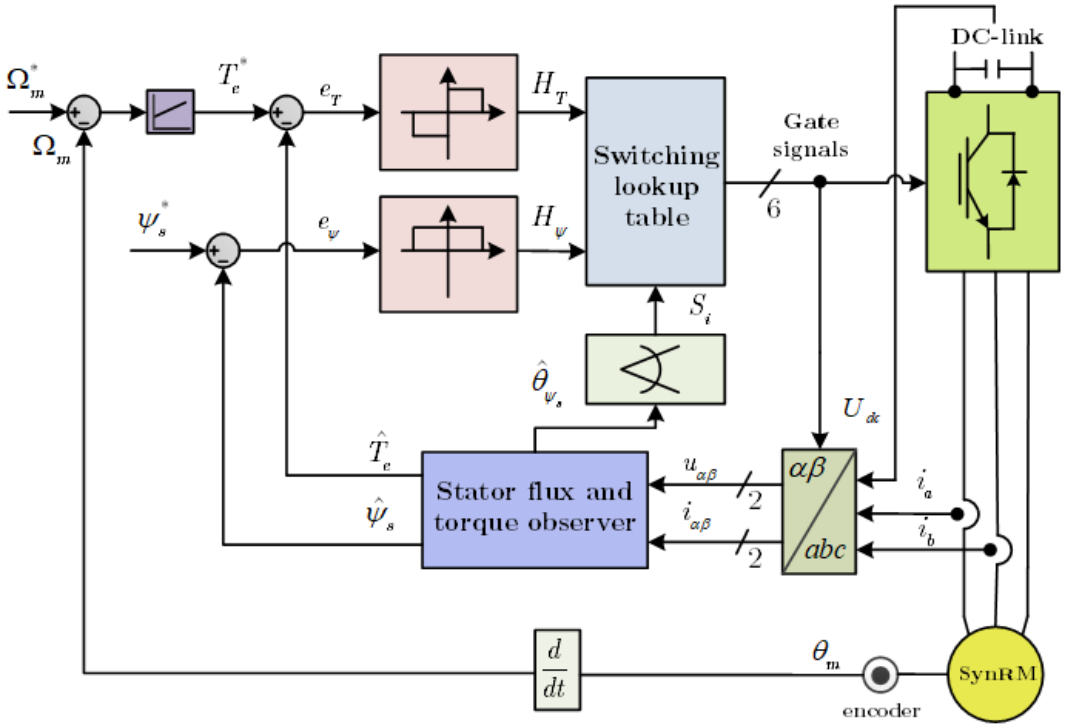

Fig. 2.7. Standard DTC scheme for SynRMs [82].

For the operation of the standard DTC two hysteresis bands have to be set up: one for the torque and another one for the stator flux magnitude. For the torque, a three-level hysteresis is used, whose outputs are as follows:

- 1: the torque must be increased.
- 0: the torque has to be kept constant.
- -1: the torque should be decreased.

For the stator flux magnitude, a two-level hysteresis controller is used with two possible output values as follows:

- 1: the stator flux magnitude must be increased.
- 0: the stator flux magnitude has to be decreased.

A two-level classical voltage inverter can generate seven different voltage vectors, corresponding to the eight switching states of the inverter. There are six voltage vectors of equal magnitude and arranged 60° apart in the complex plane, and two null vectors, as shown in

Fig. 2.8.

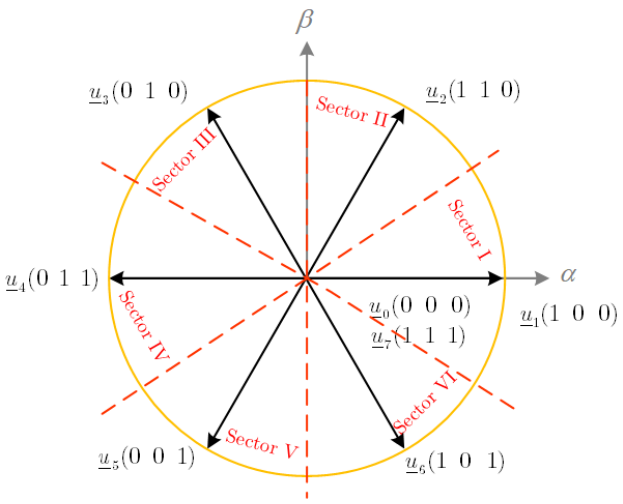

Fig. 2.8. Different voltage space vectors produced by a 2L-VSI [83].

The selection of the appropriate voltage vector is based on a functional block labeled switching table given by Table 2.1 that generates binary signals applied to the states of the inverter power switches. The input quantities are the stator flux sector and the outputs of the two hysteresis controllers, while the outputs are the voltage vectors.

Table 2.1: Switching table of the standard DTC [83].

H_ψ	H_T	Sector I	Sector II	Sector III	Sector IV	Sector V	Sector VI
1	1	$\underline{u}_2$	$\underline{u}_3$	$\underline{u}_4$	$\underline{u}_5$	$\underline{u}_6$	$\underline{u}_1$
	0	$\underline{u}_0$	$\underline{u}_7$	$\underline{u}_0$	$\underline{u}_7$	$\underline{u}_0$	$\underline{u}_7$
	-1	$\underline{u}_6$	$\underline{u}_1$	$\underline{u}_2$	$\underline{u}_3$	$\underline{u}_4$	$\underline{u}_5$
0	1	$\underline{u}_3$	$\underline{u}_4$	$\underline{u}_5$	$\underline{u}_6$	$\underline{u}_1$	$\underline{u}_2$
	0	$\underline{u}_7$	$\underline{u}_0$	$\underline{u}_7$	$\underline{u}_0$	$\underline{u}_7$	$\underline{u}_0$
	-1	$\underline{u}_5$	$\underline{u}_6$	$\underline{u}_1$	$\underline{u}_2$	$\underline{u}_3$	$\underline{u}_4$

The stator flux of the motor is estimated in the stationary reference frame according to

$$\begin{cases} \hat{\psi}_\alpha = \int (u_\alpha - R_s i_\alpha)\, dt \\ \hat{\psi}_\beta = \int (u_\beta - R_s i_\beta)\, dt \end{cases}, \tag{2.32}$$

where $\hat{\psi}_\alpha$, $\hat{\psi}_\beta$, i_α and i_β are the $\alpha\beta$ components of the stator flux and the motor stator

currents, respectively. The amplitude and angle of the stator flux vector are given by

$$\begin{cases} \hat{\psi}_s = \sqrt{\psi_\alpha^2 + \psi_\beta^2} \\ \hat{\theta}_{\psi_s} = \tan^{-1}\left(\frac{\psi_\beta}{\psi_\alpha}\right) \end{cases} . \tag{2.33}$$

In the DTC, the electromagnetic torque is also estimated in the stationary reference frame using the following expression:

$$\hat{T}_e = \frac{3}{2} p \left(\psi_\alpha i_\beta - \psi_\beta i_\alpha\right). \tag{2.34}$$

In [84] a DTC scheme with modified integrator is proposed for SynRMs in order to solve the practical issues associated with pure integrator by replacing it with a low-pass filter and a compensation term. In [85], the impact of magnetic saturation and cross-coupling phenomena in an encoderless DTC for SynRMs running at very low speeds is presented based on voltage signal injection method. In [82], an adaptive backstepping control and model reference adaptive control system is proposed to improve the performance of a sensorless DTC for SynRMs. The online procedure for the automatic search of the MTPA operating region is presented in [86]. This algorithm was applied in DTC SynRM drives based on a signal injection method with a random-based perturbation. In [50], a DTC strategy is applied to the SynRM drive with the combination of MTPA control, maximum torque per flux (MTPF) control, FW control, and torque limitation. In [36, 51] an improved FW algorithm for DTC SynRM drives is presented. The proposed algorithm proved its effectiveness and capability in different operating regions (MTPA and FW region).

The DTC strategy is easily implemented in DSPs, and it shows very good dynamic performance in torque and flux regulation. The two control loops of torque and flux can compensate the imperfection of FOC caused by parameter variations. Furthermore, there is no need to measure the rotor position as in the case of FOC, although these days, rotor position can be estimated.

The standard DTC method shown in Fig. 2.7 has some disadvantages such as high-frequency torque ripple, which may lead to a low performance of the drive system. To

reduce the torque and flux ripples that standard DTC involves, the space vector modulation (SVM) based DTC was applied to SynRM drives in [87, 88]. However, in the DTC-SVM method, the reference voltage components are obtained from the outputs of two PI controllers, which means that two extra controllers in addition to the speed PI controller are needed. One can conclude that the DTC-SVM is a useful solution to attenuate the flux and torque ripples but at the cost of increasing the complexity of the standard DTC scheme.

2.5 Model Predictive Control

In recent years, a very promising alternative to traditional controllers in the field of electric drives is model predictive control (MPC). The basic principle of MPC is to use a system model to predict its future behaviour. This information is then used to obtain the optimal control input according to a predefined optimization criterion [89, 90].

There is a wide range of predictive controllers available for power converters and electric drives. The basic idea of these predictive controllers is common, but there are differences regarding for instance the switching frequency (fixed or variable) and the necessity of using an additional modulator for generating the optimal switching states of the inverter. The available predictive control methods can be broadly classified based on the decision of selecting the optimization criterion into four main groups (see Fig. 2.9) [91]: deadbeat control, hysteresis control, trajectory-based control and model predictive control.

The optimization criterion in the hysteresis-based predictive control is to keep the controlled variables within the boundaries of a hysteresis area, while in the trajectory based, the variables are forced to follow a predefined trajectory. In deadbeat control, the optimal control input is the one that makes the error equal to zero in the next sampling instant. A more flexible criterion is used in MPC, expressed as a cost function to be minimized.

The difference between these groups of controllers is that deadbeat control and MPC with continuous control set use a modulator, in order to generate the required voltage. This leads to a fixed switching frequency. The other controllers directly generate the switching signals for the converter, do not need a modulator, and present a variable switching frequency.

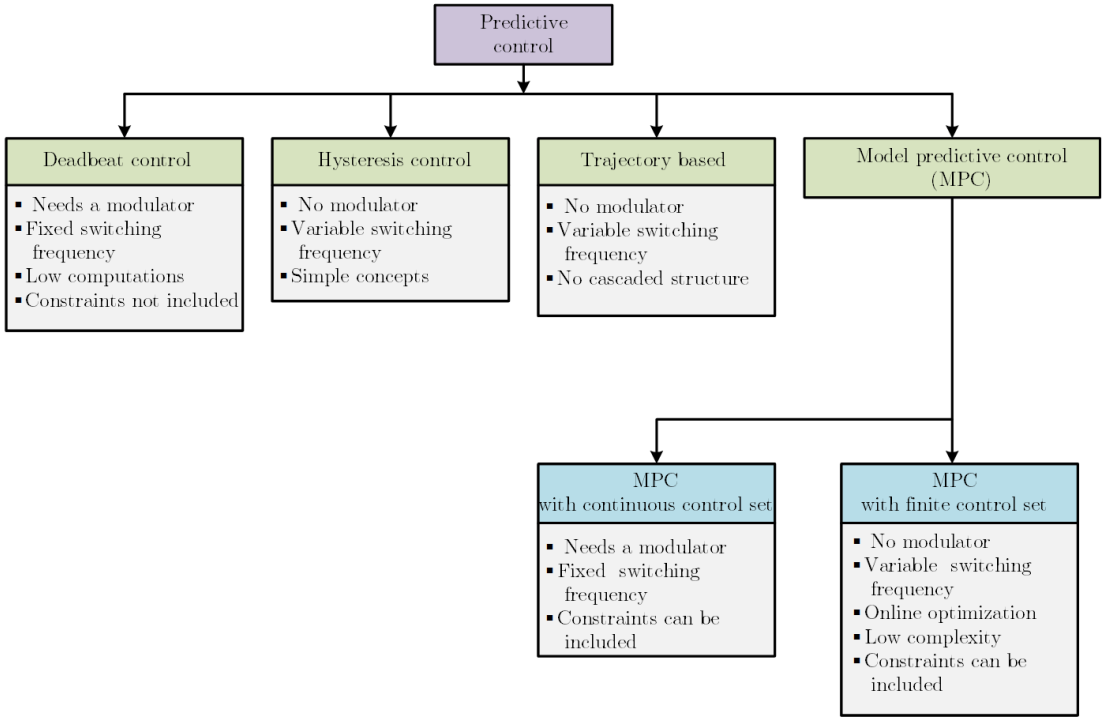

Fig. 2.9. Classification of predictive control methods [91, 92].

MPC for electrical drive systems has become more popular in the research community in the last few years, due to its simple concept, intuitive features, easy inclusion of non-linearities, multivariable optimization and ease of practical implementation [93]. Besides, MPC meets the requirements of modern control systems, such as using the system model and digital control platforms, and allows to consider the system constraints and restrictions.

The generic working principle of MPC is illustrated in Fig. 2.10. For the simplicity, the reference control variable $\underline{x}^*$ is set constant to simplify the analysis. The MPC is formulated in discrete-time, thus it allows the variables to change their values only at discrete sampling instants. The MPC has a capability to consider the past, present, and the future values of the variable. In other words, the MPC predicts future errors and takes preventive control actions such that the system will not be subjected to huge error, thereby making the overall system robust. The principle of MPC consists of three main parts as demonstrated below [92, 94]:

- **Prediction:** In this step, the discrete-time model of the system is used for prediction. This model can be expressed as a state space according to:

$$\underline{x}\,(k+1) = \Phi \underline{x}\,(k+1) + \Gamma \underline{u}\,(k) \tag{2.35}$$

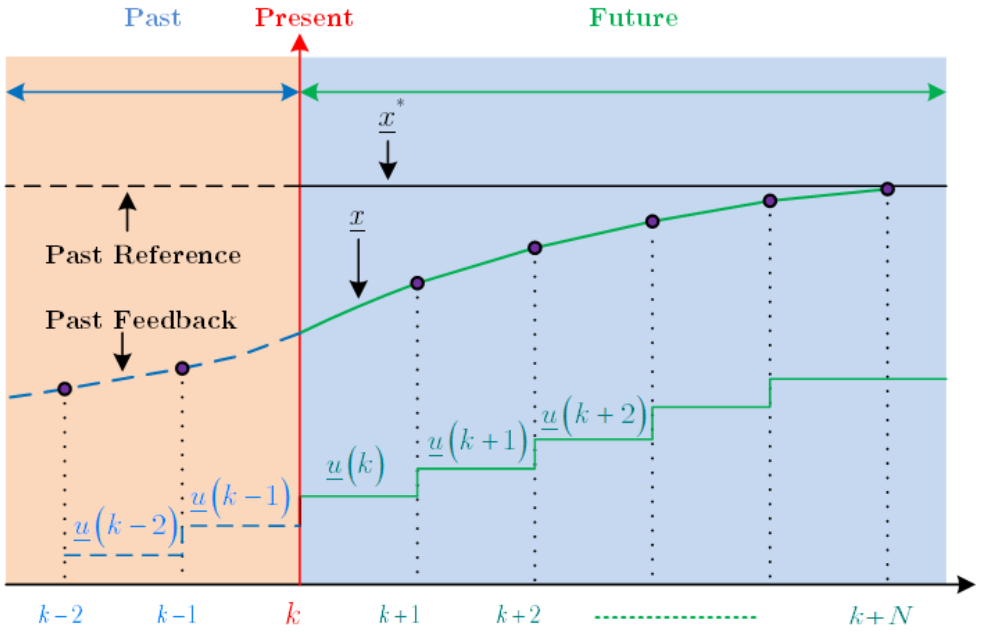

Fig. 2.10. Operating principle of MPC (N=prediction horizon) [94].

$$\underline{y}(k) = \mathrm{C}\underline{x}(k) + \mathrm{D}\underline{u}(k) \tag{2.36}$$

The vector $\underline{x}(k)$ is the state variable at instant k, the vector $\underline{x}(k+1)$ is the state variable at instant $k+1$, the vector $\underline{u}(k)$ represents the input vector of the controller at instant k, the vector $\underline{y}(k)$ represents the output vector. The matrices Φ, Γ, C, and D stand for the matrix of the state system, input, output and feed-forward, respectively. As there is no connection between the input vector $\underline{u}(k)$ and the output vector $\underline{y}(k)$ in the control of the electric drive, the feed-forward matrix D can be set to zero (D=0). The future values of state variable $\underline{x}$ and the control input sequence $\underline{u}$ can be predicted for a prediction horizon N by using the system model and the measurements at instant k.

- **Optimization:** The predictions of the state variable $\underline{x}(k+1)$ at instant $k+1$ are evaluated by a cost function which defines the desired behaviour and control objectives of the system. A general form of the cost function is defined considering the references, future states, and future control inputs as follows:

$$J(k) = f\left(\underline{x}^*(k), ..., \underline{x}^*(k+N), \underline{x}(k), \underline{u}(k), ..., \underline{u}(k+N)\right) \tag{2.37}$$

The input control sequence that minimizes $J(k)$ is selected as an optimal control input:

$$\underline{u}^{opt}(k) = \arg \min_{u} J(k) \tag{2.38}$$

- **Receding Horizon Strategy:** In this step, the controller will apply to the system the first element of the optimal input sequence $\underline{u}(k) = \underline{u}^{opt}(k)$. As a consequence, the state variable $\underline{x}$ moves towards the reference trajectory $\underline{x}^*$. The process of measuring new data, predicting new system behaviour, and optimizing cost is repeated during each sampling interval. This procedure is called a receding horizon strategy.

When applied to electric drives, MPC can be divided into two main categories: continuous control set MPC (CCS-MPC) and FCS-MPC [43,95]. In CCS-MPC, the controller generates a continuous output for a modulator, and the modulator generates the switching states for the inverter to generate the required voltage. Due to the presence of the modulator, the controller yields a constant switching frequency. Conversely, in FCS-MPC, the finite number of the inverter switching states is evaluated against the desired control objectives. The outputs of the controller are discrete, and are directly used to control the power switches of the inverter. The controller, in general, yields a variable switching frequency due to the absence of a modulator [96,97]. In light of the easiness of inclusion of nonlinearities and constraints in the control system, compared to CCS-MPC, FCS-MPC has more overall advantages [43]. Thus, in later sections, only FCS-MPC is discussed and analysed.

2.5.1 Introduction to FCS-MPC

The general scheme of FCS-MPC applied to power converters and electric drives is presented in Fig. 2.11. The power converter can be of any topology (two or three-level inverter, matrix converter, etc). This converter is used to feed a generic load and presents n different switching states. The generic load shown in Fig. 2.11 can represent an electric machine (IM, PMSM or SynRM), the grid or any other type of load.

The control objective pursuits that variable $\boldsymbol{x}(k+1)$ has to follow the reference $\boldsymbol{x}^*(k+1)$. The implementation of FCS-MPC strategies can be divided into three main steps: estima-

tion or measurement, prediction, and optimization. In the first step, the controlled variables are measured or can be estimated such as flux in the case of electric machines. In the second step, the measured variables $\boldsymbol{x}(k)$ are used in the discrete-time model of the system to calculate predictions $\boldsymbol{x}^p(k+1)$ of the controlled variables for each one of the n possible switching states of the inverter. In the third step, the predicted variables $\boldsymbol{x}^p(k+1)$ are

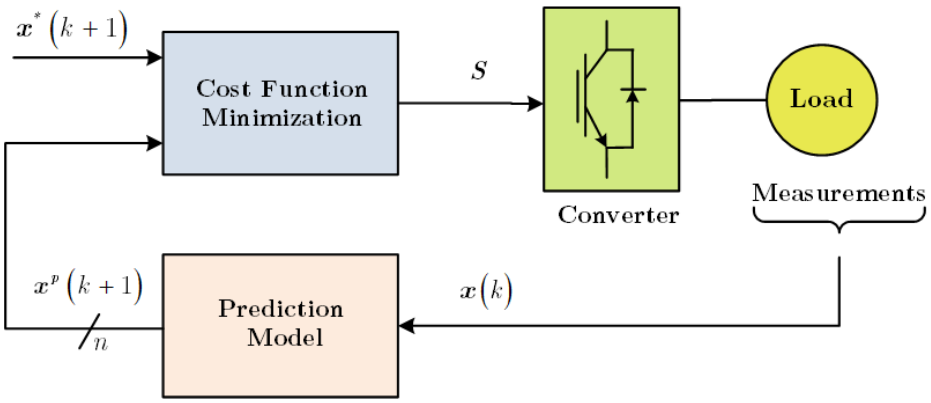

Fig. 2.11. General block diagram of the FCS-MPC strategies [95].

compared with their future reference values $\boldsymbol{x}^*(k+1)$ in order to minimize their difference using a cost function g as follows:

$$g = \left|\boldsymbol{x}^*(k+1) - \boldsymbol{x}^p(k+1)\right|. \tag{2.39}$$

It is important to mention that, as the inverter switching state is taken into consideration in the controller design of standard FCS-MPC strategies, the cost function is evaluated for each possible inverter switching state. The optimal switching state S that minimizes the cost function is chosen and then applied to the inverter at the next sampling instant.

One of the crucial points in FCS-MPC is reference tracking. The switching state that minimizes the reference tracking error at instant $k+1$ is selected and applied directly to the inverter. When sampling time T_s is small compared to the dynamic behaviour of the drive system, no extrapolation is needed. This is the case when the sampling frequency is much higher than the fundamental frequency of the controlled variables and thus the reference values can be considered constant over T_s. In other words, the future reference values $\boldsymbol{x}^*(k+1)$ which appear in the cost function, can be replaced with the actual values

$\boldsymbol{x}^*(k)$. Nevertheless, the future reference values $\boldsymbol{x}^*(k+1)$ can be estimated via extrapolation methods if a high dynamic system is being considered [98, 99].

The 2L-VSI is one of the most widespread converter topologies found in most drive applications. Moreover, it features a generic structure and operating principle that can be easily extended to other converter topologies. Therefore, this topology has been chosen here for explaining the basic principle of FCS-MPC in power electronic applications.

A block diagram of the FCS-MPC strategy applied for the current control of a 2L-VSI is shown in Fig. 2.12. The current control is performed in the following steps [40, 100]:

- The value of the reference current $i^*(k)$ is obtained (from an outer control loop), and the load current $i(k)$ is measured.
- The system model is used to predict the value of the load current in the next sampling interval $i^p(k+1)$ for each of the different voltage vectors.
- In this case, the cost function g evaluates the error between the reference and the predicted currents at the next sampling interval. The voltage vector that minimizes the current error is selected and applied to the load.

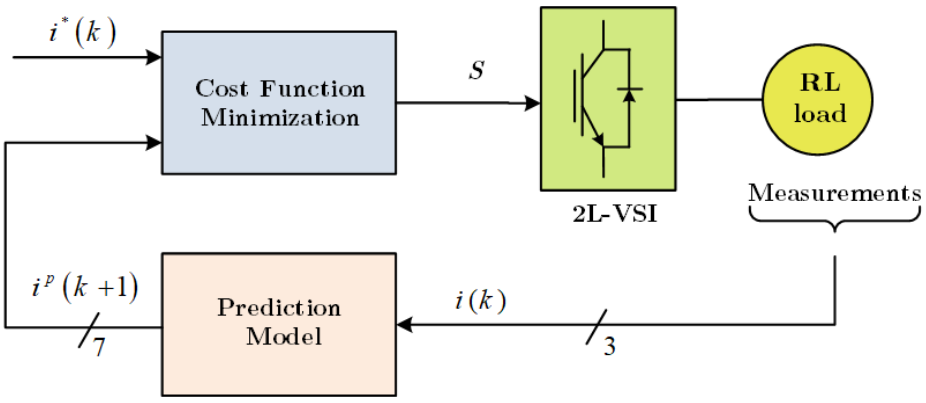

Fig. 2.12. FCS-MPC block diagram for current control in a 2L-VSI [100].

The power circuit of the 2L-VSI is shown in Fig. 2.13. The output voltage space vector generated by this inverter is defined as

$$\underline{u} = \frac{2}{3}\left(u_{aN} + \underline{a}u_{bN} + \underline{a}^2 u_{cN}\right) \tag{2.40}$$

where $\underline{a} = e^{i2\pi/3}$, and u_{aN}, u_{bN} and u_{cN} are the phase-to-neutral voltages of the inverter.

Then, the load voltage vector $\underline{u}$ can be related to the switching state vector $\underline{S}$ by

$$\underline{u} = U_{dc}\,\underline{S}, \tag{2.41}$$

where U_{dc} is the DC-link voltage.

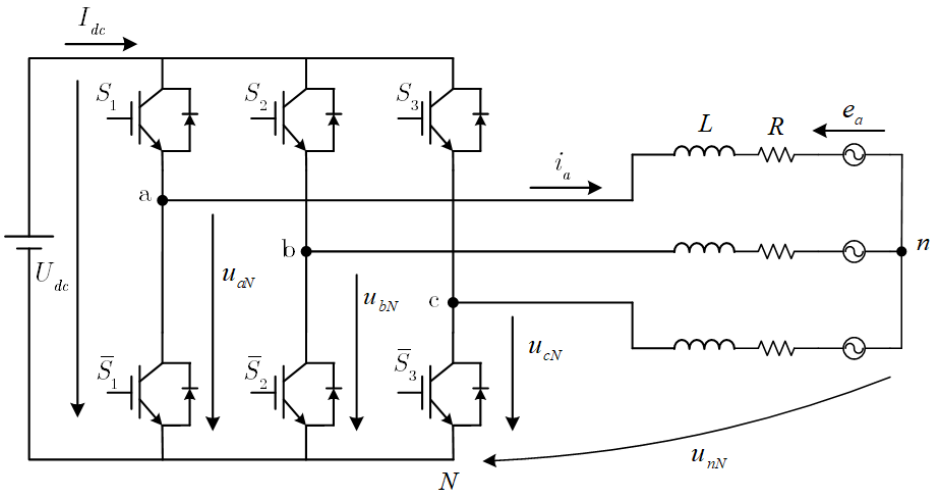

Fig. 2.13. Voltage source inverter power circuit [40, 100].

By evaluating each of the switching states in (2.39), eight voltage vectors ($u_0 - u_7$) can be generated by the inverter resulting in only seven different voltage vectors because u_0 and u_7 produce the same zero voltage vector, this means a 2L-VSI can deliver only 7 different voltage vectors, although there are 8 different switching combinations as it can be seen in Fig. 2.14.

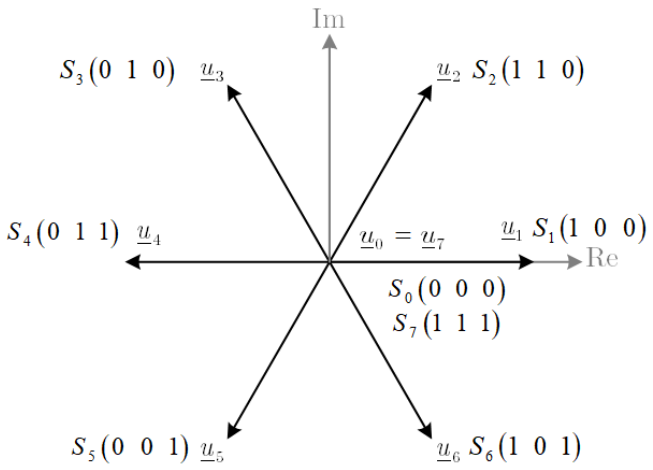

Fig. 2.14. Voltage vectors generated by a 2L-VSI in complex plane.

Taking into account the definitions of variables from the circuit shown in Fig. 2.13, the equations for the load current dynamics for each phase can be written as

$$u_{aN} = L\frac{di_a}{dt} + Ri_a + e_a + u_{nN} \tag{2.42}$$

$$u_{bN} = L\frac{di_b}{dt} + Ri_b + e_b + u_{nN} \tag{2.43}$$

$$u_{cN} = L\frac{di_c}{dt} + Ri_c + e_c + u_{nN} \tag{2.44}$$

where R is the load resistance and L is the load inductance.

By substituting (2.42)-(2.44) into (2.40) a voltage equation for the load current dynamics can be obtained:

$$\begin{aligned}\underline{u} = L\tfrac{d}{dt}\left(\tfrac{2}{3}\left(i_a + \underline{a}i_b + \underline{a}^2 i_c\right)\right) + R\left(\tfrac{2}{3}\left(i_a + \underline{a}i_b + \underline{a}^2 i_c\right)\right) \\ + \tfrac{2}{3}\left(e_a + \underline{a}e_b + \underline{a}^2 e_c\right) + \tfrac{2}{3}\left(u_{nN} + \underline{a}u_{nN} + \underline{a}^2 u_{nN}\right)\end{aligned} \tag{2.45}$$

Considering the space vector definition for the inverter voltage given by (2.40), and the following definitions for load current and back-emf space vectors

$$\underline{i} = \frac{2}{3}\left(i_a + \underline{a}i_b + \underline{a}^2 i_c\right) \tag{2.46}$$

$$\underline{e} = \frac{2}{3}\left(e_a + \underline{a}e_b + \underline{a}^2 e_c\right), \tag{2.47}$$

and assuming that the last term of (2.45) is equal to zero;

$$\frac{2}{3}\left(u_{nN} + \underline{a}u_{nN} + \underline{a}^2 u_{nN}\right) = u_{nN}\frac{2}{3}\left(1 + \underline{a} + \underline{a}^2\right) = 0, \tag{2.48}$$

the load current dynamics can be described by the equation

$$\underline{u} = R\underline{i} + L\frac{d\underline{i}}{dt} + \underline{e} \tag{2.49}$$

where $\underline{u}$ is the voltage vector generated by the inverter, $\underline{i}$ is the load current vector, and $\underline{e}$ is the load back-emf vector.

A discrete time form of the load current (2.49) for a sampling time T_s can be used to predict the future value of load current with the voltage and measured current at instant k.

The load current derivative $d\underline{i}/dt$ is replaced by a forward Euler approximation, that is the derivative is approximated as follows:

$$\frac{d\underline{i}}{dt} \approx \frac{\underline{i}\,(k+1) - \underline{i}\,(k)}{T_s} \tag{2.50}$$

which is substituted in (2.49) to obtain an expression that allows prediction of the future load current at time $k+1$, for each one of the seven voltage vectors $\underline{u}\,(k)$ generated by the inverter. This expression is

$$\underline{i}^{p}\,(k+1) = \left(1 - \frac{RT_s}{L}\right)\underline{i}\,(k) + \frac{T_s}{L}\left(\underline{u}\,(k) - \underline{\hat{e}}\,(k)\right) \tag{2.51}$$

where the term $\underline{\hat{e}}\,(k)$ denotes the estimated back-EMF. The superscript "p" denotes the predicted variables.

The back-EMF can be calculated from (2.49) considering measurements of the load voltage and current with the following expression:

$$\underline{\hat{e}}\,(k-1) = \underline{u}\,(k-1) - \frac{L}{T_s}\underline{i}\,(k) - \left(R - \frac{L}{T_s}\right)\underline{i}\,(k-1) \tag{2.52}$$

where $\underline{\hat{e}}(k-1)$ is the estimated value of $\underline{e}(k-1)$. The present back-EMF $\underline{e}(k)$ can be estimated using an extrapolation of the past values of the estimated back-EMF. Alternatively, as the frequency of the back-EMF is much smaller when compared to the sampling frequency, it will not change considerably in one sampling interval and thus one can assume $\underline{e}\,(k) = \underline{\hat{e}}\,(k-1)$.

In the FCS-MPC algorithm, (2.51) is evaluated for each one of the possible seven voltage vectors, giving seven different current predictions. The voltage vector whose current prediction is closest to the expected current reference is applied to the load at the next sampling instant. In other words, the selected vector will be the one that minimizes the cost function

$$g = \left|i_{\alpha}^{*}\,(k+1) - i_{\alpha}^{p}\,(k+1)\right| + \left|i_{\beta}^{*}\,(k+1) - i_{\beta}^{p}\,(k+1)\right| \tag{2.53}$$

where $i_\alpha^p(k+1)$ and $i_\beta^p(k+1)$ are the real and imaginary parts of the predicted load current vector $\underline{i}^p(k+1)$, for a given voltage vector. This prediction is obtained using the load model. The reference currents $i_\alpha^*(k+1)$ and $i_\beta^*(k+1)$ are the real and imaginary parts of the reference current vector $\underline{i}^*(k+1)$. Usually, this reference current does not change sufficiently in one sampling interval, thus one can consider $\underline{i}^*(k+1) = \underline{i}^*(k)$.

A flowchart of the different tasks involved in FCS-MPC to control the current in a 2L-VSI feeding a RL load is shown in Fig. 2.15. Here, the outer loop is executed every sampling time, and the inner loop is executed for each possible state, obtaining the optimal switching state to be applied during the next sampling period.

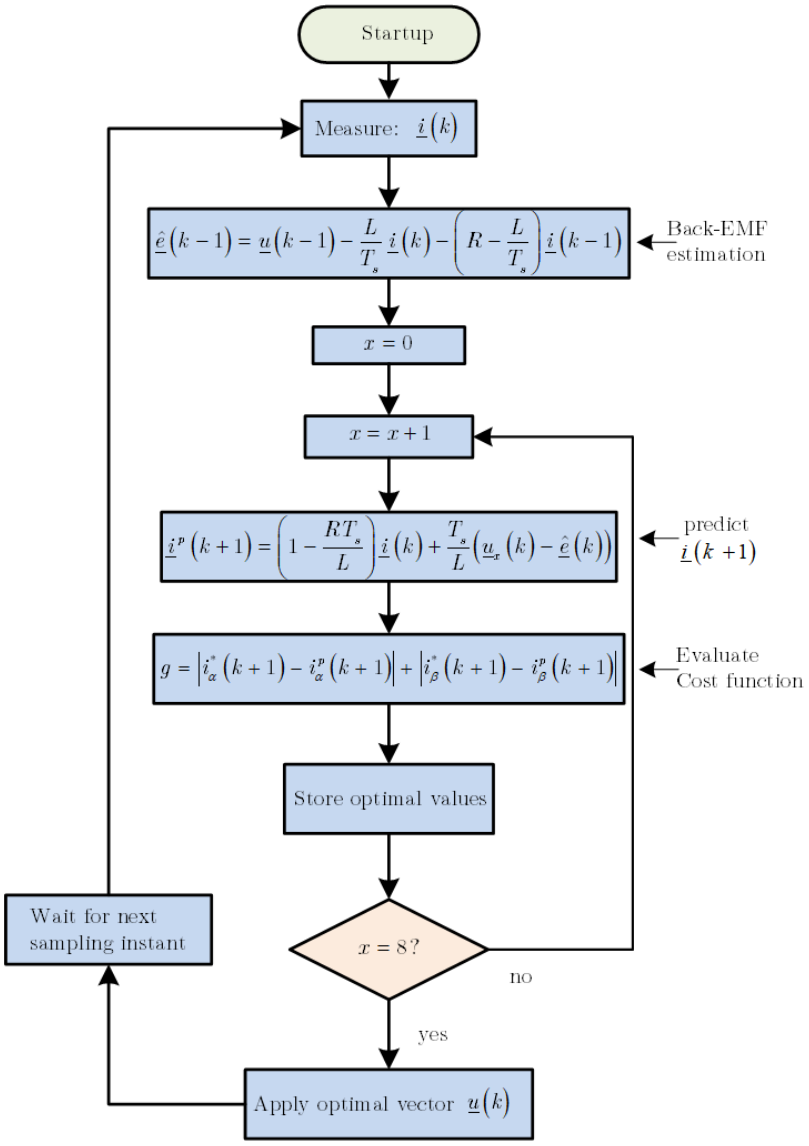

Fig. 2.15. Flowchart of the FCS-MPC applied for current control of a 2L-VSI [40, 92, 100].

One of the main advantages of FCS-MPC is that several control targets, variables (current, voltage, torque and flux) and constraints such as overcurrent protection, switching frequency, and efficiency, can be taken into consideration in the cost function [101]. In [102], an overcurrent protection is added to the cost function to ensure that the stator current of the IM remains within acceptable limits. In [103], the DC-link capacitor voltage balance of a three-level neutral-point-clamped inverter (3L-NPC) is realized by adding an extra term in the cost function. Moreover, it is always desirable to reduce the switching losses of the power converter in inverter-fed drives. Thus, the switching losses reduction term can be easily incorporated in the cost function as exemplified in [104].

Various types of FCS-MPC methods have been investigated in the electric drives field, namely predictive current control (PCC) and predictive torque control (PTC) [43,102,105–107]. To control electric motors, the PTC method evaluates the stator flux and electromagnetic torque in the cost function. The switching state selected for the inverter is the one that minimizes the error between the references and the predicted values of torque and stator flux. The PCC method considers the errors between the current references and predicted current values. Both PTC and PCC methods are useful direct control methods that do not require the use of a modulator. However, PTC has a faster dynamic response and less torque ripple in comparison with PCC [108].

Based on the prediction horizon N, FCS-MPC can be divided into two groups [109–113]:

- Short prediction horizon ($N = 1$), where the calculation burden is small and can be easily implemented in modern digital signal processors (DSPs).
- Long prediction horizon ($N > 1$), where it is possible to obtain a better control performance.

With a long prediction horizon, it is expected to obtain a better performance especially in steady-state [110]. However, the calculation time will increase significantly and the predictions for all possible switching states of the converter become difficult to be applied in a real system. Therefore, a prediction horizon of one sample ahead ($N = 1$) is a better solution and it has been successfully applied to various power electronics applications [111, 112].

Delay compensation is another important issue in the implementation of FCS-MPC ap-

plied to electric drives [114–118]. In an ideal condition, the required time for the calculations can be ignored. Thus, the variables are measured at instant k and the optimal switching state is calculated instantaneously. In other words, the delay in applying this optimal switching state is zero. On the contrary, in a real-time implementation of FCS-MPC, the control algorithm cannot be executed in zero time because the online calculations introduce one sampling time delay between the instant at which the variables are measured and the instant of application of the optimal switching state [117, 118]. This delay, which is caused by the DSP, is significant and must be compensated and considered in the design of the controller otherwise its performance will be deteriorated. This problem can be solved if a two-step ahead prediction is considered. Consequently, the cost function presented in (2.53) should be modified for the evaluation of the predicted load current at instant $k+2$ resulting in

$$g = \left|i_\alpha^* (k+2) - i_\alpha^p (k+2)\right| + \left|i_\beta^* (k+2) - i_\beta^p (k+2)\right|. \tag{2.54}$$

where $i_\alpha^p(k+2)$ and $i_\beta^p(k+2)$ are the real and imaginary parts of the predicted load current vector $\underline{i}^p(k+2)$. This prediction is obtained with the knowledge of the measured current $\underline{i}(k)$, voltage vector $\underline{u}(k)$ applied at instant k, and the estimated current $\hat{\underline{i}}(k+1)$ at instant $k+1$. The reference currents $i_\alpha^*(k+2)$ and $i_\beta^*(k+2)$ are the real and imaginary parts of the reference current vector $\underline{i}^*(k+2)$. The future reference current vector $\underline{i}^*(k+2)$ can be replaced with the actual reference current vector $\underline{i}^*(k)$ for the same reasons stated earlier. The optimal switching state that minimizes the cost function (2.54) at instant $k+2$ is selected and applied to the converter at instant $k+1$.

The two main challenges of FCS-MPC, which confront its practical implementation, are the selection of weighting factors and the calculation time. The literature review regarding these two issues is provided below.

Weighting factor design : One of the key tasks in FCS-MPC is the definition and design of the cost function [95]. If the cost function contains two or more controlled variables with different nature (different units or different orders of magnitude), weighting factors need to be used to handle the relation between them. The weighting factors should be chosen correctly, otherwise a poor performance of the control system will result in the end [119]. The tuning of these weighting factors is still one of the complex tasks in FCS-MPC. The optimal

values of the weighting factors usually depend on the system parameters and operating point. In electric drive applications, the most common form of the cost function is the one that includes both square errors of the torque and stator flux of the motor:

$$g = (T_e^p - T_e^*)^2 + \lambda_{\psi_s}(\psi_s^p - \psi_s^*)^2, \tag{2.55}$$

where T_e^p and T_e^* are the predicted and reference torque values, ψ_s^p and ψ_s^* are predicted and reference flux values, and λ_{ψ_s} is a weighting factor which handles the relative importance between the torque and flux errors.

In this case, it would be quite difficult to choose the optimal value of the weighting factor λ_{ψ_s}, due to the difference nature of the two terms. An alternative consists in the normalization of the two terms by dividing each term by its rated value [101, 102]. Adopting this procedure, the cost function presented in (2.55) can be modified as follows:

$$g = \left(\frac{T_e^p - T_e^*}{T_{en}}\right)^2 + \lambda_{\psi_s}\left(\frac{\psi_s^p - \psi_s^*}{\psi_{sn}}\right)^2, \tag{2.56}$$

where T_{en} and ψ_{sn} are the rated values of the torque and flux of the motor. The value of the weighting factor has a direct influence on the system performance, and it is not easy to define a suitable value to achieve the desired system behaviour. Usually the weighting factor in the normalized cost function (2.56) is tuned following a trial and error process or by running time-consuming computer simulations. Thus, this process requires a considerable amount of time to obtain good results [101, 120, 121].

To avoid the use of weighting factors, a multiobjective ranking-based approach was proposed in [122, 123] for FCS-MPC. In this approach, the cost function was transformed or splitted into multiple cost functions, where the controlled variables were used separately in a individual cost functions. A fuzzy decision-making (FDM) technique was proposed in [124, 125] to alleviate the weighting factors tuning. Although the FDM and multiobjective ranking-based approaches are effective for tuning the weighting factors, their design procedures are not so intuitive and they are relatively complicated and computationally intensive. Moreover, the tuning effort for the priority coefficients of each membership function in the

case of FDM approach is still required. This means that the FDM technique does not truly solve the weighting factor problem and its practical value should be evaluated. Due to these facts, the use of a single cost function with no weighting factors, to solve the optimization problem at each sampling time is simpler and preferable. However, its implementation in electric drive applications is not straightforward. Normally, the great concerns in this type of applications, as stated earlier, are the motor torque and stator flux control, thus the weighting factors cannot be omitted in the cost function. Recently, a single cost function was applied to an IM drive in [106,126]. The single cost function was designed by converting the torque and stator flux reference values of the IM into an equivalent reference vector of stator flux, hence eliminating the weighting factor associated to stator flux in the conventional FCS-MPC strategy. However, designing such a cost function is not possible without making a major modification in the prediction process of the FCS-MPC strategy.

Computational cost reduction : The calculation time is another implementation challenge of FCS-MPC. The calculation time is more critical when the number of switching states of the power converter increases or more objectives are considered for control. Of course, if the calculation time can be reduced, this can lead to a wider acceptance of FCS-MPC in drive applications.

Recently, different methods have been proposed to decrease the computational cost in FCS-MPC [127–132]. In [127], a computationally efficient predictive DTC for medium voltage drives is proposed. By adopting a branch and bound algorithm and by discarding some optimal sequences, the number of switching sequences is reduced. The performance is further improved with a modified sphere decoding algorithm [128]. Sector distribution on input voltage vector is used in [129] to decrease the number of candidate voltage vectors for prediction. A lookup table has been proposed in [130] to decrease the number of candidate vectors for FCS-MPC of an IM fed by a 2L-VSI. In [131], interesting approaches have been proposed to decrease the calculation time in FCS-MPC. The main idea in these studies is similar: the optimum switching state is decided based on the desired voltage vectors, thus eliminating the calculations of the state variables predictions for all switching states and thus reducing the number of calculations. Another goal of this thesis is to simplify the implementation of FCS-MPC in a 2L-VSI-fed SynRM. Therefore, the ideas introduced in [132]

will be further extended for this type of drive system.

2.5.2 FCS-MPC for SynRMs

The PTC has been extensively applied for electrical drive systems, mainly for IMs and PMSMs drives [126, 133–137].

Only a few papers can be found in literature using FCS-MPC for SynRM drives. In [138], a PTC strategy was presented for SynRMs taking into account the effect of both magnetic saturation and cross-magnetic saturation. This control strategy, known as direct mean torque control (DMTC), is a kind of DTC that calculates the switch-on time of the switches in a way that the steady-state value of the motor torque is directly reached at the end of the control cycle. In other words, DMTC was developed to solve the standard DTC limitations by substituting the torque and stator flux hysteresis bands with a new switching strategy: in a constant switching interval, a suitable voltage is applied to the SynRM for the time required to reach the border of a calculated ripple bands. When this limit is reached, the zero-voltage space phasor is applied and torque returns to the minimum level. For a given steady-state operation point the torque ripple can be kept constant.

Fig. 2.16 shows a typical operation of the DMTC in steady-state. In control strategy, the switching instants are directly placed in a way that the mean torque over the cycle is equal to the reference value. Applying an active voltage space phase phasor (AVSP) first, the torque increases at the beginning. Then, when the limit of a calculated virtual hysteresis width (ΔM) is reached, a zero voltage space phasor (ZVSP) is applied and the torque decreases.

In steady-state, the torque $M(k)$ at the beginning of a cycle should be equal to its value $M(k+1)$ at the end (which results in a theoretical zero torque error at the end of a cycle). Instead of simply equalizing the different hatched areas (Fig. 2.16) for the cycle k, it is also possible to switch the AVSP to reach directly the value of $M(k+1)$ according to steady-state, thus

$$M\left(k+1\right) = M^{*} - {}^{1}\!/_{2}\Delta M \tag{2.57}$$

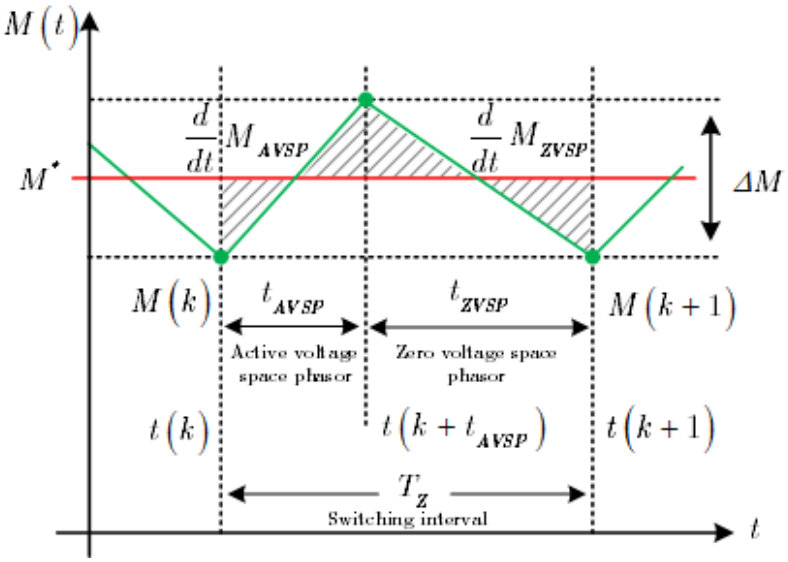

Fig. 2.16. Typical operation of the DMTC in steady-state. [138].

The torque $M(k+1)$ at the end of the cycle can be expressed as:

$$M\left(k+1\right) = M\left(k\right) + \frac{d}{dt}M_{AVSP}\, t_{AVSP} + \frac{d}{dt}M_{ZVSP}\left(T_Z - t_{AVSP}\right) \tag{2.58}$$

By assuming a linear shape of the torque during a switching interval T_Z, in which an AVSP is applied during the time t_{AVSP} and a ZVSP during t_{ZVSP} the "virtual hysteresis width" in the steady state can be calculated as:

$$\Delta M = -\frac{\frac{d}{dt}M_{AVSP}\cdot\frac{d}{dt}M_{ZVSP}}{\frac{d}{dt}M_{AVSP} - \frac{d}{dt}M_{ZVSP}}.T_Z \tag{2.59}$$

With (2.59) and solving equation (2.58) for t_{AVSP} leads finally to:

$$t_{AVSP} = \frac{M^* - M\left(k\right) - {}^1\!/_2\Delta M - \frac{d}{dt}M_{ZVSP}T_Z}{\frac{d}{dt}M_{AVSP} - \frac{d}{dt}M_{ZVSP}} \tag{2.60}$$

and

$$t_{ZVSP} = T_Z - t_{AVSP} \tag{2.61}$$

The six possible active voltage space vectors have different influences on the torque as well as on the flux. Therefore, sector comparators pre-select the two most favorable voltage space phasors and the "on" time t_{AVSP} is calculated for them.

When the ZVSP is applied to the SynRM the torque decreases and its time derivative is given by

$$\frac{d}{dt}M_{ZVSP} = \frac{3}{2}p\left(L_d - L_q\right)\left\{\left(\frac{\omega_r L_q i_q - R_s i_d}{L_d}i_q\right) - \left(\frac{\omega_r L_d i_d + R_s i_q}{L_q}i_d\right)\right\}, \tag{2.62}$$

and for an AVSP, the torque increases with the time derivative

$$\frac{d}{dt}M_{AVSP} = \frac{3}{2}p\left(L_d - L_q\right)\left\{\left(\frac{u_q i_d}{L_q}\right) + \left(\frac{u_d i_q}{L_d}\right)\right\} + \frac{d}{dt}M_{ZVSP}. \tag{2.63}$$

In order to decide which voltage space phasor has to be applied to the machine the flux has to be taken into account. In the DMTC presented in [138], the flux is predicted to know its magnitude in the next cycle to choose the optimum active voltage space phasor which offers less flux deviation at the end of its "on" time and to keep the stator flux as close as possible of a circular trajectory.

The components of the stator flux along the d-axis and the q-axis at the end of the same cycle can be predicted using the following expressions:

$$\begin{cases} \psi_{d(k+t_{AVSP})} = L_d i_{d(k+t_{AVSP})} \\ \psi_{q(k+t_{AVSP})} = L_q i_{q(k+t_{AVSP})} \end{cases} \tag{2.64}$$

where $i_{d(k+t_{AVSP})}$ and $i_{q(k+t_{AVSP})}$ are the d- and q-axis predicted currents at instant $k+1$, which are obtained with the aid of the motor voltage equations as follows:

$$\begin{cases} i_{d(k+t_{AVSP})} = \frac{t_{AVSP}}{L_d}\left\{u_{d(k)} + \omega_r L_q i_{q(k)} - R_s i_{d(k)}\right\} + i_{d(k)} \\ i_{q(k+t_{AVSP})} = \frac{t_{AVSP}}{L_q}\left\{u_{q(k)} - \omega_r L_d i_{d(k)} - R_s i_{d(k)}\right\} + i_{q(k)} \end{cases}. \tag{2.65}$$

In [139], a hierarchical direct predictive control (HDPC) strategy was proposed for SynRM drives. In this control strategy, the mathematical model of the SynRM was used considering the cross-coupling and saturation effects to improve the prediction accuracy. The main difference between HDPC and the conventional PTC lies in the process of obtaining the

solution to the minimization problem, being the optimal voltage vector applied to the motor obtained from a hierarchical selection policy.

At time step k, the optimal voltage vector to be applied at the next sampling interval is determined through a hierarchical sequence of tests, based on the state predicted at step $k+2$. By evaluating the tests sequentially, a successive refinement of the admissible voltage vectors is carried out, finally leading to the optimal solution. In defining the sequence of tests, the highest priority is given to the regulation of the d-axis current within a specified error threshold, under the mandatory constraint imposed by the motor current limits. This choice corresponds to preserve a certain magnetic flux level in the machine, regardless of its operation, so that a faster torque response can be obtained. Among all the vectors satisfying the current regulation condition, the next selection is operated according to the speed regulation requirement, and then on the reduction of the q-axis current ripple. The multi-level decisional process can be detailed as follows:

1) within the set of available voltage vectors u^n with $n \in \mathcal{N}_0 = \{1, 2, ..., 13\}$, select only those in $\mathcal{N}_1 \subseteq \mathcal{N}_0$ producing a current vector $\hat{i}^n_{k+2}$ at step $k+2$ satisfying the current limit

$$\left|\hat{i}^n_{k+2}\right| < \ I_N \tag{2.66}$$

where I_N is the motor nominal current. If none exists, then select the optimal voltage vector as the one minimising the magnitude of the predicted current vector, i.e. the one whose index is

$$n^* = \arg\min_{n \in \mathcal{N}_0} \left|\hat{i}^n_{k+2}\right| \tag{2.67}$$

2) among the voltage vectors selected at point 1, consider those $\mathcal{N}_2 \subseteq \mathcal{N}_1$ that satisfy the condition

$$|e_{d,k+2}| < |e_{d,max}| \tag{2.68}$$

where $e_{d,k+2} = i^*_{d,k+2} - \hat{i}_{d,k+2}$ is the predicted direct current error at step $k+2$. In addition to the vectors satisfying (2.68), the vectors that comply with the condition

$$|e_{d,k+2}| < |e_{d,k+1}| \tag{2.69}$$

are also considered to extend the set of admissible vectors passed to the next decisional level. In fact, operating a drastic restriction in this first step of evaluation could jeopardise the remaining choices. If no vectors satisfying (2.68) or (2.69) exist, then select the optimal voltage vector as in point 1 (but restricted to the set $\mathcal{N}_1$).

3) among the voltage vectors selected at point 2, choose those in $\mathcal{N}_3 \subseteq \mathcal{N}_2$ that satisfy the condition

$$|e_{\omega,k+2}| \leq \ e_{\omega,\max} \tag{2.70}$$

where $e_{\omega,k+2} = \omega^*_{k+2} - \hat{\omega}_{k+2}$ is the predicted speed error at step $k+2$. If none exists, then select those in $\mathcal{N'}_3 \subseteq \mathcal{N}_2$ that decrease the speed error, i.e.

$$|e_{\omega,k+2}| \leq |e_{\omega,k+1}| \tag{2.71}$$

If neither (2.70) nor (2.71) can be satisfied, then the optimal voltage vector is the one that produces the minimum increase of the speed error, i.e.

$$n^* = \arg\min_{n \in \mathcal{N}_2} \left|e^n_{\omega,k+2}\right| - \left|e^n_{\omega,k+1}\right| \tag{2.72}$$

4) among the voltage vectors selected at point 3, the optimal is chosen as the one minimising the deviation of the predicted q-axis current from its "moving average" value, i.e.

$$n^* = \underset{n \in \mathcal{N}_3 \cup \mathcal{N'}_3}{arg\,min} \left|\hat{i}^n_{q,k+2} - i_{qf,k}\right| \tag{2.73}$$

where $i_{qf,k}$ is the output at step k of a 80-taps moving average filter.

A flowchart representation of the hierarchical decisional process described above is reported in Fig. 2.17.

The authors in [140] discussed the improvement of the model-free PCC for the SynRM drives by achieving the simplicity, easy realization, and free from a modulation technique. The principle of this control strategy is illustrated in Fig. 2.18, which shows the possible current trajectories under different conduction modes of the 2L-VSI.

In Fig. 2.18, the (k)th sampled α-axis stator current under the conducting mode $S_{k-1} \in$

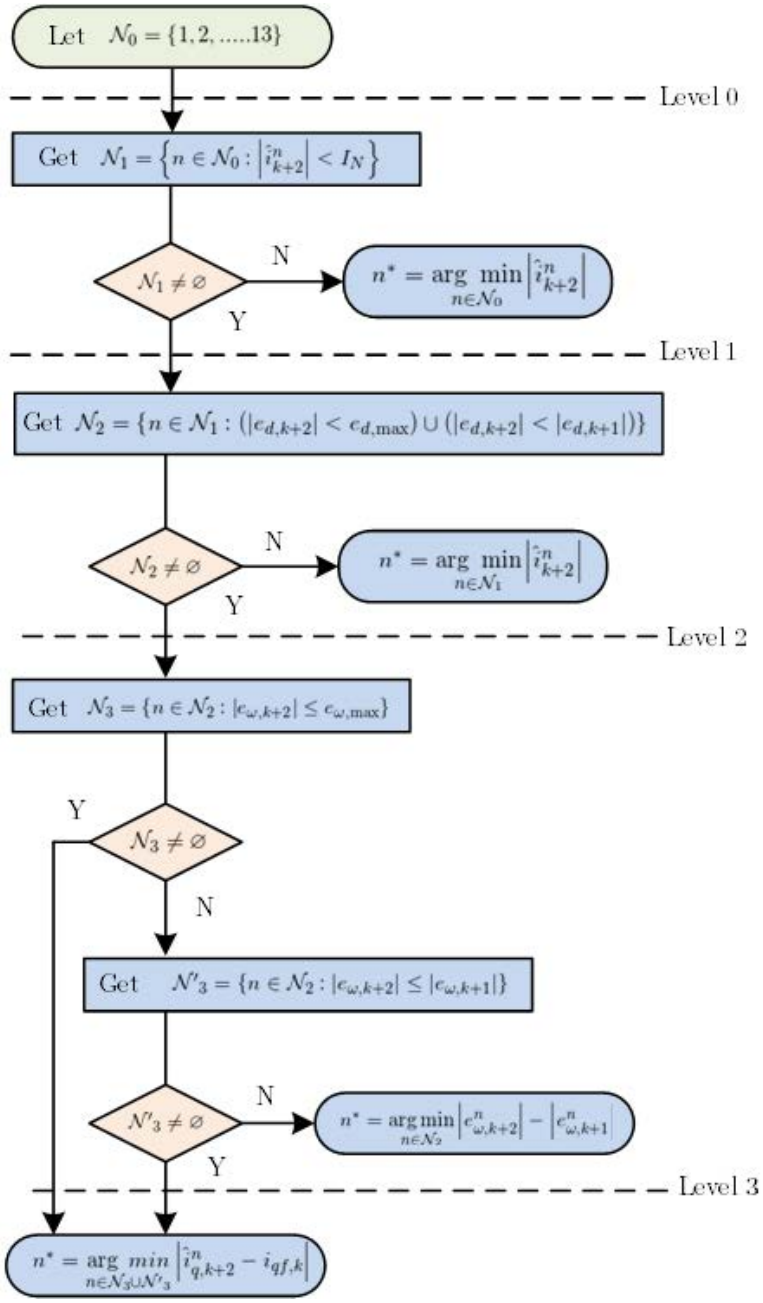

Fig. 2.17. Hierarchical decisional process for optimal input selection [139].

$\{S_0, ..., S_7\}$ is denoted as $i_\alpha[k]|_{S_{k-1}}$. In the same figure, $i^p_\alpha[k+2]|_{S_1}$, $i^p_\alpha[k+2]|_{S_3}$, $i^p_\alpha[k+2]|_{S_7}$, and $i^p_\alpha[k+2]|_{S_k}$ represent the predicted α-axis stator currents under the conducting modes S_1, S_3, S_7, and $S_k \in \{S_0, ..., S_7\}$, respectively. Similar to $i^p_\alpha[k]|_{S_{k-1}}$, the future currents $i^p_\alpha[k+1]|_{S_k}$ and $i^p_\alpha[k+2]|_{S_{k+1}}$ under the conducting modes S_k and $S_{k+1} \in \{S_0, ..., S_7\}$ will be measured in the $(k+1)$th and $(k+2)$th sampling periods, respectively. Using an add-

and-subtract technique, one can easily obtain th following equation

$$\begin{aligned} i_\alpha[k+2]|_{S_{k+1}} = i_\alpha[k]|_{S_{k-1}} + \left(i_\alpha[k+1]|_{S_k} - i_\alpha[k]|_{S_{k-1}}\right) \\ + \left(i_\alpha[k+2]|_{S_{k+1}} - i_\alpha[k+1]|_{S_k}\right) \end{aligned} \tag{2.74}$$

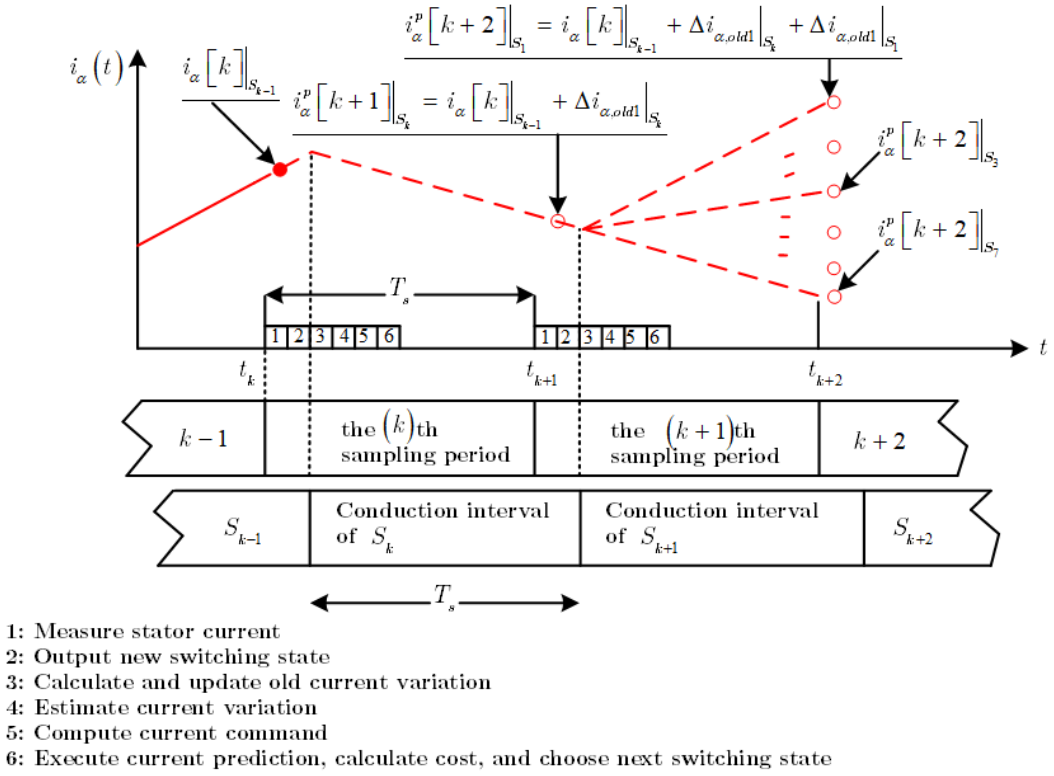

Fig. 2.18. Schematic representation of the model-free PCC [140].

For convenience, two current variations in (2.74) are defined as follows:

$$\Delta i_\alpha|_{S_k} = i_\alpha[k+1]|_{S_k} - i_\alpha[k]|_{S_{k-1}} \tag{2.75}$$

$$\Delta i_\alpha|_{S_{k+1}} = i_\alpha[k+2]|_{S_{k+1}} - i_\alpha[k+1]|_{S_k} \tag{2.76}$$

In the (k)th sampling period, the two current variations $\Delta i_\alpha|_{S_k}$ and $\Delta i_\alpha|_{S_{k+1}}$ cannot be measured because of the unavailability of the future currents $i_\alpha[k+1]|_{S_k}$ and $i_\alpha[k+2]|_{S_{k+1}}$ appearing in (2.75) and (2.76), respectively. However, their previous values can be used in this case as substitutes because any two neighboring current variations under the same

conducting modes are close to each other, provided the sampling interval T_s is fixed and sufficiently short. The two expressions that can be used to approximate (2.75) and (2.76) are given by

$$\Delta i_\alpha|_{S_k} \approx \Delta i_{\alpha,old1}|_{S_k \in \{S_0,\ldots,S_7\}} \tag{2.77}$$

$$\Delta i_\alpha|_{S_{k+1}} \approx \Delta i_{\alpha,old1}|_{S_{k+1} \in \{S_0,\ldots,S_7\}} \tag{2.78}$$

where the subscript "$old1$" refers to previous current variations stored in the microprocessor.

Consider the left-hand-side of (2.76), its previous value will be backed up and denoted with the subscript "$old2$" as follows:

$$\Delta i_{\alpha,old2}|_{S_1 \in \{S_0,\ldots,S_7\}} = \Delta i_{\alpha,old1}|_{S_1 = S_{k-1}} \tag{2.79}$$

To reduce the approximation errors in (2.77) and (2.78), the following update mechanism is adopted to refresh the current variations

$$\Delta i_{\alpha,old1}|_{S_{k-1} \in \{S_0,\ldots,S_7\}} = i_\alpha[k]|_{S_{k-1}} - i_\alpha[k-1]|_{S_{k-2}} \tag{2.80}$$

The left-hand-side of (2.80) assumes eight different values under eight different conducting modes. Given (2.74)-(2.80), together with Fig. 2.18, the predicted α-axis stator current under the conducting mode S_j can be calculated as follows:

$$i^p_\alpha[k+2]|_{S_j} = i_\alpha[k]|_{S_{k-1}} + \Delta i_{\alpha,old1}\Big|_{S_k} + \Delta i_{\alpha,old1}|_{S_j} \tag{2.81}$$

with the superscript "p" denoting the predicted value. Following the above procedures, one can obtain the predicted β-axis stator current as

$$i^p_\beta[k+2]\Big|_{S_j} = i_\beta[k]\Big|_{S_{k-1}} + \Delta i_{\beta,old1}\Big|_{S_k} + \Delta i_{\beta,old1}|_{S_j} \tag{2.82}$$

Because there are eight different conduction modes, there will also be eight current predictions for the α- and β-axis, respectively. The cost function associated with the conduction

mode S_j is defined as

$$g\left[k\right]\big|_{S_j} = \left|i_\alpha^*\left[k+2\right] - i_\alpha^p\left[k+2\right]\big|_{S_j}\right| + \left|i_\beta^*\left[k+2\right] - i_\beta^p\left[k+2\right]\big|_{S_j}\right| \tag{2.83}$$

where the superscript "*" represents the current command. The reference currents along α- and β-axis at instant $k+2$ can be calculated and approximated by

$$i_\alpha^*\left(k+2\right) = 6i_\alpha^*\left(k\right) - 8i_\alpha^*\left(k-1\right) + 3i_\alpha^*\left(k-2\right) \tag{2.84}$$

$$i_\beta^*\left(k+2\right) = 6i_\beta^*\left(k\right) - 8i_\beta^*\left(k-1\right) + 3i_\beta^*\left(k-2\right) \tag{2.85}$$

In the (k)th sampling period, (2.84) yields eight cost values. A conducting mode S_m is selected, which gives the minimum cost value, i.e.,

$$g\left[k\right]\big|_{S_m\in\{S_0,\ldots,S_7\}} = \min\left\{g\left[k\right]\big|_{S_0},\ldots,g\left[k\right]\big|_{S_7}\right\} \tag{2.86}$$

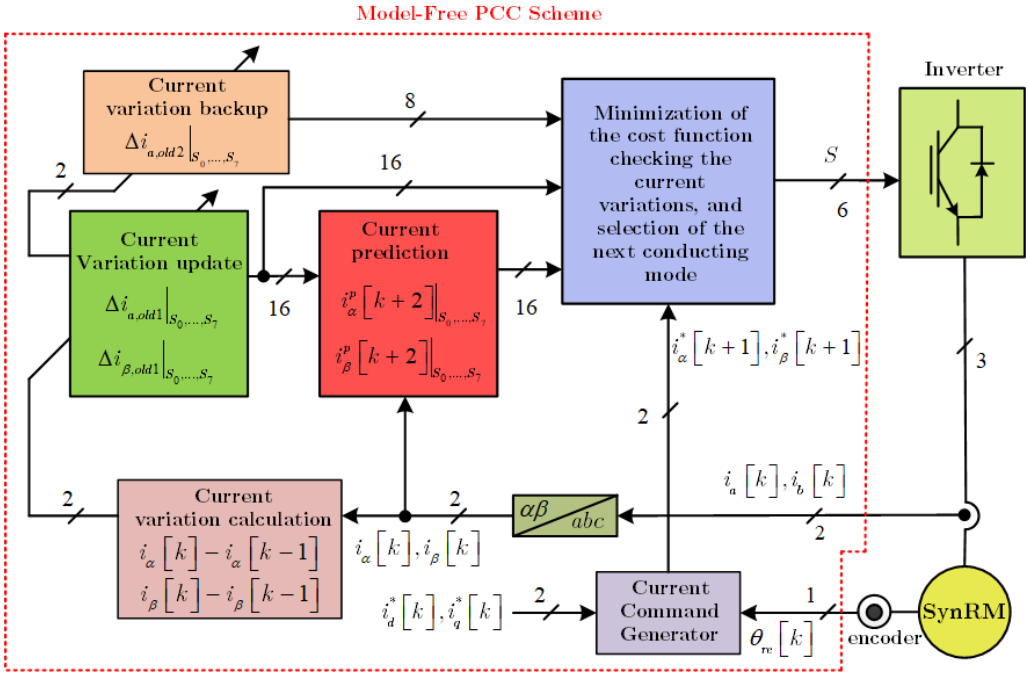

Fig. 2.19. Block diagram of the SynRM drive system with the model-free PCC [140].

The block diagram of the model-free PCC control strategy is shown in Fig. 2.19, where $i_d^*\left[k\right]$ and $i_q^*\left[k\right]$ denote the d- and q-axis current command, and $\theta_{re}\left[k\right]$ represents the rotor

position. In spite of the fact that this control strategy does not require the knowledge of the motor parameters in order to predict the future stator current, it is strongly dependent on the accuracy of current measurements and any noise or measurement errors can lead to instability of the system. In addition, this control strategy has a challenge due to the big change in current references. In view of the aforementioned reasons, FCS-MPC for SynRM drives has been barely investigated. Therefore, this work aims at filling this research gap.

3

Predictive Active Flux and Torque Control of SynRM Drives

Two predictive control strategies using the active flux concept are presented in this chapter. The first control strategy, PAFTC, follows the conventional implementation steps of existing FCS-MPC strategies. Thus, it requires the predictions of the state variables for all possible switching states generated by the inverter. On the other hand, in the second control strategy, S-PAFTC, all the predictions are replaced by the calculation of an equivalent reference voltage, done only once in a sampling period. This results in a smaller computational burden and a simpler design of the cost function compared to the PAFTC strategy.

This chapter is organised as follows: section 3.1 describes the mathematical model of the system (inverter and motor). The parameters identification of the SynRM under study is also explained in this section. Section 3.2 discusses the PAFTC strategy step-by-step. The S-PAFTC strategy is described in detail in section 3.3. Finally, in section 3.4, simulation and experimental results are provided to point out the merits and demerits of the two developed predictive control strategies.

3.1 System Mathematical Model

FCS-MPC strategies require an accurate system model. Furthermore, the model must be discretized to be digitally implemented. In this thesis, the system comprises a SynRM with an encoder mounted on the rotor shaft, the 2L-VSI and a dSPACE ds1103 control platform. The predictive control strategies presented in this work require discrete mathematical models of the inverter and motor which are presented in the following subsections.

3.1.1 Inverter Model

The power circuit of the 2L-VSI is shown in Fig. 3.1. The switching states of this converter are decided by the switching functions of the three legs: S_a, S_b and S_c, being defined as

$$S_i = \begin{cases} 1 \text{ if } S_1 \text{ is ON and } \bar{S}_1 \text{ is OFF} \\ 0 \text{ if } S_1 \text{ is OFF and } \bar{S}_1 \text{ is ON} \end{cases}, \tag{3.1}$$

where $i \in \{a,\ b,\ c\}$.

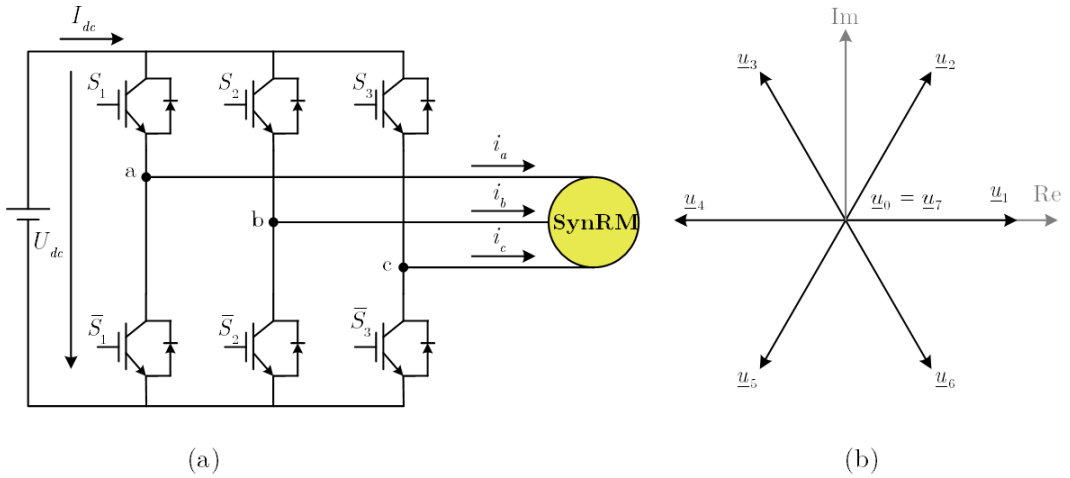

Fig. 3.1. Power converter topology: (a) 2L-VSI feeding a SynRM; (b) voltage vectors generated by the 2L-VSI.

The inverter switching state can be expressed in the form of a complex vector according to

$$\underline{S} = \frac{2}{3}\left(S_a + \underline{a}\, S_b + \underline{a}^2 S_c\right) \tag{3.2}$$

where $\underline{a} = e^{j2\pi/3}$.

The output voltage space vector generated by the 2L-VSI is given by

$$\underline{u} = \frac{2}{3}\left(u_a + \underline{a}\, u_b + \underline{a}^2 u_c\right) \tag{3.3}$$

where u_a, u_b, u_c denote the phase voltages at the motor terminals.

By neglecting the IGBTs on the state voltage drop and the dead-time, the voltage vector

$\underline{u}$ can be expressed in terms of the switching state $\underline{S}$ and the DC-link voltage, U_{dc}, according to

$$\underline{u} = U_{dc}\,\underline{S}. \tag{3.4}$$

The inverter has a total of eight switching states. As there are two identical zero voltage vectors ($\underline{u}_0 = \underline{u}_7$), this results in only seven different voltage vectors. Therefore, in the present work, a discrete system of the 2L-VSI with a total of seven different states as possible outputs is considered.

In this context, the inverter behaves as a nonlinear discrete system. Therefore, the discrete voltage vectors shown in Table 3.1 are the only possible control actions to the SynRM drive.

Table 3.1: Voltage vectors of the 2L-VSI.

$\boldsymbol{u}_n$	$\boldsymbol{S} = [S_a\ S_b\ S_c]$	$\underline{u} = u_\alpha + ju_\beta$
u_0	[0 0 0]	0
u_1	[1 0 0]	$2/3U_{dc}$
u_2	[1 1 0]	$1/3U_{dc} + j\sqrt{3}/3U_{dc}$
u_3	[0 1 0]	$-1/3U_{dc} + j\sqrt{3}/3U_{dc}$
u_4	[0 1 1]	$-2/3U_{dc}$
u_5	[0 0 1]	$-1/3U_{dc} - j\sqrt{3}/3U_{dc}$
u_6	[1 0 1]	$1/3U_{dc} - j\sqrt{3}/3U_{dc}$
u_7	[1 1 1]	0

3.1.2 SynRM Model

The SynRM drive control system usually uses a mathematical model with equations in a rotor reference frame. Thus, the mathematical model of the SynRM is herein presented in this reference frame.

The vector diagram of the SynRM in the dq rotor reference frame, under steady-state conditions is illustrated in Fig. 3.2. In this figure, $\underline{i}_s$ is the stator current vector, θ_i is the angle of the current space vector measured from the SynRM d-axis, $\underline{\psi}_s$ is the stator flux vector, and $\underline{u}_s$ is the stator voltage space vector. The figure also shows the phase angle φ between the stator voltage $\underline{u}_s$ and the stator current $\underline{i}_s$, which determines the power factor

$\cos\varphi$, and the angle δ between the stator flux vector $\underline{\psi}_s$ and the d-axis, which is usually known as the load angle of the SynRM.

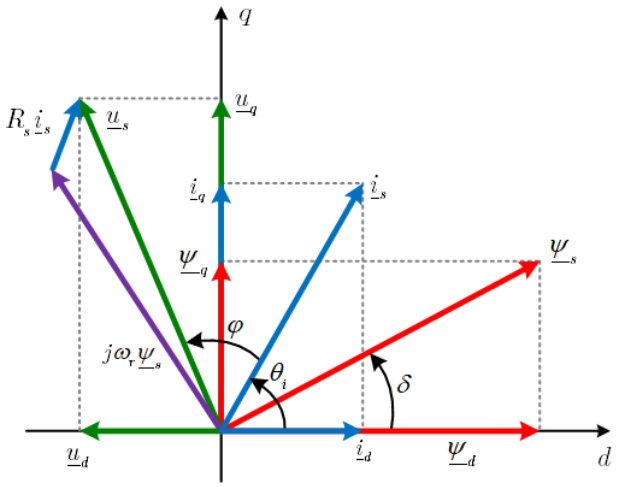

Fig. 3.2. Vector diagram of the SynRM, at steady-state, in the dq rotor reference frame [141, 142].

Fig. 3.3 shows the equivalent circuits of the SynRM in the rotor reference frame, where the quantities u_d, u_q, i_d, i_q, ψ_d and ψ_q represent the voltages, currents, and fluxes of the SynRM along dq-axes, respectively [143]. R_s stands for the stator resistance and ω_r is the rotor electrical angular speed.

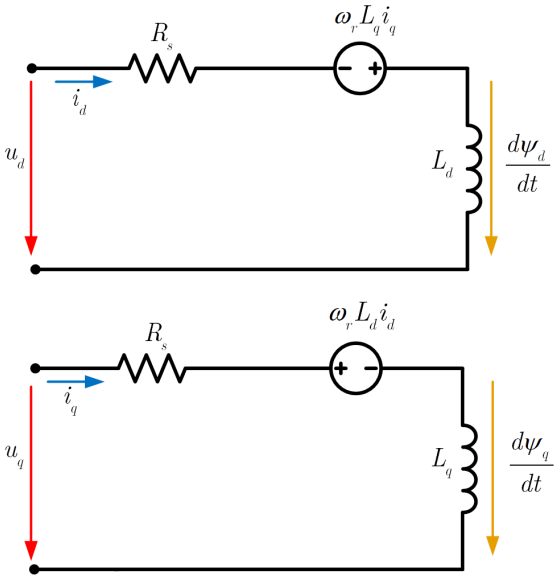

Fig. 3.3. Equivalent circuits of a SynRM in a rotor reference frame [143].

The equivalent circuits shown in Fig. 3.3 do not involve the iron loss resistance, R_c, because the process of obtaining an accurate value for this resistance is a complex task.

Thus, this resistance is very often neglected. Moreover, the motor used in the experimental tests is an efficient one (rated efficiency around 90.4 %), as a consequence, the iron losses of this motor are very small in comparison with the other losses. In view of these reasons, and for the sake of simplicity, the iron loss resistance is not taken into account in the motor model.

The voltage equations of the SynRM, are now described as [144].

$$u_d = R_s i_d + \frac{d\psi_d}{dt} - \omega_r \psi_q \tag{3.5}$$

$$u_q = R_s i_q + \frac{d\psi_q}{dt} + \omega_r \psi_d. \tag{3.6}$$

The electromagnetic torque T_e developed by the SynRM is given by

$$T_e = \frac{3}{2} p \left(\psi_d i_q - \psi_q i_d \right), \tag{3.7}$$

where p is the number of pole-pairs.

Due to the nonlinear magnetic properties of the SynRM and due to the non-negligible cross-saturation between the two axes [143, 145], these phenomena must be taken into consideration in its mathematical model. Furthermore, an accurate representation of these phenomena in the SynRM model can enhance the controller performance, allowing the SynRM to operate with optimum torque density, efficiency, dynamic response, and FW capability [78, 146–148].

The two-dimensional relationship between the flux linkage and current components of the SynRM are given by

$$\psi_d = L_d \left(i_d, i_q \right) i_d + L_{dq} \left(i_d, i_q \right) i_q \tag{3.8}$$

$$\psi_q = L_{qd} \left(i_d, i_q \right) i_d + L_q \left(i_d, i_q \right) i_q. \tag{3.9}$$

where $L_d(i_d, i_q)$ and $L_q(i_d, i_q)$ represent the self-inductances along the d- and q-axis, respectively, and $L_{dq}(i_d, i_q)$ and $L_{qd}(i_d, i_q)$ stand for the cross-saturation inductance components.

The inductance matrix can be given by

$$\boldsymbol{L} = \begin{bmatrix} L_d\left(i_d, i_q\right) & L_{dq}\left(i_d, i_q\right) \\ L_{qd}\left(i_d, i_q\right) & L_q\left(i_d, i_q\right) \end{bmatrix}. \tag{3.10}$$

The inductances $L_d\left(i_d, i_q\right)$ and $L_q\left(i_d, i_q\right)$ shown in (3.10) are commonly referred to as self-apparent inductances while $L_{dq}\left(i_d, i_q\right)$ and $L_{qd}\left(i_d, i_q\right)$ are referred as cross-apparent inductances. Because of the non-linearity of the magnetic circuit of the SynRM, the self- and cross-apparent inductances are not constant and they not only depend on the self-axis current (magnetic saturation) but also on the other axis current (cross-magnetic saturation).

Considering (3.8) and (3.9) into the voltage equations (3.5) and (3.6), leads to

$$u_d = R_s i_d + \frac{\partial \psi_d}{\partial i_d}\frac{di_d}{dt} + \frac{\partial \psi_d}{\partial i_q}\frac{di_q}{dt} - \omega_r \psi_q \tag{3.11}$$

$$u_q = R_s i_q + \frac{\partial \psi_q}{\partial i_d}\frac{di_d}{dt} + \frac{\partial \psi_q}{\partial i_q}\frac{di_q}{dt} + \omega_r \psi_d. \tag{3.12}$$

This allows to define the partial derivatives of the flux linkage components in (3.11) and (3.12) as incremental inductances according to

$$\boldsymbol{L}^{inc} = \begin{bmatrix} \frac{\partial \psi_d}{\partial i_d} & \frac{\partial \psi_d}{\partial i_q} \\ \frac{\partial \psi_q}{\partial i_d} & \frac{\partial \psi_q}{\partial i_q} \end{bmatrix} = \begin{bmatrix} L_d^{inc}\left(i_d, i_q\right) & L_{dq}^{inc}\left(i_d, i_q\right) \\ L_{qd}^{inc}\left(i_d, i_q\right) & L_q^{inc}\left(i_d, i_q\right) \end{bmatrix}. \tag{3.13}$$

The self-incremental inductances $L_d^{inc}(i_d, i_q)$ and $L_q^{inc}(i_d, i_q)$, and the cross-incremental inductances $L_{dq}^{inc}(i_d, i_q)$ and $L_{qd}^{inc}(i_d, i_q)$, govern the transient behaviour of the SynRM. These incremental inductances can be graphically represented as the slope of the tangential line at the operating point, as illustrated in Fig. 3.4. Moreover, in the same plot, the apparent inductances are defined as the slope of the linearized characteristic of the flux linkage versus current through the origin and the operating point. Apparent and incremental inductances are not equal to each other ($\boldsymbol{L} \neq \boldsymbol{L}^{inc}$) unless the machine has a linear magnetic circuit.

Considering the definition in (3.13) and neglecting the cross-apparent inductances $L_{dq}(i_d, i_q)$

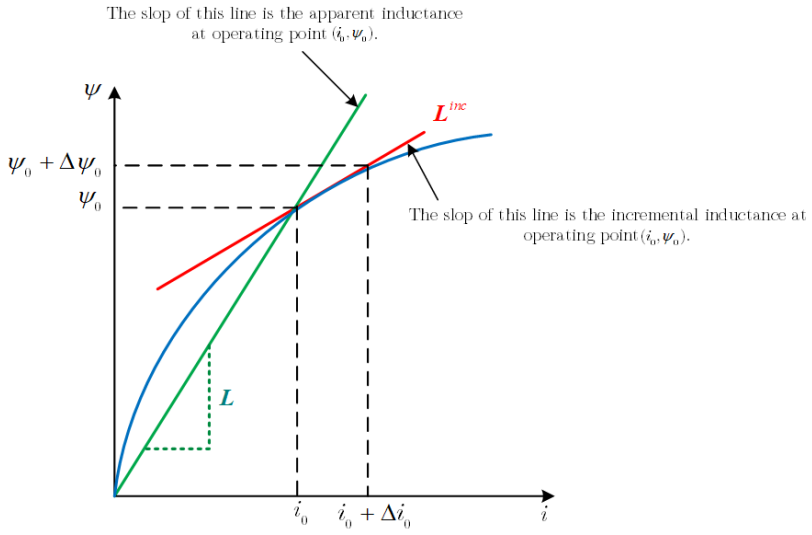

Fig. 3.4. Incremental and apparent inductances definition [149].

and $L_{qd}(i_d, i_q)$ as their effects can be incorporated into the self-apparent inductances $L_d(i_d, i_q)$ and $L_q(i_d, i_q)$, (3.11) and (3.12) can be written as [141]

$$u_d = R_s i_d + L_d^{inc}(i_d, i_q)\frac{di_d}{dt} + L_{dq}^{inc}(i_d, i_q)\frac{di_q}{dt} - \omega_r L_q(i_d, i_q)\, i_q \tag{3.14}$$

$$u_q = R_s i_q + L_q^{inc}(i_d, i_q)\frac{di_q}{dt} + L_{qd}^{inc}(i_d, i_q)\frac{di_d}{dt} + \omega_r L_d(i_d, i_q)\, i_d. \tag{3.15}$$

The torque equation, as a function of the apparent inductances, can now be written as follows:

$$T_e = \frac{3}{2} p\left(L_d(i_d, i_q) - L_q(i_d, i_q)\right) i_d i_q. \tag{3.16}$$

From this point on, the dependency of apparent and incremental inductances with the current components i_d and i_q will be omitted in (3.14), (3.15) and (3.16) for simplicity of writing.

As stated earlier, the proposed control strategies rely heavily on the accuracy of the motor model. This means that to obtain a satisfactory performance with these control strategies, the SynRM model must be well-characterized and include the apparent, self-incremental and cross-incremental inductances. These parameters have a direct influence not only on the dynamic performance of the drive system but also on the prediction accuracy of the controlled variables.

The combination of the electric model presented above with a mechanical model creates the complete mathematical model of the SynRM. The mechanical model of the drive is shown in (3.17), where J_m is the inertia of the rotating parts of the drive system, B_m is the viscous friction coefficient, Ω_m is the mechanical rotor speed, and T_L is the load torque. The electrical speed is related to the mechanical speed by the number of the pole-pairs p, as shown in (3.18).

$$T_e = J_m \frac{d\Omega_m}{dt} + B_m \Omega_m + T_L \tag{3.17}$$

$$\frac{d\theta_r}{dt} = \omega_r = p\Omega_m. \tag{3.18}$$

3.1.3 SynRM Parameter Identification

Due to the necessity of having accurate motor parameters to be used along with the developed predictive control strategies, a simple and robust process for self-commissioning of the SynRM is crucial.

Usually, motor manufactures do not provide the complete model data of the motor, only the nameplate motor parameters are available, so it is important to the end users to have the possibility to identify the parameters. In literature, the magnetic models of SynRMs and interior permanent magnet synchronous motors (IPMSMs) have been identified in several ways. For example in [78], these parameters are determined by finite-element method (FEM). Experimental tests with the locked-rotor are performed to detect the variation of inductances of an IPMSM in [150]. Another parameter identification algorithm based on the high-frequency voltage injection is adopted in [149] to obtain the inductances information of the IPMSM. Furthermore, recent self-commissioning techniques have been presented to identify the flux maps of both IPMSMs and SynRMs in [151, 152]. In [151], the commissioning procedure evaluates the dq flux linkages in a very short time by including both magnetic saturation and cross-magnetic saturation. The machine is driven by the inverter with the shaft left free and current controlled. Thus, the two flux linkage tables are obtained as the outputs of this procedure. In [152], a self-identification procedure is proposed using a convenient flux saturation approximating function. The adopted technique is performed at

standstill by injecting a proper voltage without involving the current control. As a result, a good fitting for the flux curves on both axes is obtained. A good overview of the parameter identification techniques for both PMSMs and SynRMs can be found in [153].

The parameter identification of the SynRM under study was processed experimentally in [154]. The adopted identification procedure relies on the sinusoidal current signal injection along the rotor dq-axes in order to identify the flux curves representing the magnetic model. A predictive current control (PCC) scheme is used for the purpose of imposing the sinusoidal current signal [154].

The frequency of the sinusoidal current signal injection is selected to be 30 Hz, since higher frequencies lead to noise and vibrations at the motor coupling whereas lower frequencies might be unreliable due to the small back-EMF voltage. To estimate the inductances along the two axes, the sinusoidal current signal is injected and held constant at a value of $0.8^{*}I_n$ (80 % of the motor rated current) along one axis while a DC current is injected in the orthogonal axis. In this manner, it is possible to identify the saturation characteristics of one axis while considering at the same time the cross-saturation effect. The test is repeated for different values of the DC current and carried out for both axes, and then the flux surface (flux as a function of both d- and q-axis current) is constructed by interpolating the flux curves corresponding to each level of the injected DC current.

The experimental flux maps along the dq-axes, obtained by following the procedure described above, are shown in Fig. 3.5. This figure clearly shows that the flux linkage of the SynRM is neither constant nor linear as a function of the current components, due to the saturation and cross-magnetic saturation.

After obtaining the flux surfaces along the d- and q-axis, shown in Fig. 3.5, the apparent, self- and cross-incremental inductances can be extracted using a polynomial curve fitting approach. It is good to mention that the order of the polynomial should be carefully selected as it is highly dependent on the consistency of the data. In other words, if the polynomial order is low, inaccuracies in curve fitting would lead to significant errors in the flux values, while a higher polynomial order might lead to oscillations of the curves between the points, affecting the computation of the derivative-dependent variables such as the incremental

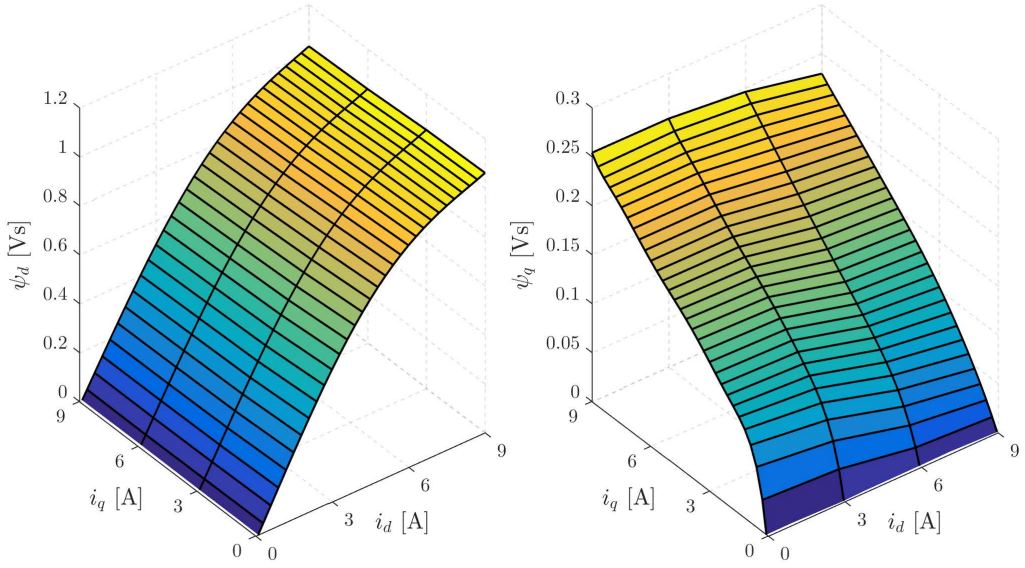

Fig. 3.5. Experimental flux maps along the dq-axes of the SynRM.

inductances.

With regard to this a polynomial order of 7 is chosen to fit the obtained flux and current curves along the d-axis at each level of the current along the q-axis with a sufficient accuracy, whereas the flux and current curves along q-axis at each value of constant d-axis current are fitted with a polynomial order of 6 since the flux curve is saturated at lower values of i_q while it has an almost linear behaviour at higher currents. The apparent inductances L_d and L_q, which are extracted by fitting the flux curves as a function of the dq current components, are shown in Fig. 3.6.

The apparent inductance profile, L_d, starts with a constant trend at the linear region of the saturation curve, and then decreases smoothly due to saturation. Different from L_d, the inductance L_q drops faster at lower current values according to the saturation effect in this region, while it reaches a steady condition at higher current values.

The self-incremental inductances, L_d^{inc} and L_q^{inc}, shown in Fig. 3.7, are computed as the derivative of the flux with respect to the currents i_d and i_q, respectively. As can be seen, the self-incremental inductance profile, L_d^{inc}, has always a decreasing trend with the increase of the current values and its value at high currents lower than that one of the apparent inductance L_d. Unlink, L_d^{inc}, the self-incremental inductance along q-axis, L_q^{inc}, drops very fast and reaches its steady-state condition at lower current values. Moreover, it can be

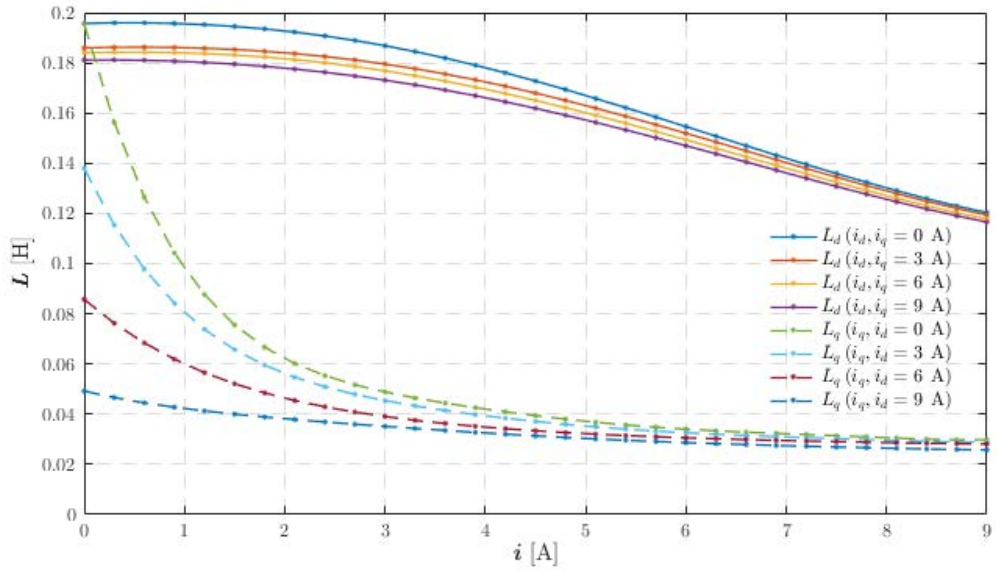

Fig. 3.6. Apparent inductances at different cross-axis currents for the SynRM used in the experimental tests.

observed from Fig. 3.7 that both L_d^{inc} and L_q^{inc} present a slight increasing trend at higher currents, the cause of this being to the use of the polyfit tool that has been selected. However, this issue has no influence on the performance of the proposed control strategies as it was extensively tested and confirmed in [154].

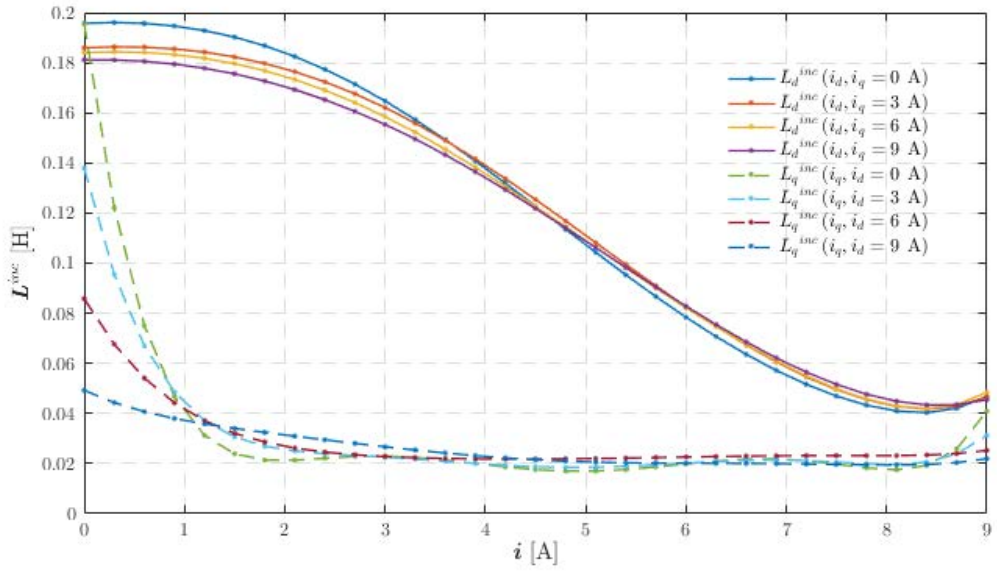

Fig. 3.7. Self-incremental inductances at different cross-axis currents for the SynRM.

The cross-incremental inductances are determined by finding the derivative of the flux surfaces along the d- and q-axis, with respect to the currents i_q and i_d, respectively. The

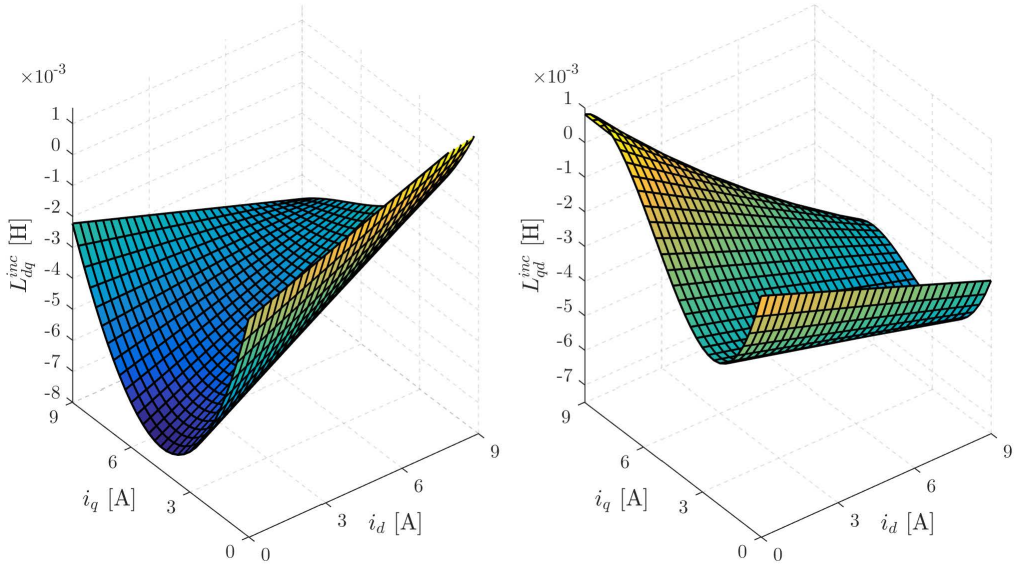

Fig. 3.8. Cross-incremental inductances at different cross-axis currents for the SynRM.

obtained results are shown in Fig. 3.8. L_{dq}^{inc} and L_{qd}^{inc} shown in Fig. 3.8 present negative values, being this due to the fact that the slope of the flux curves tends to decrease at higher levels of the cross-axis currents [154].

All types of the inductances plotted above are stored in the form of lookup tables (LUTs) which are then used during the validation process of the proposed predictive control strategies.

3.2 Predictive Active Flux and Torque Control Strategy

As stated earlier, the PAFTC strategy is based on the active flux concept. Thus, a brief description of this concept is provided here.

By definition, the active flux ψ_a of an AC machine is the flux that multiplied by i_q gives the developed torque. Fig. 3.9 illustrates the steady-state vector vector diagram of the SynRM with the active flux vector represented in red.

From this figure, it is observed that the relationship between the active flux and the stator

flux in a SynRM is given by

$$\underline{\psi}_s = \psi_d + j\psi_q = L_d i_d + jL_q i_q \tag{3.19}$$

$$\underline{\psi}_a = \underline{\psi}_s - L_q \underline{i}_s = \underline{\psi}_s - L_q \left(i_d + j i_q\right) \tag{3.20}$$

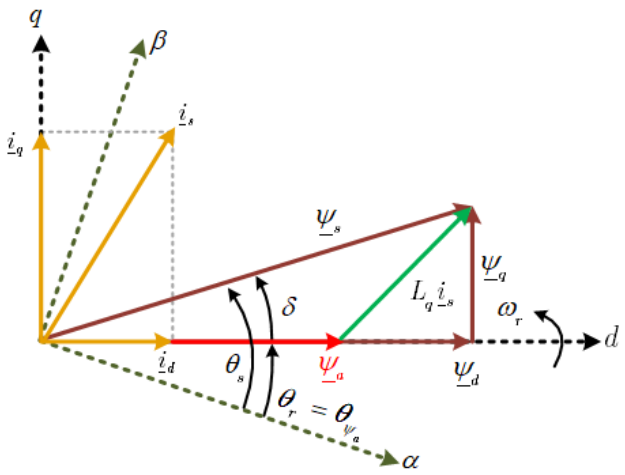

Fig. 3.9. Vector diagram of a SynRM operating in steady-state with the active flux representation [155].

By replacing (3.19) into (3.20) yields

$$\psi_a = \left(L_d - L_q\right) i_d \tag{3.21}$$

The electromagnetic torque developed by the SynRM is then given by

$$T_e = \frac{3}{2} p \psi_a i_q. \tag{3.22}$$

The previous equations show that i_d is the active flux producing current component while i_q is the torque producing current component, allowing an independent control of the active flux and electromagnetic torque of the SynRM.

The torque and the active flux are chosen as the controlled variables in the PAFTC strategy in order to have an easy control of the losses in the machine and at the same time a fast dynamic response. Thus, this strategy is similar to PTC as both of these strategies

have the same implementation process. However, the difference is that the active flux, in the case of PAFTC, is being selected instead of stator flux as the variable under control.

The general control diagram of the PAFTC strategy proposed for SynRM drives is shown in Fig. 3.10. In this diagram, one can see that the two stator currents i_a and i_b are measured at instant k and then transformed to a rotor reference frame. In addition, the DC-link voltage U_{dc} and rotor position θ_m are also measured, which are needed to execute this control strategy.

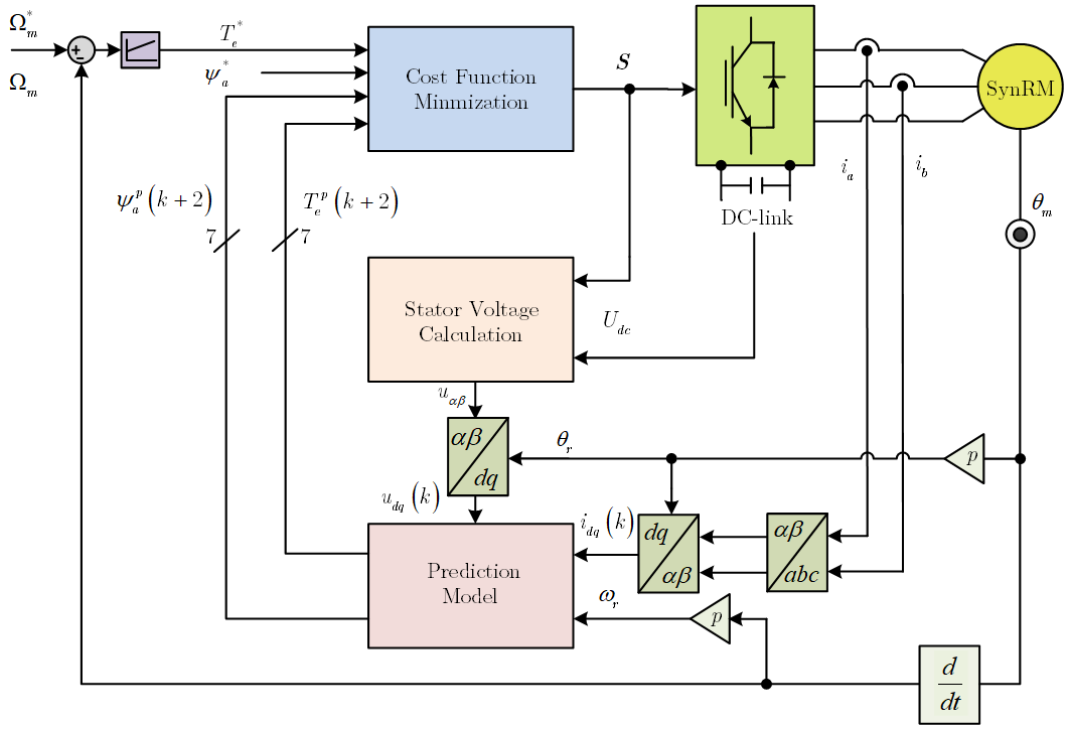

Fig. 3.10. Block diagram of the proposed PAFTC strategy for SynRMs [156].

The prediction model is based on the voltage equations (3.14) and (3.15). These equations are used to estimate the currents along the dq-axes for instant $k+1$. To achieve this objective, the Forward Euler discretization equation is herein adopted, being this discretization done using

$$\frac{dx}{dt} \approx \frac{x\left(k+1\right) - x\left(k\right)}{T_s}, \tag{3.23}$$

where x is the state variable that needs to be discretized and T_s is the sampling time.

The voltage equations (3.14) and (3.15) can now be discretized using (3.23), thus obtaining

the estimated values of the two current components for instant $k+1$:

$$\begin{aligned}\hat{i_d}\,(k+1) = i_d\,(k) + \frac{T_s}{\gamma L_d^{inc}}\Big(u_d\,(k) - R_s i_d\,(k) + \omega_r L_q i_q\,(k)\Big) - \\ - \frac{T_s L_{dq}^{inc}}{\gamma L_d^{inc} L_q^{inc}}\Big(u_q\,(k) - R_s i_q\,(k) - \omega_r L_d i_d\,(k)\Big)\end{aligned} \tag{3.24}$$

$$\begin{aligned}\hat{i_q}\,(k+1) = i_q\,(k) + \frac{T_s}{L_q^{inc}}\Big(u_q\,(k) - R_s i_q\,(k) - \omega_r L_d i_d\,(k)\Big) + \\ + \frac{L_{qd}^{inc}}{L_q^{inc}}\Big(i_d\,(k) - \hat{i}_d\,(k+1)\Big)\end{aligned} \tag{3.25}$$

where $i_d\,(k)$ and $i_q\,(k)$ are the measured stator currents at instant k, $u_d\,(k)$ and $u_q\,(k)$ are the voltage components at instant k which are calculated with the knowledge of the switching state at instant k and the measured DC-link voltage U_{dc}, γ is defined in (3.26) and the superscript "ˆ" indicates estimated quantities.

$$\gamma = 1 - \frac{L_{dq}^{inc} L_{qd}^{inc}}{L_d^{inc} L_q^{inc}}. \tag{3.26}$$

In real-time applications, the time required to compute the control algorithm takes a significant portion of the sampling time, resulting in one sampling delay. The effect of this delay has an impact on the controller performance, therefore a delay compensation must be implemented. Here, and in order to compensate the calculation delay, the estimated currents are used as an initial condition to the predictions for instant $k+2$. Thus, the two current components i_d and i_q are predicted for instant $k+2$ using each one of the seven different voltage vectors the 2L-VSI can apply to the motor at instant $k+1$:

$$\begin{aligned}i_d^p\,(k+2) = \hat{i_d}\,(k+1) + \frac{T_s}{\gamma L_d^{inc}}\Big(u_d\,(k+1) - R_s \hat{i_d}\,(k+1) + \omega_r L_q \hat{i_q}\,(k+1)\Big) - \\ - \frac{T_s L_{dq}^{inc}}{\gamma L_d^{inc} L_q^{inc}}\Big(u_q\,(k+1) - R_s \hat{i_q}\,(k+1) - \omega_r L_d \hat{i_d}\,(k+1)\Big)\end{aligned} \tag{3.27}$$

$$\begin{aligned}i_q^p\,(k+2) = \hat{i_q}\,(k+1) + \frac{T_s}{L_q^{inc}}\Big(u_q\,(k+1) - R_s \hat{i_q}\,(k+1) - \omega_r L_d \hat{i_d}\,(k+1)\Big) + \\ + \frac{L_{qd}^{inc}}{L_q^{inc}}\Big(\hat{i}_d\,(k+1) - i_d^p\,(k+2)\Big)\end{aligned} \tag{3.28}$$

With the predicted stator currents, the active flux and electromagnetic torque can now be predicted for instant $k+2$ by

$$\psi_a^p\left(k+2\right) = \left(L_d - L_q\right) i_d^p\left(k+2\right) \tag{3.29}$$

$$T_e^p\left(k+2\right) = \frac{3}{2} p \psi_a^p\left(k+2\right) i_q^p\left(k+2\right). \tag{3.30}$$

The final step of the PAFTC strategy is the evaluation of the cost function for each one of the seven different voltage vectors, and the choice of the optimal voltage vector to be applied to the motor at instant $k+1$, which is the one that minimizes the cost function.

The cost function g adopted here is given by (3.31) and includes three terms: the first two terms represent the normalized error of the torque and the active flux, respectively, while the third term P is included to avoid an overcurrent in the drive during startup or during strong acceleration/deceleration. Basically, this last term is the current limit protection mechanism that exists in all drives.

$$g = \left(\frac{T_e^* - T_e^p\left(k+2\right)}{T_n}\right)^2 + \lambda_{\psi_a}\left(\frac{\psi_a^* - \psi_a^p\left(k+2\right)}{\psi_{an}}\right)^2 + P\left(\underline{i}_s^p\left(k+2\right)\right) \tag{3.31}$$

In (3.31), T_n and ψ_{an} represent the rated values of the active flux and electromagnetic torque, The reference torque T_e^* is either the reference torque set by the user (drive operating in torque control mode) or the reference torque generated by the PI speed controller, ψ_a^* is the active flux reference which is calculated and updated in the real-time based on the equation (C.1) presented in Appendix C, λ_{ψ_a} is the weighting factor that increases or decreases the relative importance of the normalized torque error in relation to the normalized active flux error, and $P\left(\underline{i}_s^p\left(k+2\right)\right)$ is defined as follows

$$P\left(\underline{i}_s^p\left(k+2\right)\right) = \begin{cases} 0 & \Leftarrow \left|\underline{i}_s^p\left(k+2\right)\right| \leq i_{max} \\ \infty & \Leftarrow \left|\underline{i}_s^p\left(k+2\right)\right| > i_{max} \end{cases} \tag{3.32}$$

The weighting factor λ_{ψ_a} in (3.31) is the only parameter to be adjusted in this control strategy. In this study, the weighting factor is adjusted taking into account its effect on the

stator current waveforms and their ripple content. The selected value of λ_{ψ_a}, which leads to a good performance in all operating conditions, has been determined following a trial and error procedure and set to 0.2.

The implementation of the PAFTC strategy can be summarized by the following sequences (see Fig. 3.11):

1) Measure the $\theta_m(k)$, $U_{dc}(k)$ and currents $i_a(k)$, $i_b(k)$.

2) Estimate currents $\hat{i}_{dq}(k+1)$ for instant $k+1$.

3) Predict currents $i_{dq}^p(k+2)$, electromagnetic torque $T_e^p(k+2)$, and active flux $\psi_a^p(k+2)$ for instant $k+2$ for all possible switching states.

4) Evaluate the cost function g for all possible switching states.

5) Select the switching state that minimizes the cost function.

6) Apply the optimal voltage vector $u_{opt}(k+1)$.

These six steps are repeated during each control cycle, taking into consideration the new measurements and references.

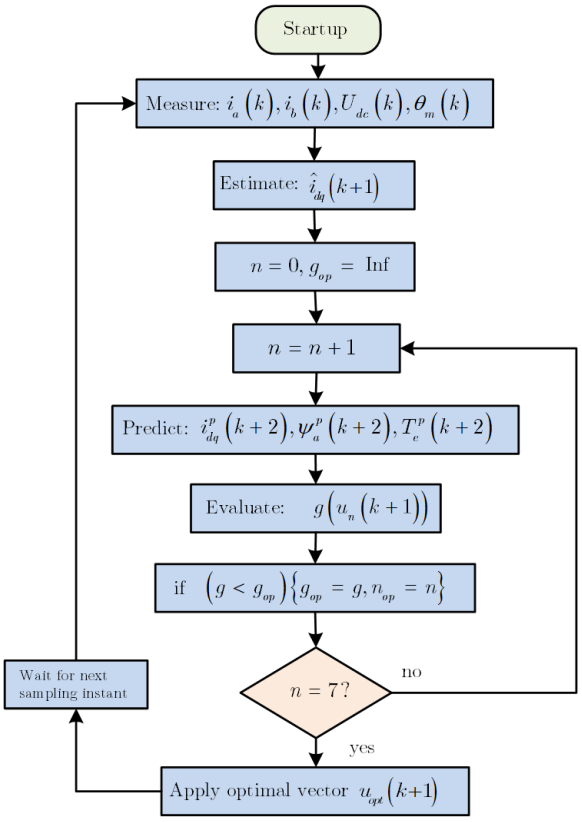

Fig. 3.11. Flowchart diagram of the PAFTC strategy.

3.3 S-PAFTC Strategy

Based on the conventional principle of FCS-MPC, the number of prediction calculations is directly related to the number of the possible voltage vectors the inverter can apply to the motor. In the case of a 2L-VSI, there are six active voltage vectors and two zero vectors available. Thus, the calculations for the predictions have to be performed seven times in each control cycle. This number increases in an exponential manner if more complex power converters like multilevel converters or matrix converters feed the motor.

In order to reduce the computation time that conventional FCS-MPC strategy involves, while maintaining the same control performance, it was proposed in [132] a simplified version of FCS-MPC applied to two- and three-level power converters. The basic idea of this method relies on avoiding the seven predictions of the currents for instant $k+2$ used in the conventional FCS-MPC strategy and calculate instead the reference voltage vector $u^*(k+1)$ that would make the two current components i_d and i_q reach their reference values at instant $k+2$. The voltage vector that will be applied to the motor at instant $k+1$ is the one that is closer to the reference vector $u^*(k+1)$.

Using this procedure, only one set of the calculations is performed in the prediction stage instead of the seven needed in the traditional approach. Moreover, the final process of choosing the actuation voltage vector is quite simple, decreasing the total control cycle time. Lastly, no weighting factors are needed, which significantly simplifies the implementation of the FCS-MPC strategy.

The basic concept of this simplified FCS-MPC, originally presented in [132] only for power converters and without delay compensation, is here explored and extended for the case of SynRM drives, including one step delay compensation feature. The overall control diagram of the proposed S-PAFTC strategy is shown in Fig. 3.12.

In the control diagram, one can see that the two stator currents i_a and i_b are measured at instant k and then transformed to the rotor reference frame.

The reference values of the active flux and the machine torque are also needed in the S-PAFTC strategy to calculate the reference currents i_d^* and i_q^*. The reference values of the

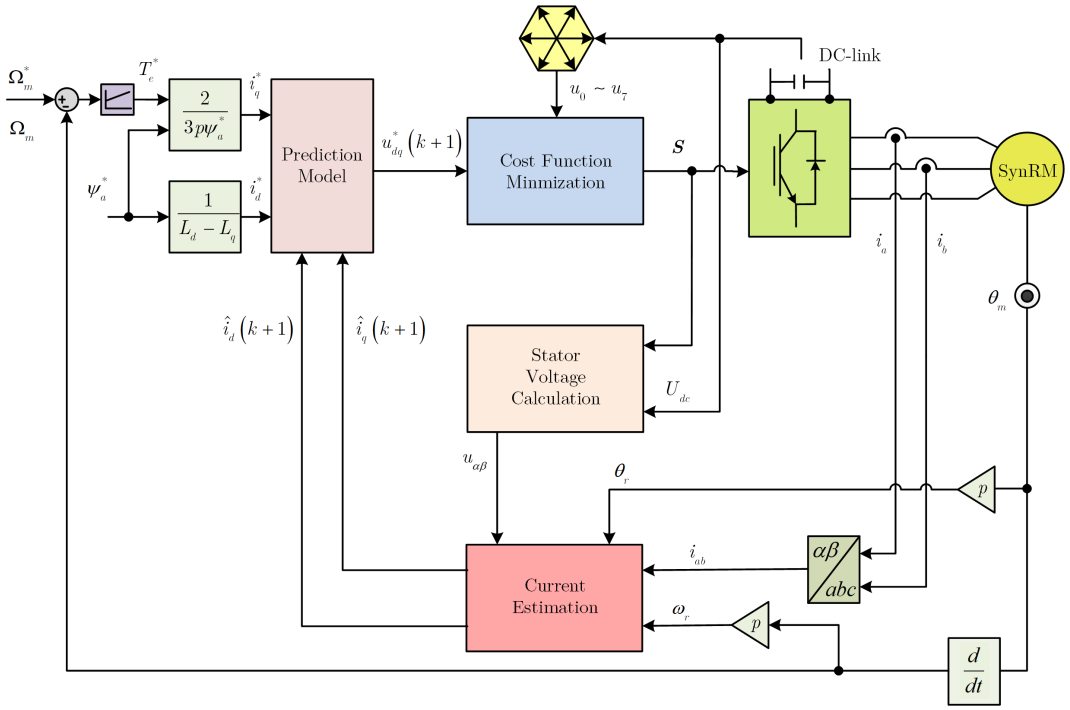

Fig. 3.12. Proposed S-PAFTC for SynRMs [156].

torque and the active flux are obtained in the same way as explained in the previous section.

The S-PAFTC strategy for SynRMs starts by assuming that the variation of T_e^* is very slow in comparison with the control cycle time T_s, therefore one can assume that

$$\psi_a^*(k+2) = \psi_a^*(k) \tag{3.33}$$

$$T_e^*(k+2) \approx T_e^*(k) \tag{3.34}$$

By translating the reference values of the active flux and electromagnetic torque to the corresponding reference currents, using (3.29) and (3.30), one obtains

$$i_d^*(k+2) = i_d^*(k) \tag{3.35}$$

$$i_q^*(k+2) \approx i_q^*(k)\,. \tag{3.36}$$

This simplification step is very important because it will allow later on to avoid the use of any flux or torque estimated values in the cost function, and can be applied because there are linear relationships between the active flux and electromagnetic torque and the two current

components, i_d and i_q, respectively.

By knowing the switching state of the inverter and the measured currents at instant k, the currents for instant $k+1$ are estimated using the relationships already presented in (3.24)-(3.25). Now, the key idea is to calculate the reference voltage vector that, if applied at instant $k+1$, would make the currents reach their reference values given by (3.35)-(3.36) at instant $k+2$. The calculation of this reference vector can be performed using the voltage and flux equations of the motor (in discrete form using the forward Euler method) or, in a more straightforward manner, by the manipulation and adaptation of (3.27)-(3.28) (replacing the predicted currents by their corresponding reference values) and by solving these equations in relation to the voltage components that now have the meaning of reference voltages at instant $k+1$:

$$\begin{aligned} u_d^*(k+1) = R_s\hat{i}_d(k+1) + \frac{L_d^{inc}}{T_s}\left(i_d^*(k+2) - \hat{i}_d(k+1)\right) + \\ + \frac{L_{dq}^{inc}}{T_s}\left(i_q^*(k+2) - \hat{i}_q(k+1)\right) - \omega_r L_q \hat{i}_q(k+1) \end{aligned} \tag{3.37}$$

$$\begin{aligned} u_q^*(k+1) = R_s\hat{i}_q(k+1) + \frac{L_q^{inc}}{T_s}\left(i_q^*(k+2) - \hat{i}_q(k+1)\right) + \\ + \frac{L_{qd}^{inc}}{T_s}\left(i_d^*(k+2) - \hat{i}_d(k+1)\right) + \omega_r L_d \hat{i}_d(k+1). \end{aligned} \tag{3.38}$$

In general, the reference voltage vector, whose components are given by (3.37)-(3.38), will not coincide with any of the active or zero vectors that the inverter can synthesize, hence the final stage of the S-PAFTC strategy will be the evaluation of a very simple cost function which represents the square of the Euclidean distance between the reference voltage vector and each one of the different voltage vectors the inverter can apply to the motor:

$$g = \left|u_d^*(k+1) - u_{dn}\right|^2 + \left|u_q^*(k+1) - u_{qn}\right|^2, \quad n = 0, 1, ..6 \tag{3.39}$$

The voltage vector to be applied to the motor at instant $k+1$ will be the one that minimizes this cost function.

The S-PAFTC strategy requires less computation time for its execution as instead of

seven predictions for the currents, active flux, and electromagnetic torque, a reference voltage vector is calculated only once and a much simpler cost function is evaluated at the end. It is important to note that there is no need to include in the cost function an extra term to avoid overcurrents, similar to the one used in (3.31) for the PAFTC strategy, because here the reference currents given by (3.35)-(3.36) can be automatically limited so that no overcurrent will be produced, independently of the working conditions of the drive system.

The implementation of the S-PAFTC strategy can be summarized by the following sequences (see Fig. 3.13):

1) Measure the $\theta_m(k)$, $U_{dc}(k)$ and currents $i_a(k)$, $i_b(k)$.

2) Calculate the reference currents $i^*_{dq}(k)$ at instant k.

3) Estimate the currents $\hat{i}_{dq}(k+1)$ for instant $k+1$.

4) Predict the reference voltages $u^*_{dq}(k+1)$ for instant $k+1$.

5) Evaluate the cost function g for all possible switching states.

6) Select the switching state that minimizes the cost function.

7) Apply the optimal voltage vector $u_{opt}(k+1)$.

These seven steps are executed during each control period, taking into consideration the new measurements and references.

3.4 Validation of the Control Strategies

To evaluate the performance of the two proposed control strategies, a simulation study is performed first using a simulation model of the drive system under analysis, afterwards the experimental tests are carried out in order to provide a comparative analysis of simulation and experimental results.

3.4.1 Simulation Model

The two predictive control strategies proposed in the previous sections are firstly tested in *Matlab/Simulink* environment in order to evaluate the advantages and disadvantages of each

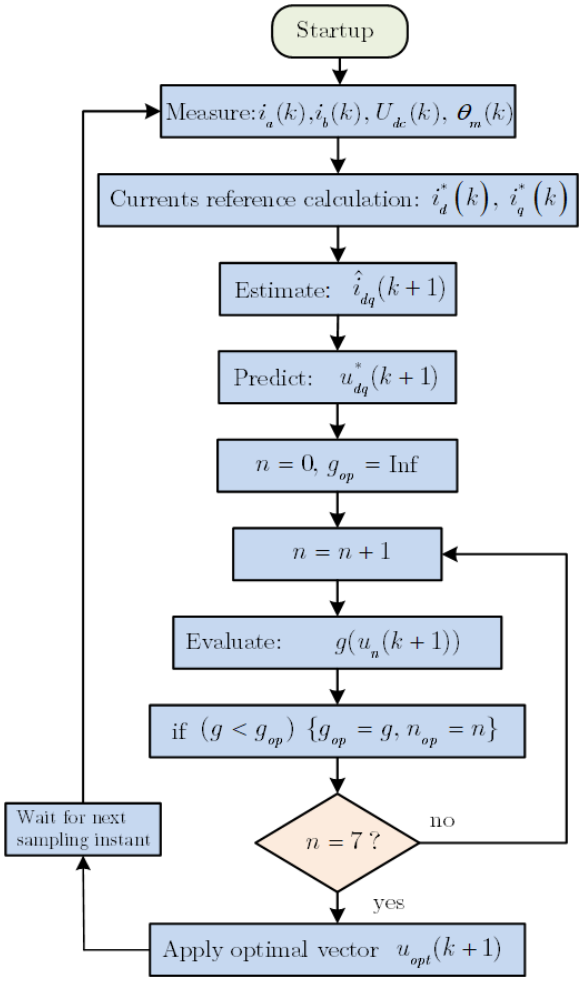

Fig. 3.13. Flowchart diagram of the S-PAFTC strategy.

one before moving to the experimental implementation. It is good to note that the value of the weighting factor and the proportional and integral gains of the PI speed controller used in the simulation study are the same as the ones used in experimental tests, for all control strategies presented in this thesis.

The simulation model of the SynRM was developed in [157], in which the effects of the magnetic saturation and cross-magnetic saturation are included. It is worth mentioning that the stator flux is selected as state variable in the simulation model of the machine, and hence the self-incremental and cross-incremental inductances are inherently accounted for.

In Appendix A the simulation models, developed in *Matlab/Simulink* environment, for both predictive control strategies are presented. The parameters of the SynRM and the two proposed control strategies are given in Appendix C in Table C.1 and Table C.2. Furthermore, the reference active flux calculation is also presented in this appendix.

3.4.2 Experimental Setup

In addition to the simulation study, the effectiveness of the two proposed control strategies were also validated by experimental tests, performed in the laboratory with the aid of a dSPACE real-time control platform.

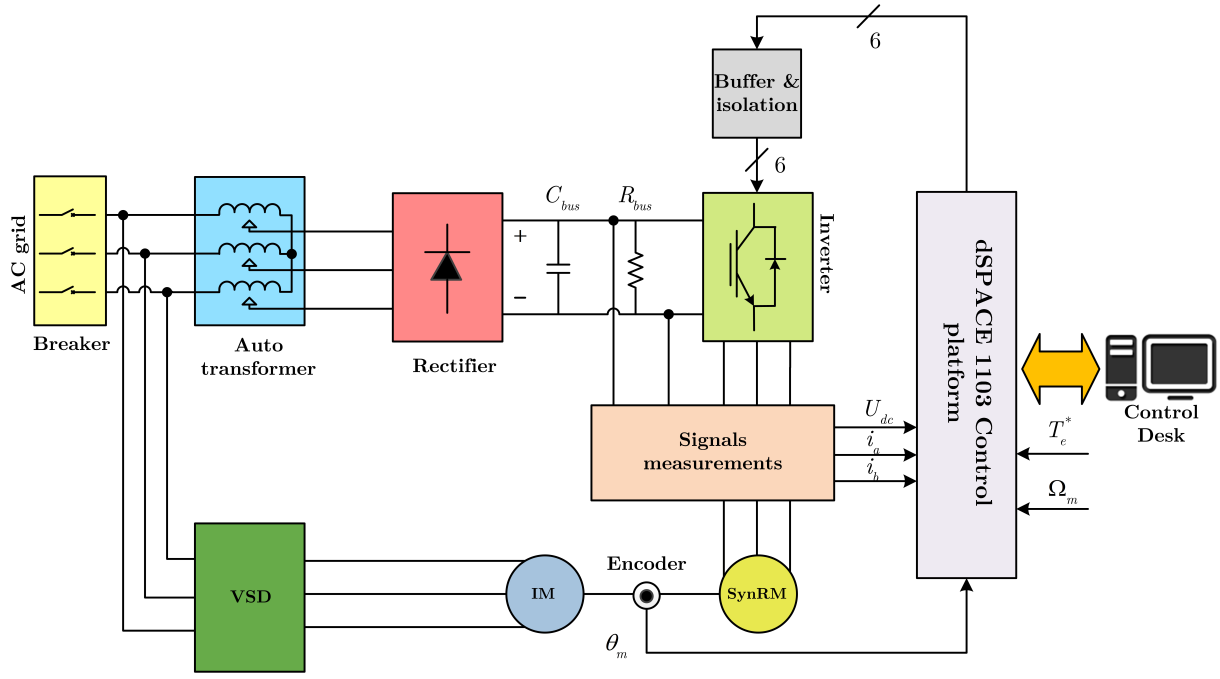

Fig. 3.14. Configuration of the experimental setup.

Fig. 3.14. shows the scheme of the experimental setup for carrying out the laboratory tests. The main components of the electric drive shown in this figure are the SynRM to be controlled, which is coupled to an auxiliary induction motor (IM) fed by a variable speed drive (VSD). The IM acts as a controlled mechanical load to the SynRM. The SynRM is of high efficiency (IE4), 3 kW, 4-poles, manufactured by KSB, and its parameters are presented in Appendix C. In this drive system, there are also a three-phase rectifier, which is connected to the AC supply of 400 V (line voltage) through an autotransformer, a capacitor bank in the DC-link with a capacitance of 4700 μF, a braking resistor, buffer and isolation circuits, voltage and currents measurements circuits, and the dSPACE control platform.

The rectifier consists of a three-phase diode bridge. In parallel with the rectifier, a capacitor bank C_{bus} is connected to filter the rectified voltage. Since the diode bridge cannot

send the energy back to the three-phase grid, the DC-link voltage will rise if the SynRM is operated in generator mode (deceleration and sudden braking case). In order to avoid damages to the drive system, a braking resistor R_{bus} is connected to dissipate some energy so that the DC-link voltage level does not become critical.

The inverter is a 2L-VSI which consists of six IGBTs. The control signals of the IGBTs are transmitted to the inverter through a buffer and isolation circuit whose function is to ensure an isolation between the dSPACE control platform, which operates with low voltage, and the high voltage of the inverter, which feeds the motor.

In order to measure the rotor angular position of the SynRM, the dSPACE platform also receives signals from an incremental encoder, with 1024 ppr mounted on the shaft of the two machines. As this encoder is of incremental type, there is the need of knowing or set the initial rotor position of the SynRM. To achieve this, a rotor alignment process is performed by injecting a DC current of 6 A along the d-axis, for a short period of 7 s, setting the initial rotor position to zero.

The control strategies designed in previous sections are introduced in a Real-Time Interface (RTI) model, in Simulink. The RTI model consists of two main blocks: measurement and control blocks. The measurement block contains all the interface Simulink blocks for capturing the measured signals and IBGT gate signals, as well as the protection blocks. The control block contains the actual discrete model of each developed control strategy.

The *ControlDesk* software is used for the real-time management, and graphical visualization of the process data. The control panel designed for all control strategies is illustrated in Appendix B (see Fig. B.7). Appendix B shows the main equipments used in the experimental tests. The sampling time of the two proposed control strategies is set to 40 μs, while the sampling time of the speed controller, T_{speed}, is set to $25 * T_s$ in order to reduce the quantization error of the speed signal derived from the incremental encoder position.

3.4.3 Results Obtained

The effectiveness of the proposed predictive strategies for the SynRM drive, in terms of dynamic response, and total harmonics distortion (THD) of the stator currents and torque ripple are now evaluated. The SynRM drive is tested against the following operation conditions:

a) Steady-state operation;
b) Speed reversal test;
c) Torque step response;
d) Speed step response.

3.4.3.1 Steady-State Operation

The steady-state behaviour of both control strategies, PAFTC and S-PAFTC, is now evaluated. Several tests conducted at different operating points are observed and discussed. The operating points are chosen and captured when the motor is operating at a speed of 700 rpm with three levels of load torque: 5 N.m, 10 N.m and 19 N.m. The simulation and experimental are presented in Fig. 3.15 – Fig. 3.17.

Fig. 3.15 – Fig. 3.17 plot the estimated and reference torque, $\hat{T}_e$ and T_e^*, currents along the d- and q-axis, and the measured stator phase currents i_{abc}. As can be observed in these figures, the two control strategies exhibit a good and similar performance. In all operating conditions, the control strategies are able to track the desired reference torque with an acceptable torque ripple. To provide a general overview of the torque ripple variation under each one of the operating points, the torque ripple is calculated and represented in Fig. 3.18 as a percentage of peak error referred to the average torque. It is possible to observe that the torque ripple decreases with the increase of the load torque, being less than 10% at rated load torque for the two control strategies.

The currents i_d and i_q in the three operating conditions have an expected behaviour where both of them vary according to the load torque level and the value of the active flux

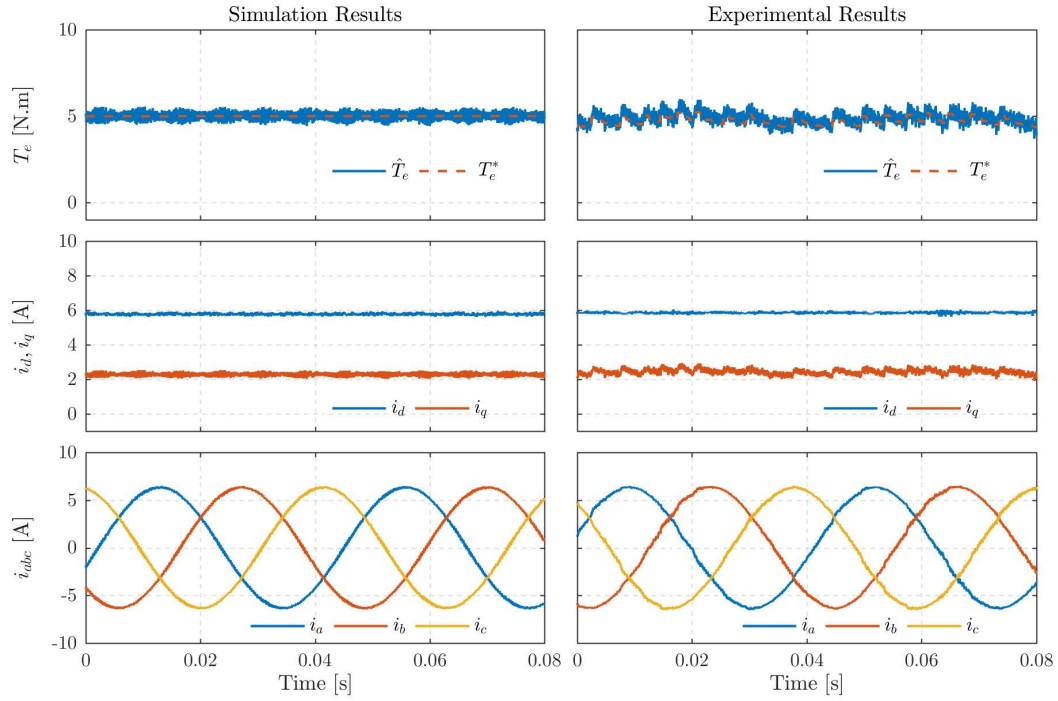

(a)

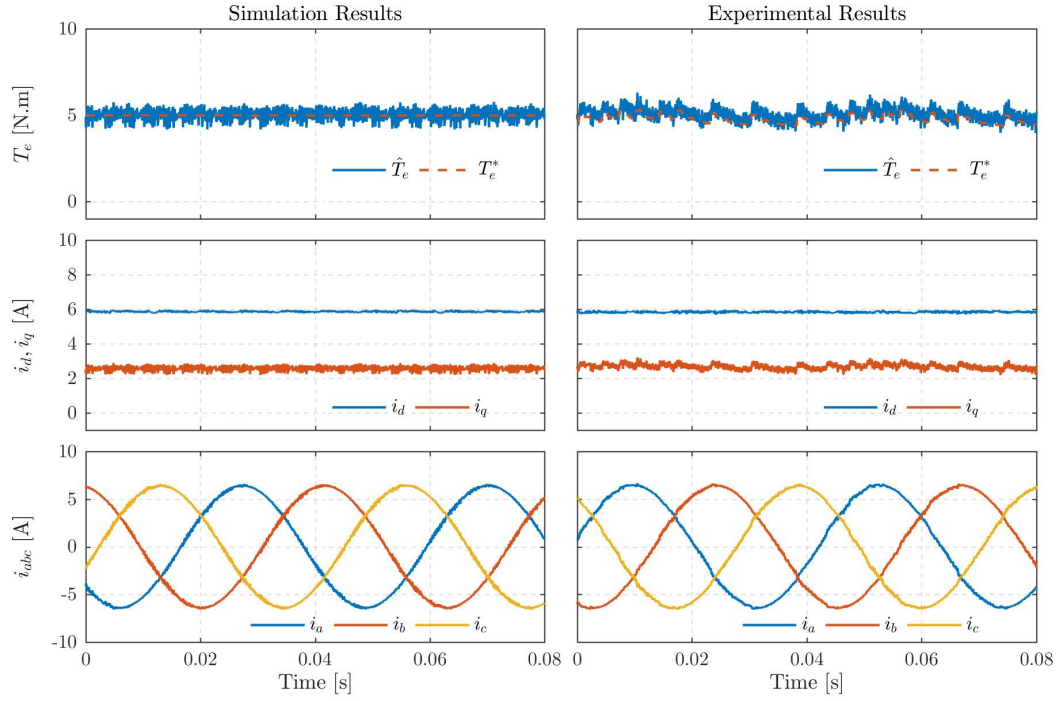

(b)

Fig. 3.15. Results for the steady-state operation of the SynRM at a speed of 700 rpm with 5 N.m: (a) PAFTC; (b) S-PAFTC.

reference which is updated in real-time. Moreover, it is visible that these currents have a similar ripple content for the two control strategies. In addition, the current waveforms of i_{abc}, for both control strategies, are observed to be sinusoidal. Additionally, to evaluate the

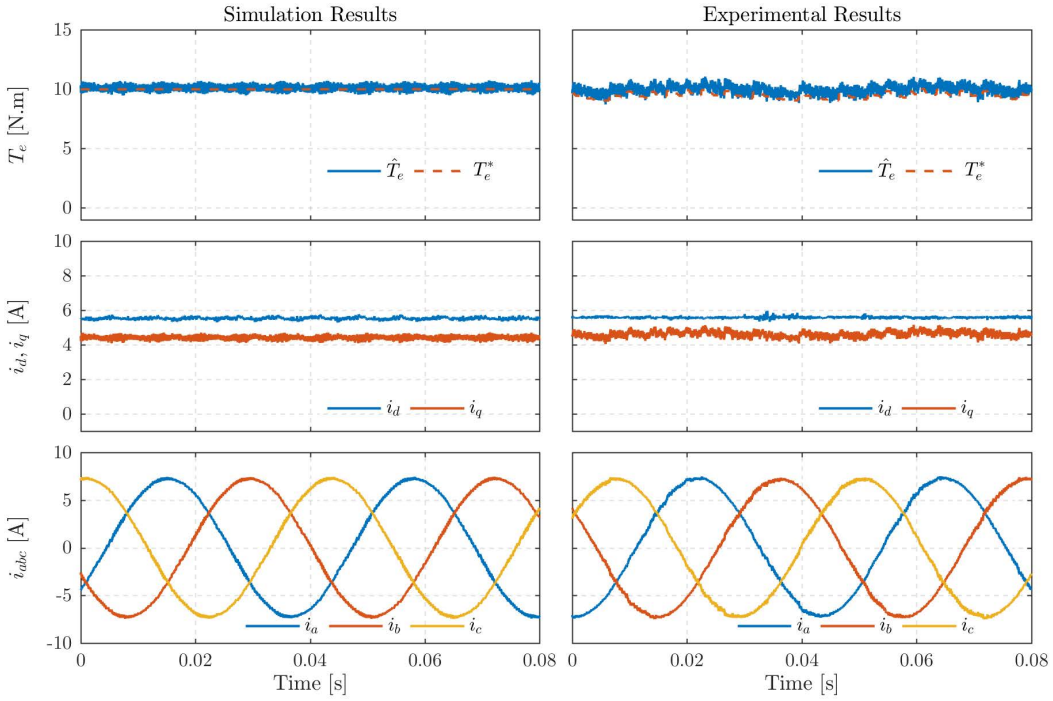

(a)

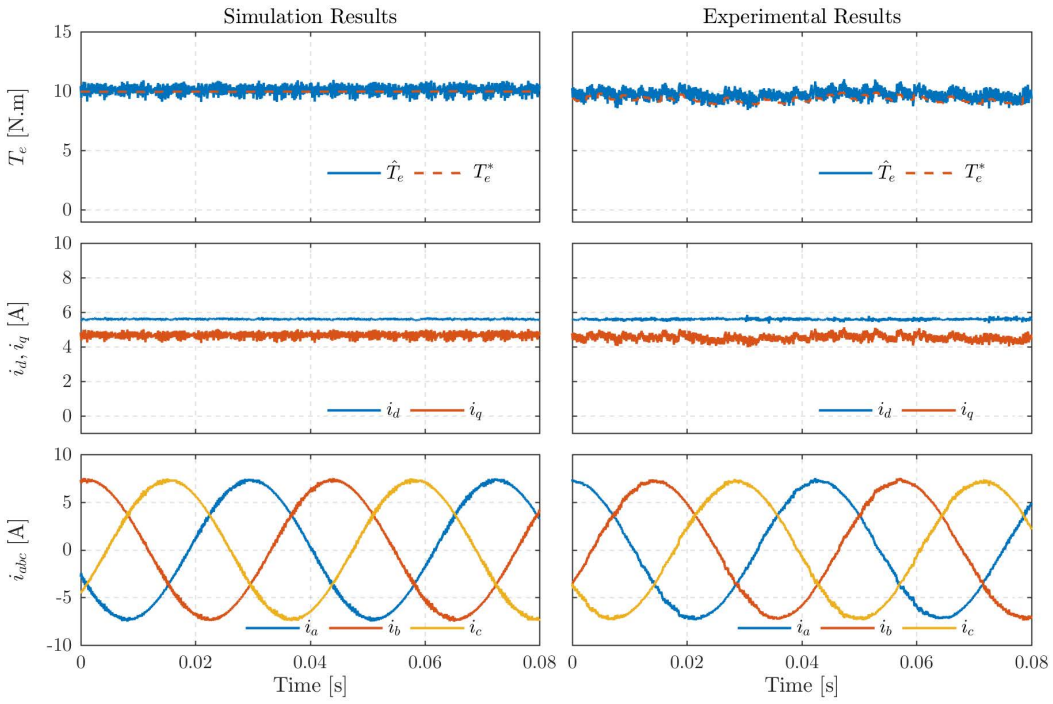

(b)

Fig. 3.16. Results for the steady-state operation of the SynRM at a speed of 700 rpm with 10 N.m: (a) PAFTC; (b) S-PAFTC.

distortion of the stator currents, the THD of phase current i_a, obtained in the experiments, was calculated.

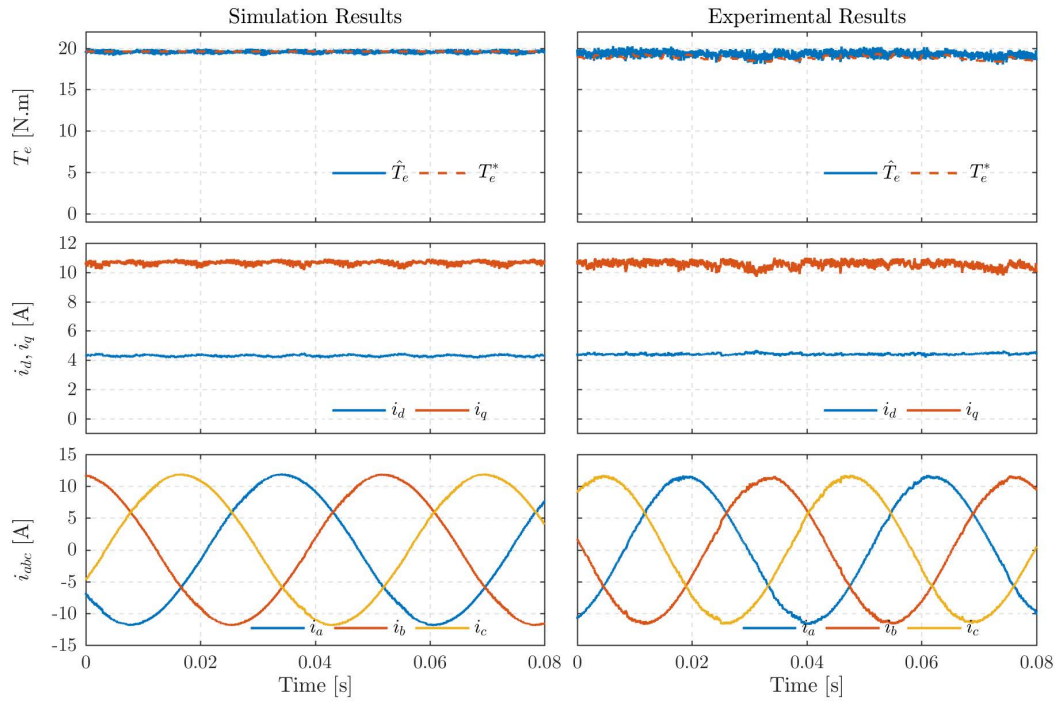

(a)

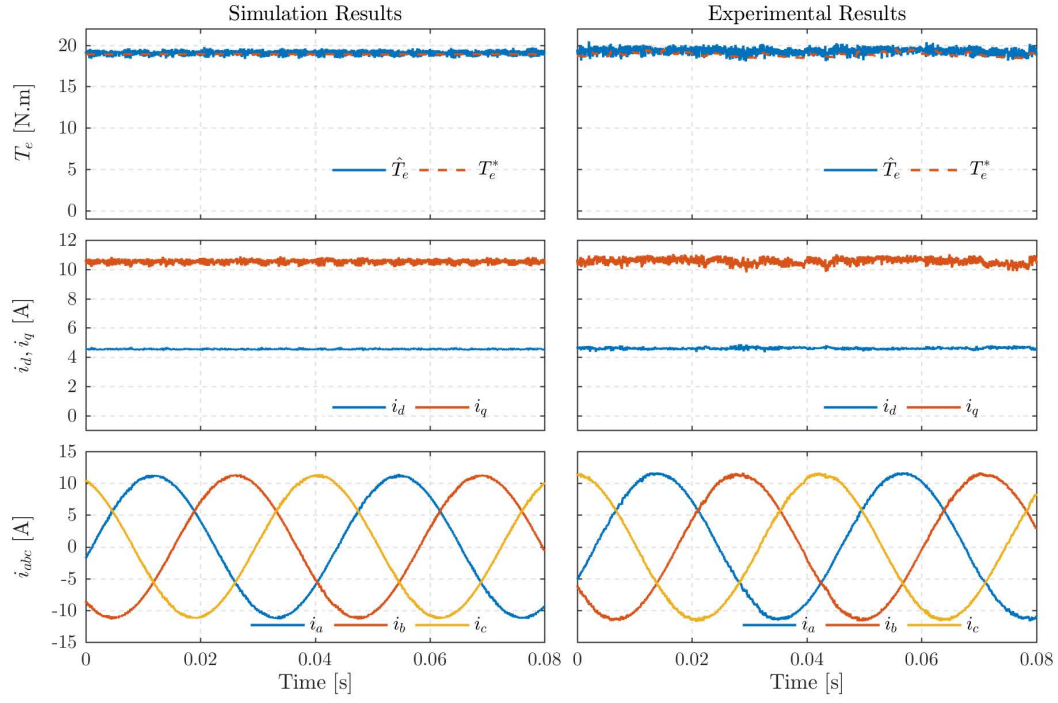

(b)

Fig. 3.17. Results for the steady-state operation of the SynRM at a speed of 700 rpm with 19 N.m: (a) PAFTC; (b) S-PAFTC.

By definition, the THD of a current signal is a measurement of the harmonic distortion present and is expressed as the ratio of the sum of the power of all harmonic current

components to the power of the fundamental frequency current according to

$$THD = \frac{\sqrt{I_2^2 + I_3^2 + I_4^2 ... + I_n^2}}{I_1} \times 100\% \tag{3.40}$$

where I_n are the individual harmonic current distortion values in amps, I_1 is the fundamental current distortion value in amps, and I_2 is the second harmonic current distortion value in amps.

The THD of phase current i_a, when the SynRM operates at 700 rpm, with different loading conditions, is illustrated in Fig. 3.19. It is worth noting that similar THD curves are obtained for phase currents i_b and i_c.

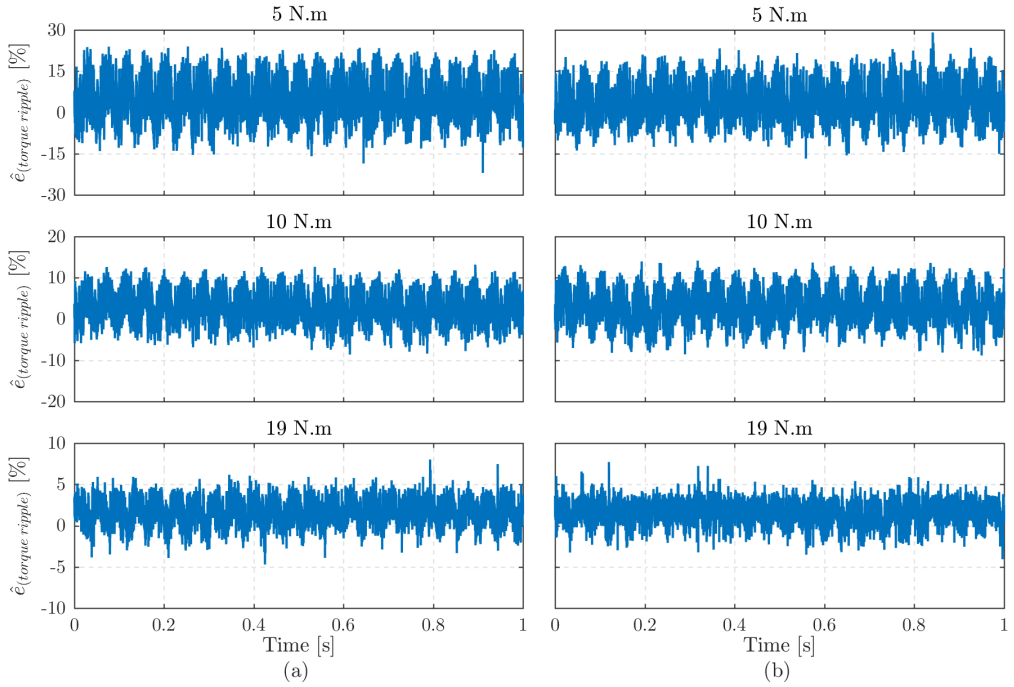

Fig. 3.18. Experimental results of the torque ripple percentage for the operating points shown in Fig. 3.15 – Fig. 3.17: (a) PAFTC; (b) S-PAFTC.

As can be seen in Fig. 3.19, the THD of current i_a for the two control strategies has similar small values. However, the PAFTC presents a slightly higher THD value compared to the one of the S-PAFTC. Moreover, the THD of current, for the two control strategies, has a tendency to decrease with the increase of the load torque.

In order to show the distribution and magnitude of the high frequency harmonics present in the motor supply currents over the frequency range, the obtained spectra of the current

i_a, using the two control strategies and with the motor running at a speed of 700 rpm with different loading conditions, is plotted in Fig. 3.20.

One can observe that the high-frequency harmonics distribution and their magnitudes, for the two control strategies at each operating point, are almost analogous in a wide frequency range. This justifies the similarity of the THD variation presented in Fig. 3.19.

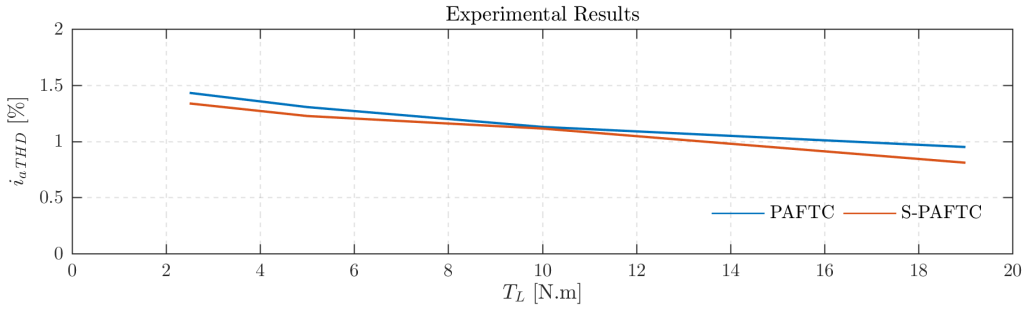

Fig. 3.19. Experimental results for the THD of the phase current i_a when the SynRM is running at 700 rpm with different load torque values.

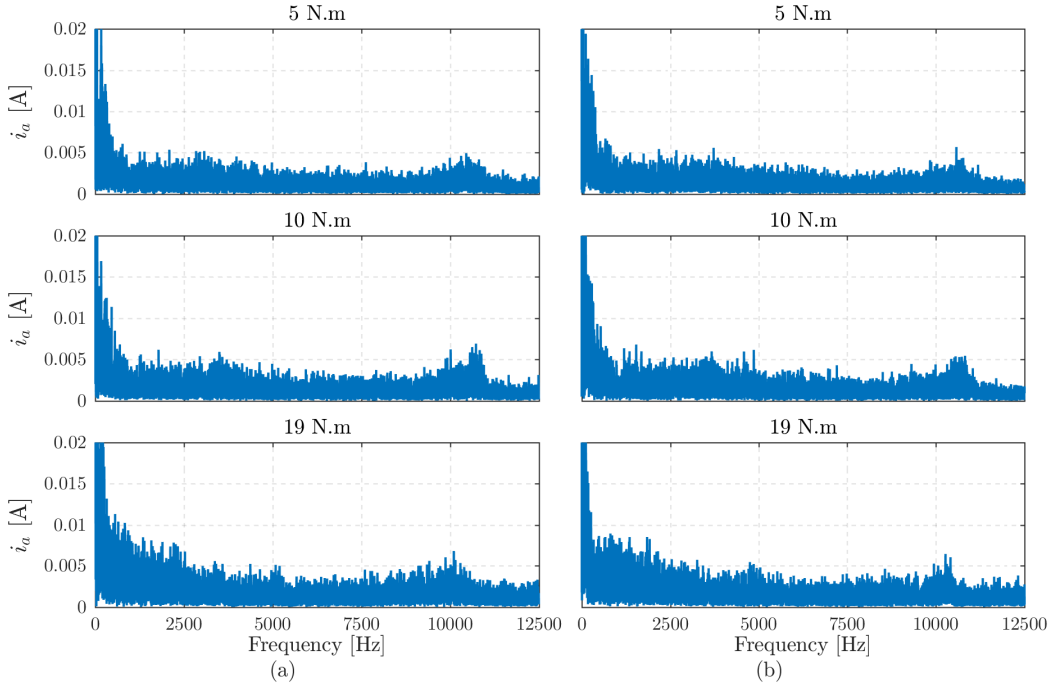

Fig. 3.20. Experimental results for the frequency spectrum of stator current i_a (motor running at 700 rpm with different load torque values) using: (a) PAFTC; (b) S-PAFTC.

The average switching frequency (ASF) of the inverter was also investigated for both control strategies. The ASF is derived from the value of the switching states change during

a time window of 1 s considering the present and past gate pulses. Afterwards, the obtained value is divided by six to get the switching frequency per IGBT. The experimental results of the ASF, obtained when the SynRM is running with a rated load torque at different rotor speeds, is presented in Fig. 3.21. As can be seen, the two control strategies present a high value of the ASF at zero and low speeds, because the motor voltage at this operating point is small. With the increase of the rotor speed, the required motor voltage increases, thus the ASF will decrease. The S-PAFTC strategy is observed to have a higher switching frequency compared to the PAFTC. However, at high speeds it starts to approach the switching frequency curve of the PAFTC strategy.

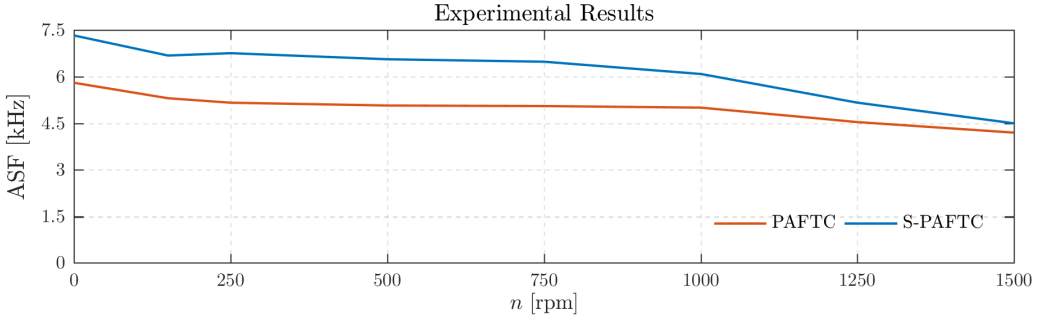

Fig. 3.21. Experimental results for the average switching frequency of the inverter, when the SynRM drive runs at rated load torque, for different rotor speeds.

3.4.3.2 Speed Reversal Test

In order to assess the transient capability of the proposed control strategies, a speed reversal test with the motor initially running at 1300 rpm is performed.

Fig. 3.22 and Fig. 3.23 present the simulation and experimental results obtained during the speed reversal test.

From these figures, it can be observed that the measured speed has a smooth response and reaches its desired value in a very short time (approximately 1 s). Based on these results, one can conclude that both control strategies regulate very well the currents along the d- and q-axis and consequently the active flux and electromagnetic torque due to the linear relationship between them. As expected, the current along the q-axis and the torque have similar profiles. Furthermore, during the transient process, the electromagnetic torque

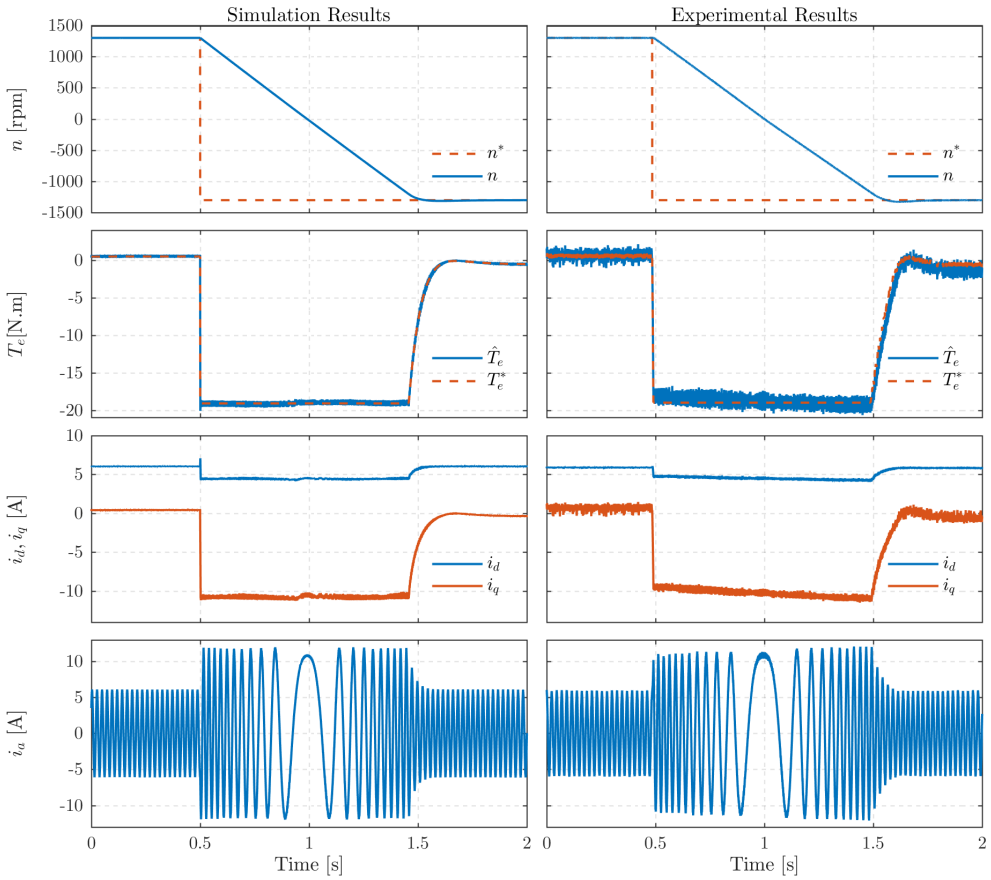

Fig. 3.22. Speed reversal test of the PAFTC when the SynRM operates at no-load. From top to bottom: rotor speed, estimated and reference torque, currents along the *dq*-axes, and stator current waveform.

reaches its rated value (19.1 N.m) to achieve the fastest settling time; once the desired speed of -1300 rpm is reached, the developed electromagnetic torque becomes zero. These results reveal a good speed and torque control capability of both proposed control strategies. Moreover, it is possible to observe that the current limit is respected at all times as current i_a is always lower than the maximum allowed value (11.2 A). The stator current is limited by the overcurrent protection term in the cost function in the case of the PAFTC, whereas it is limited in a direct way in the simplified control version.

3.4.3.3 Torque Step Response

To further evaluate the dynamic response of the proposed control strategies, a torque step test was conducted. In this test, the SynRM drive is changed to torque control mode by disconnecting the speed controller and setting manually the value of the reference torque,

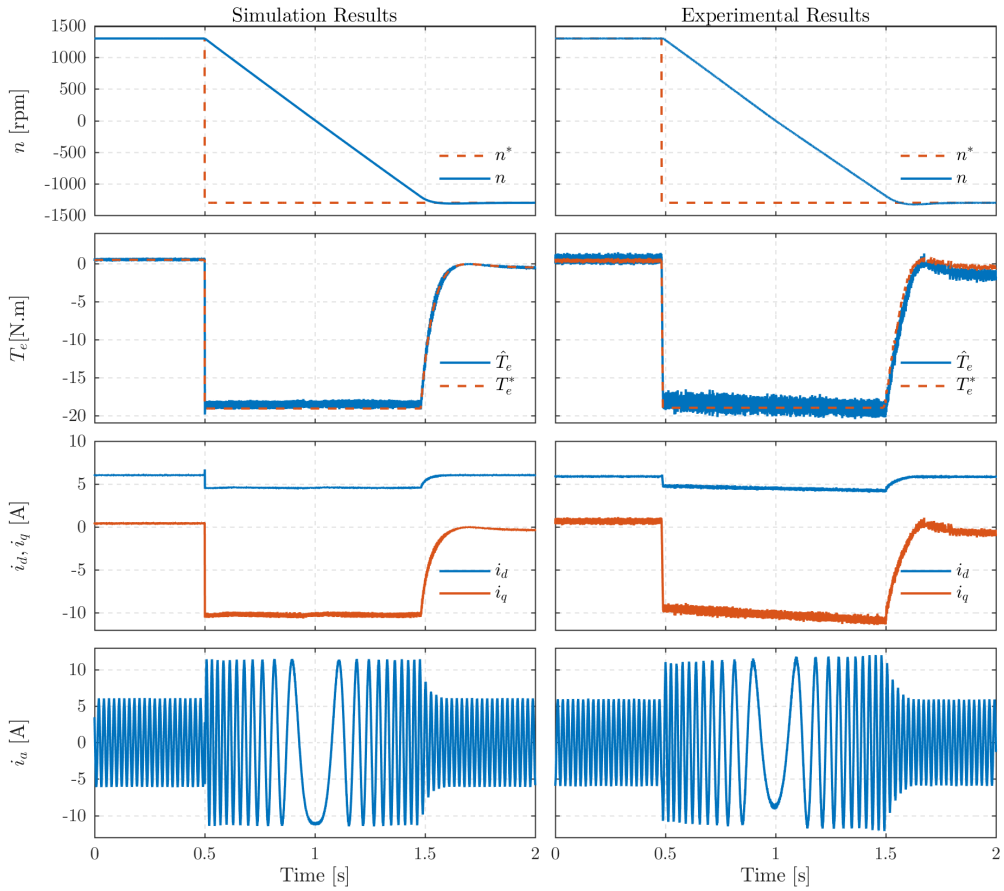

Fig. 3.23. Speed reversal test of the S-PAFTC when the SynRM operates at no-load. From top to bottom: rotor speed, estimated and reference torque, currents along the dq-axes, and stator current waveform.

while the auxiliary IM drive acts as a controlled load, in speed control mode, in order to maintain the speed roughly constant during the application of the torque variations to the SynRM drive.

A step change of the reference torque, from 0 N.m to 19.1 N.m (rated torque) at 0.1 s is imposed to the SynRM while it is running at 700 rpm. The results obtained for the torque step test are shown in Fig. 3.24 and Fig. 3.25. From top to bottom, the curves are the reference and estimated torque of the SynRM $T_e{}^*$ and $\hat{T}_e$, currents along the d- and q-axis, and the measured stator currents, i_{abc}. As can be noticed, the estimated torque tracks very well its reference value and both control strategies yield fast dynamic response, thus demonstrating the high performance of the developed SynRM drive system. Furthermore, the profiles of the estimated torque and the q-axis current component are identical, which means that the control strategies regulate very well the torque. In addition, during this test,

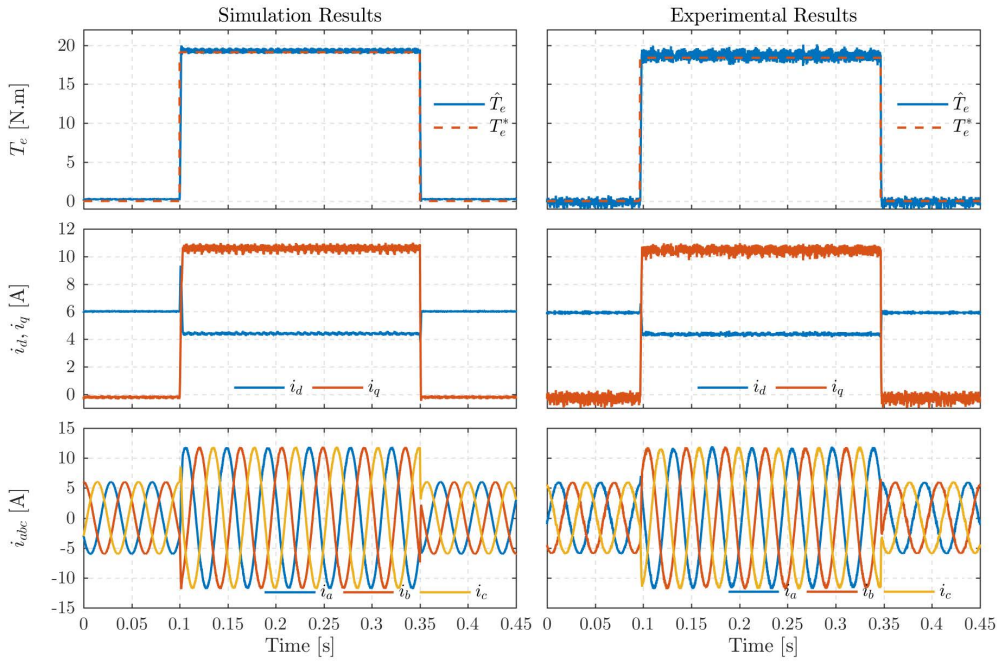

Fig. 3.24. Results for the torque step response of the PAFTC strategy (torque command from 0 N.m to 19.1 N.m) when the SynRM is running at 700 rpm.

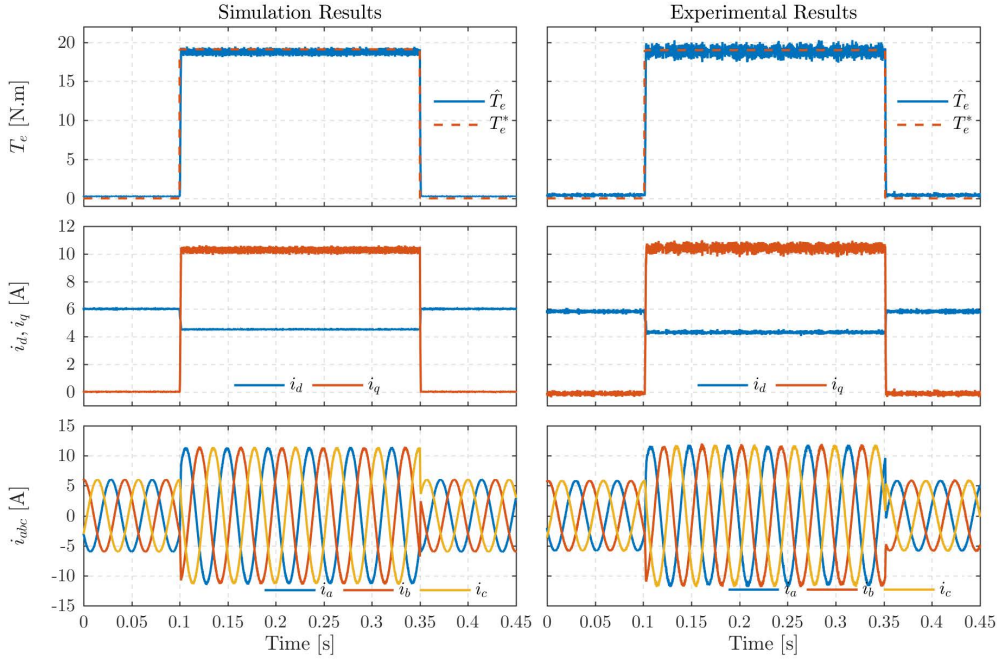

Fig. 3.25. Results for the step torque response of the S-PAFTC strategy (torque command from 0 N.m to 19.1 N.m) when the SynRM is running at 700 rpm.

the stator currents comply with the maximum current limitation (11.2 A) in this operating condition. Moreover, it is possible to observe in Fig. 3.24 and Fig. 3.25 a change of the d-axis current component which is due to the value of the reference active flux calculated based on

equation (C.1). This new value of the active flux is determined according to the updated values of L_q and currents i_d and i_q.

The results shown in Fig. 3.24 and Fig. 3.25 are also supported by the results shown in Fig. 3.26, which are a zoomed version of the torque variations obtained in the experimental tests in the vicinity of $t = 0.1$ s. According to these results, a variation from zero to the rated load torque is achieved in approximately 1.3 ms, which can be considered a very fast response.

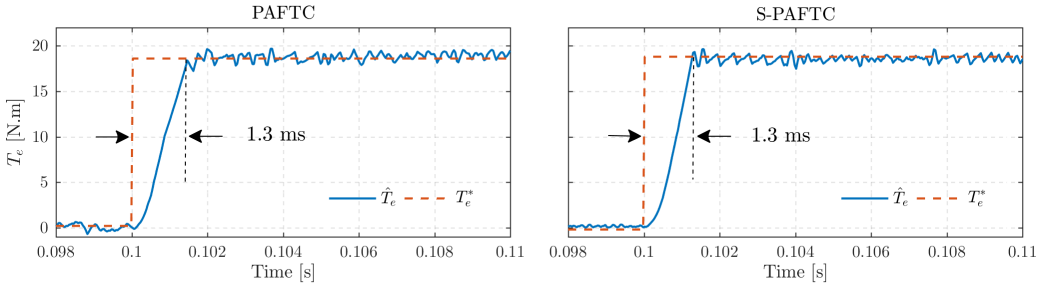

Fig. 3.26. Zoomed version of the torque step responses in Fig. 3.24 and Fig. 3.25, showing the variation of the reference torque and actual motor torque in the vicinity of t =0.1 s.

3.4.3.4 Speed Step Response

Fig. 3.27 and Fig. 3.28 show a speed transition from 100 rpm to 1200 rpm with a load torque of 15 N.m applied to the motor. For both control strategies, the speed tracks its reference value accurately without any significant overshoot. Moreover, the speed rise time for both control strategies is approximately comparable.

In the experimental tests, during the operation at 100 rpm, the estimated torque exhibits an oscillation of 1 N.m, which is introduced by the VSD that controls the load motor (auxiliary IM). During the acceleration period, the torque developed by the motor is the rated one, after reaching the desired speed, it develops a torque of 15 N.m to satisfy the required load torque. It is also possible to observe that i_q and the electromagnetic torque have similar profiles, which is expected. In addition, i_d also shows an expected behaviour since it changes according to the operating condition of the drive system. This happens because the active flux is calculated and updated in real-time and it relies on the variation of L_q, as well as the current components along the d- and q-axis.

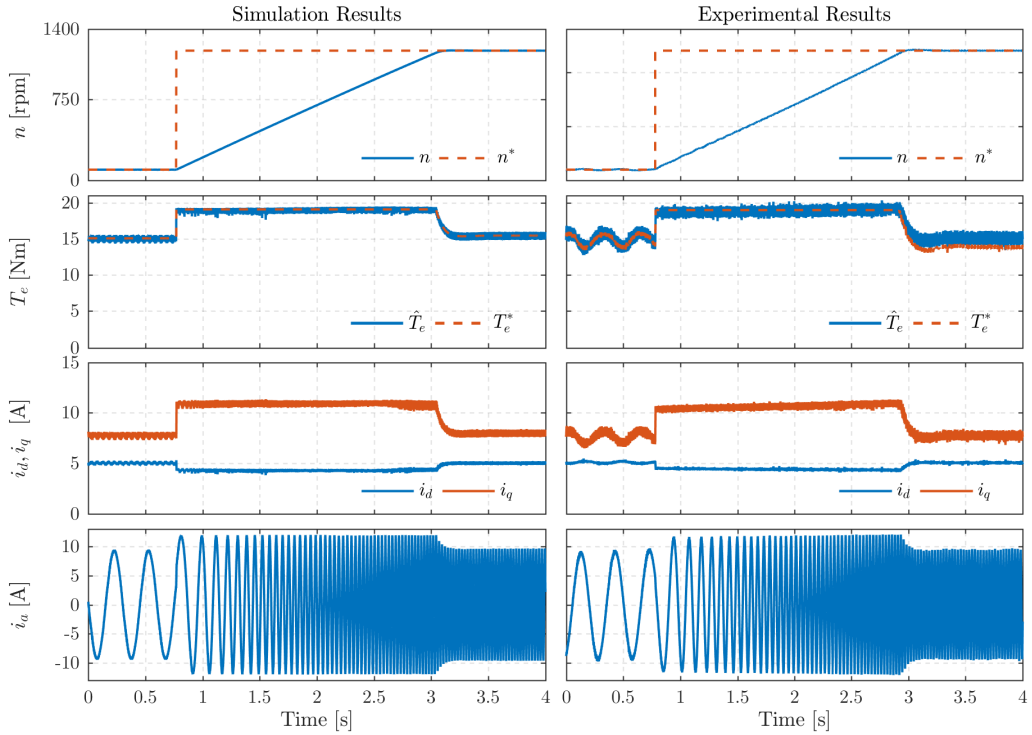

Fig. 3.27. Speed step response of the PAFTC strategy for a step speed command from 100 rpm to 1200 rpm, with a load torque of 15 N.m.

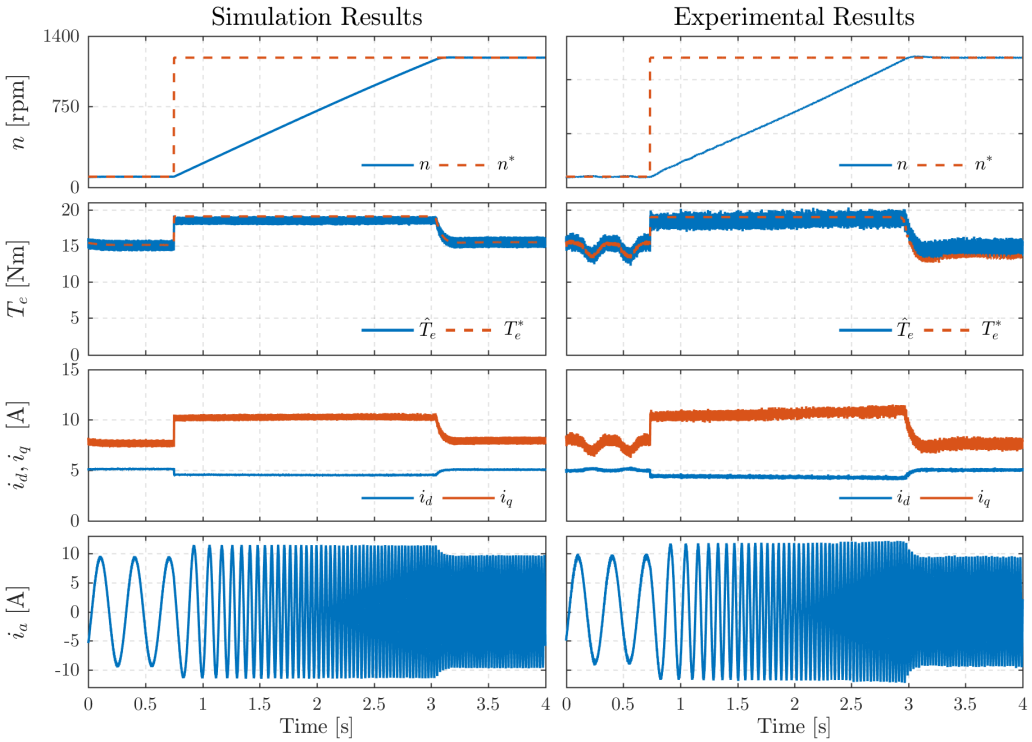

Fig. 3.28. Speed step response of the S-PAFTC strategy for a step speed command from 100 rpm to 1200 rpm, with a load torque of 15 N.m.

In addition to the preceding tests, the execution time of these strategies was measured with the aid of the dSPACE platform. The control algorithms of the PAFTC and the S-PAFTC take 27 and 22 μs to run, respectively. It can be seen that the PAFTC takes more time mainly because of the calculation of the current predictions in each control cycle. This is a disadvantage of the PAFTC compared to the S-PAFTC, where the current predictions have been reduced to only one set of calculations.

Finally, a brief comparison of some features of the two proposed control strategies is shown in Table 4.1

Table 3.2: Comparison between the PAFTC and the S-PAFTC strategies.

Feature	**PAFTC Strategy**	**S-PAFTC Strategy**
Weighting factors	Yes	No
Computational cost	Higher	Lower
Stator current THD	Low	Low

3.5 Conclusion

The simulation and experimental results verify that the PAFTC and S-PAFTC strategies can achieve comparable performances both in transient and in steady-state conditions. In steady-state operation, and under the same operation condition, both strategies have similar performances and allow to obtain very low values of the current THD factor. In transient conditions, the simulation and experimental tests verify that both control strategies can achieve a very fast dynamic response, due to the absence of current PI-controllers and modulator. Nevertheless, the S-PAFTC strategy has some advantages over the PAFTC strategy due to the following aspects:

- No tuning process is needed due to the absence of the weighting factors in the cost function, thus saving time during its implementation phase;
- The prediction stage of the control strategy is significantly simplified, thus reducing the control execution time, while maintaining the same performance of the PAFTC.

4

Predictive Load Angle and Stator Flux Control of SynRM Drives

This chapter presents a new control strategy for SynRM drives, called PLASFC, exploring its advantages in the control of SynRMs in the full speed range. This control strategy regulates directly the stator flux and the load angle of the motor in the stator flux reference frame. Thus, the limitations of voltage, current and load angle, which are necessary to operate effectively the SynRM drive in the different operating regions, are easily incorporated in this control scheme. The direct regulation of the stator flux makes the proposed control strategy very effective in terms of voltage utilization in the FW region. The choice of the load angle as a control variable instead of the electromagnetic torque also leads to some advantages, namely it ensures a smooth transition between the operation of the drive in the constant power and MTPV regions, as discussed in detail later on.

This chapter is organised as follows: section 4.1 reviews the control strategies of SynRMs in the FW region. The proposed PLASFC strategy is then discussed step-by-step in section 4.2, while simulation and experimental results are presented and discussed in section 4.3, demonstrating the very good steady-state and dynamic performance of the new control strategy here proposed.

4.1 Control Strategies of SynRMs in the Field-Weakening Region

By definition, the FW term is used to describe the operation of the SynRM above its base speed ω_b. If the resistance of the stator windings R_s is neglected, the supply voltage of the SynRM at steady-state can be simply considered as linearly dependent on the stator flux amplitude according to the following expression [34, 158, 159]:

$$u_s \approx \omega_r \times \psi_s, \tag{4.1}$$

where ω_r is the rotor electrical angular speed.

By keeping (4.1) in mind, as long as the electrical angular speed ω_r increases, the supply voltage of the SynRM will increase until the base speed ω_b is reached. At this point, the motor supply voltage is at its rated value and can no longer be increased. To further accelerate the SynRM to speeds above ω_b, and to maintain at the same time the supply voltage at its rated value, the stator flux magnitude must be decreased in a way that is inversely proportional to the increase of the electrical angular speed ω_r. This can be done by adopting an appropriate control strategy to regulate the stator flux magnitude of the SynRM in the full speed range.

As far as speed is concerned, the operation of the SynRM drive in the full speed range can be divided into three main regions, as shown in Fig. 4.1. Each one of these regions has its own characteristics and mode of operation [158].

The operation of the SynRM between zero and base speed ω_b is called the constant torque region or Region I. At low speeds and up to ω_b, the motor operates at rated stator flux and is capable of developing rated torque as long as its stator current limitation is respected and does not exceed the rated value. When the motor reaches the base speed, the supply voltage will be at its rated value and cannot be increased further. In order to operate the motor beyond this point, the stator flux has to be reduced with the increase of speed: the SynRM drive starts to enter into the FW region.

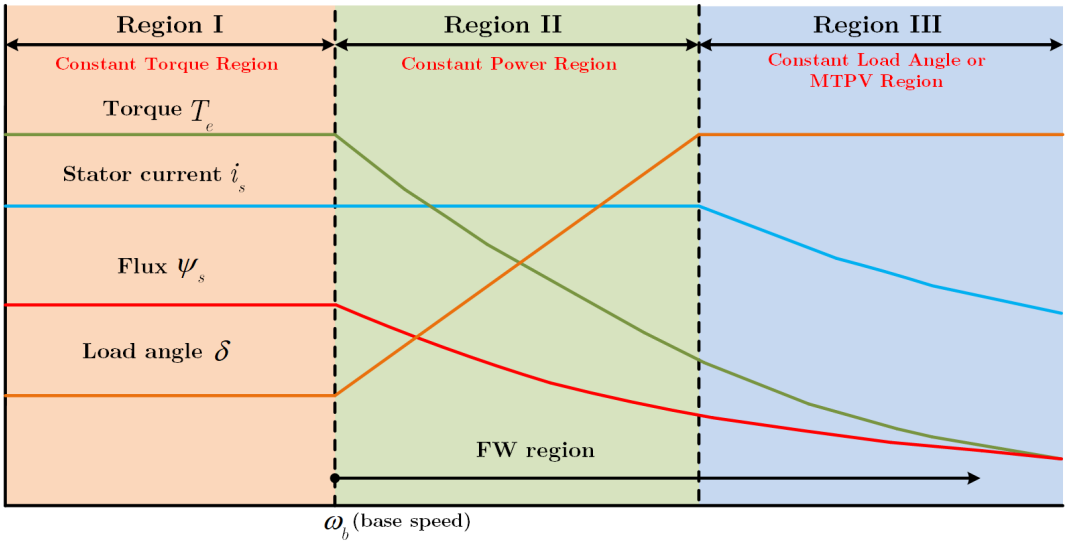

Fig. 4.1. Regions and limits of operation of a SynRM drive [158].

The FW region is divided into two main subregions: constant power region (Region II) and MTPV region (Region III). In Region II, the maximum current is the rated value but the stator flux is inversely proportional to speed; in addition, the maximum torque developed by the motor will be inversely proportional to speed as well, while the maximum power is still the rated one. The load angle in this region increases with speed until, at very high speeds, it reaches the stability limit of δ=45°. From this point on, the load angle cannot be increased further to ensure drive stability. Thus, the drive system at this stage must trigger an additional restriction to the load angle, thus entering into the second subregion of FW: Region III. In Region III, the SynRM drive operates at very high speeds with the load angle limited to ±45°, thus ensuring the stability of the drive system. On the other hand, the load angle limitation leads to a reduction of the motor stator current. The torque developed by the SynRM in this region decreases dramatically as the speed increases. It is worth mentioning that the maximum speed of the SynRM will be limited solely by the load torque applied to the motor and by mechanical constraints. From the electrical point of view, the maximum speed of the SynRM drive would be infinity.

It is good highlighting that the maximum torque developed by the SynRM in all operating regions is strongly dependent on the adopted control strategy. Furthermore, if the full SynRM drive capabilities are to be explored in Region III, the load angle limitation has to be effective in the drive system otherwise it will loose its stability. The way of including

such limitation is highly reliant on the type of control strategy.

By far, FOC is the most common control strategy employed to operate the SynRM in the FW region. According to this category of control strategies, and above base speed, the d- and q-axis reference currents are regulated to satisfy the current and the voltage constraints [34, 159, 160]. In [159], the reference current components along the dq-axes are determined, in order to operate the SynRM in Region II. In [34], the author proposed the use of Maximum Torque per Flux (MTPF) control law to maximize the torque developed by the SynRM in Region III. In Region II, the reference currents are determined in order to meet the current and voltage constraints as follows [34]:

$$i_d^* = \sqrt{\left(\frac{\frac{u_{max}^2}{\omega_r^2} - i_{max}^2 L_q^2}{\left(L_d^2 - L_q^2\right)} \right)} \tag{4.2}$$

$$i_q^* = \sqrt{i_{max}^2 - i_d^2} \tag{4.3}$$

where i_{max} is the maximum available current of the inverter, u_{max} is the minimum value between the maximum output voltage the inverter can produce from the DC-link voltage and the rated voltage of the motor, ω_r is the electrical angular speed of the rotor, and L_d and L_q stand for inductances along d-and q-axis, respectively.

In Region III, the reference currents that produce a maximum torque at this level of speed and the relation between these two currents are derived as follows [34]:

$$i_d^* = \frac{1}{\sqrt{2}} \frac{u_{max}}{\omega_r L_d} \tag{4.4}$$

$$i_q^* = \frac{1}{\sqrt{2}} \frac{u_{max}}{\omega_r L_q} \tag{4.5}$$

The i_d, i_q based control proposed in [160] is used in the SynRM drive for an electric steering system. Usually, the motors used in the electric power steering systems have low rated voltages, low output power and low rated speed. As a result, they have relatively a larger stator resistance. Therefore, in [160] the stator resistance value has been used in the calculation of the reference currents required to exploit the capability of the SynRM in

Region II and Region III.

Another control strategy that has been adopted to operate the SynRM in the FW region is DTC. In contrast to i_d,i_q based control, in DTC is easy to accomplish FW control because it regulates directly and independently the stator flux and the electromagnetic torque. The FW algorithm for SynRM drives based on a standard DTC has been developed in [161]. This FW algorithm imposes the voltage limitation once the SynRM reaches its base speed, by adjusting the stator flux reference levels in Regions II and III according to the continuous analysis of the torque error (output of the torque hysteresis band). For further improvement of the FW algorithm addressed in [161], the authors in [36, 51] proposed a FW algorithm that modifies the stator flux reference in Regions II and III based on the continuous analysis of duty ratio of the DTC. Although the FW algorithms in [36, 51, 161] exploit the capability of the SynRM drive to operate in Regions II and III, these FW algorithms do not consider the effects of magnetic saturation and cross-magnetic saturation in the SynRM (constant inductances have been used). In addition, the standard DTC algorithm exhibits high torque and flux ripples due to the use of torque and flux hysteresis controllers.

In [50], another control scheme for maximum power operation of direct torque controlled SynRMs is proposed. This control strategy is called a rotor flux vector calculator DTC (RFVC DTC). The RFVC DTC scheme shown in Fig. 4.2 combines MTPA, FW and MTPF controls. These controls are mathematically described in a reference frame synchronized with the stator flux linkage vector, being called *f-t* reference frame. The operating conditions and corresponding expressions used for the calculation of the torque and stator flux references in Regions II and III are given in Table 4.1. It is worth mentioning that in this control strategy, once again magnetic saturation was neglected. Moreover, the control scheme has some PI controllers, meaning that more tuning effort is required to reach a good performance.

The direct-flux vector control (DFVC), whose control system regulates directly the stator flux amplitude and torque (through the control of the q-axis current) in a stator flux reference frame was proposed to control SynRMs in the full speed range [48, 49, 162]. Fig. 4.3 presents the general scheme of the DFVC strategy for the SynRM drive, while the block diagram shown in Fig. 4.4 illustrates the implementation of the control strategy in the FW region, as well as the other limitations required for the drive operation. In the DFVC system, two

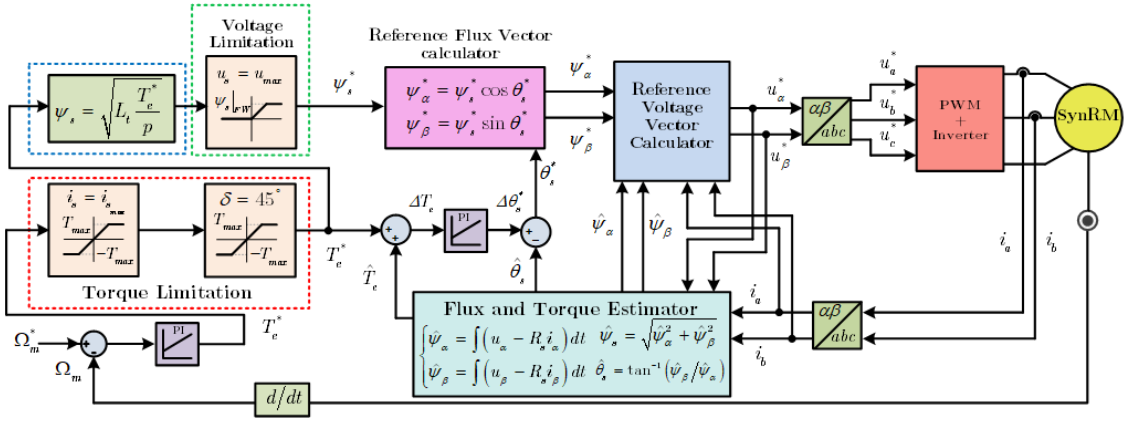

Fig. 4.2. The SynRM drive system based on RFVC DTC proposed in [50].

Table 4.1: An overview with the conditions and control equations for each of the operating regions of the RFVC DTC [50].

			Field-weakening	
Control method		MTPA (Region I)	Region II	MTPF (Region III)
Conditions	Voltage	$u_s < u_{max}$	$u_s = u_{max}$	
	Current	$i_s \leq i_{max}$		$i_s < i_{max}$
	Load angle	$\delta < 45°$		$\delta = 45°$
Equations	Torque limitation	$T_{max} = \sqrt{(p\psi_s i_{max})^2 - p\,(\psi_\alpha i_\beta - \psi_\beta i_\alpha)}$		$T_{max} = p\psi_s / L_{t-FW}$
	Stator flux reference	$\psi_s = \sqrt{L_t \frac{T_e}{p}}$	$\psi_s = \frac{1}{\omega_r}\left[-R_s i_t + \sqrt{u_{max}^2 - (R_s i_f)^2}\right]$	

PI regulators are required to regulate the stator flux and the q-axis current plus a third PI regulator to handle the operation of the drive in the MTPV region, which occurs when the motor pull-out torque has been reached and the load angle has to be limited to avoid system instabilities. Of course, the use of PI controllers always involves some tuning effort which ideally should be avoided. Keeping this in mind, reference [163] presents a model-based version of the DFVC for PMSM drives, which avoids the use of PI regulators by generating the inverter reference voltages from the flux-linkage and q-axis current set points and feedbacks. Although, the model-based version of the DFVC strategy is developed in the stator flux reference frame by choosing the stator flux amplitude and the quadrature current as the control variables, it requires an additional analytical work to obtain the information of the load angle variation, thus increasing the complexity of its implementation process.

To this date, the development of FCS-MPC strategies for SynRM drives able to operate

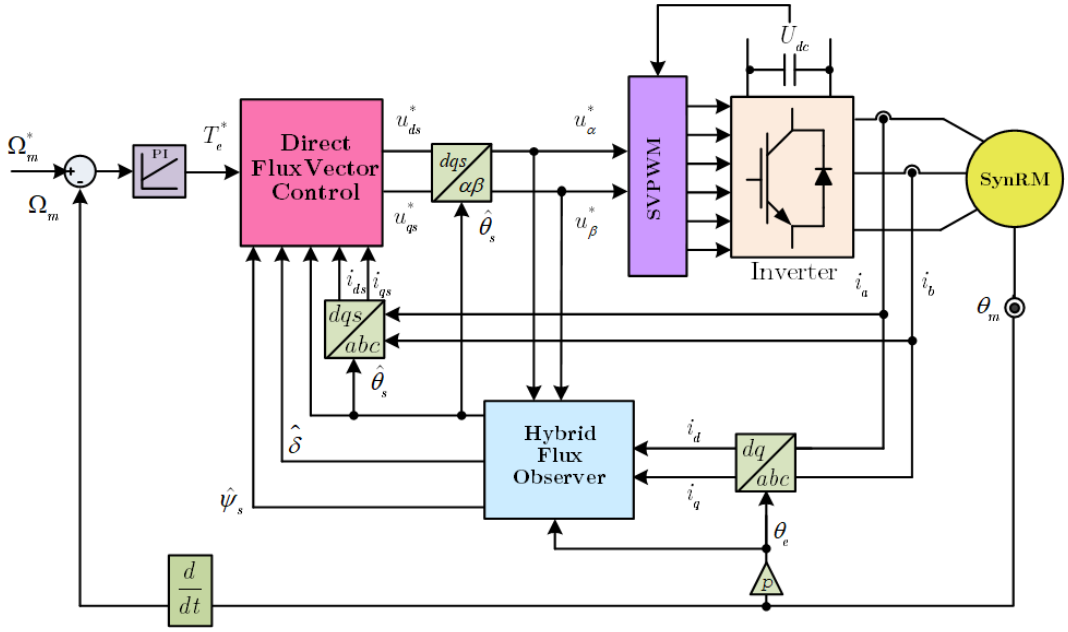

Fig. 4.3. The SynRM drive system based on DFVC proposed in [48, 49, 162].

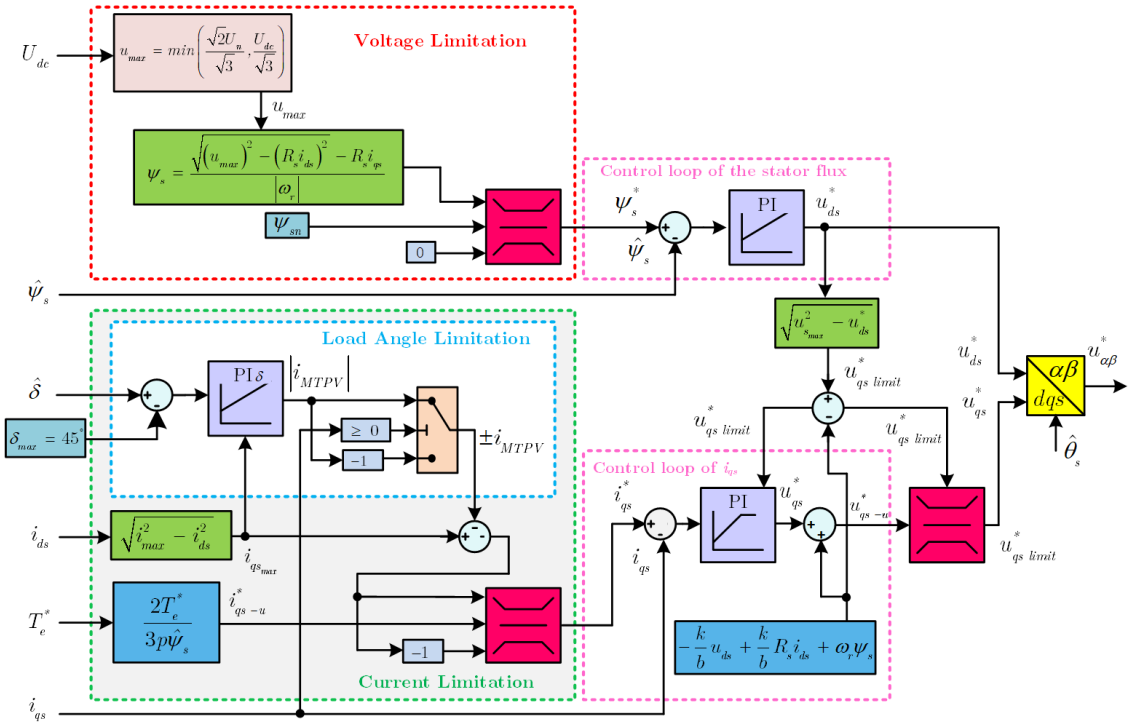

Fig. 4.4. Limits of operation and generation of the reference quantities in the DFVC scheme [48, 49, 162].

in the FW region is very scarce. In [164], a FCS-MPC strategy was developed for PMSMs in order to achieve optimal performance and ability to operate the motor in the FW region. Nevertheless, the designed cost function has three mains terms in order to take into account different criteria, each term having a weighting factor, hence requiring some tuning effort

which is still considered one of the complex task of traditional FSC-MPC. In addition, the proposed control system uses constant inductances which is not the real case as they vary significantly with respect to currents. As far as FCS-MPC strategies specifically proposed for SynRM drives, no work has been reported yet in literature. For this reason, the PLASFC is developed and proposed to enhance the operation of the SynRM drive in the full speed range.

4.2 Predictive Load Angle and Stator Flux Control

As mentioned before, the PLASFC strategy is developed in the $d_s q_s$ frame and controls directly the SynRM stator flux and load angle. In Fig. 4.5, the dq rotor reference frame and the stator flux reference frame are presented. The dq rotor reference frame is used in the current model of the stator flux and load angle observer and in the estimation of the motor inductances, as detailed later on. The load angle δ (or the phase angle of the stator flux) is measured with respect to the d-axis, θ_r is the electrical rotor position, θ_s is the phase angle of the stator flux vector with respect to the α-axis and $\underline{i}_s$ is the stator current vector. The instantaneous angular supply frequency ω_e is related to ω_r by

$$\omega_e = \frac{d\delta}{dt} + \omega_r. \tag{4.6}$$

Of course, in steady-state conditions, $\omega_e = \omega_r$. In transient conditions, and considering a discretization time step relatively small, which is always the case when dealing with predictive control strategies, the approximation $\omega_e \simeq \omega_r$ does not introduce any significant error and will be considered.

The voltage equations of the SynRM in the stator flux reference frame are given by [48].

$$u_{ds} = R_s i_{ds} + \frac{d\psi_s}{dt} \tag{4.7}$$

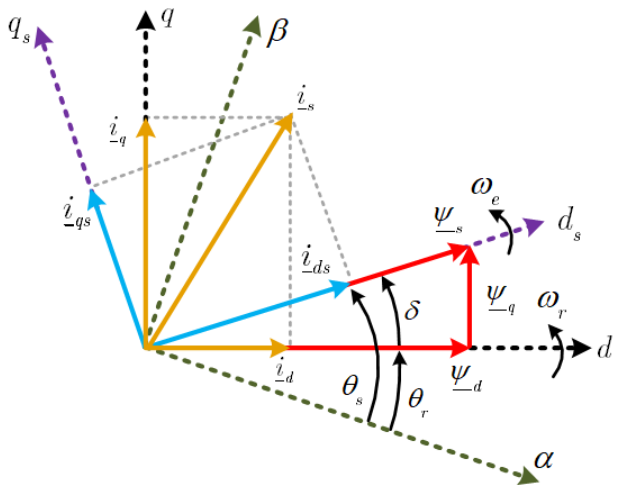

Fig. 4.5. Vector diagram of the SynRM and different coordinate axes.

$$u_{qs} = R_s i_{qs} + \left(\frac{d\delta}{dt} + \omega_r\right)\psi_s, \tag{4.8}$$

where u_{ds}, u_{qs}, i_{ds}, i_{qs} are the d_s-axis and q_s-axis components of the stator voltages and currents, respectively, R_s is the stator winding resistance, ψ_s is the amplitude of the stator flux vector.

The electromagnetic torque can be expressed as a function of the load angle according to [49]

$$T_e = \frac{3}{4}p\left(\frac{1}{L_q} - \frac{1}{L_d}\right)\psi_s^2 \sin(2\delta) = \frac{3}{2}p\psi_s i_{qs} \tag{4.9}$$

where L_d and L_q are the apparent inductances along the d-axis and q-axis, respectively, taking into account the effect of magnetic and cross-magnetic saturation.

The proposed PLASFC system is a FCS strategy which ensures that the stator flux magnitude and load angle of the SynRM follow the corresponding reference values. A general diagram of the proposed control strategy is shown in Fig. 4.6.

It is possible to observe that an encoder provides the mechanical angular position of the rotor, θ_m, which is subsequently converted to an electric angular rotor position θ_r. The two phase stator currents i_a and i_b are measured directly, while the third phase current i_c is calculated from the measured i_a and i_b. The currents, i_a, i_b and i_c are then transformed to the $\alpha\beta$ reference frame and used in the stator flux and load angle observer and inductances estimation blocks. The voltage components u_α and u_β in the $\alpha\beta$ stationary reference frame

are calculated in a direct way using the switching state of the inverter and the measured DC-link voltage, being also used in the stator flux and load angle observer and prediction model. The reference torque T^* is either the reference torque set by the user (torque control mode) or the output of the PI speed controller, while the reference stator flux can be set to its rated value ψ_{sn} or to an optimal value ψ_s^{opt} if desired. The main blocks that constitute the PLASFC scheme are described in detail in the following subsection.

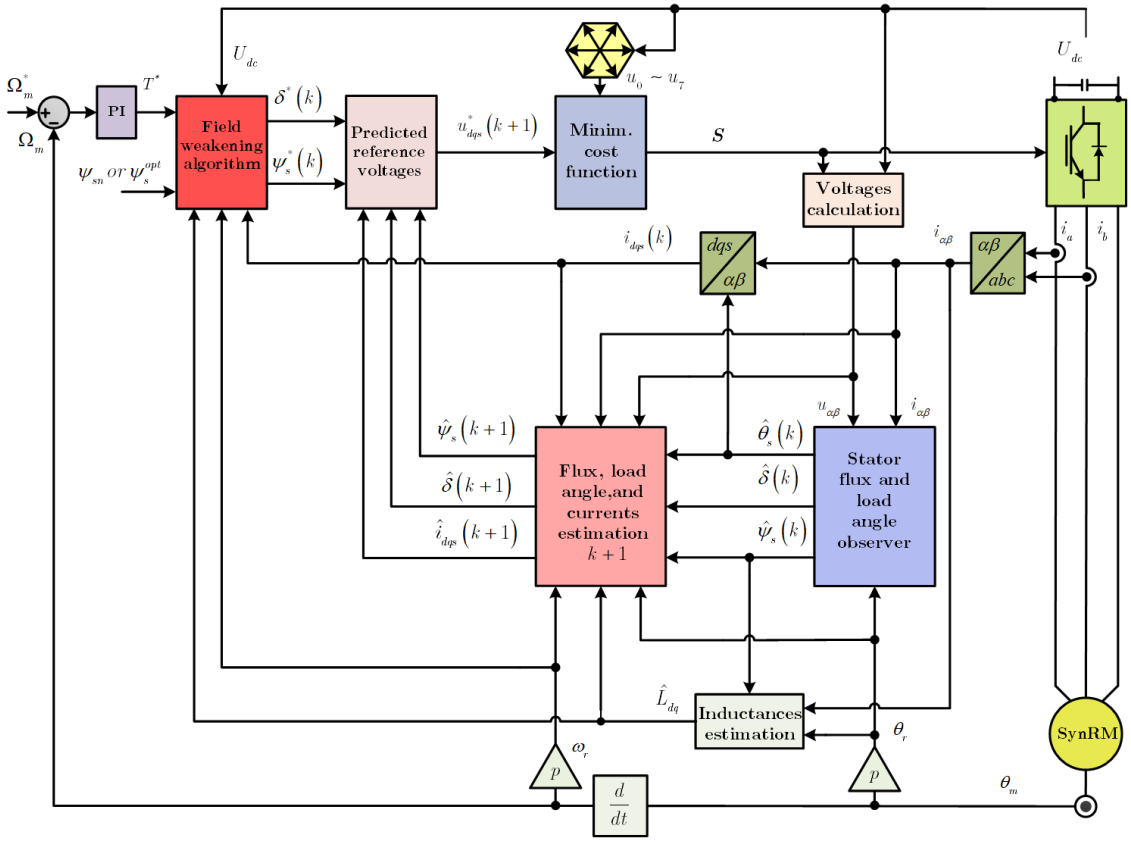

Fig. 4.6. Proposed PLASFC scheme for SynRM drives.

4.2.1 Prediction Model

In the PLASFC system, ψ_s and δ are chosen as state variables. Therefore, the voltage equations (4.7) and (4.8) are solved for the stator flux and the load angle derivatives, and rewritten as follows

$$\frac{d\psi_s}{dt} = u_{ds} - R_s i_{ds} \tag{4.10}$$

$$\frac{d\delta}{dt} = \frac{u_{qs} - R_s i_{qs}}{\psi_s} - \omega_r. \tag{4.11}$$

The equations (4.10) and (4.11), after discretization using a forward Euler method, allow to obtain the estimated values of ψ_s and δ for instant $k+1$ according to

$$\hat{\psi}_s(k+1) = \hat{\psi}_s(k) + T_s\left[u_{ds}(k) - R_s i_{ds}(k)\right] \tag{4.12}$$

$$\hat{\delta}(k+1) = \hat{\delta}(k) + \frac{T_s}{\hat{\psi}_s(k)}\left[u_{qs}(k) - R_s i_{qs}(k) - \omega_r \hat{\psi}_s(k)\right] \tag{4.13}$$

In the equations above, T_s is the sampling period and the estimated quantities $\hat{\psi}_s(k)$ and $\hat{\delta}(k)$ are obtained with a stator flux and load angle observer.

As with any conventional FCS-MPC strategy, the actuation delay corresponding to one sampling period would lead to the need of predicting the values of the state variables for time instant $k+2$, considering all possible voltage vectors that can be applied to the motor by the inverter (seven different voltage vectors in the case of a 2L-VSI). Nevertheless, the S-PAFTC strategy presented in the previous chapter, and the one proposed for 2L-VSI and three-level power converters in [132,165], can avoid this procedure. The idea of this strategy is to reduce the computation time by eliminating the need of the seven predictions and calculate instead the reference voltage vector $u^*(k+1)$ that applied to the motor at instant $k+1$, would force the state variables to reach the corresponding reference values at instant $k+2$.

Adopting a similar concept of the S-PAFTC presented in the previous chapter, it is considered that the reference values of ψ_s and δ, which are calculated at the sampling instant k by the FW algorithm, are reached by the system at instant $k+2$. This is equivalent to establish the following relations

$$\psi_s(k+2) = \psi_s^*(k) \tag{4.14}$$

$$\delta(k+2) = \delta^*(k). \tag{4.15}$$

Taking into account (4.14)-(4.15), the discretization of (4.10)-(4.11) for instant $k+1$, and

after solving the obtained equations for the voltage components at instant $k+1$, yields

$$u_{ds}^{*}\left(k+1\right)=R_{s}\hat{i}_{ds}\left(k+1\right)+\left(\frac{\psi_{s}\left(k+2\right)-\hat{\psi}_{s}\left(k+1\right)}{T_{s}}\right) \tag{4.16}$$

$$u_{qs}^{*}\left(k+1\right)=R_{s}\hat{i}_{qs}\left(k+1\right)+\frac{\hat{\psi}_{s}\left(k+1\right)}{T_{s}}\left(\delta\left(k+2\right)-\hat{\delta}\left(k+1\right)\right)+\omega_{r}\hat{\psi}_{s}\left(k+1\right). \tag{4.17}$$

The predicted current values needed for the calculation of the reference voltages in (4.16)-(4.17) are first estimated for instant $k+1$ in the dq rotor reference frame according to

$$\begin{aligned}\hat{i_{d}}\left(k+1\right)=i_{d}\left(k\right)+\frac{T_{s}}{\gamma L_{d}^{inc}}\left(u_{d}\left(k\right)-R_{s}i_{d}\left(k\right)+\omega_{r}\hat{L}_{q}i_{q}\left(k\right)\right)-\\-\frac{T_{s}L_{dq}^{inc}}{\gamma L_{d}^{inc}L_{q}^{inc}}\left(u_{q}\left(k\right)-R_{s}i_{q}\left(k\right)-\omega_{r}\hat{L}_{d}i_{d}\left(k\right)\right)\end{aligned} \tag{4.18}$$

$$\begin{aligned}\hat{i_{q}}\left(k+1\right)=i_{q}\left(k\right)+\frac{T_{s}}{L_{q}^{inc}}\left(u_{q}\left(k\right)-R_{s}i_{q}\left(k\right)-\omega_{r}\hat{L}_{d}i_{d}\left(k\right)\right)+\\+\frac{L_{qd}^{inc}}{L_{q}^{inc}}\left(i_{d}\left(k\right)-\hat{i}_{d}\left(k+1\right)\right).\end{aligned} \tag{4.19}$$

where $\hat{L}_{d}$ and $\hat{L}_{q}$ are estimated apparent inductances, L_{d}^{inc} and L_{q}^{inc} are self-incremental inductances, L_{dq}^{inc}, L_{qd}^{inc} are cross-incremental inductances and $\gamma=1-\frac{L_{dq}^{inc}L_{qd}^{inc}}{L_{d}^{inc}L_{q}^{inc}}$.

The equations (4.18)-(4.19) are transformed to the stator flux reference frame by

$$\hat{i}_{ds}\left(k+1\right)=\cos\hat{\delta}\left(k+1\right)\hat{i}_{d}\left(k+1\right)+\sin\hat{\delta}\left(k+1\right)\hat{i}_{q}\left(k+1\right) \tag{4.20}$$

$$\hat{i}_{qs}\left(k+1\right)=-\sin\hat{\delta}\left(k+1\right)\hat{i}_{d}\left(k+1\right)+\cos\hat{\delta}\left(k+1\right)\hat{i}_{q}\left(k+1\right). \tag{4.21}$$

The final stage of the PLASFC strategy is the choice of the actuation voltage vector at instant $k+1$, which is selected based on the minimization of a very simple cost function g representing the square of the Euclidean distance between the reference voltage vector, whose components are given by (4.16)-(4.17), and each one of the voltage vectors that the inverter can apply to the motor:

$$g=\left|u_{ds}^{*}\left(k+1\right)-u_{dsn}\right|^{2}+\left|u_{qs}^{*}\left(k+1\right)-u_{qsn}\right|^{2},\qquad n=0,1,.....,6 \tag{4.22}$$

The PLASFC strategy requires less computation time compared to more traditional FCS-MPC approaches as instead of seven predictions for the stator flux and load angle, a reference voltage vector is calculated only once and a much simpler cost function is evaluated in the end, without the need of tuning any weighting factor.

4.2.2 Field-Weakening Operation

According to the PLASFC strategy proposed in this thesis, the control system must impose certain limitations in each one of the three operating regions (Region I, Region II and Region III) to ensure the stable and safe operation of the SynRM drive in the full speed range.

The block diagram shown in Fig. 4.7 illustrates the implementation of the PLASFC strategy in the FW region with the main limitations (voltage, current and load angle) required for the drive variables. Below base speed (Region I), the reference value of the stator flux is the rated one (or an optimal flux level, as detailed later on in the following section). Once the speed starts to increase, the supply voltage of the SynRM will increase to keep the stator flux at its rated value. As soon as the SynRM reaches its base speed ω_b, the supply voltage will be at its maximum (rated) value , and thus the stator flux has to be decreased so that the SynRM is able to operate beyond the base speed. Hence, the reference stator flux in the FW region (Region II and Region III) will be given by

$$\psi_s^* = \frac{\sqrt{u_{max}^2 - (R_s i_{ds})^2} - R_s i_{qs}}{|\omega_r|}, \tag{4.23}$$

where u_{max} is updated in the real-time according to the measured DC-link voltage U_{dc} and the rated voltage of the motor $U_{n(motor)}$ which is given by

$$u_{max} = min\left(\frac{\sqrt{2}U_{n(motor)}}{\sqrt{3}}, \frac{U_{dc}}{\sqrt{3}}\right) \tag{4.24}$$

The limit u_{max} is the minimum value between the maximum output voltage the inverter can produce from the available DC-link voltage and the rated voltage of the motor (which

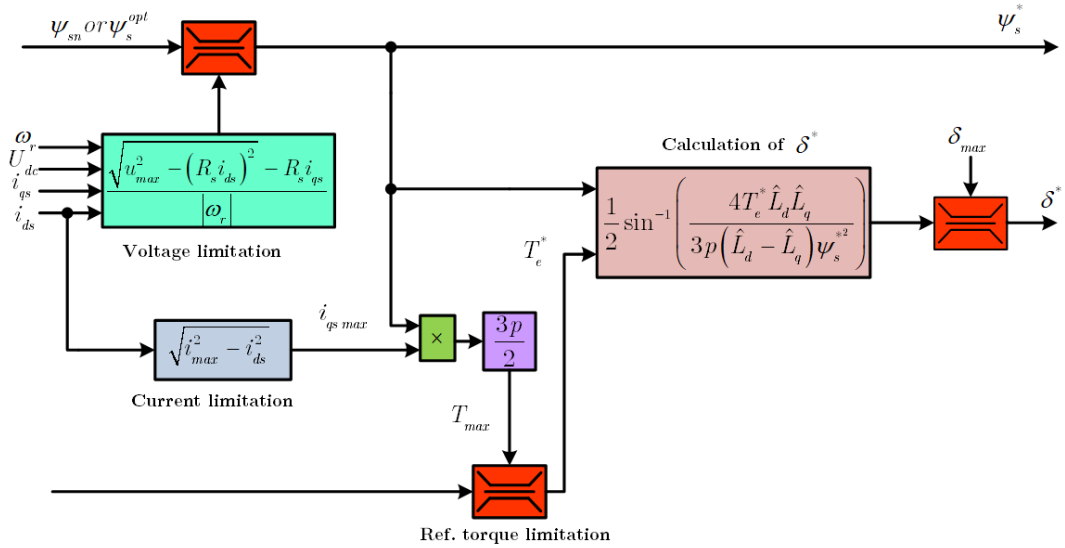

Fig. 4.7. Limitations and generation of the reference quantities in the PLASFC strategy.

will be the case of the SynRM used in the experimental tests, as it has a rated voltage smaller than the maximum available voltage).

In Regions I and II, the motor current has to be limited at all times to a maximum motor current i_{max}. The current component i_{ds} is responsible for the magnetization of the motor, hence the current limitation must be imposed on the q_s-axis current component as follows

$$i_{qs\,max} = \sqrt{i_{max}^2 - i_{ds}^2}. \tag{4.25}$$

The current limitation (4.25) can be translated into a maximum torque the motor can develop as

$$T_{max} = \frac{3}{2} p \psi_s^* i_{qs\,max} \tag{4.26}$$

These limitations, in conjunction, ensure the safe operation of the SynRM drive in Regions I and II.

The reference value of the load angle δ^* is needed by the PLASFC strategy. Taking the first term in the second side of (4.9) and solving for δ, the reference load angle can be given by

$$\delta^* = \frac{1}{2}\sin^{-1}\left[\frac{4T_e^* \hat{L}_d \hat{L}_q}{3p\left(\hat{L}_d - \hat{L}_q\right)\psi_s^{*2}}\right] \tag{4.27}$$

where T_e^* is the reference torque set by the user (drive operating in torque control mode) or the torque generated by the speed controller, after passing through the torque limitation block.

To operate the drive system in Region III, the load angle of the SynRM must be limited to the maximum value δ_{max} to ensure a smooth transition between Region II and Region III. The value δ_{max} for the SynRM is obtained through the partial derivative of the torque equation (4.28) in order to δ:

$$T_e = \frac{3}{4} p \left(\frac{1}{L_q} - \frac{1}{L_d} \right) \psi_s^2 \sin(2\delta) \tag{4.28}$$

$$\frac{\partial T_e}{\partial \delta} = \frac{3}{2} p \left(\frac{1}{L_q} - \frac{1}{L_d} \right) \psi_s^2 \cos(2\delta) \tag{4.29}$$

Equating (4.29) to zero, one obtains the maximum load angle of the SynRM: $\delta_{max} = \pm 45°$, where the positive and negative values apply to the cases when the machine operates as a motor or generator, respectively. Hence, $|\delta|$ must always be $\leq 45°$ to ensure the drive stability. While this condition is always satisfied at low operating speeds, along the MTPV trajectory, $\delta = 45°$ and the SynRM has reached its stability limit. Some authors have addressed this issue and proposed an appropriate load angle limitation to avoid the instability of the drive in Region III. In [48,166], the load angle was limited with the aid of a PI regulator that corrects the q_s-axis current limit according to the phase angle of the observed stator flux with respect to the setpoint of the maximum load angle δ_{max}. In the PLASFC strategy, the load angle in (4.27) is limited easily using a simple saturation block because the proposed control strategy regulates directly the load angle. This was the main reason why the load angle was chosen as a control variable instead of torque.

4.2.3 Stator Flux and Load Angle Observer

The developed PLASFC strategy regulates both the load angle and the stator flux. Thus, its performance highly depends on the information provided by the load angle and stator flux observer. With the impossibility of measuring these quantities, it is necessary to estimate

them based on the measured variables (voltage and current), so that they can be used in the control system. In this context, the adoption of a hybrid stator flux observer, which comprises a voltage and current model, is the best option to fulfil these requirements. The scheme of the hybrid stator flux observer adopted in this work is illustrated in Fig. 4.8.

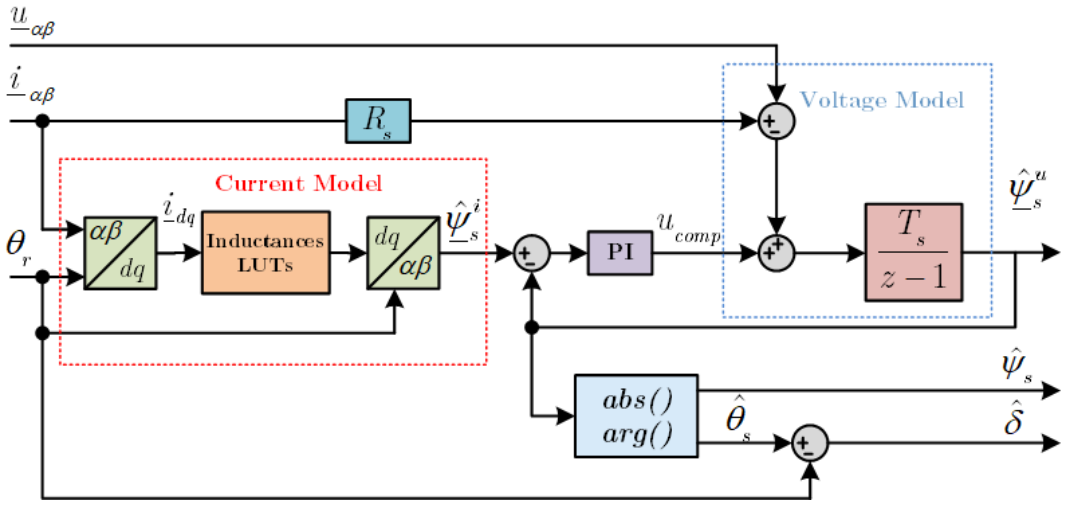

Fig. 4.8. Stator flux and load angle observer.

In the high speed region, the amplitude of the applied voltage is high this makes the voltage model preferable due to its robustness to the parameter error namely inductances. However, in the low speed region the current model is more suitable and must be chosen as the magnitude of the applied voltage is small and thus this leads to the failure of the voltage model.

In the hybrid stator flux observer, the stator voltage $\underline{u}_{\alpha\beta}$, current $\underline{i}_{\alpha\beta}$ and θ_r are used to estimate the stator flux. The stator flux of the SynRM, calculated based on the current model, is given by

$$\underline{\psi}_s^i = (L_d i_d + jL_q i_q)\, e^{-i\theta_r}. \tag{4.30}$$

where the i_d and i_q stand for the currents along d- and q-axis, and L_d and L_q are the apparent inductances along d- and q-axis.

The voltage model dominates the behaviour of the stator flux observer at medium and high speeds, being based on the integration of the back-EMF of the motor, as it is more robust against parameter variations. The stator flux, calculated through the voltage model

is given by

$$\underline{\psi}_s^u = \int \left(\underline{u}_s - R_s \underline{i}_s + \underline{u}_{comp} \right) dt. \tag{4.31}$$

In order to avoid a discontinuous transition between the current and voltage models, and make it as smooth as possible, a PI controller is used. The input of this PI controller is the difference between the outputs of the two models, being its output the compensation term $\underline{u}_{comp}$:

$$\underline{u}_{comp} = \left(K_p^{ui} + \frac{1}{T_i^{ui} s} \right) \left(\underline{\psi}_s^i - \underline{\psi}_s^u \right). \tag{4.32}$$

The PI controller was tuned according to the rules proposed in [167]:

$$K_p^{ui} = \sqrt{2}\omega_c \tag{4.33}$$

$$T_i^{ui} = \frac{1}{\omega_c^2}, \tag{4.34}$$

where ω_c is the cutoff angular frequency for the transition between the two models, and K_p^{ui} and T_i^{ui} are the proportional gain and integral time of the PI controller. The speed at which the transition between the two models occurs is chosen to be approximately 400 rpm, which implies a cutoff angular frequency of $\omega_c = 52.36$ rad/s ($\simeq 13.5$ Hz). Consequently, the values obtained for the PI controller parameters are K_p^{ui}=120 and T_i^{ui}=1.4×10^{-4}.

The stator flux observer provides the amplitude $\hat{\psi}_s$ and the phase angle $\hat{\theta}_s$ of the stator flux. The load angle $\hat{\delta}$ is estimated as the difference between the flux phase angle $\hat{\theta}_s$ and the measured electrical rotor position θ_r.

As previously described, the hybrid stator flux estimator at low speeds relies mainly on the current model of the SynRM. However, the voltage model is still there and, even at low or zero speeds, still disturbs to some point the estimated stator flux. Hence, an inaccurate stator voltage vector $\underline{u}_{\alpha\beta}$, which feeds the voltage model, would lead to some errors in the estimated stator flux which in turn leads to an error in the estimated load angle and estimated torque. The stator voltage used in the voltage model is calculated based on the switching state of the inverter and the measured DC-link voltage, thus it is affected by the inverter dead-time.

To improve the accuracy of the stator flux and load angle estimation when the motor is operating in the low speed range, the inverter dead-time is compensated in the calculation of the stator voltage $\underline{u}_{\alpha\beta}$ by adopting the dead-time compensation algorithm proposed in [168]. According to this algorithm, the first step is to determine if the compensation is necessary or not. In other words, if no switching occurs in the inverter compared to the previous control cycle, then no compensation is required. On the contrary, if a switching occurs, for instance from vector $\underline{u}_1$ to vector $\underline{u}_2$, and depending on the current signs of the three output currents of the inverter, the modified voltage vector $\underline{u}_{mod}$ will be considered.

$$\underline{u}_{mod} = \frac{T_D}{T_s}\underline{\tilde{u}}^{DT} + \frac{T_s - T_D}{T_s}\underline{u}_2 \tag{4.35}$$

where $\underline{u}_2$ is the voltage vector to be considered by the control system if no dead-time is required, while the voltage vector $\underline{\tilde{u}}^{DT}$ is applied to the motor during the dead-time T_D, and is determined based on the sign of the three phase currents i_{abc}, as well as the voltage vectors before and after switching. Table 4.2 shows how the dead-time voltage vector $\underline{\tilde{u}}^{DT}$ is determined based on the sign of the three phase currents when switching from $\underline{u}_1$ to $\underline{u}_2$.

Table 4.2: Determination of the dead-time voltage vector based on the sign of phase currents [168].

$\text{sgn}(i_a)$	$\text{sgn}(i_b)$	$\text{sgn}(i_c)$	$\underline{\tilde{u}}^{DT}$
+	+	+	$\underline{u}_1$
+	+	−	$\underline{u}_1$
+	−	+	$\underline{u}_2$
+	−	−	$\underline{u}_2$
−	+	+	$\underline{u}_1$
−	+	−	$\underline{u}_1$
−	−	+	$\underline{u}_2$
−	−	−	$\underline{u}_2$

4.2.4 Apparent Inductances Estimation

In the FCS-MPC strategy, the accuracy of the motor parameters is of paramount importance to achieve a better performance with regard to drive stability, high motor efficiency,

low current ripple and good motor tracking of the reference values set by the controller. This is particularly important when dealing with a SynRM where magnetic saturation and cross-magnetic saturation are non-negligible phenomena, affecting directly the values of the motor inductances.

When dealing with motor inductances, one has to distinguish three types of inductances used by the control system: apparent inductances, self-incremental inductances, and cross-incremental inductances. In the PLASFC strategy, errors introduced in the values of the self- and cross-incremental inductances lead to errors in the values of the predicted current for instant $k+1$ but they do not affect significantly the motor steady-state tracking capability of the reference values set by the control system. Thus, no error compensation mechanism is included for the self- and cross-incremental inductances.

On the other hand, the apparent inductance errors have a much higher influence on the performance of the proposed control system. The values of apparent inductances L_d and L_q, stored in LUTs and used by the current model of the stator flux and load angle observer, are inevitably affected by some uncertainty, being the source of some errors in the estimated stator flux and load angle values in the low speed region. In the medium and high speed regions, the voltage model stands, almost eliminating the influence of inductance values mismatch in the outputs of the stator flux and load angle observer.

The apparent inductances are used in the current prediction equations and more importantly in the calculation of the reference load angle using (4.27). Due to the fact that the currents are neither directly controlled in the proposed control strategy nor evaluated in the cost function, the apparent inductance values mismatch does not affect significantly the operation of the drive system, but the calculation of the reference load angle is significantly affected by the errors in those inductances, especially the error in L_q, leading the SynRM drive to operate with a torque and load angle quite different from the ones set by the control system. To mitigate or minor these effects, the prediction model and the reference load angle generation block use inductance values estimated online by

$$\hat{L}_d = \frac{\hat{\psi}_d}{i_d} \tag{4.36}$$

$$\hat{L}_q = \frac{\hat{\psi}_q}{i_q}, \tag{4.37}$$

with all variables in (4.36)-(4.37) expressed in a rotor reference frame.

Both apparent inductances can be reliably estimated as long as the currents have a reasonable minimum value, say 1 A, to avoid a division by zero and to obtain estimated inductance profiles with a low noise content. In practice, i_d is always much higher than this minimum value, allowing the estimation of $\hat{L}_d$ at all times, while the estimation of $\hat{L}_q$ has to be disabled when the motor operates at very low load levels, using in those cases the values stored in the corresponding LUTs.

The changeover between the estimated $\hat{L}_q$ and the one obtained with the LUTs (L_q^{LUT}) needs to be gradual and smooth in order to prevent any instability or bumps in the operation of the SynRM. The transition process is implemented according to the following conditions

$$L_q \begin{cases} L_q^{LUT} & ; |i_q| \leq i_q^{tra} \\ L_q^{LUT}\left(1 - \frac{|i_q| - i_q^{tra}}{\Delta i_q}\right) + \hat{L}_q \frac{|i_q| - i_q^{tra}}{\Delta i_q} & ; i_q^{tra} \leq |i_q| \leq i_q^{tra} + \Delta i_q \\ \hat{L}_q & ; |i_q| > i_q^{tra} + \Delta i_q \end{cases} \tag{4.38}$$

where $i_q^{tra} = 1\,\text{A}$ is the value of current at which the transition is started and $\Delta i_q = 0.2\,\text{A}$ is a current band for the transition from L_q^{LUT} to the estimated $\hat{L}_q$.

4.2.5 Stator Flux Level Optimization

The efficiency optimization of electric drive systems has been extensively studied. When an AC drive system operates at constant flux linkage magnitude at all load levels, the low efficiency at light loads is highly expected. Accordingly, several papers have been reported on the adaptation of the control algorithm to get the best efficiency of the drive system at all load levels. Generally, the proposed efficiency optimization techniques have been focused on the adjustment of the flux level to get the maximum motor efficiency for a given torque demand. The MTPA technique is the most common method to maximize the developed torque by the motor for a certain level of current and thus plays an important role in the

enhancement of the overall drive efficiency.

In current-controlled system (like FOC), the total losses can be minimized by adjusting the d- and q-axis current ratio. In such control systems, loss minimization control methods can be classified into two main categories: loss-model controllers (LMC) and search controllers (SCs). SCs entail minimizing the input power by searching the d-axis current (or stator flux) in real time. They are basically insensitive to electrical motor parameters [169]. However, LMCs, which generate the optimum current (or stator flux) command vector from a loss equation, are more often employed in industrial drives. This is because they are superior to SCs with regard to control stability and current pulsation reduction [170].

In spite of the great number of studies dealing with MTPA for SynRM drives based on FOC [33, 34, 52, 53], in DTC- and FCS-MPC-based SynRM drives this has been scarcely investigated [50, 86, 171]. As DTC has no current control loops, current is not regulated directly. Thus, it is difficult to regulate the current in DTC drives. Therefore, to ensure the efficient operation of the DTC-based SynRM drives, an optimal reference value for the stator flux magnitude is needed. In [86] an online procedure for the automatic search of the MTPA operating point for DTC-based SynRM was proposed. The algorithm is perturbation based and it injects a random pattern into the stator flux reference of the DTC-based SynRM drive, and thus the information of the MTPA point is retrieved from the sampled current magnitude. Although, the motor parameters in this algorithm are not needed, the tedious searching process causes torque ripple and the sluggish dynamic response.

In [50], a control scheme was proposed for direct torque controlled SynRM. The proposed scheme consists of a combination of MTPA control, maximum torque per flux control and flux weakening. For the MTPA control, the magnetic saturation was neglected and the current angle was set to 45°, thus leading to a non-optimal motor operation.

In [171], the cost function of the proposed PTC strategy was designed to meet multiple demands: torque reference tracking, online MTPA tracking for the high electrical efficiency, and the limitation of the current to its maximum value. The online MTPA term in the designed cost function evaluates the partial derivative of the torque with respect to the current angle for a given stator current magnitude. Since, the partial derivative is dependent

on both apparent and incremental inductances, a recursive least squares (RLS) algorithm was implemented to estimate these quantities in real-time. However, although the proposed PTC strategy led to promising results, the process of the adaptive weighting factor selection was not discussed as it plays an important role in the performance of the control system.

Similar to DTC, the PLASFC strategy does not directly regulate the current, thus the MTPA trajectory has to be translated into an optimum stator flux reference. To calculate the optimum reference stator flux which be used by this control strategy, some additional analytical work is required as discussed below.

Considering the equivalent circuit of the SynRM in the rotor reference frame and including the iron losses, represented by the iron losses resistance R_c [172]. It can be shown that the power losses in the motor are given by [173]

$$P_e = \frac{3}{2}\frac{u_s^2}{R_s + R_c} + \frac{3}{2}\frac{R_s R_c}{R_s + R_c}\left[\left(\frac{\psi_d}{\hat{L}_d}\right)^2 + \left(\frac{\psi_q}{\hat{L}_q}\right)^2\right]. \tag{4.39}$$

The equation above contains a first term that roughly represents the iron losses, and a second one that is directly related to the stator copper losses. The motor used in this study is a high efficiency one with very low iron losses, therefore, and for the sake of simplicity, the first term will be neglected. Moreover, u_s is considered constant, leading to the same final result as far as optimal flux level is concerned. On the other side, the losses given by the second term change with the motor load level and can be minimized.

Let us define M as

$$M = \left(\frac{\psi_d}{\hat{L}_d}\right)^2 + \left(\frac{\psi_q}{\hat{L}_q}\right)^2. \tag{4.40}$$

In a rotor reference frame, the electromagnetic torque developed by the SynRM can be given by

$$T_e = \frac{3}{2}p\left(\frac{1}{\hat{L}_q} - \frac{1}{\hat{L}_d}\right)\psi_d\psi_q. \tag{4.41}$$

By solving (4.41) for ψ_q and using the result in (4.40), one can write M as a function of

ψ_d. The value of ψ_d that minimizes M is obtained by solving $\partial M/\partial \psi_d = 0$, yielding

$$\psi_d^{opt} = \hat{L}_d \times \sqrt[4]{\frac{4T_e^2}{9p^2\left(\hat{L}_d - \hat{L}_q\right)^2}}. \tag{4.42}$$

The optimal value ψ_d^{opt} is calculated using (4.42) considering $T_e = T^*$. The optimal value ψ_q^{opt} is then calculated using that result in (4.41). With these two flux components, the optimum stator flux level used by the control system (see Fig. 4.6) is calculated by

$$\psi_s^{opt} = \sqrt{\left(\psi_d^{opt}\right)^2 + \left(\psi_q^{opt}\right)^2}. \tag{4.43}$$

It is important to mention that although the inductances change with the motor operating condition inside the control system, the above calculated optimum reference stator flux is performed assuming that the inductances are constant, meaning that the current angle is 45°. The reason for not including the derivative of the inductances in the process of obtaining the optimum stator flux level is to avoid further complications in the analytical process which would not be translated into a significant gain in terms of motor efficiency. However, if the variation of the parameters are considered, the current angle will be higher than 45°, this conclusion has been drawn based on the results presented in [171]. Therefore, the optimal stator flux, in this study, is computed considering the variation of the parameters that will be updated in every control cycle of the real time implementation.

The main steps involved in the implementation of the PLASFC strategy presented in previous sections are shown in Fig. 4.9. It has nine main steps that can be summarized as follows:

1) Measure the speed $\theta_m(k)$, $U_{dc}(k)$ and currents $i_a(k)$ and $i_b(k)$.

2) Calculate the torque reference T^*.

3) Estimate $\hat{L}_d$ and $\hat{L}_q$, $\hat{\psi}_s(k)$, and $\hat{\delta}(k)$ at instant k.

4) Predict $\hat{\psi}_s(k+1)$, $\hat{\delta}(k+1)$ and $\hat{i}_{dqs}(k+1)$ for instant $k+1$.

5) Calculate ψ_s^* and $\delta^*(k)$.

6) Predict $u_{dqs}^*(k+1)$ for instant $k+1$.

7) Evaluate the cost function g for all possible switching states.

8) Select the switching state that minimizes the cost function.

9) Apply the optimal voltage vector $u_s\,(k+1)$.

These nine steps are executed during each sampling period, taking into consideration the new available measurements and references.

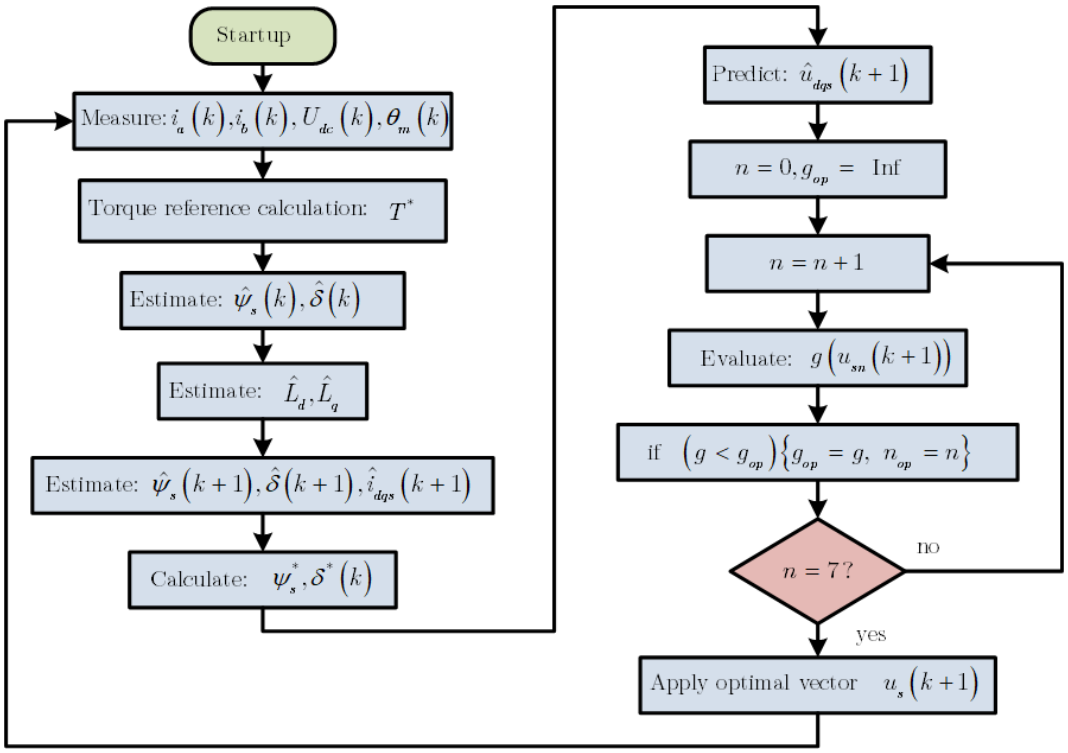

Fig. 4.9. Main steps involved in the implementation of the PLASFC strategy.

4.3 Results Obtained

The simulation model of the SynRM drive using PLASFC was developed in *Simulink* environment. A general overview of such simulation model is presented in Appendix A (Fig. A.5 and Fig. A.6).

The experimental setup presented in the previous chapter is also used here to test the SynRM with the PLASFC strategy. It is complemented with a high precision power analyser, Yokogawa WT300 and a torque sensor so that the SynRM efficiency can be computed. The sampling period of the proposed predictive control strategy is set at $T_s = 40\,\mu$s, while the

speed loop is implemented at a slower ($T_{speed} = 25 * T_s$) to reduce the quantization error in the speed signal derived from the incremental encoder.

The performance of the PLASFC strategy was evaluated with the SynRM drive operating in different conditions. The following test conditions were considered to validate this approach:

a) Parameters mismatch;
b) Steady-state operation;
c) Speed reversal test;
d) Torque step response;
e) Speed step response;
f) Operation in field-weakening region;
g) Operation with an optimized stator flux level.

4.3.1 Parameters Mismatch

In order to illustrate the importance of estimating online the values of the apparent inductances, some simulation results are presented instead of the experimental ones. The reason for making this decision relies on the purpose of showing the true impact of the errors in the values of the apparent inductances in difference SynRM variables, namely in the stator flux level, load angle and actual motor torque values. The objective here is to investigate if the motor stator flux level follows or not the reference value set by the control system (as it influences the saturation level in the motor); if the SynRM load angle coincides or not with the corresponding reference value set by the control system and if the reference torque (output of the speed controller) matches the true motor electromagnetic torque (important when operating the SynRM drive in torque control mode). All this information is readily available in the simulation model, where one can get the "true" motor quantities using the motor model and observe how this information matches the reference quantities or estimated variables as calculated by the control system. In experiments, there is no direct access for instance to the motor stator flux level or to the motor load angle as it has to be estimated using information obtained with the stator flux and load angle observer (which is affected by

errors in the parameters used by the control system) and position of the rotor. Hence, the experimental analysis appears to be of less value than the simulation study, using a detailed simulation model which had been validated in a previous work.

As mentioned before, the influence of the detuned values of self- and cross-incremental inductances on the steady-state tracking capability of the reference values set by the proposed predictive control strategy is negligible. On the contrary, the detuned values of these parameters certainly lead to errors in the values of the predicted currents for instant $k+1$. The calculation of the current prediction error is performed by the comparison between the estimated currents for instant $k+1$ ($\hat{i}_d(k+1)$, $\hat{i}_q(k+1)$) calculated at instant k but affected by a unit delay block, and the measured currents at instant k ($i_d(k)$, $i_q(k)$). The difference between the estimated and measured currents is defined here as the current prediction error.

Fig. 4.10 and Fig. 4.11 show the prediction errors of i_d and i_q for three cases of self-incremental inductance values: real values (blue plots), positive detuned values (red plots), and negative detuned values (yellow plots). The prediction errors in i_d and i_q are computed at different operating: speeds of $n = \{250,\ 750,\ 1200,\ 1500\}$ rpm and load torque $T_L = \{1,\ 5,\ 10,\ 15,\ 18\}$ N.m.

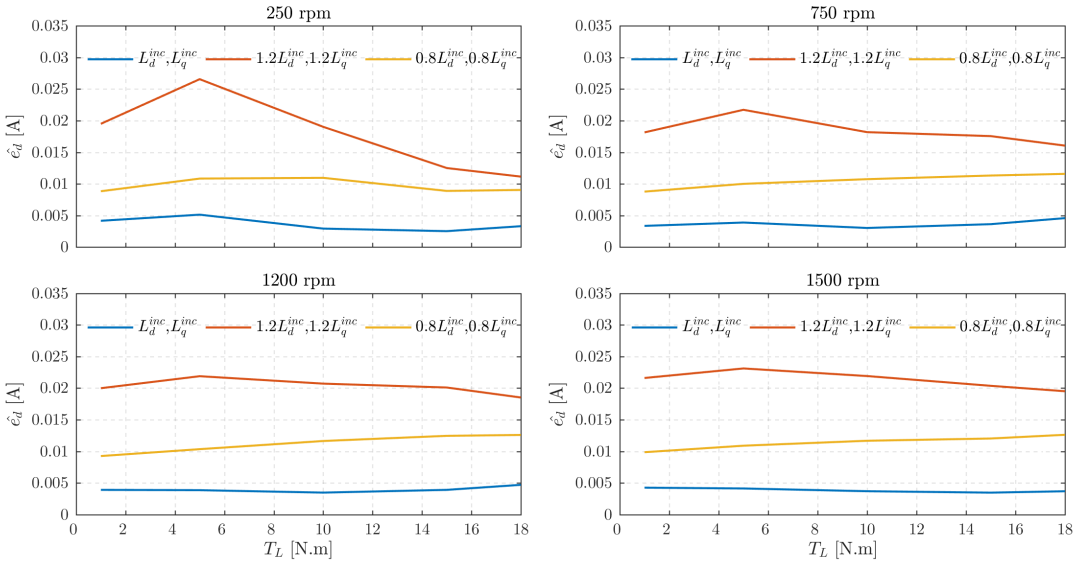

Fig. 4.10. Simulation results for the prediction error in i_d for the three cases of self-incremental inductance values: real values (blue plots), positive detuned values (red plots), and negative detuned values (yellow plots).

As can be seen in Fig. 4.10, the prediction error of i_d increases significantly mainly for

positive detuned self-incremental inductances, reaching the maximum value of 0.026 A at 250 rpm. Besides, it has a small tendency to decrease with the increase of the load torque. Moreover, it is possible to observe that the prediction errors for the d-axis current, in the case of negative detuned values, have the same behaviour at different operating points, and remain lower than 0.014 A all the time. As opposed to what has been observed under positive and negative detuned self-incremental inductance values, the prediction errors of i_d for the real values of self-incremental inductances are always small, being less than 5 mA for all operating points.

The prediction errors in i_q, shown in Fig. 4.11, are higher at low speeds but they decrease once the speed starts to increase. In addition, their variation for different load torque values is insignificant. The current prediction errors resulting from positive detuned self-incremental inductance values are higher in comparison with the ones obtained for the case of negative detuned self-incremental inductances, and approach each other at higher load torque values. Finally, as expected, the prediction errors for the q-axis current with real values of the self-incremental inductances are small, being less than 20 mA. These results demonstrate a good match between the estimated and measured currents.

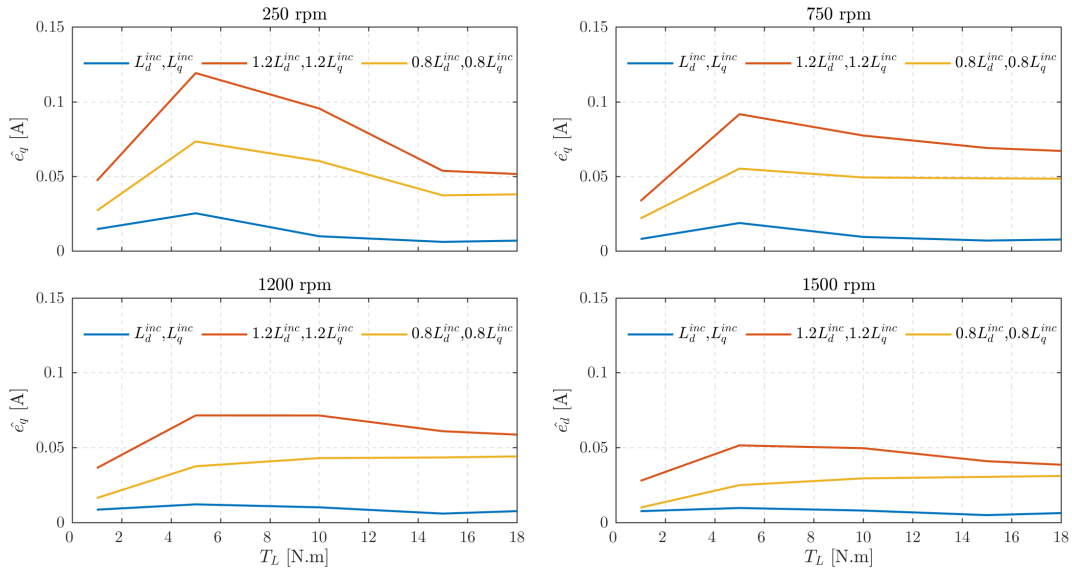

Fig. 4.11. Simulation results for the prediction error in i_q for the three cases of self-incremental inductance values: real values (blue plots), positive detuned values (red plots), and negative detuned values (yellow plots).

Fig. 4.12 and Fig. 4.13 present the prediction errors in both i_d and i_q for the three cases of cross-incremental inductance values: real values (blue plots), positive detuned values (red

plots), and negative detuned values (yellow plots). The prediction errors in i_d and i_q are computed at different operating points, the load torque is set as $T_L = \{1,\ 5,\ 10,\ 15,\ 18\}$ N.m, while the SynRM drive is running at different speeds $n = \{250,\ 750,\ 1200,\ 1500\}$ rpm. The prediction errors for the d-axis current shown in Fig. 4.12 are in general small,

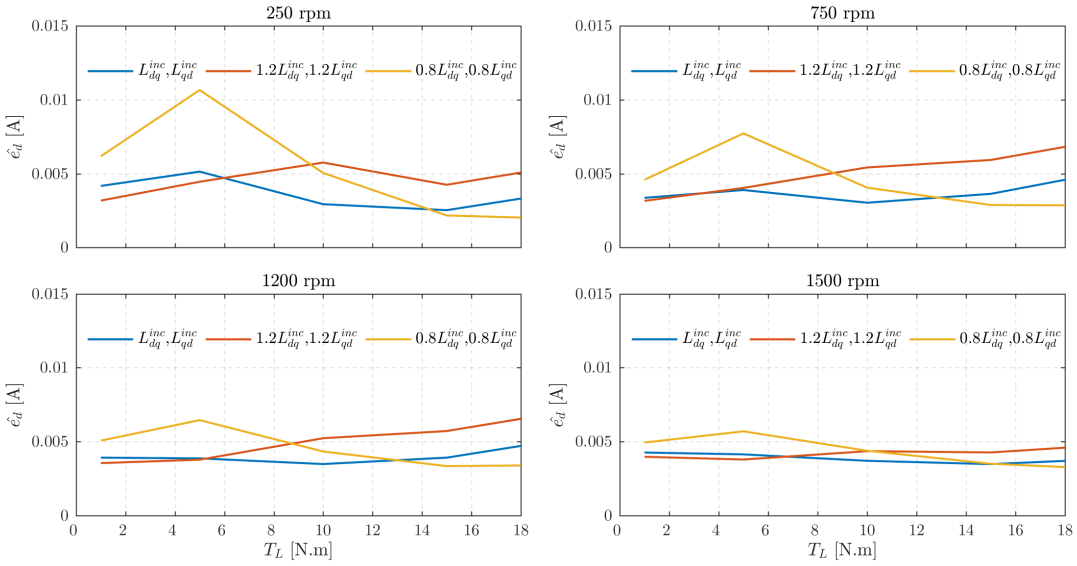

Fig. 4.12. Simulation results for the prediction error in i_d for the three cases of cross-incremental inductance values: real values (blue plots), positive detuned values (red plots), and negative detuned values (yellow plots).

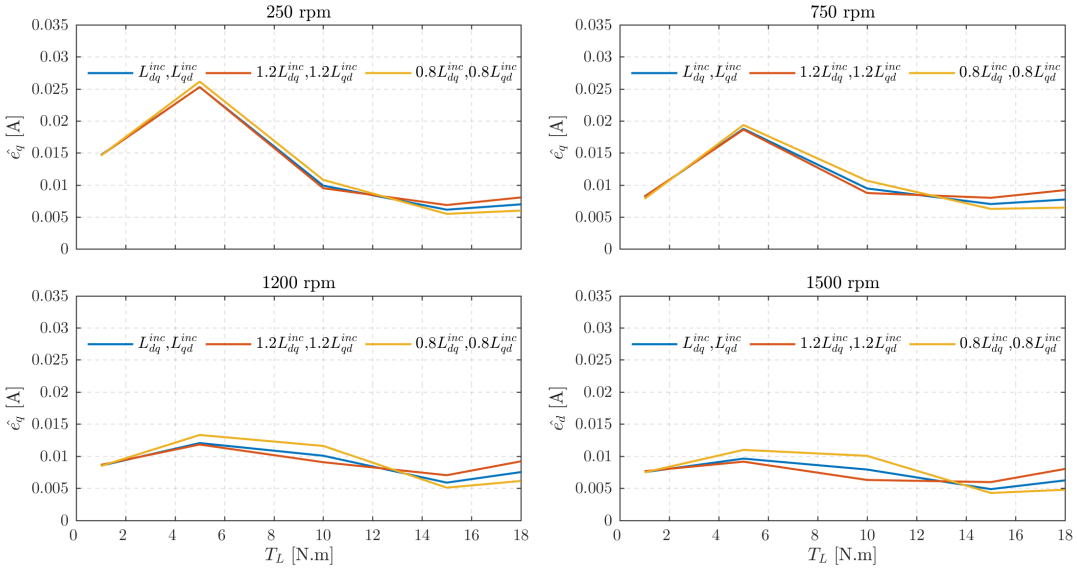

Fig. 4.13. Simulation results for the prediction error in i_q for the three cases of cross-incremental inductance values: real values (blue plots), positive detuned values (red plots), and negative detuned values (yellow plots).

in comparison with the errors due to the detuned values of self-incremental inductances

because the magnitude of cross-incremental inductances is also small, making the system less sensitive to errors in these parameters.

The prediction errors for the q-axis current depicted in Fig. 4.13 clearly indicate that positive and negative detuned cross-incremental inductances lead to almost identical prediction errors for i_q.

To verify the effectiveness of the compensation mechanism proposed for the apparent inductances, a simulation study has been conducted. The first test is performed with a $-20\,\%$ detuning in the inductance values, L_d and L_q, used by the control system. The obtained simulation results are depicted in Fig. 4.14.

As can be seen from this figure, without an online inductance estimation procedure, the torque and the load angle of the motor (T_{em} and δ_m) are lower than the reference values (T_e^* and δ^*) set by the control system, which may even prevent the drive from starting if the starting load torque is high. When the inductance online estimation procedure is activated, the control and actual motor variables are much closer to their reference values, allowing to operate satisfactorily the drive in the entire speed range, thus increasing significantly the robustness of the control system to parameter uncertainties.

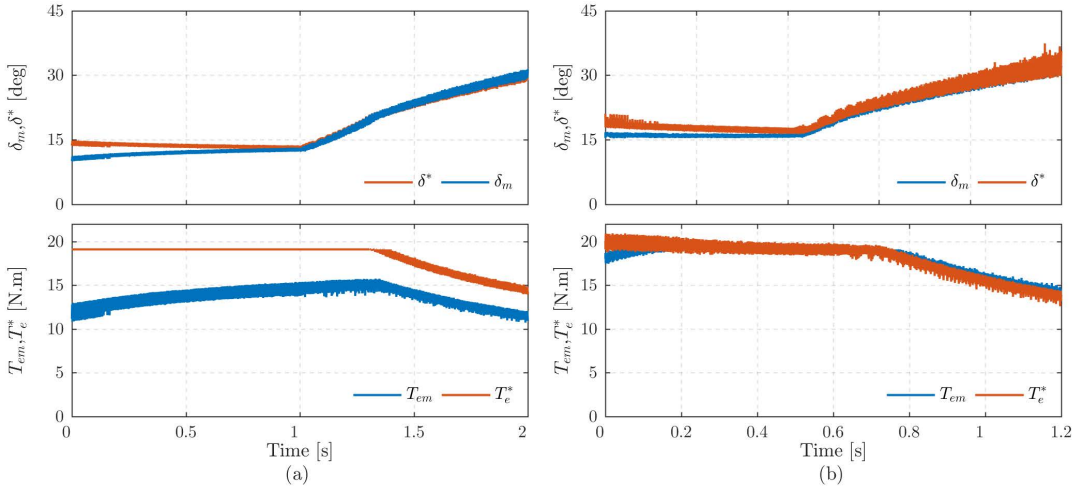

Fig. 4.14. Simulation results for the reference load angle and electromagnetic torque set by the control system (red plots) versus the corresponding motor quantities (blue plots) when the SynRM drive is accelerating with a load torque of 5 N.m and with $-20\,\%$ detuning in L_d and L_q: (a) without inductance estimation (speed range: 450 to 2550 rpm); (b) with inductance estimation (speed range: 450 to 2440 rpm).

The second test follows the same process of the first one but in this case a positive error of $+20\,\%$ is introduced in the inductance values used by the control system. Once again, as can

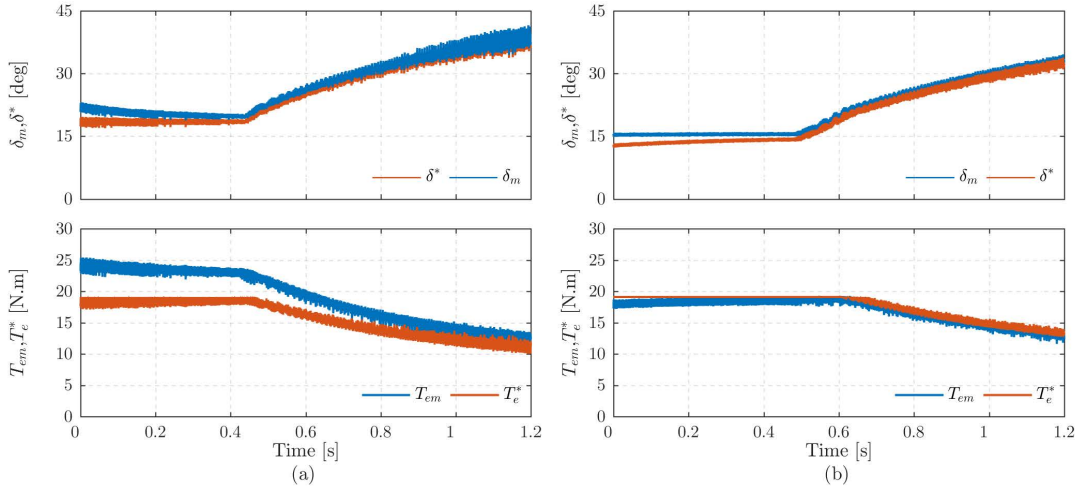

Fig. 4.15. Simulation results for the reference load angle and electromagnetic torque set by the control system (red plots) versus the corresponding motor quantities (blue plots) when the SynRM drive is accelerating with a load torque of 5 N.m and with +20 % detuning in L_d and L_q: (a) without inductance estimation (speed range: 450 to 2650 rpm); (b) with inductance estimation (speed range: 450 to 2330 rpm).

be noticed from Fig. 4.15, without inductance compensation mechanism the load angle and torque of the motor are higher than their reference values set by the control system. Once the compensation mechanism is turned on these quantities track closely their reference values. It is noteworthy to point out that there is an almost symmetric behaviour of the system with regard to positive and negative detuning of the motor apparent inductances. Moreover, the results obtained for two conditions of parameter detuning indicate the importance of the inductance estimation mechanism implemented in the control system.

Since the maximum current limitation is closely linked to the FW algorithm described before, a parameter detuning might violate this restriction if an online apparent inductance estimation mechanism is not included. For simplicity's sake, the torque equation (4.27) is presented here again

$$T_e = \frac{3}{4} p \left(\frac{1}{L_q} - \frac{1}{L_d} \right) \psi_s^2 \sin(2\delta) \,. \tag{4.44}$$

Let us consider that the detuning in the inductances is positive (L_d and L_q used by the control are higher than the actual motor inductance values) as this is the worst scenario. By looking closely to (4.44), the term inside the parenthesis is dominated by the inverse of L_q and $L_d >> L_q$, hence the error in L_q dominates the error in that term. Under these conditions, for the maximum value of the reference torque, the reference load angle given by (4.25) would be higher than the rated load angle and the actual motor torque would be

higher than the reference value set by the control system. As a result, the actual current amplitude i_s would go above the limit set by the control system (see Fig. 4.16(a)) which is the apposite of the negative detuning case, where the actual current amplitude i_s is lower than the limit set by the control system (see Fig. 4.16(b)). The overcurrent that is happening under a positive detuning can be prevented by estimating in real-time the value of L_q and use it in (4.25).

The results presented in Fig. 4.16 demonstrate that with a negative detuning of the apparent inductances, no problem arises. On the contrary, if the detuning is positive and if there is no inductance estimation feature, the maximum current set by the control system will be violated. The results shown in Fig. 4.17 demonstrate that the online inductance estimation procedure solves this issue.

It is important to mention that under the presence of a positive error in the apparent inductances, if no online inductance estimation technique is used, the control system will not be able to limit the motor stator current to the maximum value i_{max} used in (4.23). Hence, the online estimation inductance technique again plays an important role in the current limitation process. The online inductance estimation procedure is always activated in all operating conditions in both simulation and experimental results presented in subsequent subsections.

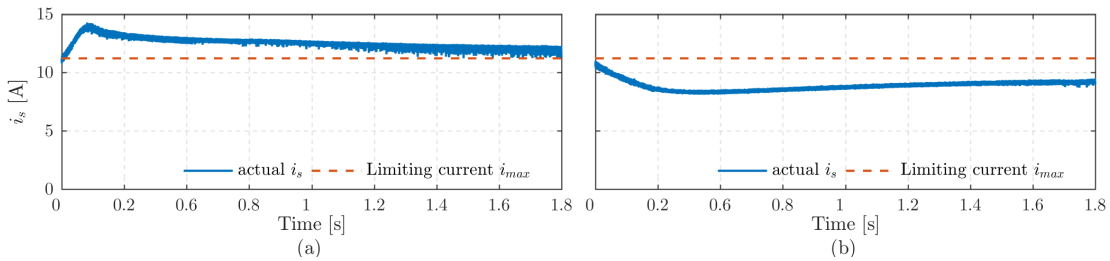

Fig. 4.16. Simulation results for the stator current behaviour when the SynRM is accelerating from 220 to 2800 rpm with a load torque of 5 N.m and without online estimation inductance feature for: (a) +20 % detuning in apparent inductance values; (b) −20 % detuning in apparent inductance values.

4.3.2 Steady-State Operation

The steady-state performance of the SynRM drive with the PLASFC strategy is here shown. Several tests, conducted at different operating conditions are presented and discussed.

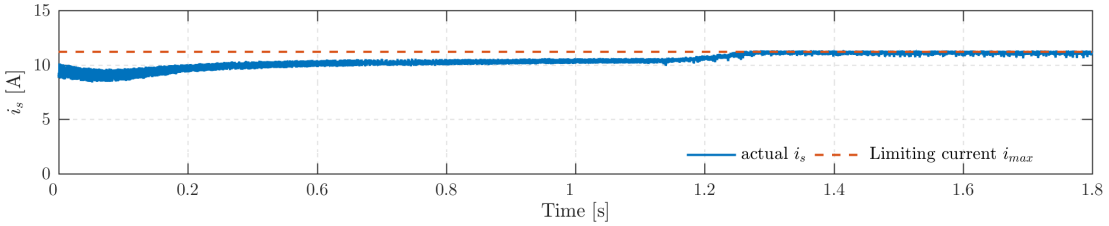

Fig. 4.17. Simulation results for the stator current behaviour with +20 % detuning in apparent inductance values and with online inductance estimation when the SynRM is accelerating from 220 to 2800 rpm with a load torque of 5 N.m.

The simulation and experimental results are plotted side by side in order to better evaluate the agreement between them.

The results obtained are presented in Fig. 4.18 – Fig. 4.20, respectively for a speed of 700 rpm and a load torque of 5 N.m, 10 N.m and 19 N.m. In these tests, the DC-link voltage is its maximum value (650 V), making the drive to operate in Region I.

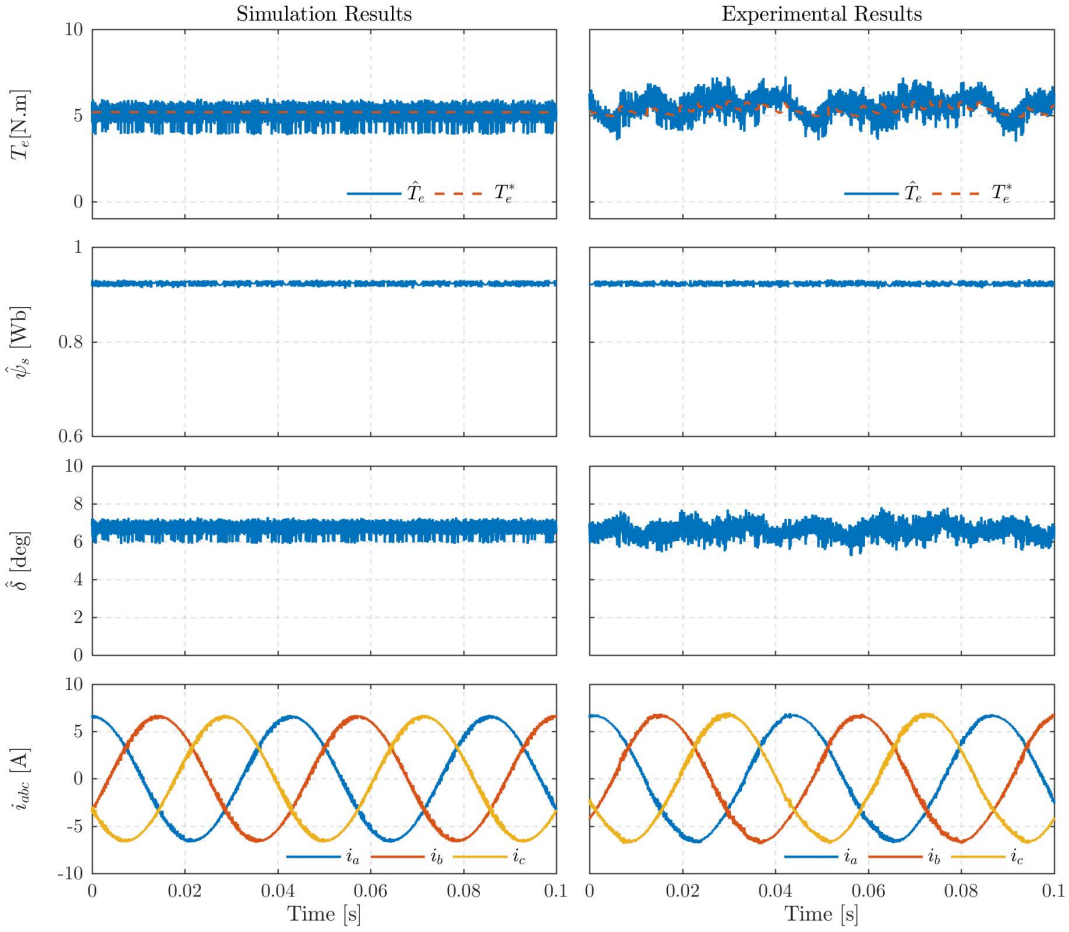

Fig. 4.18. Results for the steady-state operation of the SynRM at a speed of 700 rpm and a load of 5 N.m.

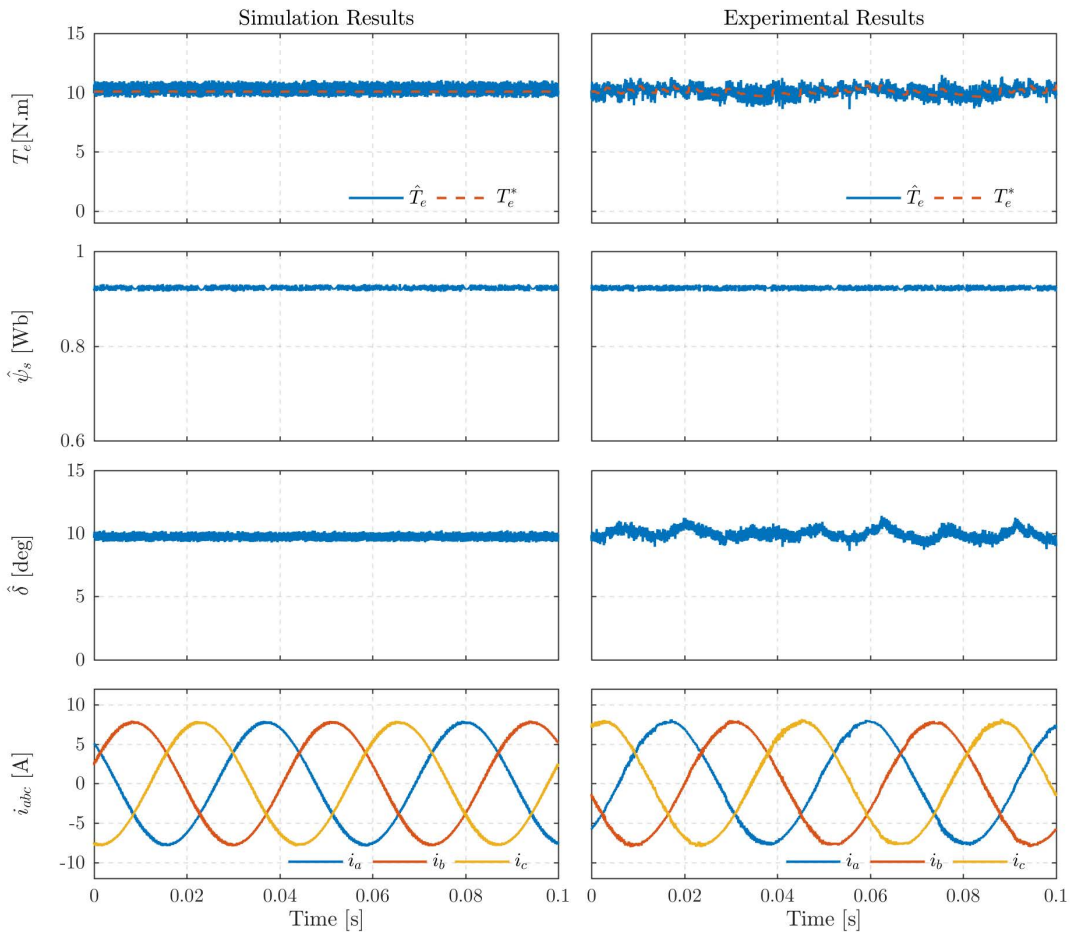

Fig. 4.19. Results for the steady-state operation of the SynRM at a speed of 700 rpm and a load of 10 N.m.

Looking to these results, a very good agreement between the simulation and experimental results is observable. At all operating conditions, the motor torque closely follows the desired reference torque with an acceptable torque ripple. The torque ripple is calculated and represented in Fig. 4.21 as a percentage of the peak torque error in relation to the average torque. It is possible to observe that the torque ripple decreases with the increase of the load torque, reaching values smaller than 10 % at rated load torque.

The estimated stator flux $\hat{\psi}_s$ in the three studied operating conditions has an expected behaviour. It tracks its reference value (0.923 Wb) and is maintained constant during the tests. The estimated load angle, $\hat{\delta}$ varies according to the load torque level applied to the motor and its ripple content decreases with the increase of the load torque. In addition, the measured phase current waveforms, i_{abc}, are observed to be sinusoidal. In order to evaluate the distortion of these currents, the THD of the phase current i_a, obtained in the experiment

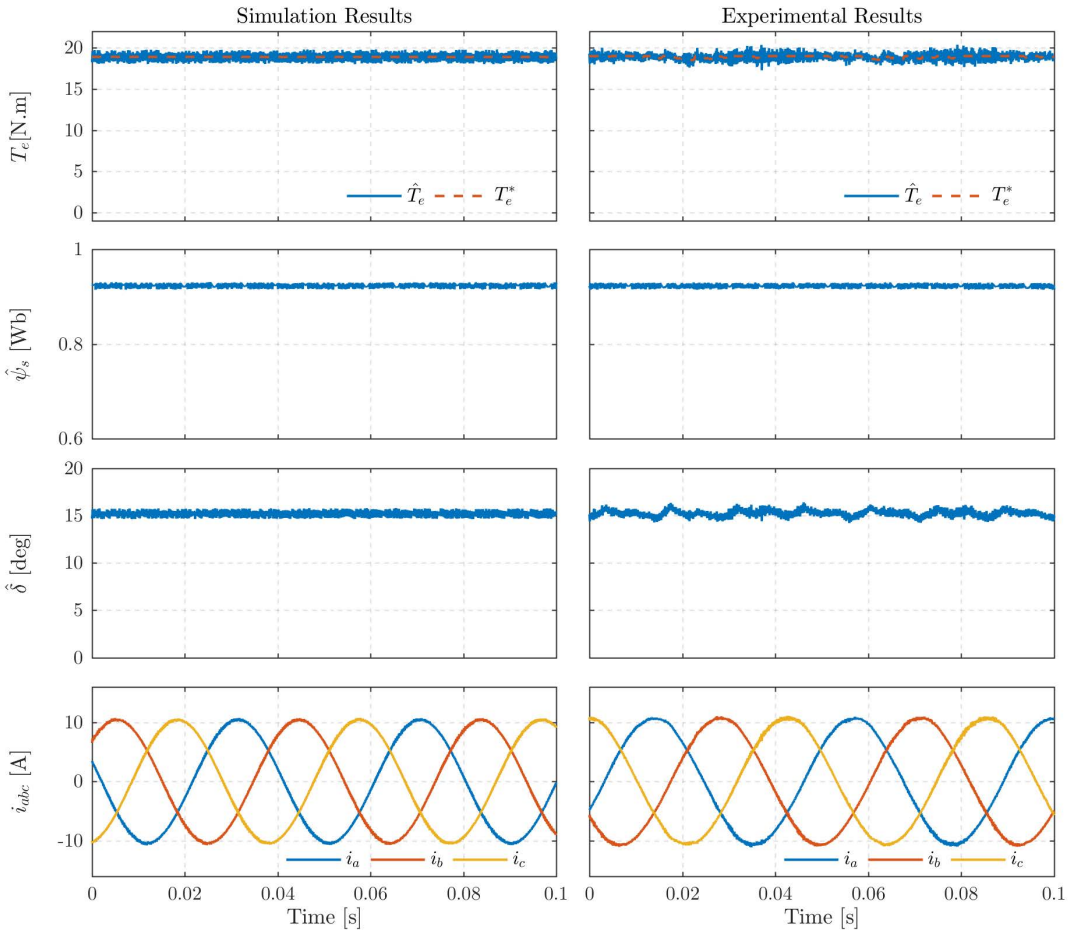

Fig. 4.20. Results for the steady-state operation of the SynRM at a speed of 700 rpm and a load of 19 N.m.

tests, was calculated and is presented in Fig. 4.22, with the SynRM operating at 700 rpm and at different load levels.

As can be seen in Fig. 4.22, the THD of the phase current i_a is less than 3.5 % and has a decreasing trend when the motor load increases up to rated load torque.

The spectra of current i_a obtained when the SynRM drive is running at 700 rpm, for different load conditions, is plotted in Fig. 4.23. It can be seen that the high frequency harmonics mostly appear around the frequency of 6 kHz for all load cases. However, as there is not a fixed switching frequency, these harmonics appear spread across a wide frequency range.

The average switching frequency variation of the inverter for different load torques and speeds is presented in Fig. 4.24. It is possible to observe that the average switching frequen-

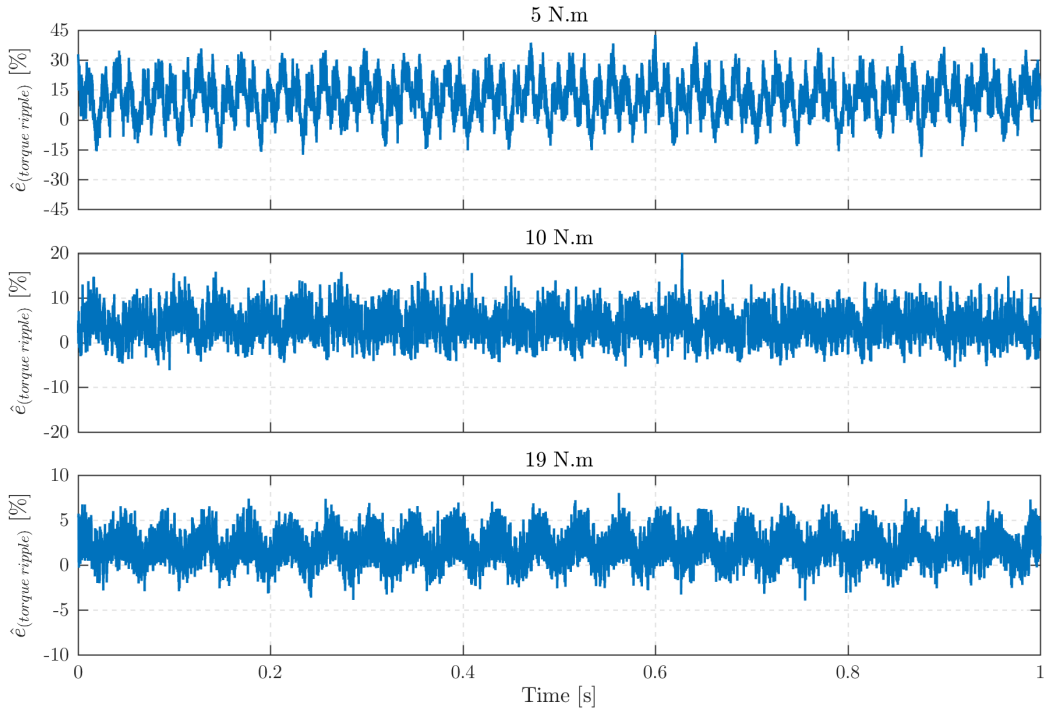

Fig. 4.21. Experimental results for the torque ripples percentage related to the results shown in Fig. 4.18 – Fig. 4.20.

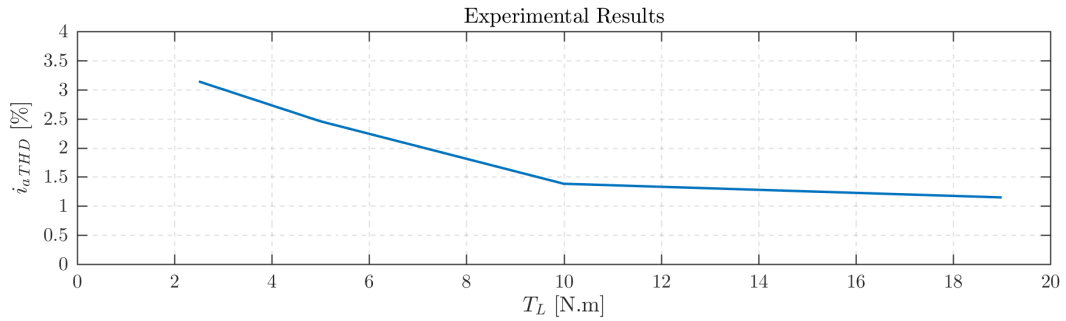

Fig. 4.22. Experimental results for the THD of phase current i_a when the SynRM is running at 700 rpm with different load torque values.

cies at load torque of 5 N.m and 10 N.m, respectively, are almost comparable and they start to slightly decrease with the increase of the speed. On the contrary, the average switching frequency at load torque of 19 N.m is lower than those ones of the other loading conditions (5 N.m and 10 N.m) and it also has a small tendency to decrease with the increase of the speed.

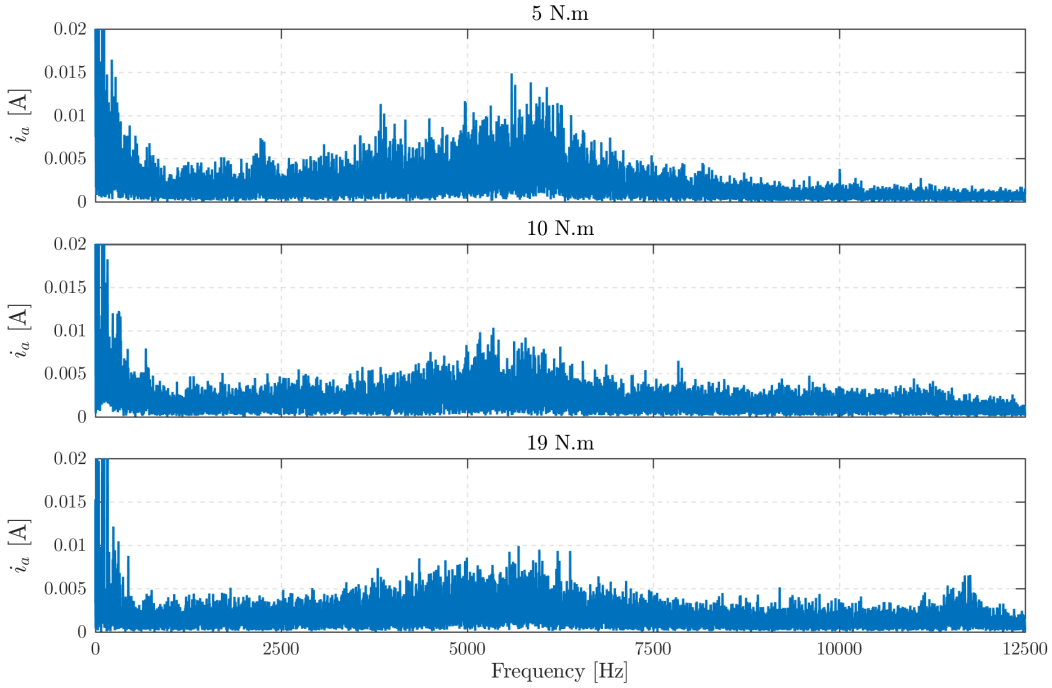

Fig. 4.23. Experimental results for the frequency spectrum of the phase stator current i_a at 700 rpm with different load torque values using the PLASFC strategy.

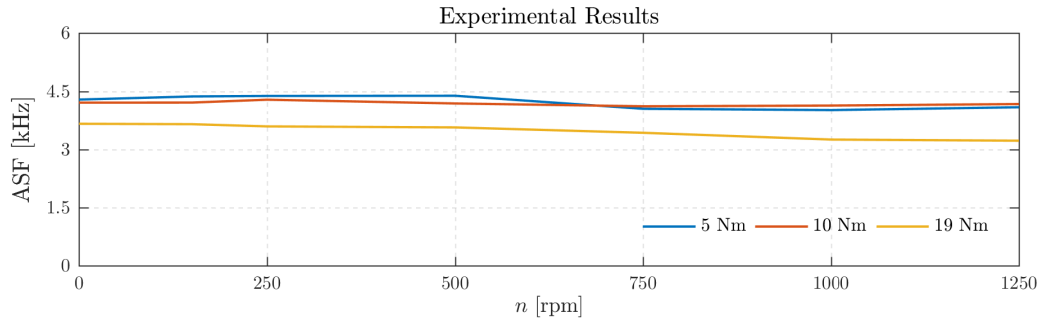

Fig. 4.24. Experimental results for the inverter average switching frequency, at different load torques and speeds.

4.3.3 Speed Reversal Test

To observe the performance of the SynRM using PLASFC in the whole speed range a speed reversal test is tested. This test was conducted with the SynRM initially running at 1300 rpm with no-load, and then imposing a reference speed of -1300 rpm at $t = 0.5$ s. The obtained results are shown in Fig. 4.25. It can be seen that the SynRM drive works well in the whole speed range. During the transient period ($0.5 \rightarrow 1.5$ s), the electromagnetic torque reaches its rated value (19.1 N.m) to achieve the fastest settling time. At $t = 1$s when the direction of rotation is reversed the polarity of the currents is changed resulting

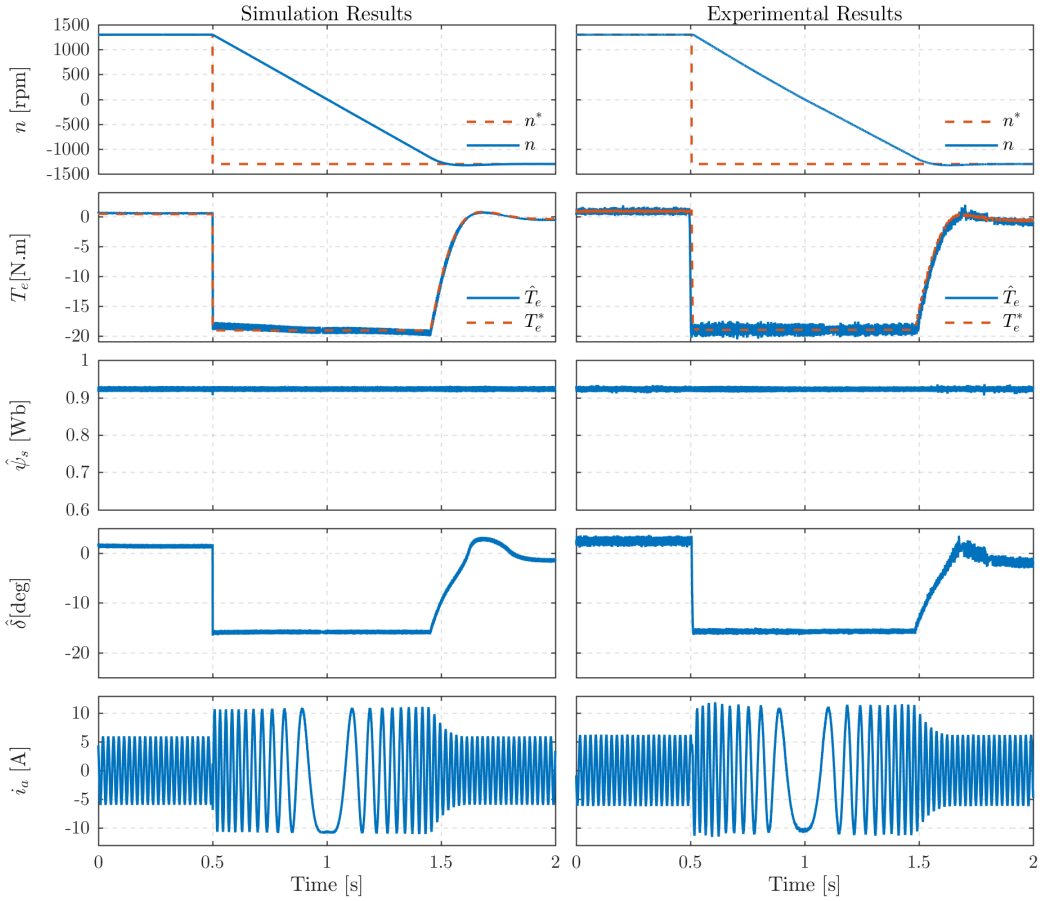

Fig. 4.25. Speed reversal test with the SynRM operating at no load. From top to bottom: rotor speed, electromagnetic torque, stator flux, load angle, and stator current waveform.

in a phase shaft of 180°. Moreover, it is possible to observe that the current limitation is respected, as the stator current amplitude is always lower than the maximum allowed value (11.2 A). Furthermore, the obtained results indicate that there is a decoupled control of the stator flux and electromagnetic torque developed by the SynRM. It is also visible that the load angle and electromagnetic torque profiles are identical, which is an expected result since the stator flux level is fixed and set to the motor rated value.

4.3.4 Torque Step Response

Fig. 4.26 illustrates the dynamic response of the drive system to a torque step, from 0 to 19.1 N.m (rated torque) with the SynRM operating at a constant speed of 700 rpm.

In this test, the SynRM drive is operated in the torque control mode, by setting manually

the value of the reference torque, while the auxiliary IM drive is operated in speed control mode in order to maintain the speed roughly constant during the test.

The results show that the estimated torque tracks very well its reference value. Furthermore, the profiles of the estimated torque and load angle are identical because the stator flux is constant and set to its rated value. In addition, during this test, the stator phase

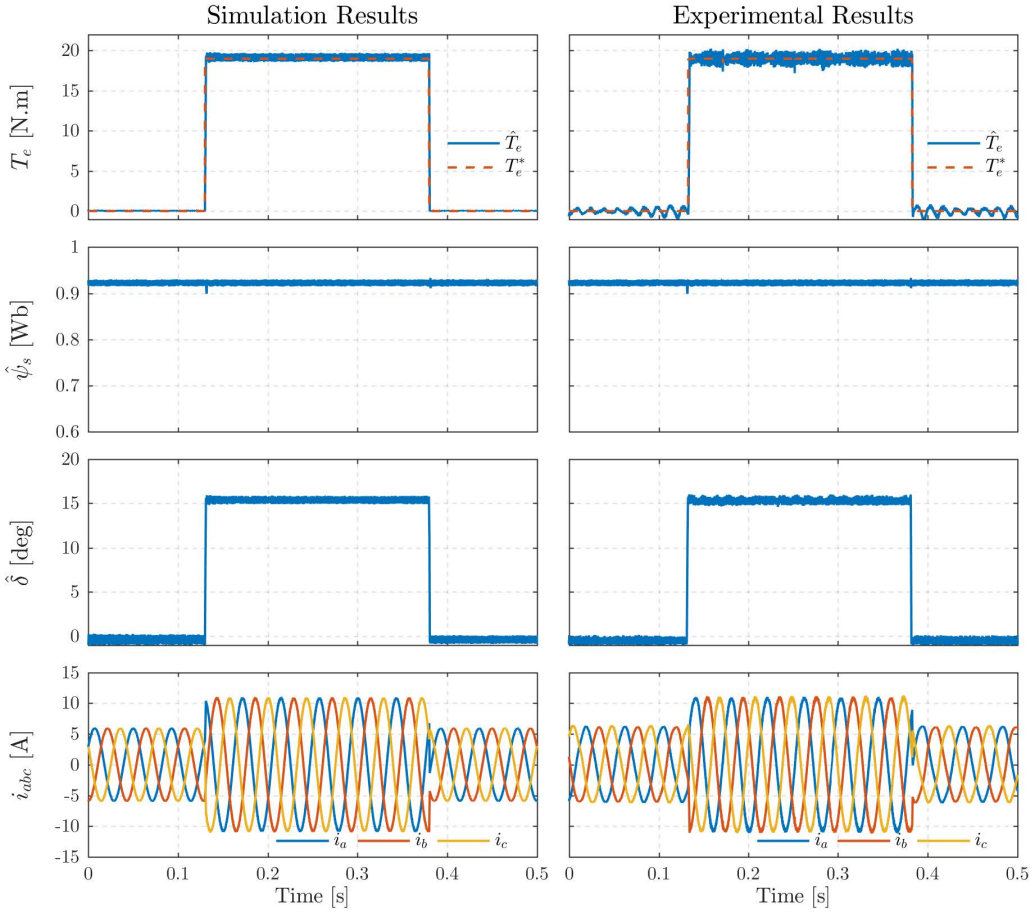

Fig. 4.26. Torque step response of the SynRM drive operating at 700 rpm.

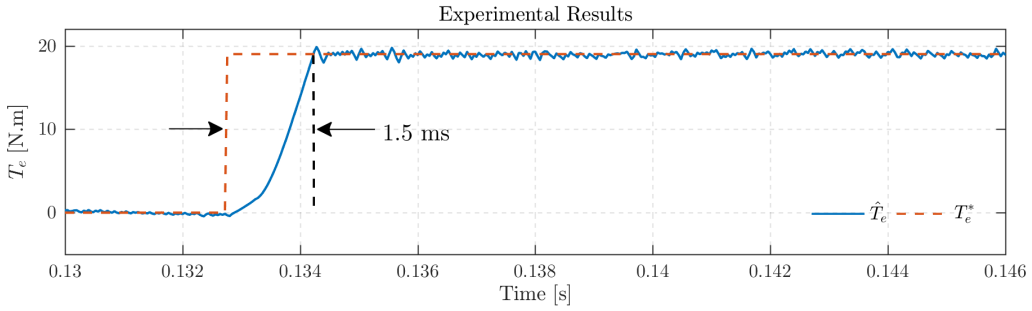

Fig. 4.27. Zoomed version of the torque step response shown in Fig. 4.26, showing the variation of the reference torque and actual motor torque in the vicinity of t =0.133 s.

currents comply with the maximum current limitation (11.2 A) in this operating region.

Fig. 4.27 shows a zoomed version of the torque step response obtained in the experiment. It can be seen from this figure that the torque response is fast, as the drive only takes approximately 1.5 ms to increase the SynRM torque from no-load to the rated value (19.1 N.m).

4.3.5 Speed Step Response

The speed step response of the PLASFC strategy with a full DC-link voltage is investigated and presented in Fig. 4.28.

Initially, the machine is started with 100 rpm and a load torque of 15 N.m, and then a step speed reference of 1280 rpm is imposed at $t = 0.5$ s.

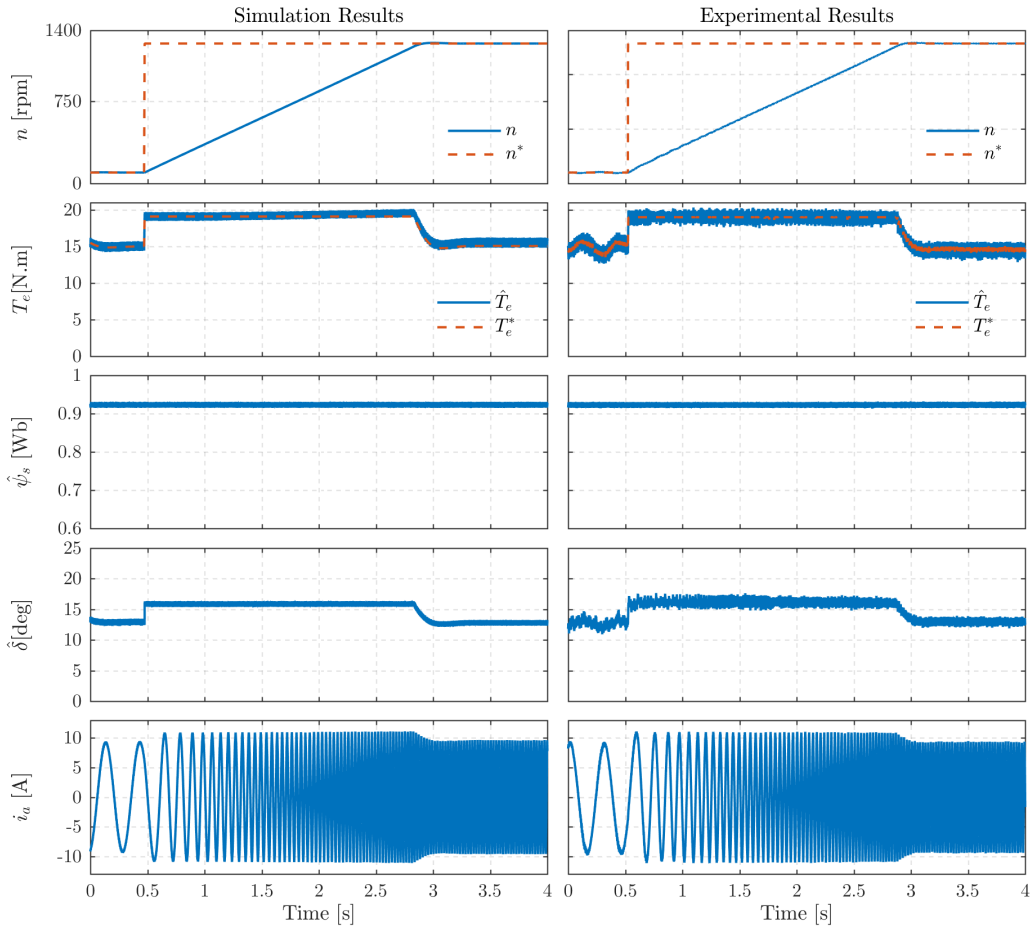

Fig. 4.28. Results for the SynRM acceleration from 100 rpm to 1280 rpm with a load torque of 15 N.m.

As can be seen, the speed tracks its reference value accurately without any significant overshoot. Moreover, the speed rise time for the PLASFC strategy is approximately 2.4 s. In the experimental results, during operating at 100 rpm, the estimated torque exhibits an oscillation of 1 N.m, which is introduced by the VSD that controls the load motor (auxiliary IM). At $t = 0.5\,\text{s}$, when the reference speed is imposed, the developed torque increases instantly to its rated value and maintains constant at this value until the end of the acceleration period. At the end of the acceleration period, the motor develops a torque of 15 N.m to satisfy the required load torque. The estimated load angle has the same profile of the torque hence same discussions as before apply. Moreover, it is possible to observe that during the acceleration period the current limitation is respected, as the stator current amplitude is always lower than the maximum value (11.2 A). Also, it can be observed that the stator flux does not present any change in the acceleration period, remaining constant, meaning that the direct and decoupled torque and stator flux control is achieved. From this test, it is evident to conclude that the SynRM is able to develop a constant rated torque in a wide speed range within Region I.

Generally speaking, the above presented results demonstrate that the excellent steady-state and dynamic responses of the proposed control system when the motor operates in the constant torque region (Region I).

4.3.6 Operation in the Field-Weakening Region

In this section, the drive is tested in the FW region,which comprises Region II and Region III, to prove the ability of the control system to impose the current and voltage limitations as well as the load angle limitation (Region III), hence demonstrating the ability of the drive to operate at very high speeds, and ensuring the stability of the drive in the full speed range.

In the test results reported in this section, the DC-link voltage is reduced to 200 V. The reduction of the DC-link voltage has been decided due to mechanical limitations, not to limitations of the control system. It is well known that the SynRM is able to operate at very high speeds with no theoretical speed limit thus the limitation for the maximum speed is purely mechanical. Thereby, lowering the DC-link voltage forces the SynRM to enter in

the FW region at a lower speed and thus it is possible to safely demonstrate the operation of the drive in the three regions.

The simulation and experimental results for the acceleration of the SynRM from 100 to 1280 rpm at no-load are illustrated in Fig. 4.29. In Region I and during the acceleration, the motor develops the rated torque (19.1 N.m) and draws rated current (11.2 A) as marked in Fig. 4.29. During this phase, the stator flux remains at its rated value (0.923 Wb). During the acceleration, the rotor speed increases and so does the required voltage to maintain the stator flux constant at its rated value. With the increase of the rotor speed, the voltage limit imposed by the inverter is finally reached and, from this point on, the stator flux has to be decreased, forcing the SynRM to enter into FW operation at 480 rpm (Region II).

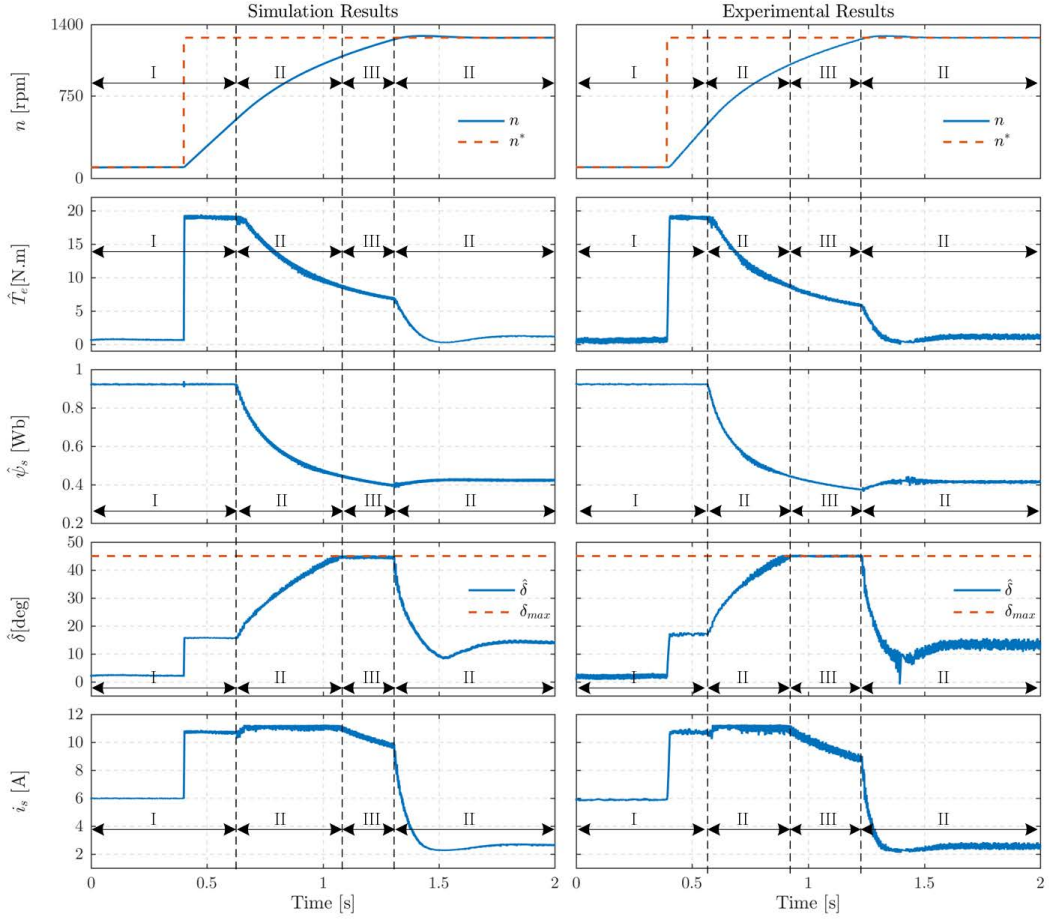

Fig. 4.29. Results for the acceleration of the SynRM from 100 rpm to 1280 rpm (no-load).

In this region, the stator flux is calculated based on the rotor speed of the SynRM and the available DC-link voltage (see (4.23)). The torque developed by the SynRM decreases

with the speed increase while the stator current is maintained nearly at its rated value and the load angle starts to increase. At a certain operating point of acceleration, specifically at a speed of 920 rpm, the load angle reaches its limit of 45°. This is the point where the MTPV limit is reached, setting the beginning of Region III. In this region, the current has to be decreased to respect the load angle limitation, leading to an accelerated reduction of the maximum torque the motor can develop at this high speed. The actual speed eventually reaches its reference value and the torque reference decreases below the MTPV limit and the drive system starts to operate again in Region II.

Fig. 4.30 shows the results obtained during an acceleration of 100 rpm to 1280 rpm with a load torque of 5 N.m. Similarly to the operation condition discussed before, the SynRM drive also operates here in all three regions, while respecting the limits of current, voltage and load angle.

The SynRM drive takes about 2.1 s to reach the speed of 1280 rpm. The transition to Region II occurs approximately at 400 rpm where the motor supply voltage is at its maximum value. Once the load angle of the SynRM reaches 45°, the SynRM switches to Region III at a speed of 940 rpm, with a stator flux of 0.45 Wb and the MTPV limit imposed. The motor operates approximately 1.2 s in this region until it reaches the desired speed and the steady-state operation. Finally, after completing the acceleration phase, the SynRM maintains the load torque of 5 N.m initially imposed on its shaft. As can be seen, the FW algorithm using the proposed predictive control strategy guarantees a stable and smooth transition between all operating regions.

Fig. 4.31(a) and (b) depict the estimated stator flux components, for the acceleration of the SynRM from 100 rpm to 1280 rpm with a load torque of 5 N.m. As expected, these two components have all the time a sinusoidal waveform shape with a phase shift of 90° between them. Furthermore, the polar plot of the estimated stator flux during the acceleration period is presented in Fig. 4.31(c). The radius of this polar plot is inversely proportional to the motor speed. In other words, the polar plot starts to decrease in size and approaches the centre with the increase of the speed.

Fig. 4.32 shows a speed reversal from -1280 to 1280 rpm, at no-load. As can be seen, the

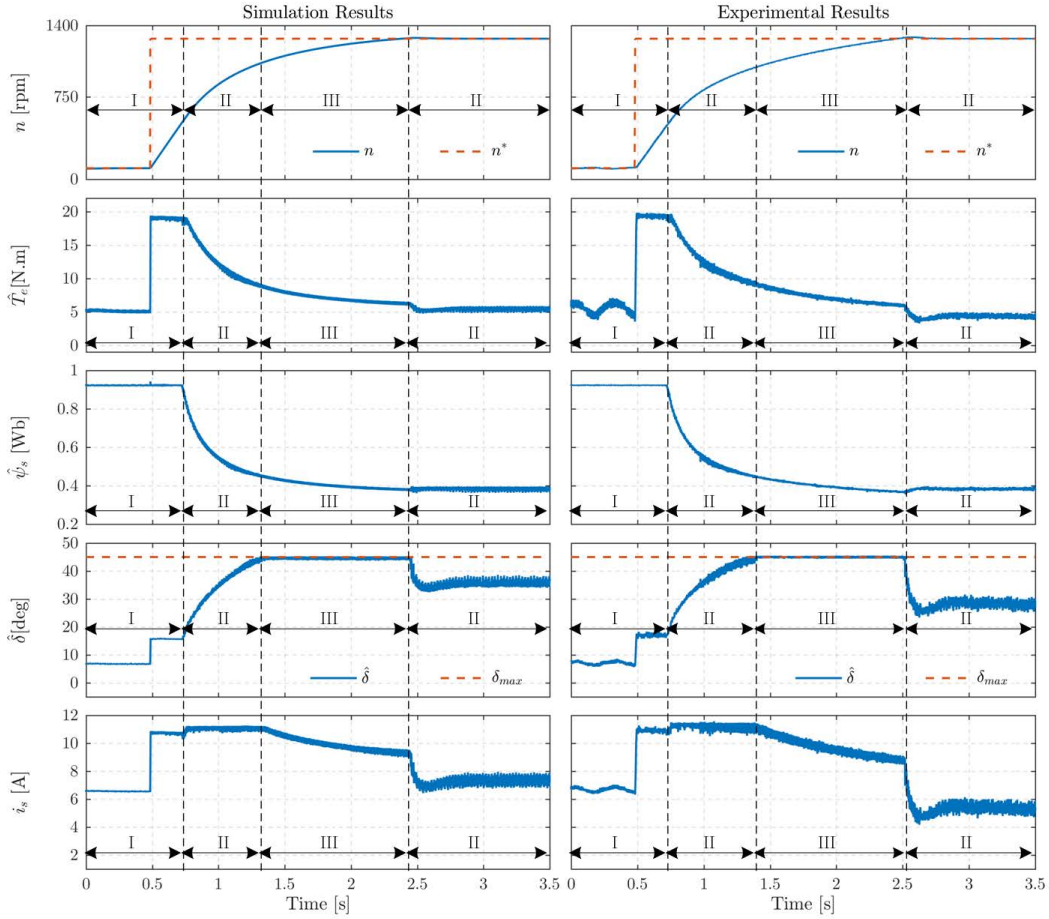

Fig. 4.30. Results for an acceleration of the SynRM from 100 rpm to 1280 rpm, with a load torque of 5 N.m.

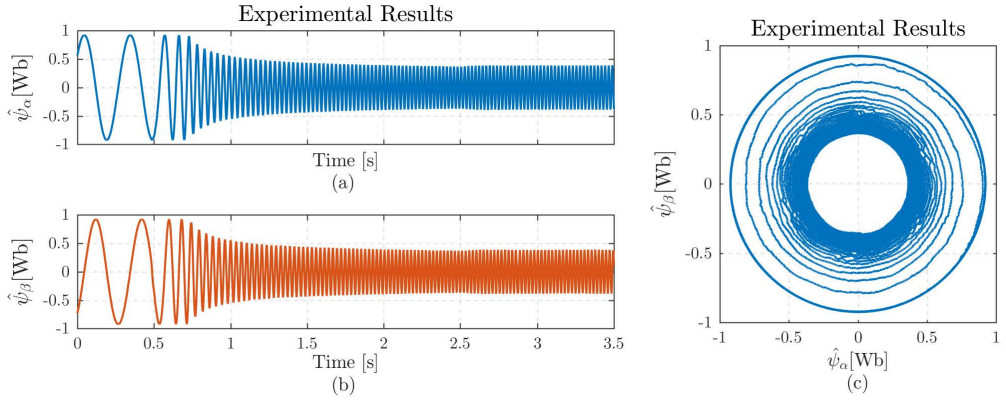

Fig. 4.31. Results for the acceleration of the SynRM from 100 rpm to 1280 rpm, with a load torque of 5 N.m : (a) $\hat{\psi}_\alpha$ component of the estimated stator flux; (b) $\hat{\psi}_\beta$ component of the estimated stator flux; (c) polar plot of the estimated stator flux.

motor current is well limited at the maximum allowed value of 11.2 A. The same thing can be noticed for the load angle as it is being limited at 45° with the activation of the MTPV limit in Region III. Moreover, and as expected, the deceleration or braking mode of the

SynRM is faster than the acceleration phase. The motor takes approximately 0.5 s to brake (from -1280 rpm to zero) and 0.9 s to accelerate (from zero to 1280 rpm). It is also observed that the variation of the stator flux is stronger during the deceleration phase of the SynRM. The reason is that during the deceleration phase, until the SynRM has reached zero speed, the SynRM operates in generating mode. Because of this, the DC-link voltage rises up to almost 500 V, which results in increasing the u_{max} term that appears in the expression of the reference stator flux calculation (see (4.23)). When the speed becomes positive, the DC-link voltage drops since the SynRM operates again as a motor (see Fig. 4.33). Finally the estimated load angle increases very fast during the initial braking phase, since the developed torque by the SynRM increases in the same manner. In addition, the same behaviour can also be observed in the stator current.

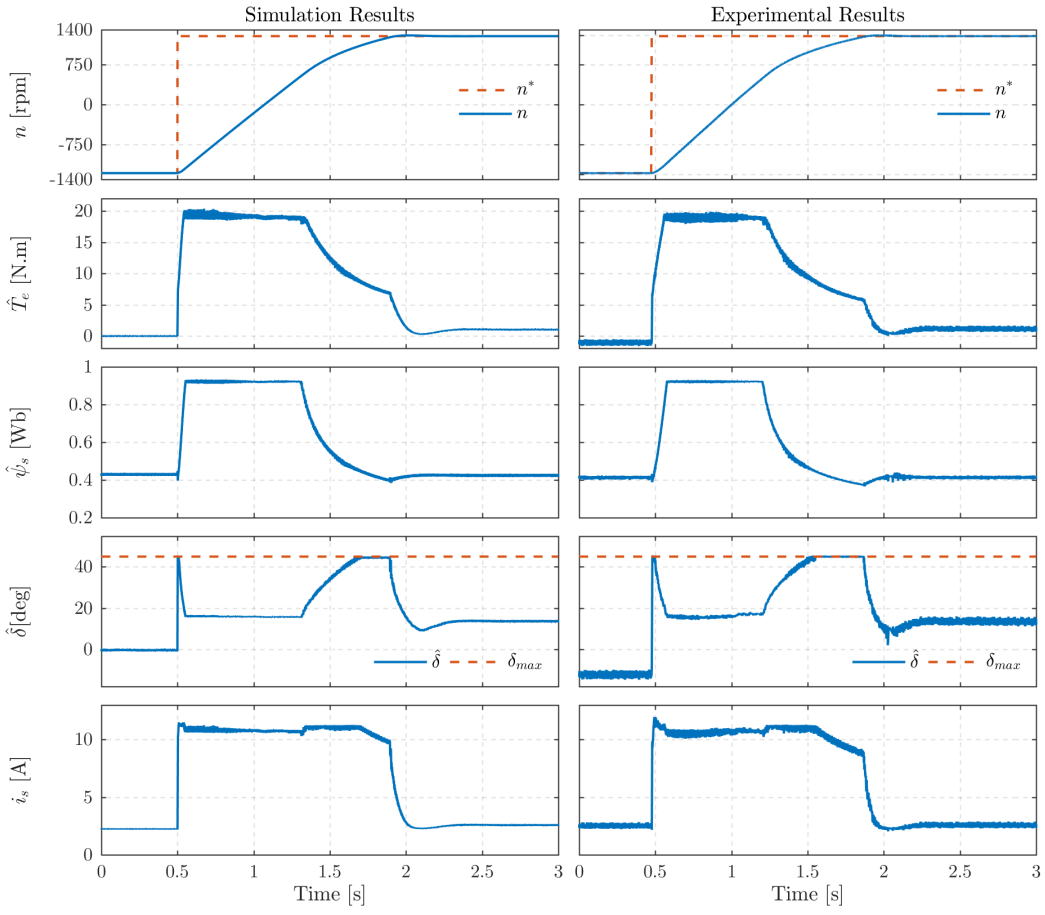

Fig. 4.32. Results for speed reversal of the SynRM from -1280 to 1280 rpm without load torque.

The DFVC strategy shown in Fig. 4.3 was also implemented in the laboratory using the

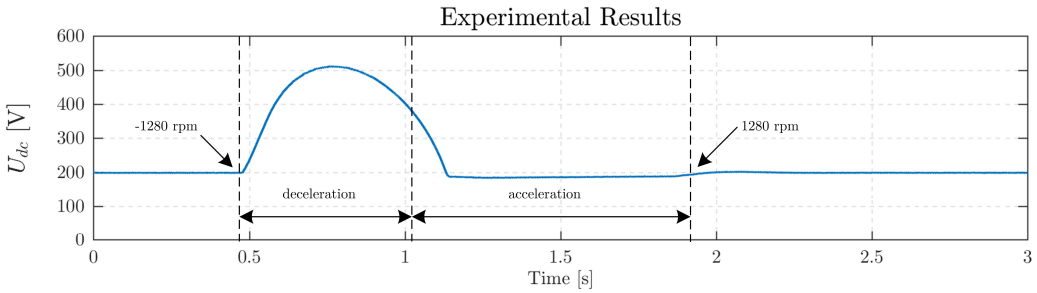

Fig. 4.33. Variation of the DC-link voltage during the speed reversal of the SynRM from -1280 to 1280 rpm at no-load.

same test bench for the purpose of comparison in the FW region. This control strategy has three PI controllers, in which six parameters need to be tuned. These parameters and other ones, regarding its implementation, are presented in Appendix C. As it was stated in the literature review, this type of control is also preferable to operate the drive system at very high speeds. For this reason, in Fig. 4.34, the results for the acceleration of the SynRM from 100 rpm to 1280 rpm with a load torque of 5 N.m using the PLASFC strategy are presented and compared with the ones obtained with the DFVC strategy. As can be seen, the speed response of the DFVC strategy is obviously slower than that one obtained with the proposed control strategy. This is because the presence of the PI controllers and modulator generate system delays. The settling time that the DFVC strategy takes to reach the desired speed is 3.2 s whereas it is 1.8 s for the PLASFC. A different setting or tuning of the PI controllers, in particular the one for i_q, could produce a better response at the expense of worse behaviour in other situations. This is to say that the PI controller parameters of i_q in this control strategy would need to be adaptive according to the operating point of the drive to reproduce the same response of the PLASFC strategy. Moreover, the obtained experimental results using the DFVC strategy clearly illustrate that the transitions between the different regions have not been achieved as smoothly as with the PLASFC strategy. It is visible to see a drop in the stator current amplitude curve in the vicinity of the base speed. The cause of this phenomenon is linked to the sensitivity of this control strategy to the variation of the motor inductances. It can be inferred from this comparison that the PLASFC strategy retains the advantages of the direct flux and torque controller with ease of FW operating capability and good quality of the speed and torque dynamics.

With respect to the MTPV limit exploitation, which is needed to operate the drive system

in Region III, the PLASFC strategy shows superiority over the DFVC strategy due to the direct and explicit prediction of the load angle. In addition, it does not require a high tuning effort, being preferred in practice due to its easy commissioning.

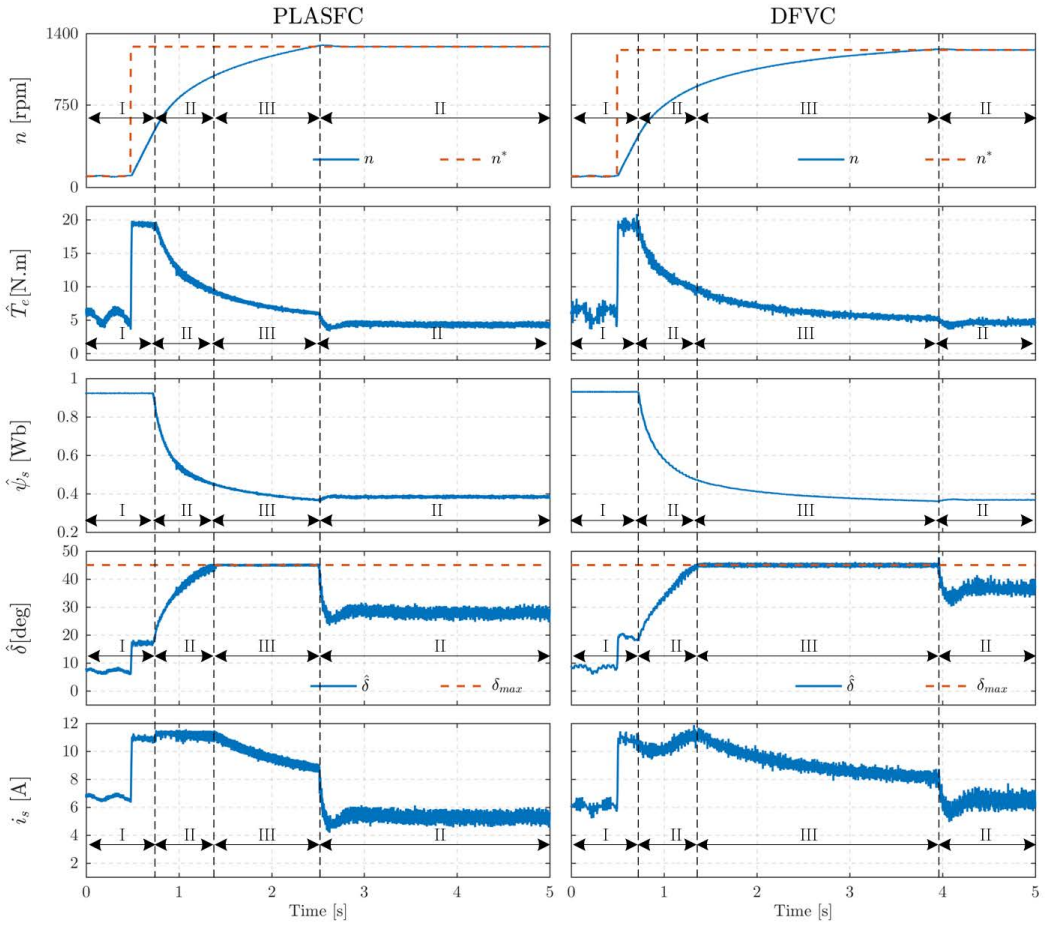

Fig. 4.34. Experimental results for the acceleration of the SynRM from 100 rpm to 1280 rpm with a load torque of 5 N.m using two control strategies: (a) PLASFC; (b) DFVC.

As it was stated earlier, the decision of lowering the DC-link voltage in the experiments has been taken due to the mechanical restriction of the experimental setup and not due to a control limitation. In the experimental setup, the studied SynRM , whose rated speed is 1500 rpm and maximum speed is 2100 rpm, is coupled mechanically to an IM whose synchronous speed is also 1500 rpm. Hence, if the drive system was operated at full DC-link voltage and respecting the mechanical limitations of the motors, the SynRM would never reach the third region of operation, namely Region III.

Several simulation tests have been performed to operate the SynRM with the proposed

control system at a very high speeds and with full DC-link voltage. In view of the adopted control structure, as long as the stator flux level is not too low, the drive operates without any problems as can be seen in the simulation results presented in Fig. 4.35, which reports an acceleration test up to 13590 rpm. In this test, to shorten the acceleration period, a negative load torque of -10 N.m until 2.9 s is applied while the inertia of the motor has been decreased to one third of its rated value. It is easy to see that the SynRM drive operates properly in the full speed range. There is only a slight increase of the ripple in the load angle at very high speeds mainly due to the low value of stator flux at which the motor operates at those speeds.

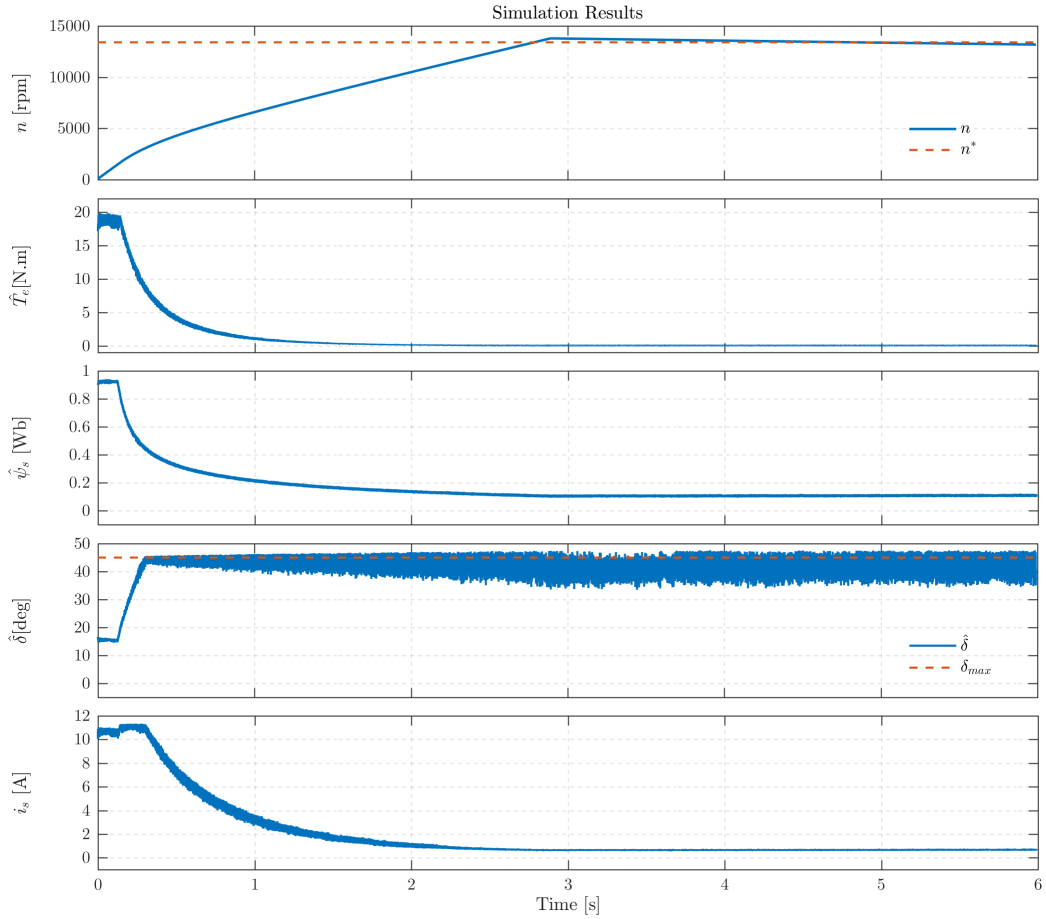

Fig. 4.35. Simulated response to an 13950 rpm speed reference step. From top to bottom: measured and reference speed, estimated load torque, estimated stator flux, estimated load angle and its maximum value, and stator current amplitude.

On the whole, the simulation and experimental results presented in this section demonstrate that the PLASFC strategy proposed for SynRM drives is capable of controlling the SynRM in the high speed range with and without load torque. Moreover, this control stra-

tegy ensures very stable and smooth transitions from Region I to Region II and from Region II to Region III, without the need of any elaborated controller tuning process. Additionally, the voltage and current limits are fully exploited by limiting the stator flux and torque references with simple control laws, while the MTPV limit is handily exploited due to the explicit prediction of the load angle and thus confirming the feasibility of the control strategy for SynRMs.

4.3.7 Operation with an Optimized Stator Flux Level

In the simulation and experimental results previously presented, the stator flux reference was set with the rated value. Thus, a faster torque response is achieved. However, if the system efficiency is more important, the stator flux can be adjusted using the loss minimization algorithm described before. The aim of this algorithm is to minimise the SynRM copper losses, at a given load torque, in the constant torque region i.e. below base speed, consequently maximizing the overall system efficiency. For a given torque demand, the loss minimization algorithm requires the minimum amount of current to produce that torque, thus reducing the motor copper losses.

Since the FW operation is one of the major merits of the proposed PLASFC strategy, the transition between Region I, where the loss minimization algorithm is turned on, and FW regions (Region II and III) should be smooth. Therefore, to ensure a smooth transition, the reference flux calculated in FW regions using (4.21) is compared with stator flux obtained from the loss minimization algorithm and the minimum of these two is selected as the stator flux reference to be fed to the control system.

The main idea underlying the loss minimization algorithm is to identify an optimal stator flux at a given load torque. Thus, there is always a correlation between the torque and stator flux. In other words, the zero torque corresponds to a zero stator flux amplitude. However, the zero stator flux situation would lead to the cancellation of the machine back-EMF, thus affecting the stator flux estimation. Therefore, a minimum excitation stator flux must be

guaranteed for the sake of stator flux estimation improvement around zero load torque. The minimum excitation level is set here to 0.25 Wb as this value guarantees a good stator flux estimating over the whole speed range.

To demonstrate the increase of the SynRM efficiency when it operates with an optimal stator flux level, thus minimizing the stator copper losses for a given torque demand, some experimental tests are conducted in both transient and steady-state regimes. In this section, the SynRM efficiency is calculated in the experiment, at different torque references, with the aid of the torque sensor and the precision power analyzer shown in Appendix B.

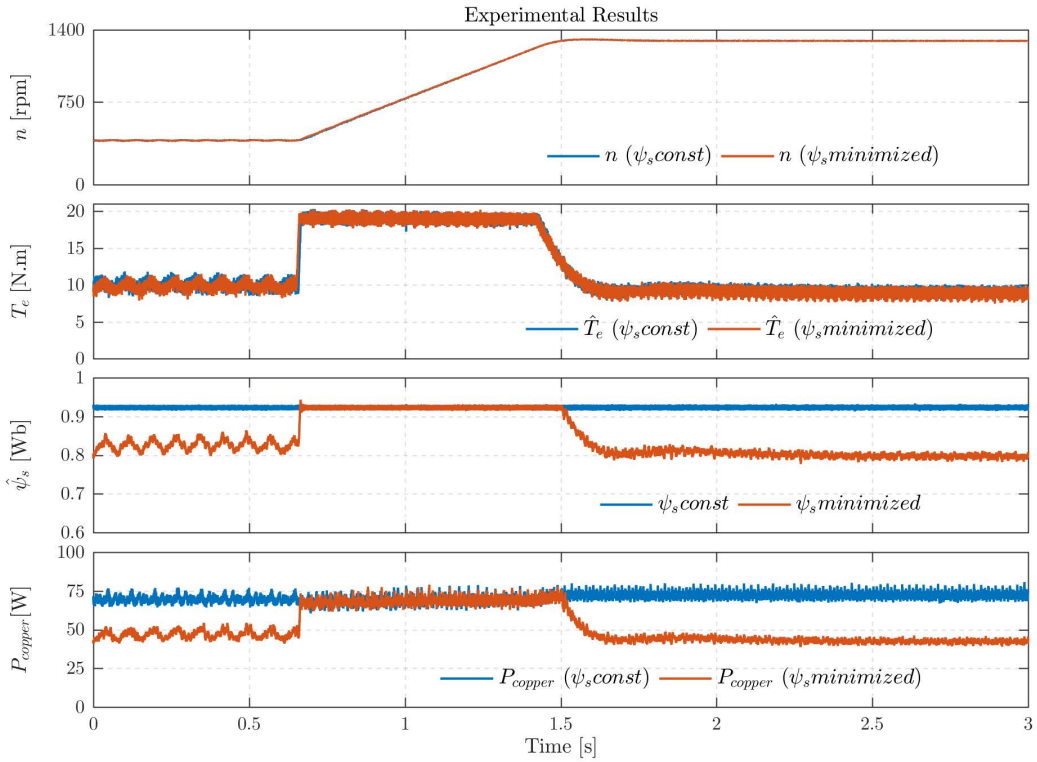

Fig. 4.36. Results for a speed transition from 400 rpm to 1300 rpm with a constant load of 10 N.m for constant stator flux and for minimized stator flux. From top to bottom: rotor speed, electromagnetic torque, stator flux, and copper losses.

Fig. 4.36 shows the experimental results for the acceleration of the SynRM from 400 rpm to 1300 rpm at 52 % of rated torque with and without loss minimization. The results are obtained considering the full DC-link voltage and thus the drive system still operates in the constant torque region (Region I). In Fig. 4.36, it is possible to observe that the speed response is identical in the two situations, and the speed rise time is fast being approximately 0.7 s. Moreover, even with the loss minimization strategy, the torque dynamic response is

fast and equivalent to the one obtained with a constant stator flux. In addition, once the loss minimization algorithm is used, the stator flux reference reduces according to the load torque level. When the reference speed is increased, the machine needs to develop torque and in this case, the loss minimization algorithm sets the stator flux at its rated value, As soon as the machine reaches the reference speed, the need for torque decreases to 10 N.m (to maintain the load) and the algorithm calculates the new stator flux reference. This causes a drop in the copper losses of the machine as shown in Fig. 4.36. With the loss minimization algorithm it is possible to decrease the losses from 75 W to 40 W, which corresponds to a decrease of 53 % in the copper losses.

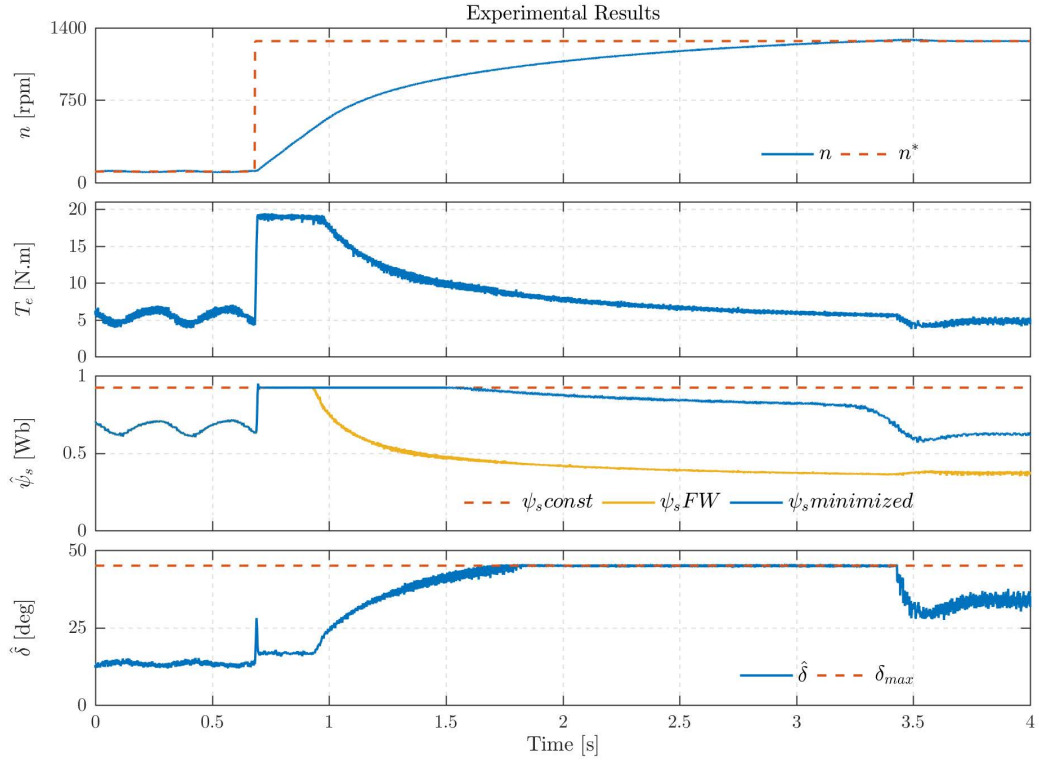

Fig. 4.37. Results for a speed transition from 100 rpm to 1280 rpm with a load of 5 N.m and loss minimization turned on.

Fig. 4.37 shows the results for the speed transition from 100 rpm to 1280 rpm with a load torque of 5 N.m and 200 V of DC-link voltage. These results present the behaviour of the drive system in all operating regions with the loss minimization algorithm turned on. As can be seen, the loss minimization algorithm in Region I calculates the value of the stator flux reference corresponding to 5 N.m of load torque. However, when the reference speed is increased, the machine needs to develop torque and thus the loss minimization algorithm

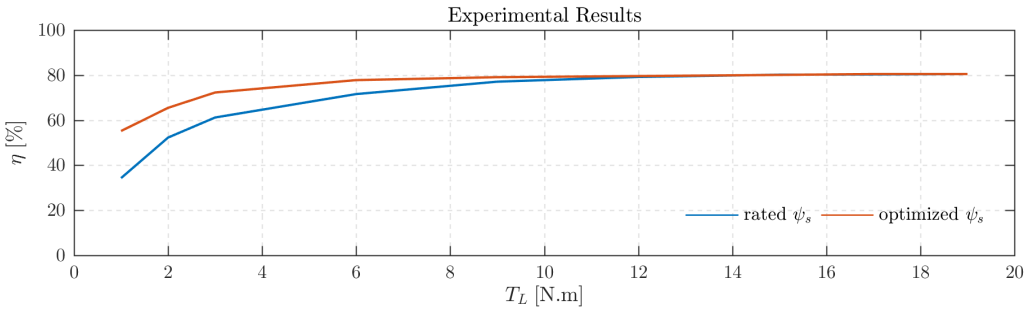

Fig. 4.38. SynRM efficiency with and without stator flux level optimization (SynRM running at 700 rpm).

sets the stator flux to its rated value. As soon as the machine enters into the FW region, the comparison between the two stator flux values obtained from the FW equation and from the loss minimization algorithm, respectively, must be done. As it is observed, the stator flux calculated based on the FW equation has a smaller value compared to the one generated using the loss minimization algorithm. Thereby, in Regions II and III, the stator flux obtained from the FW equation is selected and fed to the control system. Based on this test, one can see that the transition between Region I and Region II is seamless and the machine continues to track the desired speed correctly. Once this desired speed is attained, the need for torque decreases to 5 N.m (to maintain the load) and the motor remains running in Region II.

To measure the efficiency of the drive system in steady-state, the power analyzer and torque sensor were used to accomplish this task. It is good to mention herein that the efficiency measurement has been performed in the speed range below the base speed (Region I), with a full DC-link voltage, and at different load torque values.

Fig. 4.38 shows the efficiency for the SynRM operation with a constant value for the reference stator flux and using the loss minimization algorithm. This test has been conducted by maintaining a constant speed of 700 rpm while the load torque was varied between zero and the rated value. As can be seen, with a constant stator flux the maximum efficiency is only achieved when the load torque is close to the rated value. On the contrary, using loss minimization algorithm it is possible to reach the maximum efficiency with smaller values of the load torque (above 7 N.m). Below this value, the efficiency drops because it is necessary to maintain a minimum value for the stator flux reference in order to ensure a

good estimation of the stator flux that feeds the control system as mentioned before.

Finally, the execution time of the PLASFC strategy is measured and compared with the traditional FCS-MPC approach. It is important to mention that in the traditional FCS-MPC approach, the stator flux and load angle are chosen as control variables in the cost function. Thus, the weighting factor is required to handle the relation between these control variables. The execution time of the PLASFC and the traditional FCS-MPC approach is measured with the aid of the dSPACE platform, the savings in computation time with the PLASFC are around $3\,\mu$s using a 2L-VSI. Of course, if the motor was fed by a multilevel converter or by a matrix converter, the savings in terms of computation time would be higher.

4.4 Conclusion

In this chapter, the PLASFC strategy to improve the operation of the SynRM in the full speed range was presented. The inclusion of the FW algorithm in the PLASFC strategy was described in detail and the more attractive features of this control algorithm were highlighted. The robustness of the proposed control strategy against parameters mismatch was tested. The simulation results have shown the importance of the online estimation, especially for the case of a positive detuning of the apparent inductance values.

The simulation and experimental results confirm that the PLASFC strategy regulates with precision the load angle (torque) and the stator flux in all operating regions. In Region I, the proposed control strategy works very well both in steady-state and in transient conditions. In addition, the control system has a very fast dynamic response because of the absence of inner current controllers or modulators. In the FW region, the test results have demonstrated that the PLASFC strategy ensures very stable and seamless transitions from Region I to Region II and from Region II to Region III, without the need of any elaborated controller tuning process. The proposed control scheme satisfies effectively the limitations of current, voltage, and load angle. The MTPV limit is easily exploited due to the explicit prediction of the load angle.

Moreover, the comparison with the DFVC strategy has been conducted, demonstrating

that the proposed control strategy has a better performance. Finally, a loss minimization algorithm was incorporated into the PLASFC strategy for the purpose of minimizing the motor copper losses when operating at low load levels. The experimental tests show that using the loss minimization algorithm, it is possible to guarantee a significant improvement of the motor efficiency in the constant torque region.

5

Conclusions and Future Work

5.1 Conclusions

This thesis deals with FCS-MPC strategies able to operate successfully the SynRM drive in the full speed range. FCS-MPC was selected to control the SynRM drive due to its advantages: excellent dynamic response, ease of implementation and flexibility in the definition of control objectives. However, it presents two main drawbacks such as high computational cost and non-trivial weighting factor tuning. In this context, and in order to solve these limitations of FCS-MPC, two control strategies were developed, namely, predictive active flux and torque control (PAFTC) and simplified PAFTC (S-PAFTC). For the purpose of obtaining a good performance with these strategies, a mathematical model of the SynRM considering saturation and cross-saturation effects was used. The two control strategies mentioned above were evaluated through several simulation and experimental tests, in order to identify the merits and demerits of each one. As far as the dynamic performance is concerned, the PAFTC and the S-PAFTC lead to a comparable and small settling time of torque, as concluded from the analysis of the torque step response tests. Furthermore, it was observed that both control strategies deliver almost identical performance in terms of steady-state performance such as current and torque ripples. A decreasing trend of current and torque ripples was observed with an increase of the load torque for both control strategies. Nonetheless, the S-PAFTC strategy has several advantages over the PAFTC, due to the following aspects: (i) the cost function does not have weighting factors to be tuned because it considers the error between the equivalent reference voltage and the available voltage vectors generated by the 2L-VSI; (ii) the prediction stage of the S-PAFTC strategy

is simplified as all predictions were replaced by the calculation of the equivalent reference voltages, being this done only once per sampling period. Therefore, this leads to a lower computational cost in comparison with the PAFTC strategy. A saving of 5 μs was found in the computation time, while obtaining a performance identical to that of the PAFTC strategy.

To operate effectively the SynRM drive in the full speed range, a third control strategy, predictive load angle and stator flux control (PLASFC), was developed in the stator flux reference frame. The PLASFC was examined and tested successfully, through several simulation and experimental tests. The conclusions drawn from these tests prove that this control strategy is robust, reliable, stable and safe. In general, the experimental results have shown a good agreement with the ones obtained by simulation.

As a whole, the control strategy retains the advantages of direct flux and load angle (torque) control. The transitions between the different motor operating regions are straightforward and smooth, ensuring at the same time a good torque dynamics. Besides, the MTPV limit is easily exploited due to the explicit prediction of the load angle. In addition, a state-of-the-art control technique like DFVC has been considered for the sake of performance comparison in the FW region. The experimental results have verified that the PLASFC strategy preserves the advantages of direct flux and torque controllers, with ease of FW operation capability and good quality of torque dynamics.

A loss minimization algorithm was developed and incorporated into the PLASFC with the purpose of minimizing the motor copper losses in Region I. The experimental results have shown that the motor efficiency was increased for low torque values, when the stator copper losses represent a high percentage of the motor input power.

The robustness of the PLASFC strategy against parameters mismatch was also investigated. The obtained results demonstrate that detuned values of the self-incremental inductances have a small influence on the prediction error of currents i_d and i_q. On the other hand, the detuned apparent inductance values affect severely the steady-state performance of the control system. Therefore, an online estimation mechanism of the apparent inductances has been developed to overcome this problem. The proposed online estimation mechanism allows

to operate satisfactorily the drive system in the full speed range, thus increasing significantly the robustness of the control system to parameter uncertainties.

In general, the PLASFC strategy possesses several advantages compared to conventional control schemes: no PI controller calibration is needed, it uses a simple cost function without the inclusion of weighting factors, it has a good robustness against parameter mismatch and it reduces the computational cost required in the implementation of the prediction stage of the control algorithm. In view of these features, this control strategy can be applied in applications requiring a high control performance in a wide speed range, such as electric vehicles and public transportation.

5.2 Future Work

The following future research works are suggested as an extension to the research work carried out along this thesis.

- Development of a mechanism for the estimation of the SynRM incremental inductances using for example a recursive least squares (RLS) algorithm or other estimation techniques, in conjunction with the PLASFC strategy.
- Elimination of the speed sensor (encoder) and modify the PLASFC strategy in order to obtain an encoderless control system.
- Study the PLASFC for SynRM drives with a fixed switching frequency. The control scheme calculates the voltage components that are required to reach the desired stator flux and load angle values after a sampling period, and a SVM modulator would translate these desired voltages (after subsequent transformation to alpha-beta components) into the inverter.
- Develop a stator resistance estimation algorithm to be incorporated into the PLASFC strategy.

Bibliography

[1] B. L. Mbula and S. P. D. Chowdhury, "Performance improvement of synchronous reluctance motors: A review," in *IEEE PES PowerAfrica*, Jun. 2017, pp. 402–406.

[2] J. K. Kostko, "Polyphase reaction synchronous motors," *Journal of the American Institute of Electrical Engineers*, vol. 42, no. 11, pp. 1162–1168, 1923.

[3] T. Matsuo and T. A. Lipo, "Rotor design optimization of synchronous reluctance machine," *IEEE Transactions on Energy Conversion*, vol. 9, no. 2, pp. 359–365, 1994.

[4] R. E. Betz, "Theoretical aspects of control of synchronous reluctance machines," *IEE Proceedings B - Electric Power Applications*, vol. 139, no. 4, pp. 355–364, Jul. 1992.

[5] J. Kolehmainen, "Synchronous Reluctance Motor With Form Blocked Rotor," *IEEE Transactions on Energy Conversion*, vol. 25, no. 2, pp. 450–456, Jun. 2010.

[6] D. A. Staton, T. J. E. Miller, and S. E. Wood, "Maximising the saliency ratio of the synchronous reluctance motor," *IEE Proceedings B - Electric Power Applications*, vol. 140, no. 4, pp. 249–259, Jul. 1993.

[7] P. J. Lawrenson and S. K. Gupta, "Developments in the performance and theory of segmental-rotor reluctance motors," *Proceedings of the Institution of Electrical Engineers*, vol. 114, no. 5, pp. 645–653, May 1967.

[8] A. J. O. Cruickshank, A. F. Anderson, and R. W. Menzies, "Theory and performance of reluctance motors with axially laminated anisotropic rotors," *Proceedings of the Institution of Electrical Engineers*, vol. 118, no. 7, pp. 887–894, Jul. 1971.

[9] I. Boldea, Z. X. Fu, and S. A. Nasar, "Performance evaluation of axially-laminated anisotropic (ALA) rotor reluctance synchronous motors," *IEEE Transactions on Industry Applications*, vol. 30, no. 4, pp. 977–985, Jul. 1994.

[10] S. Cai, J. Shen, H. Hao, and M. Jin, "Design methods of transversally laminated synchronous reluctance machines," *CES Transactions on Electrical Machines and Systems*, vol. 1, no. 2, pp. 164–173, 2017.

[11] T. J. E. Miller, A. Hutton, C. Cossar, and D. A. Staton, "Design of a synchronous reluctance motor drive," *IEEE Transactions on Industry Applications*, vol. 27, no. 4, pp. 741–749, Jul. 1991.

[12] S. M. Taghavi and P. Pillay, "A Mechanically Robust Rotor With Transverse Laminations for a Wide-Speed-Range Synchronous Reluctance Traction Motor," *IEEE Transactions on Industry Applications*, vol. 51, no. 6, pp. 4404–4414, Nov. 2015.

[13] C. Desai, H. Mehta, and P. Pillay, "A novel fabrication and assembly method for synchronous reluctance machines," in *IEEE Energy Conversion Congress and Exposition (ECCE)*, Oct. 2017, pp. 3921–3926.

[14] K. Wang, Z. Q. Zhu, G. Ombach, M. Koch, S. Zhang, and J. Xu, "Optimal slot/pole and flux-barrier layer number combinations for synchronous reluctance machines," in *Eighth International Conference and Exhibition on Ecological Vehicles and Renewable Energies (EVER)*, Mar. 2013, pp. 1–8.

[15] M. N. Ibrahim, P. Sergeant, and E. M. Rashad, "Synchronous Reluctance Motor Performance Based on Different Electrical Steel Grades," *IEEE Transactions on Magnetics*, vol. 51, no. 11, pp. 1–4, Nov. 2015.

[16] A. Boglietti and M. Pastorelli, "Induction and synchronous reluctance motors comparison," in *34th Annual Conference of IEEE Industrial Electronics*, Nov. 2008, pp. 2041–2044.

[17] R. Moghaddam, F. Magnussen, and C. Sadarangani, "Theoretical and Experimental Reevaluation of Synchronous Reluctance Machine," *IEEE Transactions on Industrial Electronics*, vol. 57, no. 1, pp. 6–13, Jan. 2010.

[18] S. Taghavi and P. Pillay, "A Sizing Methodology of the Synchronous Reluctance Motor for Traction Applications," *IEEE Journal of Emerging and Selected Topics in Power Electronics*, vol. 2, no. 2, pp. 329–340, Jun. 2014.

[19] I. H. Lin, M. F. Hsieh, H. F. Kuo, and M. C. Tsai, "Improved Accuracy for Performance Evaluation of Synchronous Reluctance Motor," *IEEE Transactions on Magnetics*, vol. 51, no. 11, pp. 1–4, Nov. 2015.

[20] K. Lang, A. Muetze, R. Bauer, and S. Pircher, "Comparison of Induction and Synchronous Reluctance Machine Based Actuators for Elevated Temperature Environments," *IEEE Transactions on Energy Conversion*, vol. 31, no. 3, pp. 1012–1022, Sep. 2016.

[21] P. Guglielmi, M. Pastorelli, and A. Vagati, "Cross-Saturation Effects in IPM Motors and Related Impact on Sensorless Control," *IEEE Transactions on Industry Applications*, vol. 42, no. 6, pp. 1516–1522, Nov. 2006.

[22] E. Capecchi, P. Guglielmi, M. Pastorelli, and A. Vagati, "Position-sensorless control of the transverse-laminated synchronous reluctance motor," *IEEE Transactions on Industry Applications*, vol. 37, no. 6, pp. 1768–1776, Nov. 2001.

[23] M. Morimoto, "Rare earth free, traction motor for electric vehicle," in *International Electric Vehicle Conference (IEVC)*, 2012, pp. 1–4.

[24] N. Bianchi, S. Bolognani, E. Carraro, M. Castiello, and E. Fornasiero, "Electric Vehicle Traction Based on Synchronous Reluctance Motors," *IEEE Transactions on Industry Applications*, vol. 52, no. 6, pp. 4762–4769, Nov. 2016.

[25] M. Ferrari, N. Bianchi, A. Doria, and E. Fornasiero, "Design of Synchronous Reluctance Motor for Hybrid Electric Vehicles," *IEEE Transactions on Industry Applications*, vol. 51, no. 4, pp. 3030–3040, Jul. 2015.

[26] C. Babetto, G. Bacco, G. Berardi, and N. Bianchi, "High speed motors: A comparison between synchronous PM and reluctance machines," in *IEEE Energy Conversion Congress and Exposition (ECCE)*, Oct. 2017, pp. 3927–3934.

[27] M.-J. Jin, S. Cai, H. Hao, and J.-X. Shen, "Comparative study on synchronous reluctance and PM machines," *COMPEL - The International Journal for Computation and Mathematics in Electrical and Electronic Engineering*, vol. 35, no. 2, pp. 607–623, Mar. 2016.

[28] P. Matyska, "Advantages of synchronous reluctance motors," in *Transactions on Electrical Engineering*, vol. 3, no. 2, 2014, pp. 44–47.

[29] "DTC - A Motor Control Technique for all Seasons, ABB White Paper," https://library.e.abb.com/public/0e07ab6a2de30809c1257e2d0042db5e/ABB_WhitePaper_DTC_A4_20150414.pdf, Accessed: 02-03-2015.

[30] C. Donaghy-Spargo, "Synchronous reluctance motor technology: industrial opportunities, challenges and future direction," *Engineering and Technology Reference*, vol. 1, no. 1, May 2016.

[31] V. Dmitrievskii, V. Prakht, V. Kazakbaev, A. Pozdeev, and S. Oshurbekov, "Development of a high efficient electric drive with synchronous reluctance motor," in *18th International Conference on Electrical Machines and Systems (ICEMS)*, Oct. 2015, pp. 876–881.

[32] J. W. Finch and D. Giaouris, "Controlled AC Electrical Drives," *IEEE Transactions on Industrial Electronics*, vol. 55, no. 2, pp. 481–491, Feb. 2008.

[33] A. P. Goncalves, S. M. A. Cruz, F. Ferreira, A. M. S. Mendes, and A. T. De Almeida, "Synchronous Reluctance Motor Drive for Electric Vehicles Including Cross-Magnetic Saturation," in *Vehicle Power and Propulsion Conference (VPPC)*, 2014, pp. 1–6.

[34] K. Malekian, M. R. Sharif, and J. Milimonfared, "An optimal current vector control for synchronous reluctance motors incorporating field weakening," in *10th IEEE International Workshop on Advanced Motion Control, AMC'08.*, 2008, pp. 393–398.

[35] X. Zhang and G. H. B. Foo, "Over-modulation of Constant Switching Frequency based DTC for Reluctance Synchronous Motors incorporating Field-weakening Operation," *IEEE Transactions on Industrial Electronics*, 2018, early access.

[36] G. H. B. Foo and X. Zhang, "Robust Direct Torque Control of Synchronous Reluctance Motor Drives in the Field-Weakening Region," *IEEE Transactions on Power Electronics*, vol. 32, no. 2, pp. 1289–1298, Feb. 2017.

[37] G. S. Buja and M. P. Kazmierkowski, "Direct torque control of PWM inverter-fed AC motors - a survey," *IEEE Transactions on Industrial Electronics*, vol. 51, no. 4, pp. 744–757, Aug. 2004.

[38] S. Vazquez, J. Rodriguez, M. Rivera, L. G. Franquelo, and M. Norambuena, "Model Predictive Control for Power Converters and Drives: Advances and Trends," *IEEE Transactions on Industrial Electronics*, vol. 64, no. 2, pp. 935–947, Feb. 2017.

[39] C. Liu and Y. Luo, "Overview of advanced control strategies for electric machines," *Chinese Journal of Electrical Engineering*, vol. 3, no. 2, pp. 53–61, Sep. 2017.

[40] J. Rodriguez, M. P. Kazmierkowski, J. R. Espinoza, P. Zanchetta, H. Abu-Rub, H. A. Young, and C. A. Rojas, "State of the Art of Finite Control Set Model Predictive Control in Power Electronics," *IEEE Transactions on Industrial Informatics*, vol. 9, no. 2, pp. 1003–1016, May 2013.

[41] S. Vazquez, J. I. Leon, L. G. Franquelo, J. Rodriguez, H. A. Young, A. Marquez, and P. Zanchetta, "Model Predictive Control: A Review of Its Applications in Power Electronics," *IEEE Industrial Electronics Magazine*, vol. 8, no. 1, pp. 16–31, Mar. 2014.

[42] Y. Zhang, B. Xia, and H. Yang, "Performance evaluation of an improved model predictive control with field oriented control as a benchmark," *IET Electric Power Applications*, vol. 11, no. 5, pp. 677–687, 2017.

[43] F. Wang, X. Mei, J. Rodriguez, and R. Kennel, "Model predictive control for electrical drive systems-an overview," *CES Transactions on Electrical Machines and Systems*, vol. 1, no. 3, pp. 219–230, Sep. 2017.

[44] Y. Zhang, B. Xia, H. Yang, and J. Rodriguez, "Overview of model predictive control for induction motor drives," *Chinese Journal of Electrical Engineering*, vol. 2, no. 1, pp. 62–76, Jun. 2016.

[45] M. Xiao, T. Shi, Y. Yan, W. Xu, and C. Xia, "Predictive Torque Control of Permanent Magnet Synchronous Motor Using Flux Vector," *IEEE Transactions on Industry Applications*, pp. 1–1, 2018.

[46] M. Yildirim, M. Polat, and H. Kürüm, "A survey on comparison of electric motor types and drives used for electric vehicles," in *16th International Power Electronics and Motion Control Conference and Exposition*, Sep. 2014, pp. 218–223.

[47] M. Zeraoulia, M. E. H. Benbouzid, and D. Diallo, "Electric Motor Drive Selection Issues for HEV Propulsion Systems: A Comparative Study," *IEEE Transactions on Vehicular Technology*, vol. 55, no. 6, pp. 1756–1764, Nov. 2006.

[48] G. Pellegrino, R. I. Bojoi, and P. Guglielmi, "Unified Direct-Flux Vector Control for AC Motor Drives," *IEEE Transactions on Industry Applications*, vol. 47, no. 5, pp. 2093–2102, Sep. 2011.

[49] G. Pellegrino, E. Armando, and P. Guglielmi, "Direct-Flux Vector Control of IPM Motor Drives in the Maximum Torque Per Voltage Speed Range," *IEEE Transactions on Industrial Electronics*, vol. 59, no. 10, pp. 3780–3788, Oct. 2012.

[50] Y. Inoue, S. Morimoto, and M. Sanada, "A Novel Control Scheme for Maximum Power Operation of Synchronous Reluctance Motors Including Maximum Torque Per Flux Control," *IEEE Transactions on Industry Applications*, vol. 47, no. 1, pp. 115–121, Jan. 2011.

[51] X. Zhang and G. H. B. Foo, "A Robust Field-Weakening Algorithm Based on Duty Ratio Regulation for Direct Torque Controlled Synchronous Reluctance Motor," *ASME Transactions on Mechatronics*, vol. 21, no. 2, pp. 765–773, Apr. 2016.

[52] S. M. Ferdous, P. Garcia, M. A. M. Oninda, and M. A. Hoque, "MTPA and Field Weakening Control of Synchronous Reluctance motor," in *9th International Conference on Electrical and Computer Engineering (ICECE)*, Dec. 2016, pp. 598–601.

[53] V. Manzolini, D. D. Rù, and S. Bolognani, "A new control strategy for high efficiency wide speed range synchronous reluctance motor drives," in *IEEE International Electric Machines and Drives Conference (IEMDC)*, May 2017, pp. 1–7.

[54] E. Trancho, E. Ibarra, A. Arias, I. Kortabarria, J. Jurgens, L. Marengo, A. Fricassè, and J. V. Gragger, "PM-Assisted Synchronous Reluctance Machine Flux Weakening Control for EV and HEV Applications," *IEEE Transactions on Industrial Electronics*, vol. 65, no. 4, pp. 2986–2995, Apr. 2018.

[55] P. Krause, *Analysis of electric machinery and drive systems.* New York, USA: Mcgraw-Hill Book Company Inc, 1986.

[56] E. Clarke, *Circuit Analysis of AC Power Systems*. Wiley, 1943.

[57] R. H. Park, "Two-reaction theory of synchronous machines-II," *Transactions of the American Institute of Electrical Engineers*, vol. 52, no. 2, pp. 352–354, Jun. 1933.

[58] ——, "Two-reaction theory of synchronous machines generalized method of analysis-part I," *Transactions of the American Institute of Electrical Engineers*, vol. 48, no. 3, pp. 716–727, Jul. 1929.

[59] J. A. d. S. Junior, D. A. Andrade, G. P. Viajante, M. A. A. d. Freitas, and V. R. Bernadeli, "Analysis and Mathematical Modeling Of The Synchronous Reluctance Motor," *IEEE Latin America Transactions*, vol. 13, no. 12, pp. 3820–3825, Dec. 2015.

[60] R. Antonello, L. Ortombina, F. Tinazzi, and M. Zigliotto, "Online Stator Resistance Tracking for Reluctance and Interior Permanent Magnet Synchronous Motors," *IEEE Transactions on Industry Applications*, vol. 54, no. 4, pp. 3405–3414, Jul. 2018.

[61] C. Liu, P. Shih, S. Yen, H. Lin, Y. Hsu, and S. Lin, "Theoretical and Experimental Investigations of the Electromagnetic Steel Compositions for Synchronous Reluctance Motors," *IEEE Transactions on Industry Applications*, vol. 54, no. 3, pp. 2947–2954, May 2018.

[62] L. Peretti, P. Sandulescu, and G. Zanuso, "Self-commissioning of flux linkage curves of synchronous reluctance machines in quasi-standstill condition," *IET Electric Power Applications*, vol. 9, no. 9, pp. 642–651, 2015.

[63] L. Masisi, P. Pillay, and S. S. Williamson, "A Modulation Strategy for a Three-Level Inverter Synchronous Reluctance Motor (SynRM) Drive," *IEEE Transactions on Industry Applications*, vol. 52, no. 2, pp. 1874–1881, Mar. 2016.

[64] ——, "A Three-Level Neutral-Point-Clamped Inverter Synchronous Reluctance Machine Drive," *IEEE Transactions on Industry Applications*, vol. 51, no. 6, pp. 4531–4540, Nov. 2015.

[65] P. Vas, *Sensorless vector and direct torque control*. Oxford, UK: Oxford University Press, 1998.

[66] R. Antonello, L. Ortombina, F. Tinazzi, and M. Zigliotto, "Advanced current control of synchronous reluctance motors," in *IEEE 12th International Conference on Power Electronics and Drive Systems (PEDS)*, Dec. 2017, pp. 1,037–1,042.

[67] M. Hinkkanen, H. A. A. Awan, Z. Qu, T. Tuovinen, and F. Briz, "Current Control for Synchronous Motor Drives: Direct Discrete-Time Pole-Placement Design," *IEEE Transactions on Industry Applications*, vol. 52, no. 2, pp. 1530–1541, Mar. 2016.

[68] K. H. Ang, G. Chong, and Y. Li, "PID control system analysis, design, and technology," *IEEE Transactions on Control Systems Technology*, vol. 13, no. 4, pp. 559–576, Jul. 2005.

[69] T. Lubin, H. Razik, and A. Rezzoug, "Magnetic saturation effects on the control of a synchronous reluctance machine," *IEEE Transactions on Energy Conversion*, vol. 17, no. 3, pp. 356–362, Sep. 2002.

[70] F. Parasiliti, M. Villani, and A. Tassi, "Dynamic analysis of synchronous reluctance motor drives based on Simulink® and finite element model," in *32nd Annual Conference on IEEE Industrial Electronics, IECON*, 2006, pp. 1516–1520.

[71] I. Boldea, M. C. Paicu, and G. D. Andreescu, "Active Flux Concept for Motion-Sensorless Unified AC Drives," *IEEE Transactions on Power Electronics*, vol. 23, no. 5, pp. 2612–2618, Sep. 2008.

[72] R. E. Betz, R. Lagerquist, M. Jovanovic, T. J. E. Miller, and R. H. Middleton, "Control of synchronous reluctance machines," *IEEE Transactions on Industry Applications*, vol. 29, no. 6, pp. 1110–1122, Nov. 1993.

[73] P. R. Ghosh, A. Das, and G. Bhuvaneswari, "Performance comparison of different vector control approaches for a synchronous reluctance motor drive," in *IEEE 6th International Conference on Computer Applications In Electrical Engineering-Recent Advances (CERA)*, Oct. 2017, pp. 320–325.

[74] J. Pyrhönen, V. Hrabovcová, and R. S. Semken, *Electrical Machine Drives Control: An Introduction.* New York: Wiley, 2016.

[75] J. Malan and M. J. Kamper, "Performance of a hybrid electric vehicle using reluctance synchronous machine technology," *IEEE Transactions on Industry Applications*, vol. 37, no. 5, pp. 1319–1324, Sep. 2001.

[76] M. Ruba, F. Jurca, C. Martis, R. Martis, and P. F. Piglesan, "Analysis of maximum torque per ampere control strategy for variable reluctance synchronous machines for traction applications," in *IEEE International Conference and Exposition on Electrical and Power Engineering (EPE)*, Oct. 2014, pp. 322–326.

[77] E. M. Rashad, T. S. Radwan, and M. A. Rahman, "A maximum torque per ampere vector control strategy for synchronous reluctance motors considering saturation and iron losses," in *IEEE 39th IAS Annual Meeting Industry Applications Conference*, vol. 4, Oct. 2004, pp. 2411–2417.

[78] M. N. Ibrahim, P. Sergeant, and E. M. Rashad, "Relevance of Including Saturation and Position Dependence in the Inductances for Accurate Dynamic Modeling and Control of SynRMs," *IEEE Transactions on Industry Applications*, vol. 53, no. 1, pp. 151–160, Jan. 2017.

[79] A. Yousefi-Talouki, P. Pescetto, G. Pellegrino, and I. Boldea, "Combined Active Flux and High-Frequency Injection Methods for Sensorless Direct-Flux Vector Control of Synchronous Reluctance Machines," *IEEE Transactions on Power Electronics*, vol. 33, no. 3, pp. 2447–2457, Mar. 2018.

[80] I. Takahashi and T. Noguchi, "A new quick-response and high-efficiency control strategy of an induction motor," *IEEE Transactions on Industry applications*, no. 5, pp. 820–827, 1986.

[81] I. Takahashi and Y. Ohmori, "High-performance direct torque control of an induction motor," *IEEE Transactions on Industry Applications*, vol. 25, no. 2, pp. 257–264, 1989.

[82] T.-H. Liu and H.-H. Hsu, "Adaptive controller design for a synchronous reluctance motor drive system with direct torque control," *IET Electric Power Applications*, vol. 1, no. 5, p. 815, 2007.

[83] S. Ozcira and N. Bekiroglu, "Direct torque control of permanent magnet synchronous motors," M. T. Lamchich, Ed. Rijeka: IntechOpen, 2011, ch. 6.

[84] L. Q. Zhou, "Direct Torque Control of ALA Synchronous Reluctance Machine Based on Modified Integrator," in *IEEE Power Conversion Conference-Nagoya, (PCC)*, June. 2007, pp. 271–274.

[85] R. Morales-Caporal and M. Pacas, "Impact of the magnetic cross-saturation in a sensorless direct torque controlled synchronous reluctance machine based on test voltage signal injections," in *IEEE 34th Annual Conference of Industrial Electronics, IECON*, Jan. 2008, pp. 1234–1239.

[86] S. Bolognani, L. Peretti, and M. Zigliotto, "Online MTPA Control Strategy for DTC Synchronous-Reluctance-Motor Drives," *IEEE Transactions on Power Electronics*, vol. 26, no. 1, pp. 20–28, Jan. 2011.

[87] S. Wiedemann and A. Dziechciarz, "Comparative evaluation of DTC strategies for the Synchronous Reluctance machine," in *IEEE Tenth International Conference on Ecological Vehicles and Renewable Energies, (EVER)*, April 2015, pp. 1–5.

[88] F. B. Ion Boldea, Lorand Janosi, "A Modified Direct Torque Control (DTC) of Reluctance Synchronous Motor Sensorless Drive," *Electric Machines and Power Systems*, vol. 28, no. 2, pp. 115–128, Feb. 2000.

[89] A. Linder, *Model-based Predictive Control of Electric Drives.* Göttingen: Cuvillier Verlag, 2010.

[90] F. Wang, Z. Zhang, X. Mei, J. Rodríguez, and R. Kennel, "Advanced Control Strategies of Induction Machine: Field Oriented Control, Direct Torque Control and Model Predictive Control," *Energies*, vol. 11, no. 1, p. 120, Jan. 2018.

[91] P. Cortes, M. Kazmierkowski, R. Kennel, D. Quevedo, and J. Rodriguez, "Predictive Control in Power Electronics and Drives," *IEEE Transactions on Industrial Electronics*, vol. 55, no. 12, pp. 4312–4324, Dec. 2008.

[92] J. Rodriguez and P. Cortes, *Predictive Control of Power Converters and Electrical Drives*. Chichester, UK: IEEE Wiley press, 2012.

[93] S. R. Karpe, S. A. Deokar, and A. M. Dixit, "Switching losses minimization and performance improvement of PCC and PTC methods of model predictive direct torque control drives with 15-level inverter," *Journal of Electrical Systems and Information Technology*, Apr. 2017.

[94] W. B. Yaramasu. V, *Model Predictive Control of Wind Energy Conversion Systems*, ser. Wiley - IEEE. Wiley, 2016.

[95] S. Kouro, P. Cortes, R. Vargas, U. Ammann, and J. Rodriguez, "Model Predictive Control-A Simple and Powerful Method to Control Power Converters," *IEEE Transactions on Industrial Electronics*, vol. 56, no. 6, pp. 1826–1838, Jun. 2009.

[96] T. Geyer, G. Papafotiou, and M. Morari, "Model Predictive Direct Torque Control-Part I: Concept, Algorithm, and Analysis," *IEEE Transactions on Industrial Electronics*, vol. 56, no. 6, pp. 1894–1905, Jun. 2009.

[97] P. Karamanakos, P. Stolze, R. M. Kennel, S. Manias, and H. du Toit Mouton, "Variable Switching Point Predictive Torque Control of Induction Machines," *IEEE Journal of Emerging and Selected Topics in Power Electronics*, vol. 2, no. 2, pp. 285–295, Jun. 2014.

[98] V. Yaramasu, M. Rivera, M. Narimani, B. Wu, and J. Rodriguez, "High performance operation for a four-leg NPC inverter with two-sample-ahead predictive control strategy," *Electric Power Systems Research*, vol. 123, pp. 31–39, Jun. 2015.

[99] V. Yaramasu, M. Rivera, B. Wu, and J. Rodriguez, "Model Predictive Current Control of Two-Level Four-Leg Inverters -Part I: Concept, Algorithm, and Simulation Analysis," *IEEE Transactions on Power Electronics*, vol. 28, no. 7, pp. 3459–3468, Jul. 2013.

[100] J. Rodriguez, J. Pontt, C. A. Silva, P. Correa, P. Lezana, P. Cortes, and U. Ammann, "Predictive Current Control of a Voltage Source Inverter," *IEEE Transactions on Industrial Electronics*, vol. 54, no. 1, pp. 495–503, Feb. 2007.

[101] P. Cortés, S. Kouro, B. La Rocca, R. Vargas, J. Rodríguez, J. I. León, S. Vazquez, and L. G. Franquelo, "Guidelines for weighting factors design in model predictive control of power converters and drives," in *IEEE International Conference on Industrial Technology, (ICIT)*, Feb. 2009, pp. 1–7.

[102] H. Miranda, P. Cortes, J. Yuz, and J. Rodriguez, "Predictive Torque Control of Induction Machines Based on State-Space Models," *IEEE Transactions on Industrial Electronics*, vol. 56, no. 6, pp. 1916–1924, Jun. 2009.

[103] R. Vargas, P. Cortes, U. Ammann, J. Rodriguez, and J. Pontt, "Predictive Control of a Three-Phase Neutral-Point-Clamped Inverter," *IEEE Transactions on Industrial Electronics*, vol. 54, no. 5, pp. 2697–2705, Oct. 2007.

[104] R. Vargas, U. Ammann, J. Rodriguez, and J. Pontt, "Reduction of switching losses and increase in efficiency of power converters using predictive control," in *IEEE Power Electronics Specialists Conference, (PESC)*, Feb. 2008, pp. 1062–1068.

[105] F. Wang, S. Li, X. Mei, W. Xie, J. Rodríguez, and R. M. Kennel, "Model-Based Predictive Direct Control Strategies for Electrical Drives: An Experimental Evaluation of PTC and PCC Methods," *IEEE Transactions on Industrial Informatics*, vol. 11, no. 3, pp. 671–681, Jun. 2015.

[106] Y. Zhang and H. Yang, "Two-Vector-Based Model Predictive Torque Control Without Weighting Factors for Induction Motor Drives," *IEEE Transactions on Power Electronics*, vol. 31, no. 2, pp. 1381–1390, Feb. 2016.

[107] M. Preindl and E. Schaltz, "Sensorless Model Predictive Direct Current Control Using Novel Second-Order PLL Observer for PMSM Drive Systems," *IEEE Transactions on Industrial Electronics*, vol. 58, no. 9, pp. 4087–4095, Sep. 2011.

[108] M. Siami, D. A. Khaburi, and J. Rodríguez, "Torque Ripple Reduction of Predictive Torque Control for PMSM Drives With Parameter Mismatch," *IEEE Transactions on Power Electronics*, vol. 32, no. 9, pp. 7160–7168, Sep. 2017.

[109] P. Karamanakos, T. Geyer, N. Oikonomou, F. D. Kieferndorf, and S. Manias, "Direct Model Predictive Control: A Review of Strategies That Achieve Long Prediction Intervals for Power Electronics," *IEEE Industrial Electronics Magazine*, vol. 8, no. 1, pp. 32–43, Mar. 2014.

[110] T. Geyer, "A Comparison of Control and Modulation Schemes for Medium-Voltage Drives: Emerging Predictive Control Concepts Versus PWM-Based Schemes," *IEEE Transactions on Industry Applications*, vol. 47, no. 3, pp. 1380–1389, May 2011.

[111] P. Kakosimos and H. Abu-Rub, "Predictive Speed Control With Short Prediction Horizon for Permanent Magnet Synchronous Motor Drives," *IEEE Transactions on Power Electronics*, vol. 33, no. 3, pp. 2740–2750, Mar. 2018.

[112] T. Laczynski and A. Mertens, "Predictive Stator Current Control for Medium Voltage Drives With LC Filters," *IEEE Transactions on Power Electronics*, vol. 24, no. 11, pp. 2427–2435, Nov. 2009.

[113] P. Cortes, J. Rodriguez, S. Vazquez, and L. G. Franquelo, "Predictive control of a three-phase UPS inverter using two steps prediction horizon," in *IEEE International Conference on Industrial Technology*, 2010, pp. 1283–1288.

[114] Y. Zhang, J. Zhu, and W. Xu, "Predictive torque control of permanent magnet synchronous motor drive with reduced switching frequency," in *IEEE International Conference on Electrical Machines and Systems, (ICEMS)*, Oct. 2010, pp. 798–803.

[115] P. Cortes, J. Rodriguez, C. Silva, and A. Flores, "Delay Compensation in Model Predictive Current Control of a Three-Phase Inverter," *IEEE Transactions on Industrial Electronics*, vol. 59, no. 2, pp. 1323–1325, Feb. 2012.

[116] D. Zhou, J. Zhao, and Y. Liu, "Finite-control-set model predictive control scheme of three-phase four-leg back-to-back converter-fed induction motor drive," *IET Electric Power Applications*, vol. 11, no. 5, pp. 761–767, 2017.

[117] P. F. C. Goncalves and S. M. A. Cruz, "A new delay compensation method for finite control set model predictive control of induction motor drives," in *IEEE 16th Euro-*

pean Conference on Power Electronics and Applications (EPE'14-ECCE Europe), Aug. 2014, pp. 1–10.

[118] J. Rodriguez, R. M. Kennel, J. R. Espinoza, M. Trincado, C. A. Silva, and C. A. Rojas, "High-Performance Control Strategies for Electrical Drives: An Experimental Assessment," *IEEE Transactions on Industrial Electronics*, vol. 59, no. 2, pp. 812–820, Feb. 2012.

[119] S. A. Davari, D. A. Khaburi, and R. Kennel, "An Improved FCS-MPC Algorithm for an Induction Motor With an Imposed Optimized Weighting Factor," *IEEE Transactions on Power Electronics*, vol. 27, no. 3, pp. 1540–1551, Mar. 2012.

[120] R. Vargas, U. Ammann, B. Hudoffsky, J. Rodriguez, and P. Wheeler, "Predictive Torque Control of an Induction Machine Fed by a Matrix Converter With Reactive Input Power Control," *IEEE Transactions on Power Electronics*, vol. 25, no. 6, pp. 1426–1438, Jun. 2010.

[121] M. Preindl and S. Bolognani, "Model Predictive Direct Speed Control with Finite Control Set of PMSM Drive Systems," *IEEE Transactions on Power Electronics*, vol. 28, no. 2, pp. 1007–1015, Feb. 2013.

[122] C. A. Rojas, J. Rodriguez, F. Villarroel, J. R. Espinoza, C. A. Silva, and M. Trincado, "Predictive Torque and Flux Control Without Weighting Factors," *IEEE Transactions on Industrial Electronics*, vol. 60, no. 2, pp. 681–690, Feb. 2013.

[123] M. Siami, H. K. Savadkoohi, A. Abbaszadeh, D. A. Khaburi, J. Rodriguez, and M. Rivera, "Predictive torque control of a permanent magnet synchronous motor fed by a matrix converter without weighting factor," in *IEEE 7th Power Electronics and Drive Systems Technologies Conference, (PEDSTC)*, Feb. 2016, pp. 614–619.

[124] C. A. Rojas, J. R. Rodriguez, S. Kouro, and F. Villarroel, "Multiobjective Fuzzy-Decision-Making Predictive Torque Control for an Induction Motor Drive," *IEEE Transactions on Power Electronics*, vol. 32, no. 8, pp. 6245–6260, Aug. 2017.

[125] C. A. Rojas, J. Rodriguez, F. Villarroel, J. Espinoza, and D. A. Khaburi, "Multiobjective fuzzy predictive torque control of an induction motor drive," in *IEEE 6th Power Electronics, Drives Systems and Technologies Conference, (PEDSTC)*, Feb. 2015, pp. 201–206.

[126] Y. Zhang, H. Yang, and B. Xia, "Model-Predictive Control of Induction Motor Drives: Torque Control Versus Flux Control," *IEEE Transactions on Industry Applications*, vol. 52, no. 5, pp. 4050–4060, Sep. 2016.

[127] T. Geyer, "Computationally Efficient Model Predictive Direct Torque Control," *IEEE Transactions on Power Electronics*, vol. 26, no. 10, pp. 2804–2816, Oct. 2011.

[128] T. Geyer and D. E. Quevedo, "Multistep Finite Control Set Model Predictive Control for Power Electronics," *IEEE Transactions on Power Electronics*, vol. 29, no. 12, pp. 6836–6846, Dec. 2014.

[129] Y. Zhang and H. Lin, "Simplified model predictive current control method of voltage-source inverter," in *8th IEEE International Conference on Power Electronics - ECCE Asia*, May 2011, pp. 1726–1733.

[130] M. Habibullah, D. D. C. Lu, D. Xiao, and M. F. Rahman, "A Simplified Finite-State Predictive Direct Torque Control for Induction Motor Drive," *IEEE Transactions on Industrial Electronics*, vol. 63, no. 6, pp. 3964–3975, Jun. 2016.

[131] W. Xie, X. Wang, F. Wang, W. Xu, R. M. Kennel, D. Gerling, and R. D. Lorenz, "Finite-Control-Set Model Predictive Torque Control With a Deadbeat Solution for PMSM Drives," *IEEE Transactions on Industrial Electronics*, vol. 62, no. 9, pp. 5402–5410, Sep. 2015.

[132] Changliang Xia, Tao Liu, Tingna Shi, and Zhanfeng Song, "A Simplified Finite-Control-Set Model-Predictive Control for Power Converters," *IEEE Transactions on Industrial Informatics*, vol. 10, no. 2, pp. 991–1002, May 2014.

[133] A. A. Ahmed, B. K. Koh, H. S. Park, K.-B. Lee, and Y. I. Lee, "Finite-Control Set Model Predictive Control Method for Torque Control of Induction Motors Using a

State Tracking Cost Index," *IEEE Transactions on Industrial Electronics*, vol. 64, no. 3, pp. 1916–1928, Mar. 2017.

[134] H. Yang, Y. Zhang, P. D. Walker, N. Zhang, and B. Xia, "A Method to Start Rotating Induction Motor Based on Speed Sensorless Model-Predictive Control," *IEEE Transactions on Energy Conversion*, vol. 32, no. 1, pp. 359–368, Mar. 2017.

[135] L. Rovere, A. Formentini, A. Gaeta, P. Zanchetta, and M. Marchesoni, "Sensorless Finite-Control Set Model Predictive Control for IPMSM Drives," *IEEE Transactions on Industrial Electronics*, vol. 63, no. 9, pp. 5921–5931, Sep. 2016.

[136] F. Mwasilu, H. T. Nguyen, H. H. Choi, and J.-W. Jung, "Finite Set Model Predictive Control of Interior PM Synchronous Motor Drives With an External Disturbance Rejection Technique," *IEEE/ASME Transactions on Mechatronics*, vol. 22, no. 2, pp. 762–773, Apr. 2017.

[137] C.-K. Lin, Y.-S. Lai, H.-C. Yu, Y.-H. Lin, F.-M. Chen, and others, "Simplified model-free predictive current control for interior permanent magnet synchronous motors," *Electronics Letters*, vol. 52, no. 1, pp. 49–50, 2015.

[138] R. Morales-Caporal and M. Pacas, "A Predictive Torque Control for the Synchronous Reluctance Machine Taking Into Account the Magnetic Cross Saturation," *IEEE Transactions on Industrial Electronics*, vol. 54, no. 2, pp. 1161–1167, Apr. 2007.

[139] R. Antonello, M. Carraro, L. Peretti, and M. Zigliotto, "Hierarchical Scaled-States Direct Predictive Control of Synchronous Reluctance Motor Drives," *IEEE Transactions on Industrial Electronics*, pp. 1–1, 2016.

[140] C.-K. Lin, J.-t. Yu, Y.-S. Lai, and H.-C. Yu, "Improved model-free predictive current control for synchronous reluctance motor drives," *IEEE Transactions on Industrial Electronics*, vol. 63, no. 6, pp. 3942–3953, Jun. 2016.

[141] G. Pellegrino, T. M. Jahns, N. Bianchi, W. Soong, and F. Cupertino, *The Rediscovery of Synchronous Reluctance and Ferrite Permanent Magnet Motors*. SpringerBriefs in Electrical and Computer Engineering Cham: Springer International Publishing, 2016.

[142] S. Taghavi, "Design of synchronous reluctance machines for automotive applications," PhD thesis, Concordia University, March 2015.

[143] Jong-Bin Im, Wonho Kim, Kwangsoo Kim, Chang-Sung Jin, Jae-Hak Choi, and Ju Lee, "Inductance Calculation Method of Synchronous Reluctance Motor Including Iron Loss and Cross Magnetic Saturation," *IEEE Transactions on Magnetics*, vol. 45, no. 6, pp. 2803–2806, Jun. 2009.

[144] A. Kilthau and J. M. Pacas, "Appropriate models for the control of the synchronous reluctance machine," in *IEEE 37th IAS Annual Meeting*, vol. 4, Oct. 2002, pp. 2289–2295.

[145] A. Vagati, M. Pastorelli, F. Scapino, and G. Franceschini, "Impact of cross saturation in synchronous reluctance motors of the transverse-laminated type," *IEEE Transactions on Industry Applications*, vol. 36, no. 4, pp. 1039–1046, 2000.

[146] F. J. W. Barnard, W. T. Villet, and M. J. Kamper, "Hybrid Active-Flux and Arbitrary Injection Position Sensorless Control of Reluctance Synchronous Machines," *IEEE Transactions on Industry Applications*, vol. 51, no. 5, pp. 3899–3906, Sep. 2015.

[147] S. Yamamoto, H. Hirahara, J. B. Adawey, T. Ara, and K. Matsuse, "Maximum efficiency drives of synchronous reluctance motors by a novel loss minimization controller with inductance estimator," *IEEE Transactions on Industry Applications*, vol. 49, no. 6, pp. 2543–2551, 2013.

[148] P. Guglielmi, M. Pastorelli, and A. Vagati, "Impact of cross-saturation in sensorless control of transverse-laminated synchronous reluctance motors," *IEEE Transactions on Industrial Electronics*, vol. 53, no. 2, pp. 429–439, Apr. 2006.

[149] W. Xu and R. D. Lorenz, "High-Frequency Injection-Based Stator Flux Linkage and Torque Estimation for DB-DTFC Implementation on IPMSMs Considering Cross-Saturation Effects," *IEEE Transactions on Industry Applications*, vol. 50, no. 6, pp. 3805–3815, Nov. 2014.

[150] B. Stumberger, G. Stumberger, D. Dolinar, A. Hamler, and M. Trlep, "Evaluation of saturation and cross-magnetization effects in interior permanent-magnet synchronous motor," *IEEE Transactions on Industry Applications*, vol. 39, no. 5, pp. 1264–1271, Sep. 2003.

[151] G. Pellegrino, B. Boazzo, and T. M. Jahns, "Magnetic model self-identification for pm synchronous machine drives," *IEEE Transactions on Industry Applications*, vol. 51, no. 3, pp. 2246–2254, May 2015.

[152] N. Bedetti, S. Calligaro, and R. Petrella, "Stand-still self-identification of flux characteristics for synchronous reluctance machines using novel saturation approximating function and multiple linear regression," *IEEE Transactions on Industry Applications*, vol. 52, no. 4, pp. 3083–3092, Jul. 2016.

[153] S. A. Odhano, R. Bojoi, M. Popescu, and A. Tenconi, "Parameter identification and self-commissioning of AC permanent magnet machines - A review," in *IEEE Workshop on Electrical Machines Design, Control and Diagnosis (WEMDCD)*, Mar. 2015, pp. 195–203.

[154] D. F. V. Garcia, "Self-commissioning and testing of synchronous reluctance motor drives," Master's thesis, Oviedo University, 2017.

[155] S.-C. Agarlita, I. Boldea, and F. Blaabjerg, "High-Frequency-Injection-Assisted-Active-Flux-Based Sensorless Vector Control of Reluctance Synchronous Motors, With Experiments From Zero Speed," *IEEE Transactions on Industry Applications*, vol. 48, no. 6, pp. 1931–1939, Nov. 2012.

[156] H. Hadla and S. Cruz, "Active flux based finite control set model predictive control of synchronous reluctance motor drives," in *IEEE 18th European Conference on Power Electronics and Applications (EPE'16 ECCE Europe)*, Sep. 2016, pp. 1–10.

[157] R. Branco, "Modelling and simulation of synchronous reluctance motors," Master's thesis, University of Coimbra, 2015.

[158] H. Hadla and S. Cruz, "Predictive Stator Flux and Load Angle Control of Synchronous Reluctance Motor Drives Operating in a Wide Speed Range," *IEEE Transactions on Industrial Electronics*, vol. 64, no. 9, pp. 6950–6959, Sep. 2017.

[159] P. Vas, *Vector control of AC machines*, ser. Monographs in electrical and electronic engineering. Clarendon Press, 1990.

[160] J. Ahn, S.-B. Lim, K.-C. Kim, J. Lee, J.-H. Choi, S. Kim, and J.-P. Hong, "Field weakening control of synchronous reluctance motor for electric power steering," *IET Electric Power Applications*, vol. 1, no. 4, p. 565, 2007.

[161] X. Zhang, G. H. B. Foo, D. M. Vilathgamuwa, and D. L. Maskell, "An Improved Robust Field-Weakeaning Algorithm for Direct-Torque-Controlled Synchronous-Reluctance-Motor Drives," *IEEE Transactions on Industrial Electronics*, vol. 62, no. 5, pp. 3255–3264, May 2015.

[162] S. Junior, "Controlo do motor síncrono de relutância numa gama alargada de velocidades," Master's thesis, University of Coimbra, Coimbra, 2017.

[163] B. Boazzo and G. Pellegrino, "Model-Based Direct Flux Vector Control of Permanent-Magnet Synchronous Motor Drives," *IEEE Transactions on Industry Applications*, vol. 51, no. 4, pp. 3126–3136, Jul. 2015.

[164] M. Preindl and S. Bolognani, "Model Predictive Direct Torque Control With Finite Control Set for PMSM Drive Systems, Part 2: Field Weakening Operation," *IEEE Transactions on Industrial Informatics*, vol. 9, no. 2, pp. 648–657, May 2013.

[165] J. D. Barros, J. F. A. Silva, and E. G. A. Jesus, "Fast-Predictive Optimal Control of NPC Multilevel Converters," *IEEE Transactions on Industrial Electronics*, vol. 60, no. 2, pp. 619–627, Feb. 2013.

[166] G. Pellegrino, E. Armando, and P. Guglielmi, "Direct-flux field-oriented control of IPM motor drives with robust exploitation of the maximum torque per voltage speed range," in *IEEE International Symposium on Industrial Electronics (ISIE)*, 2010, pp. 1271–1277.

[167] S.-K. Sul, *Control of electric machine drive system.* Wiley-IEEE, 2011.

[168] A. Imura, T. Takahashi, M. Fujitsuna, T. Zanma, and S. Doki, "Dead-time compensation in model predictive instantaneous-current control," in *IEEE 38th Annual Conference on Industrial Electronics Society, IECON*, 2012, pp. 5037–5042.

[169] Z. Qu and M. Hinkkanen, "Loss-minimizing control of synchronous reluctance motors : A review," in *IEEE International Conference on Industrial Technology (ICIT)*, Feb. 2013, pp. 350–355.

[170] Z. Qu, T. Tuovinen, and M. Hinkkanen, "Minimizing losses of a synchronous reluctance motor drive taking into account core losses and magnetic saturation," in *IEEE 16th European Conference on Power Electronics and Applications*, Aug. 2014, pp. 1–10.

[171] A. Varatharajan, S. Cruz, H. Hadla, and F. Briz, "Predictive torque control of SynRM drives with online MTPA trajectory tracking and inductances estimation," in *IEEE International Conference Electric Machines and Drives (IEMDC)*, May 2017.

[172] J. Habibi and S. Vaez-Zadeh, "Efficiency-Optimizing Direct Torque Control of Permanent Magnet Synchronous Machines," in *IEEE 36th Power Electronics Specialists Conference*, Jun. 2005, pp. 759–764.

[173] A. Oliveira, D. Cavaleiro, R. Branco, H. Hadla, and S. Cruz, "An encoderless high-performance synchronous reluctance motor drive," in *IEEE International Conference on Industrial Technology (ICIT)*, 2015.

Appendix A: Simulation Models

This appendix presents the implementation of the simulation models using the proposed predictive control strategies for the SynRM drive in *Matlab/Simulink* environment.

Simulation model of the PAFTC: The general view of the simulation model for the PAFTC strategy is presented in Fig. A.1.

The main parts that constitute this simulation model are (i) the power electronics system; (ii) the SynRM model; (iii) the PAFTC block. The power electronics system includes the three phase voltage source, rectifier and the inverter block. These blocks were selected from the SimPowerSystem Toolbox of the *Matlab/Simulink* software.

The model of the SynRM was implemented using elementary Simulink blocks. The inputs of this model are the controlled three phase voltages, which are provided by the three phase inverter and the load torque. The load torque block allows the user to set the desired load torque applied to the motor shaft. This block has as outputs the stator currents, the motor electromagnetic torque, shaft speed, as well as the rotor position. The SynRM model and the power electronics system are sampled faster than the PAFTC block. The former are sampled at $10\,\mu s$, while the PAFTC block is sampled at $40\,\mu s$, in order to ensure that the simulation model of the drive system is similar to the actual experiment.

The inputs of the PAFTC block shown in Fig. A.2, are the measured stator currents, measured DC-link voltage, measured rotor speed and rotor position, and the reference speed block. The measured quantities and the reference speed set by user are used to estimate and predict the state variables for instant $k+1$ and $k+2$. The estimation and prediction of the state variables is done by means of a discretized mathematical model of the SynRM which uses the values of the inductances stored in the LUTs block. A cost function evaluates the predicted and reference values of the electromagnetic torque and active flux. The switching state that minimizes the cost function is the only output of the PAFTC block which will be applied to the IGBTs inside the inverter.

Simulation model of the S-PAFTC: A general overview of the simulation model for

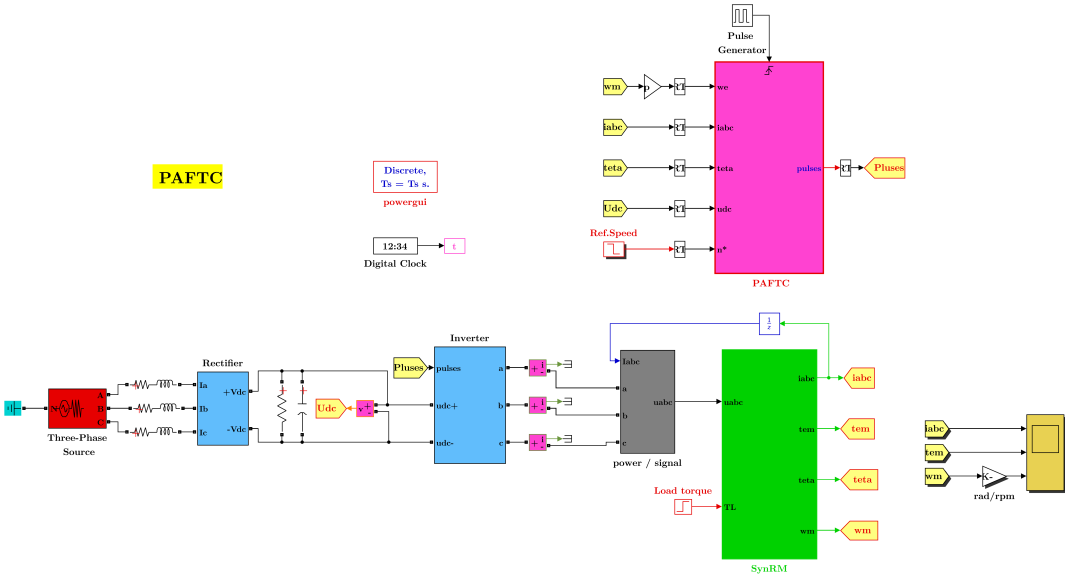

Fig. A.1. General view of the main components of the PAFTC-based SynRM drive model implemented in *Simulink*.

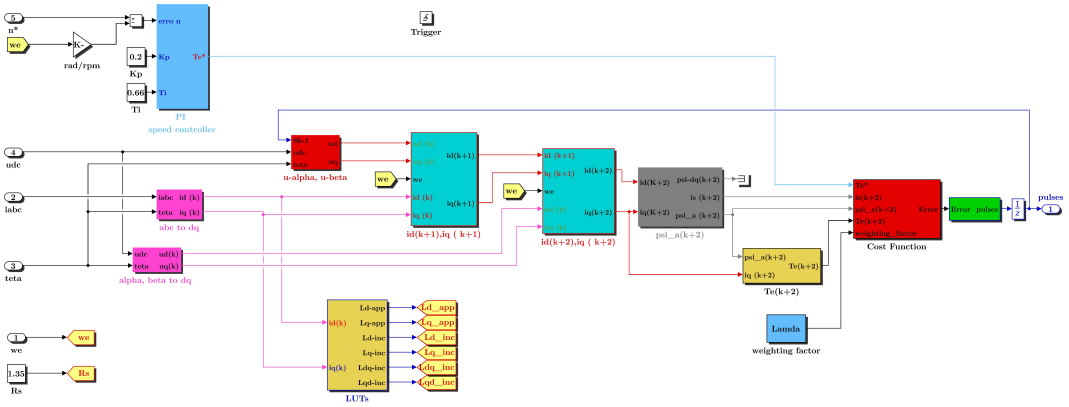

Fig. A.2. Global view of the PAFTC strategy implemented in *Simulink*.

the S-PAFTC strategy is shown in Fig. A.3. The simulation model of this control strategy is constructed with the same power electronics system and motor model already presented for the PAFTC strategy.

The S-PAFTC model block shown in Fig. A.4 differs from the model of the PAFTC. In this simulation model, the currents in the dq rotor frame are estimated for instant $k+1$ using the discretized mathematical model of the SynRM. The reference currents i_d^* and i_q^* are calculated with aid of the active flux equation and the PI speed controller block, respectively. The cost function block here evaluates the error between the seven voltage vectors generated by the inverter and the reference voltages $u_{dq}^*(k+1)$ in a rotor reference frame. The switching state that minimizes the cost function will be the output of the S-PAFTC block. Then this

switching state is applied to the inverter which in turn supplies the motor with the controlled three phase voltages.

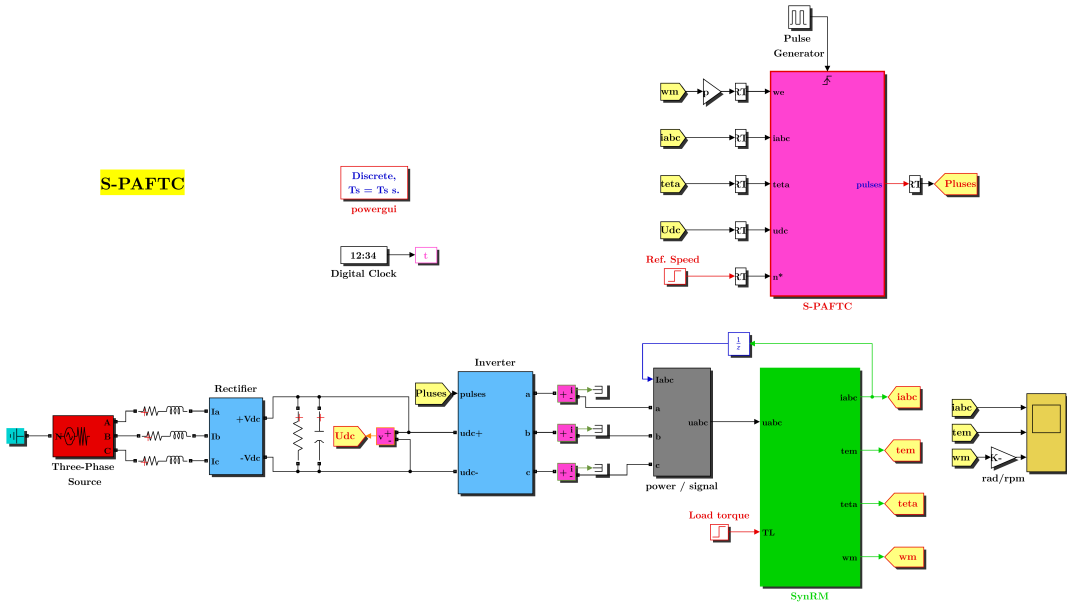

Fig. A.3. General view of the main components of the S-PAFTC-based SynRM drive model implemented in *Simulink*.

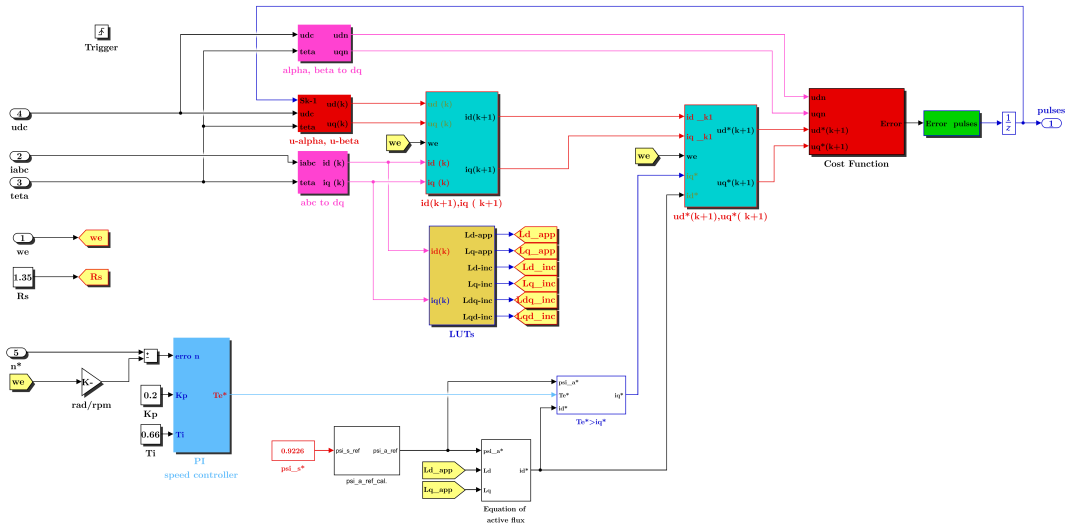

Fig. A.4. Global view of the S-PAFTC strategy implemented in *Simulink*.

Simulation model of the PLASFC: The general view of the simulation model for the PLASFC strategy is shown in Fig. A.5. The simulation model of this control strategy also comprises the power electronics system, the machine model block and the controller block. The power electronics system and the machine model block are identical to those ones of the PAFTC and S-PAFTC strategies.

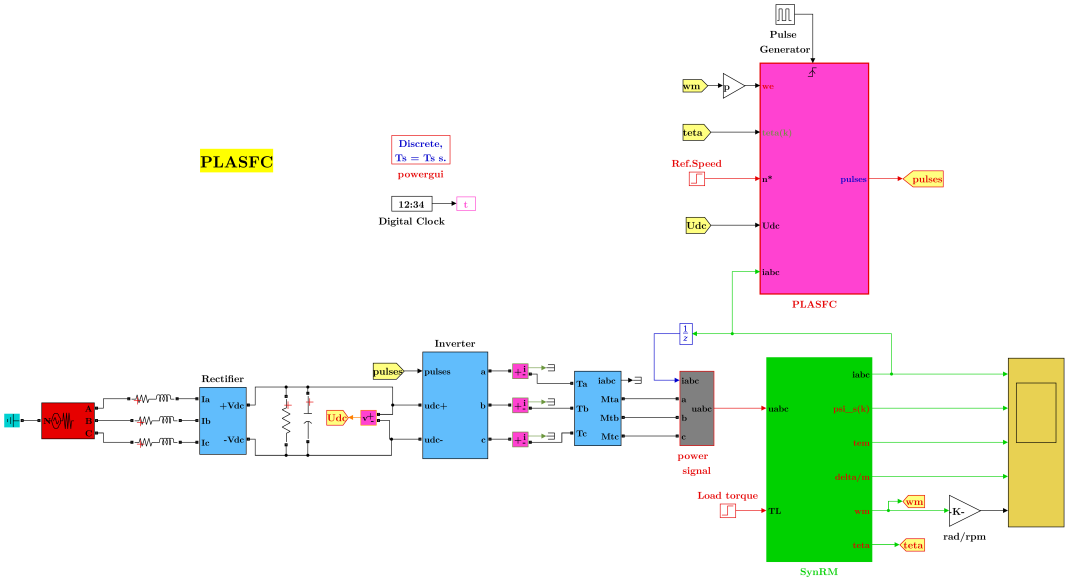

Fig. A.5. General view of the main components of the PLASFC implemented in *Simulink*.

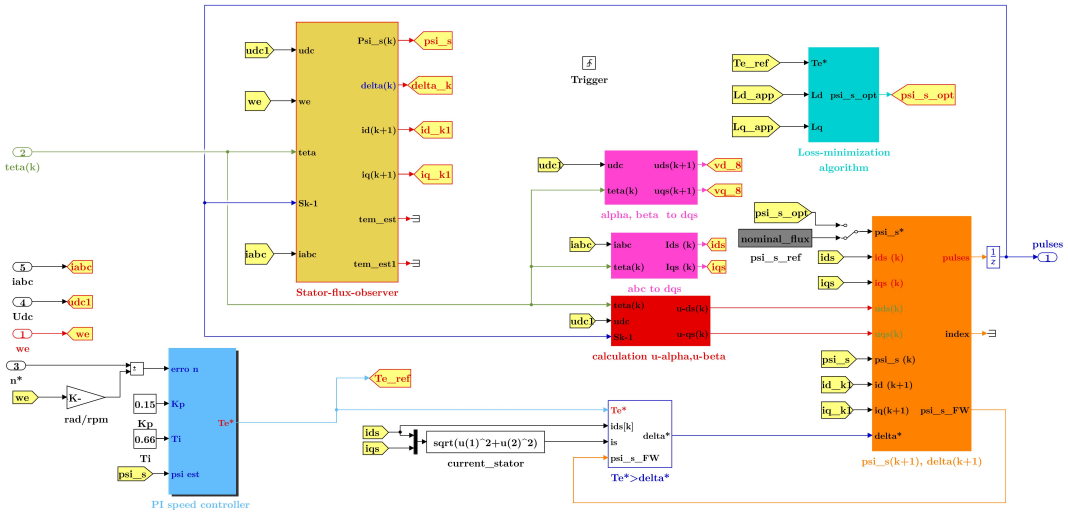

Fig. A.6. Global view of the PLASFC strategy implemented in *Simulink*.

The simulation model block of the PLASFC is illustrated in Fig. A.6. The inputs of this block are the measured stator currents, measured DC-link voltage, and the measured speed and rotor position. The stator flux observer block uses these measured quantities to estimate the stator flux amplitude and load angle at instant k, while the PI speed controller block generates the reference torque which is needed later on to calculate the reference load angle. The stator flux reference can be set to its rated value or be adjusted using the loss minimization algorithm block. A discretized mathematical model of the motor in the stator flux reference frame is utilized to estimate the stator flux and load angle for instant $k+1$.

The cost function here evaluates the error between the seven voltage vectors generated by the inverter and the reference voltages $u^*_{dqs}(k+1)$ in the stator flux reference frame. The switching state that minimizes the cost function will be the output of the PLASFC block. The selected switching state is then sent to the inverter which in turn feeds the motor with the controlled three phase voltages.

Appendix B: Components of the Experimental Setup

In this appendix the main components of the experimental SynRM drive system are presented.

- **Motors:** The Fig. B.1 shows the motors that were used in the experiments.

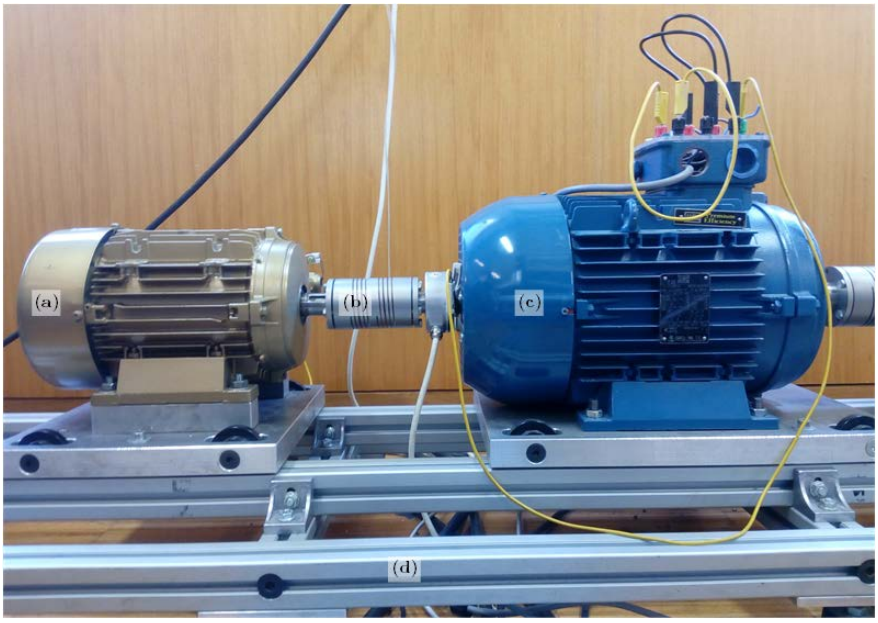

Fig. B.1. Motors used in the experimental tests (a) SynRM; (b) semi-flexible coupling; (c) three-phase IM that acts as a load, controlled by a VSD; (d) support base.

- **Power circuit Contains:** (a) a three-phase diode bridge rectifier, supplied by an autotransformer (Fig. B.2 (a)); (b) a DC-link, with capacitors of 4700 μF (Fig. B.2 (b)) and a braking resistor of 100 Ω (Fig. B.2 (c)); (c) a three-phase inverter (Fig. B.3), model SEMIKRON 132GD120-3DU, it has a nominal voltage of 1200 V and a rated current of 150 A. This inverter is used to feed the SynRM controlled by the proposed predictive control strategies. Furthermore, it allows to directly command the IGBT gate signals from the dSPACE control platform. The SynRM is coupled to a variable speed induction motor drive, model WEG CFW09 Vectrue Inverter (see Fig. B.4). Finally, the signal conditioning circuit shown in Fig. B.5 is used with the

objective of converting the measured power signals into signals compatible with the inputs of the dSPACE control platform.

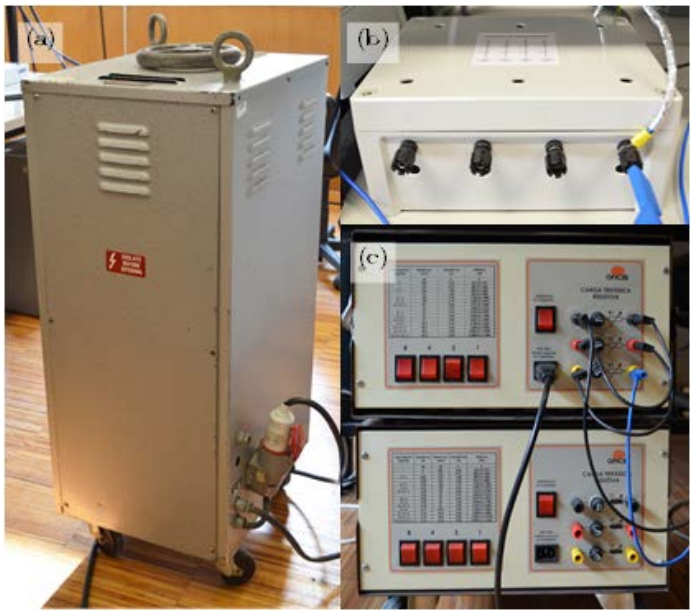

Fig. B.2. (a) Autotransformer; (b) Capacitor bank and (c) braking resistor.

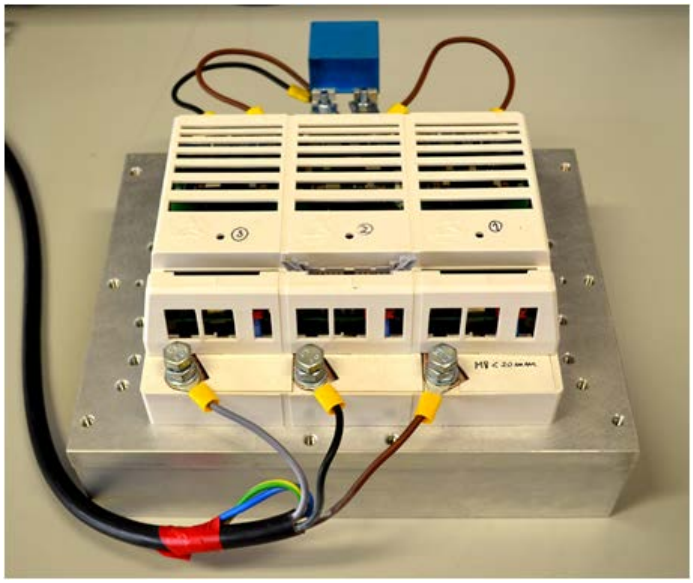

Fig. B.3. Inverter bridge.

- **Control platform:** The dSPACE platform used in the real-time control system is the ds1103 model. The interface of this platform is presented in Fig. B.6. The signals to be measured are connected to analog-to-digital conversion channels. The interaction between the operator and the control platform is realized through a control panel

Fig. B.4. Variable speed drive.

Fig. B.5. Measurement and signal conditioning circuit.

created using *ControlDesk* software, as shown in Fig. B.7. Using the Control panel allows to visualize and capture all variables of interest in real-time.

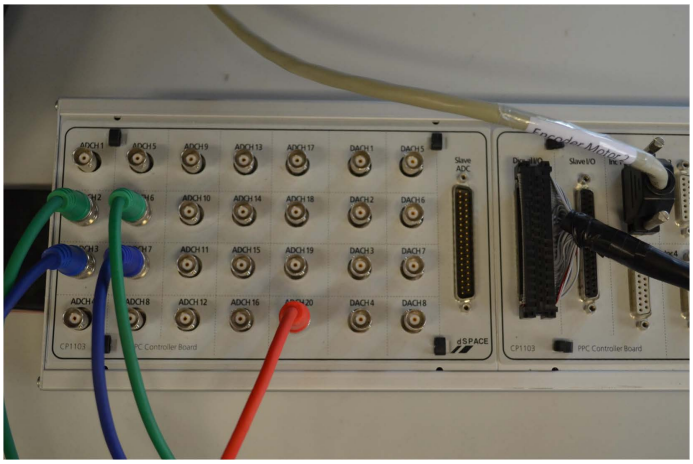

Fig. B.6. Terminal panel of the ds1103 control platform.

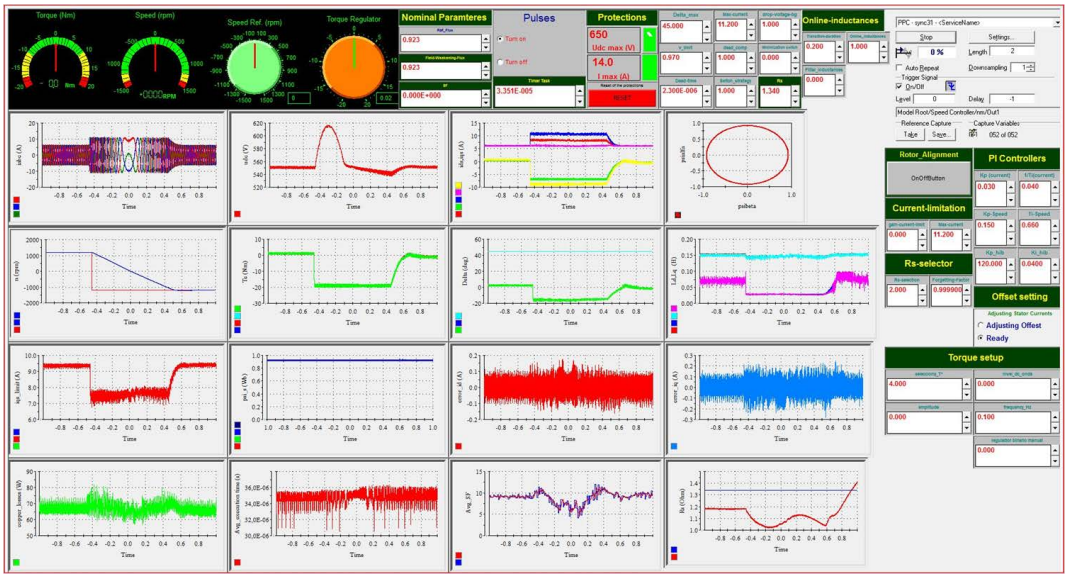

Fig. B.7. Control panel built using *ControlDesk* software.

- **Power anaylzer and torque sensor:** A high precision power analyzer, Yokogawa WT3000, shown in Fig. B.8, is used to compute the motor efficiency. This power analyzer has four channels, the first channel measures the DC-link voltage and current to calculate the input power of the inverter, the second and third channels measure the line voltages and phase currents of the SynRM in order to calculate the input power of the motor (which is equal to the output power of the inverter). Other two analog inputs are connected to the torque sensor, shown in Fig. B.9. With the data obtained from the power analyzer and torque sensor, it is possible to calculate the efficiency of both the inverter and SynRM and thereby of the entire drive system.

Fig. B.8. High precision power analyzer (Yokogawa WT3000).

Fig. B.9. Torque sensor (model RWT321).

Appendix C:Parameters of the SynRM Drive

Calculation of the reference active flux: The reference active flux ${\psi_a}^*$ used in the PAFTC and S-PAFTC strategies is calculated and updated in real-time according to

$$ {\psi_a}^* = \psi_{sn} - L_q \left| i_d + j i_q \right| . \tag{C.1} $$

The rated stator flux ψ_{sn} is given by

$$ \psi_{sn} \approx \frac{\sqrt{2}\, U_n}{\sqrt{3} \times 2\pi\, f_n}, \tag{C.2} $$

where $U_n = 355$ V and $f_n = 50$ Hz are the rated voltage and frequency values of the SynRM under study, respectively. Using these values in (C.2) one obtains $\psi_{sn} \approx 0.923$ Wb. The apparent inductance L_q in (C.1) is obtained from LUTs, using the two current components i_d and i_q. Thus, the value of L_q is dependent on the operating condition of the SynRM. As a result, the reference active flux is also varying over time and needs to be updated in real-time.

Parameters of the SynRM: The parameters of the SynRM used in the simulation and experimental tests are listed in Table C.1.

Table C.1: Parameters of the SynRM used in the tests.

Parameters	Value
Rated power P_n	3 kW
Rated voltage U_n	355 V
Rated current I_n	7.9 A
Rated frequency f_n	50 Hz
Rated stator flux ψ_n	0.923 Wb
Rated torque T_n	19.1 N.m
Rated speed n_n	1500 rpm
Rated efficiency η	90.4 %
Rotor inertia J_m	0.07941 kg.m^2
Stator resistance R_s	1.35 Ω

Parameters of the control strategies: In Table C.2, the control parameters related to the practical implementation of the proposed control strategies are listed.

Table C.2: Main control parameters used for the proposed control strategies.

Parameters		PAFTC	S-PAFTC	PLASFC
Sampling time	T_s	40 μs	40 μs	40 μs
Weighting factor	λ_{ψ_a}	0.2	-	-
Speed PI controller (sampling at 1000 Hz)	K_p	0.15	0.15	0.15
	T_i	0.66	0.66	0.66
Hybrid stator flux observer	K_P^{ui}	-	-	120
	T_i^{ui}	-	-	1.4×10^{-4}

Parameters of the DFVC strategy: In Table C.3, the control parameters related to the practical implementation of the DFVC strategy are listed.

Table C.3: Main control parameters used for the DFVC strategy.

Parameters										
Sampling time	**Speed PI controller**		**Flux PI controller**		**Current PI controller**		**Load angle PI controller**		**Hybrid stator flux observer**	
T_s	K_p	T_i	K_p	T_i	K_p	T_i	K_p	T_i	K_P^{ui}	T_i^{ui}
66.6 μs	0.15	0.66	1500	0.00005	100	0.00006	0.62	0.0079	120	1.4×10^{-4}